COMBINED ANALYTICAL AND EXPERIMENTAL APPROACHES TO DYNAMIC COMPONENT STRESS PREDICTION

A Dissertation
Presented to
The Academic Faculty

by

Maria Chierichetti

In Partial Fulfillment
of the Requirements for the Degree
Doctor of Philosophy in
Aerospace Engineering

School of Aerospace Engineering
Georgia Institute of Technology
August 2012

COMBINED ANALYTICAL AND EXPERIMENTAL APPROACHES TO DYNAMIC COMPONENT STRESS PREDICTION

Approved by:

Dr. Massimo Ruzzene, Advisor
School of Aerospace Engineering
Georgia Institute of Technology

Dr. Olivier A. Bauchau, Co-Advisor
School of Aerospace Engineering
Georgia Institute of Technology

Dr. Dewey H. Hodges
School of Aerospace Engineering
Georgia Institute of Technology

Dr. Marilyn J. Smith
School of Aerospace Engineering
Georgia Institute of Technology

Dr. Nagaraja Iyyer, TDA, Inc.
School of Aerospace Engineering
Georgia Institute of Technology

Date Approved: June 2012

To my son Pietro,

ACKNOWLEDGEMENTS

At the end of my Ph.D., I would like to particularly thank my advisor, Dr. Massimo Ruzzene, for his continuous encouragements and advices. I am mostly grateful to him for his professional and personal trust in my work and abilities, and for his special attention and care to my person and my family. His teachings go well beyond the topics of the thesis, and they will accompany me all my life.

A special thank to my husband Filippo. We started the adventure of the Ph.D. together in 2009, and offered each other unconditional support throughout the years, the study nights, the birth of our son Pietro. Sometimes in competition, always trying to help each other. I look forward all the future years to come.

I must also thank Dr. Olivier Bauchau for his advice in the first years of my Ph.D.. His enthusiasm for engineering and vast knowledge have always inspired me and stirred my curiosity. I also would like to thank my Thesis Committee Members for dedicating me their time and providing me with insightful comments, instrumental for the completion of this thesis. I would like to thank also Chance McColl and Doug Palmer for the many discussions on the project and their advices.

I would like to particularly thank my parents and brothers, as well as all my in-law family, for their continuous support throughout these years, and for coming, one after the other, to Atlanta to help me to complete my dissertation. I am mostly grateful to all of you.

A final thank to all the friends that have accompanied me in these years, and that made me feel Atlanta as my home, and my new friends as my family: Francesco, with whom we shared so many dinners and nights, Daniel, Emanuele, Anna, Steve, Timothy, Ale, Marco.

TABLE OF CONTENTS

LIST OF TABLES

LIST OF FIGURES

SUMMARY

In modern times, the ability to investigate the aeroelastic behavior of dynamic components on rotorcraft has become essential for the prediction of their useful fatigue life. At the same time, the aeroelastic modeling of a rotorcraft is particularly complex and costly. Inaccuracies in numerical predictions are mostly due to imprecisions in the structural modeling, to the presence of structural degradation or to the limited information on aerodynamic loads. The integration of experimental measurements on dynamic components such as rotor blades has the potential to improve fatigue estimation, augment the knowledge of the dynamic behavior and inform numerical models.

The objective of this research is the development of a combined numerical and experimental approach, named *Confluence Algorithm*, that accurately predicts the response of dynamic components with a limited set of experimental data. The integration of experimental measurements into a numerical algorithm enables the continuous and accurate tracking of the dynamic strain and stress fields. The Confluence Algorithm systematically updates the numerical model of the external loads, and mass and stiffness distributions to improve the representation and extrapolation of the experimental data, and to extract information on the response of the system at non-measured locations.

The capabilities of this algorithm are first verified in a numerical framework and with well-controlled lab experiments. Numerical results from a comprehensive UH-60A multibody model are then compared with available experimental data. These analyses demonstrate that the integration of the Confluence Algorithm improves the accuracy of the numerical prediction of the dynamic response of systems characterized

by a periodic behavior, even in presence of non-linearities. The algorithm enables the use of simplified models that are corrected through experimental data to achieve accurate tracking of the system.

CHAPTER I

INTRODUCTION

1.1 Background

In modern times, the ability to investigate the aeroelastic behavior of dynamic components on rotorcraft has become essential for the prediction of fatigue life. The aeroelastic modeling of a rotorcraft is particularly complex and costly. It requires the coupling of a structural dynamic module that predicts the dynamic response given the loads applied to the system, a fluid dynamic module that computes the aerodynamic loads acting on the structure, and an interaction module that captures aeroelastic effects. The complexity of this coupled behavior leads to inaccuracies in numerical predictions, which are mostly due to imprecisions in the structural modeling, to the presence of structural degradation, or to the lack of information on the aerodynamic loads. As a result, the life of rotorcraft components is often underestimated, which undermines safety and dramatically increases operational costs. For these reasons, the development of reliable response prediction methodologies for rotorcraft components is an ongoing challenge for the research community.

Improvements to the estimate of fatigue life are expected to come from the addition of experimental monitoring of dynamic components (generally defined as Usage Health Monitoring Systems - UHMS). The implementation of UHMS has the potential for a component life increase of about two-and-half times beyond the design fatigue life [77, 39]. The reason for this improvement is based on the fact that structural degradations that lead to potential failures may be detected, and that specific maintenance processes can be implemented. This process may be classified as Condition Based Maintenance (CBM), whereby maintenance operations are defined by

inputs of the monitoring system, instead of being defined by a predefined maintenance schedule.

Recent investigations performed at NASA and AFRL also suggest that the integration of experimental measurements and high-fidelity models into a real-time-mission-life virtual "twin" of the system enables a continuous monitoring and forecast of the health of the vehicle, including its remaining useful life and the probability of mission success [64, 67, 75, 41, 74]. The integration of usage monitoring systems is therefore expected to result in both improvements in the system safety and in a decrease in life cycle costs.

The introduction of UHMS in complex rotating environments is however a challenging problem and can actually result in an increase in mechanical complexity that could almost nullify the advantages. Moreover, the function of most UHMS is limited to monitoring specific locations in the system (where sensors are installed), while tracking of remote and non-accessible locations is not possible. Numerical algorithms need to be designed and integrated into UHMS so that complete accurate predictions of the response field (maps) of the rotorcraft can be obtained based on a minimal number of experimental measurements.

1.2 Objectives

A numerical procedure, called *Confluence Algorithm* (CA), is presented in this work that corrects inaccuracies in the structural modeling of a dynamic system and in the prediction of the externally applied loads based on the analysis of the experimental response measured at discrete locations. The objective is the achievement of accurate and reliable maps of the dynamic response of the system through a continuous updating of an initial model to create a tailored numerical model based on the measured dynamic response at some locations in the systems. The advantage offered by this process is a reduced cost of inspections as a more precise tracking of the response

may allow the identification of structural degradations and heavy loads.

In the context of this thesis, the updating process of aeroelastic models is divided into two separate components: (1) a module for the correction of the externally applied loads, and (2) a module for the update of the physical properties. Initially, it is assumed that inaccuracies in loads and in mass/stiffness matrices can be singularly improved by neglecting the presence of the other source of error. First, the *Load Confluence Algorithm* (LCA) identifies corrections to the external loads based on the assumption that errors in numerical predictions are due to lack of information on the external loads while physical properties are considered as accurately described. Next, a separate procedure named *Property Confluence Algorithm* (PCA) is developed for the correction of physical properties, which assumes that inaccuracies in the initial prediction of the response can be attributed to the lack of knowledge on the actual mass and stiffness distribution of the system. The assumption of a separate occurrence of inaccuracies in loads and physical properties can be then removed, and the two procedures can be combined into the *System Confluence Algorithm* (SCA), where systematic corrections are applied to both the model of the external loads and to the mass and stiffness matrices of the system to achieve a numerical model specifically tailored to the experimental measurements.

The CA can be described as a fitting process that estimates the map of the response of the system from a known number of measurements at control points (experimental measurements/reference data). In the following, this process in often denoted as *mapping* of the response. The possibility of mapping the response of a system from a few experimental measurements to a detailed numerical model consists in a way to track the history of a single machine, to tailor the model to the actual conditions each machine encounters and to estimate its remaining life independently from its initial design.

The process depicted in Figure 1 describes how the SCA could be embedded in

a UHMS to map the dynamic response of a system: from measured data during operating conditions at few locations, the complete model of the machine is improved so that the stresses and vibrations can be accurately predicted and provide accurate information on the remaining life of the system. This approach represents a significant step towards the implementation of CBM, because a set of maintenance actions based on real-time or near-real time assessment of components from experimental measurements could be defined [39].

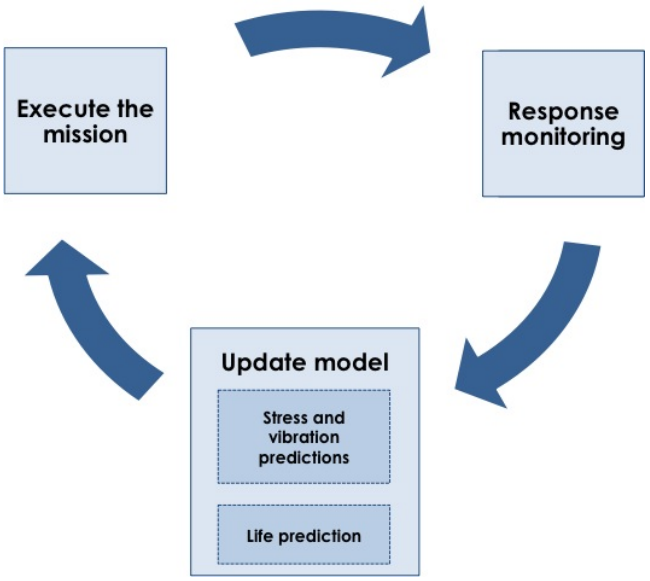

Figure 1: Calibration of a numerical model to experimental measurements.

1.3 Applications to rotorcraft and wind turbines

The CA can be embedded in UHMS to continuously monitor the structural behavior of rotor blades in helicopters and wind turbines. The advantage of this algorithm is the possibility of providing information on the entire span of the blades from a limited number of measurements at discrete locations. The Confluence Algorithm can also be embedded into the control system for the rotor as an observer of the dynamics of the state from measurements at discrete locations. The importance of the applications to rotorcraft and wind turbines is described in this section.

1.3.1 Applications to rotorcraft

Accurate prediction of rotor loads and vibrations is fundamental for effective rotorcraft design and maintenance. High vibratory loads are, in fact, an important cause of high maintenance man-hours per flight hour and of the need for frequent replacements of components. The low helicopter reliability and the unsatisfactory ability to predict vibration levels do not allow fatigue characteristics to be established and to properly evaluate the performance of vibration reduction devices [7]. Major challenges are therefore associated with the development of new processes that allow a quick and low cost evaluation of rotorcraft characteristics and performance.

Maintenance and parts replacement costs require potential vibration problems and their effects to be diagnosed as early as possible during the development cycle of an helicopter. Although vibration levels have been lowered considerably by improved design and a variety of isolation and absorber systems, they are still of concern because rotorcraft are flown faster and in more violent maneuvers where vibrations reach the highest levels. In addition, more delicate instruments, more demanding visual and tactile tasks, and demands for accurate sensor and weapon pointing lead to requirements for very low vibration levels throughout the aircraft [24].

The versatility of operation of helicopters results in the fact that new uses are added to the forecast design purposes, especially after production has been ongoing for a number of years. Also, missions may extend well beyond the originally envisaged design life. This means that helicopter designers can only make a "best guess" as to what type of missions the helicopter will fly. If a monitoring device is installed on each machine, it would be possible to establish the severity and type of missions flown, or loads and vibrations experienced, and to appropriately adjust the safe-life predictions [58].

Health and usage monitoring can therefore increase helicopter safety and has the potential to decrease operating costs. However, major drawbacks of usage monitoring

systems include high potential operating costs since they generally accumulate vast quantities of data. In addition, there will inevitably be a delay between the time that the data are recorded and processed unless a real-time procedure is provided.

One of the most common usage monitoring methods for helicopter applications, called flight load monitoring (FLM), attempts to quantify in-flight fatigue cycles from the output of strain gages mounted on several key components. The monitored components are mainly those in the rotating system since they are the most prone to fatigue failures. Once strains have been acquired, they are converted to loads. These loads are then used to derive loads in non-strain-gaged components via the use of transfer functions. After this, the fatigue damage can be determined. Currently, FLM has been restricted to applications involving testing and research because of problems associated with transferring strain gage signals from the rotating system to the airframe. New technologies in sensor design (i.e. wireless sensors) open new possibilities in this direction [58]. The CA represents a promising tool in this direction.

1.3.2 Applications to wind turbines

Another important application of the CA in combination with a structural health monitoring system consists of wind turbines, whose importance as a renewable source of energy is increasing over time because of their relative cost competitiveness and technological maturity with respect to other renewable sources of energy. Their size has been growing continuously to harvest more energy through higher efficiencies and due to cost-effective considerations. The typical diameter of the rotor has in fact increased about 10 times in the last two decades, and the improvement in power production of about 100 times (Figure 2). This increase in dimensions and the remote location in which wind plants are generally located make inspection and maintenance work difficult, undermining their cost-effectiveness and safety. Maintenance and logistic costs are enormous, and downtime of the plant is recurrent (an average wind

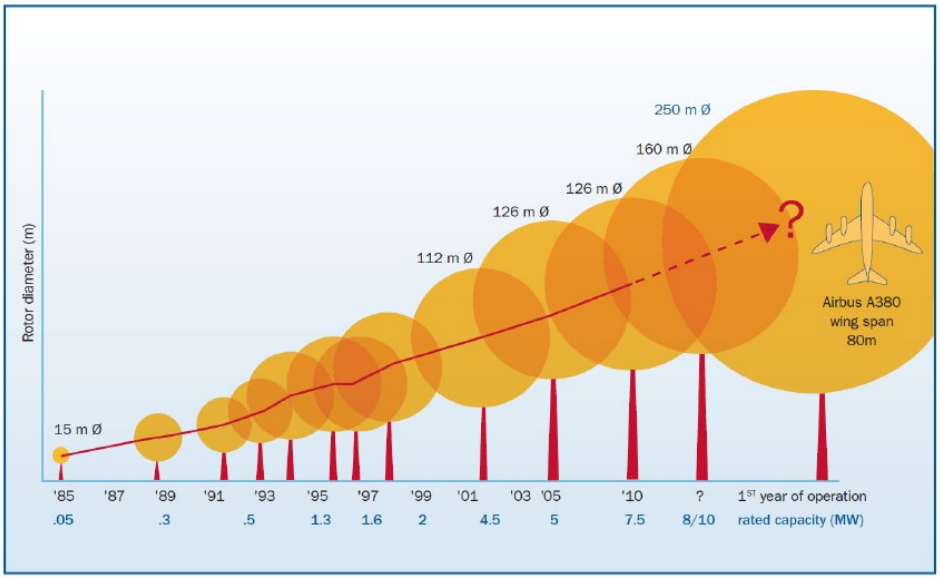

Figure 2: Wind turbine size evolution [42].

turbine is inactive for about a week per year for repairs and maintenance [43]) in an effort to avoid catastrophic failures.

The continuous monitoring of wind turbines is expected to provide the means to ensure that the turbine is in good condition [79]. Condition monitoring can be performed either off-line or on-line: off-line monitoring requires that the wind turbine is taken out of service and inspected while on-line systems continuously monitor the machine. Off-line inspections are routinely scheduled at regular time intervals, while on-line monitoring systems are incorporated into the turbine and continuously monitor parameters such as temperature, speeds, and tower vibrations.

Among all the monitoring systems, structural health monitoring (SHM) systems are of primary importance because the damage frequency of the structure and of all the other mechanical systems is almost equal. In particular, blade damage, such as surface damage, cracks, structural discontinuities, as well as catastrophic failures of the whole blade (Figure 3) are the most common type of structural failure as well as the most expensive type of damage to repair. It represents about 7% of total unforeseen malfunctions in a turbine, resulting in an average of four days of downtime

per year [43]. In addition, rotor blades are a key element in power generation and account for about 15-20% of the total cost. The structural monitoring of rotor blades is therefore of primary importance to ensure high efficiencies. A structural health

Figure 3: An example of catastrophic blade failure in a wind turbine.

monitoring system for rotor blades needs to be low cost, reliable and integrated into the structure and can result in more affordable wind energy by minimizing inspection-time, by preventing failures and by predicting the exact remaining life. SHM may allow lighter blades that would provide higher performance with less conservative margins of safety [32]. In addition, the data collected by SHM can be used to improve designs for next generation wind turbines.

In this scenario, the CA could be embedded in a monitoring system for rotor blades to provide continuous monitoring of the entire span from a limited number of sensors located along the blade. With respect to traditional monitoring systems, it would provide information for the blade even at inaccessible locations.

1.4 Mapping of the response from experimental measurements

The improvements of dynamic models based on experimental measurements is a fundamental problem in dynamics, because of the limitations of numerical models in representing real systems. Research in this field is very active and can be classified

according to the objectives of each approach. Examples are the identification of applied loads (Force Reconstruction techniques, section 1.4.1, and Force Determination techniques specifically formulated for rotorcraft, section 1.4.2), the mapping of the deflected shape (Shape Sensing methods, section 1.4.3), the correct representation of the kinematics (Inverse Dynamics methods, 1.4.4), and the updating of the physical properties of the system in terms of mass, stiffness and damping. A separate section, 1.5, has been devoted to this last class of methods, called model updating techniques, due to the maturity of the research in this field.

1.4.1 Force Reconstruction methods

The first class of methods is often denoted as *Force Reconstruction* (FR) techniques. Their main goal is to locate and identify the external forces both in terms of magnitude and phase. FR techniques are generally classified into direct and optimization methods [80]. Direct approaches are based on frequency response function (FRF) measurements, from which the input force is estimated. When dealing with nonlinear systems, these methods can be iteratively applied to achieve convergence [61]. Their major limitations are that they require the knowledge of the point of application of the input force, and they strongly rely on accurate measurements of the frequency response functions. Optimization approaches are based on least-squares optimization algorithms to match the estimated and measured response due to an unknown input force. They can be formulated both in the time and frequency domain.

Force reconstruction approaches are mostly based either on finite difference discretization of the equations of motion or on modal expansion techniques [80]. Finite difference based methods require a very detailed model of the structure, which represents a potential limitation for practical application. For example, in the analysis of a simple square, isotropic plate, Pezerat et al. [63] needs a mesh refinement of the model with an accuracy up to 2000 modes, and almost 200 measurement points

over a 1 m^2 area. Moreover, the algorithm encounters difficulties when the driving frequency is close to the natural frequencies of the system [63].

Modal approaches identify the applied loads by projecting both the external forces and the response functions into the modal space [57, 47]. In this case, the major limitation consists in the necessity of employing a large number of basis functions (of the order of 50-60) to accurately represent the forcing function, which requires numerous measurement points. Due to the limitations of these approaches, force reconstruction techniques are often considered as inefficient and impractical except for very simple structural components, such as beam or plate structures.

1.4.2 Force Determination for rotorcraft

Few attempts have been made by the helicopter community to predict the airloads from measured deformations, except for the CFD community. A methodology known as *Force Determination* (FD) was developed in the early 1970's for the early diagnosis of vibratory forces and moments [7, 38, 24, 50]. FD determines magnitudes and phasing of vibratory forces and moments using measured accelerations and calibration data. Vibratory hub loads are related to in-flight measured accelerations on the fuselage through the inverse of the acceleration mobility matrix, obtained experimentally from ground-tests. It is therefore assumed that the structural behavior is linear. The approach requires a high degree of redundancy between the number of hub loads to be determined and the measured signals to reduce the sensitivity to errors in measurements (either in the mobility matrix or in fuselage accelerations). For example, a degree of redundancy of ten was used in [7] (12 measurements, two forces to be determined). Results indicate that FD is able to predict the hub forces with a satisfactory accuracy (errors of the order of 5-9% in different flight conditions [50]), but requires extensive ground testing for the evaluation of the mobility matrix

and assumes linear structural behavior. Therefore, considerable engineering judgment is required to identify the forcing coordinates that contribute to the in-flight vibratory accelerations. The success of the method depends on both the accuracy of the calibration mobilities and the proper selection of the forcing coordinates [24].

The possibility of computing the spanwise load distribution from bending moment measurements as a way of obtaining an estimate of blade loading is investigated by Bousman [21]. This method has the ability to obtain a good estimate of the airloads acting on rotor blades using only information obtained from strain gages, thus providing a simple technique to predict the rotor aerodynamic behavior. This procedure is based on a modal expansion of the in-vacuo flap equation of motion, in which the blade is used as a force balance. The technique has the advantage that only a few modes (10) and in-flight measurements of flap bending moments (of the order of 15-20) are required. The agreement between the computed airloads and the measured ones is found to be good, especially at the inboard station of the blade. However, the method has less satisfactory capabilities in case of rapid variations in airloads as seen near the blade tip because of its inability to satisfy the boundary condition of zero airload at the blade tip. The algorithm has been generalized for the estimation of pitching moment in [78]. An application of the algorithm to wind turbine blades is described in [68].

1.4.3 Shape Sensing method

Another class of approaches can be classified as *Shape Sensing* techniques [71, 72, 70], for which the reconstruction of the displacement/strain field at every material point of the structure is achieved from a set of discrete strain or displacement measurements. This method, called Inverse Finite Element Method (iFEM), consists in fitting the measurements through the finite element discretization of the structure and the associated shape functions. Although an accurate identification of the stresses is possible,

physical insight on the updated system and on the applied loads is not provided. Furthermore, a large number of sensors is required. For example, in [72, 20], a cantilever plate, of area of 252 cm^2, is analyzed, and 28 measurement points are included in the analysis. The number of sensors is definitely reduced with respect to FR approaches but their quantity is still remarkable. Moreover, the applicability of this approach to analyze complex rotating systems such as helicopter rotors or wind turbines has not been attempted.

1.4.4 Inverse Dynamic methods in biomechanics

Methodologies for updating numerical models based on continuous experimental measurements have been proposed also in the field of biomechanics to compute stresses in human joints from body motion. These combined numerical and experimental approaches enable to track human motion during everyday life, and to analyze the resulting stresses in the system. The correct representation of the kinematics of a system is particularly important in biomechanics for movement analysis and stress predictions in joints [5]. The instantaneous position and orientation of the body is measured through a set of markers located on the skin (*skin-markers*) and its motion is reconstructed by image recording [25]. Since markers are not directly attached to bones, high measurement inaccuracies due to skin movement (soft tissue artifacts) are introduced, and they must be corrected before comparison with numerical simulations [6]. Then, kinematic data are combined with numerical models of the body (generally a multibody model of the system of the bones [5]) to solve the general dynamic problem and to find the stresses in the joints. This can be achieved either through a direct dynamic analysis with the objective of minimizing the differences between the obtained and the prescribed motion, or through an *Inverse Dynamic Analysis* (IDA) [4]. In IDA the net joint reaction forces and moments are computed through a series of differential equations, based on the equations of motion, from the

measurements of the kinematics and of the externally applied forces such as ground reaction forces.

These approaches are formulated as prescribed-motion problems and they require the use of sets of markers, the movement of which is image-recorded. This technique is therefore not practical for applications as complex as the analysis of flying vehicles. Moreover, in biomechanical problems, the major contributor to externally applied loads are gravity forces, while aerodynamic loads are negligible. This is not the case in aeronautical applications, where aerodynamic loads play a fundamental role.

1.5 Finite element model updating

Inaccuracies in numerical predictions of dynamic response due to lack of knowledge in the structural modeling and to the presence of structural degradation can be improved based on experimental measurements through model updating techniques. These approaches iteratively change some physical parameters of the model to make the system better match the target structural response. Unlike in other fields, such as control design, model updating in structural dynamic is performed off-line after the acquisition. The improved model is then used to analyze alternative loading arrangements and modified structural configurations.

The main objective of model updating in structural dynamics is the correction of a numerical model based on experimental measurements at a few locations in the system not only to achieve an accurate mimic of the dynamic response of the structure, but also to obtain a physically meaningful numerical model. Extensive review of traditional updating techniques can be found in the work of Mottershead and Friswell [60, 40]. Berman et al. [12, 16, 13, 15, 19, 17, 18, 14] extensively applied these approaches to improve the predictions of helicopter dynamic response. Modal updating techniques are based on measurements of natural frequencies, damping coefficients and mode shapes at a few locations on the system. They offer the advantage of

requiring a limited number of experimental measurements, but are generally limited to the analysis of measured modal characteristics [3]. Discussion of major limitations of model updating techniques can be found in [16, 15]. These papers describe the major drawback of these approaches that constists in the existance of multiple solutions for the correction of the model based on experimental measurements. The uniqueness of the solution is therefore not guaranteed. Moreover, the limited number of sensors introduces singularities in the updating procedure because of the spatial incompleteness of the measurement system [40, 15].

Recent advances in testing techniques such as laser scanning vibrometry and high speed cameras for digital correlation [45] allow for full-field response measurements, that can be used as input to calibrate numerical models. These methods directly compare finite element predictions and full-field measurements by projecting the measurement points onto the numerical mesh using polynomial shape functions [56, 66], or pattern recognition techniques [83, 82, 81] to reduce the number of measurements required. However, these approaches still need to handle a large amount of data to update the numerical model. They can be applied to analyze mode shapes [82, 81] or deformations [83] of the system.

Model updating techniques can also be used in conjuction with operation modal analysis (OMA) methods that identify the modal properties of the system from displacement, acceleration and/or strain measurements [2, 44, 85]. Some OMA approaches do not need knowledge of the input (i.e. applied loads) and can be used to monitor the system under operating conditions. However, these approaches are limited by strong assumptions on the form of the excitation, which often is required to be close to white noise. This is not the case, for example, for rotating systems, where important contributions are given by the harmonic components due to the rotation. Several attempts are currently being made to relax this assumption by performing initial analyses on the measured data to remove the harmonic contributions, after

which standard OMA techniques can be applied [3, 37, 62].

1.6 CA Approach

The approach for response identification presented in this research belongs to the shape sensing class, and it is based on the technique proposed by Bousman [21] for the analysis of rotor blades. The identification process is divided in a Load Confluence Algorithm, that updates the external loads acting on a dynamic system, and a Property Confluence Algorithm, that tailors the mass and stiffness distributions on the actual behavior of the system. The approach of Bousman [21] is generalized to analyze different systems other than rotor blades by applying a general Finite Element (FE) procedure. In addition, the focus is placed on the accuracy of the reconstructed response rather than on the estimation of the load distribution.

The Load Confluence Algorithm is formulated in a general FE framework, and it is based on an iterative procedure which estimates and corrects the externally applied load so that numerical predictions and measured quantities reach an agreement within a specified tolerance. This procedure can accommodate nonlinearities in the structure owing to its iterative nature. Moreover, due to the generality of the FE formulation, the algorithm can include different types of measurements (strains, displacements, velocities, accelerations) with very minor modifications to the algorithm [28, 27, 59, 26, 30]. The iterative approach computes linearized corrections to the non-linear model based on experimental measurements. These linearized corrections are based on the second order, undamped, linear equations of motion of the system. The LCA operates in the modal domain, from which the response of the structure is reconstructed using numerical modes. Reconstruction of modal loads is shown to accurately identify the response field after a few iterations, while the identification of physical loads requires a higher computational burden and detailed experimental information. Non-smooth external loads in fact require an infinite number of modes

to be represented, while they generate smooth response in the system that can be represented by a lower order modal representation. Therefore, the LCA appears as promising as it requires a limited number of measurements and of modal information to achieve accurate predictions of the dynamic response.

The Property Confluence Algorithm is based on an iterative procedure that computes new estimates of the physical parameters based on current measurements of the dynamic response. The procedure assumes that the external loads are accurately modeled, and that inaccuracies in the predicted response are solely due to inaccurate knowledge of mass and stiffness properties. Mass and stiffness distributions of the system are updated based on the measurements of the dynamic response at discrete locations [31, 29]. Similar to the LCA, the response is assumed to be periodic.

The LCA and the PCA can then be combined into a comprehensive SCA to create a tailored model of a system. The previous assumption of a separate occurrence of inaccuracies in loads and physical properties is removed, and the SCA systematically corrects both the external loads and the physical properties of the system based on the measured response.

1.7 Organization of the work

This research investigates the development and validation of a combined analytical and experimental method for the prediction of the response of dynamic components, in particular of helicopter rotor blades, from a limited number of measurements. The thesis is organized as follows: this initial chapter introduces the topic of load and response identification from experimental measurements from the state-of-the-art of available analysis methods to unsolved issues of fundamental importance. It states the goal of the present research and explains the developed approach and some possible applications. Chapter 2 describes the Load Confluence Algorithm, by which external loads are corrected as a mean to improve the prediction of dynamic

response. Applications of LCA to analyze one- and two-dimensional structures are presented in Chapter 3, along with applications to complex rotorcraft cases. Chapter 4 introduces the Property Confluence Algorithm as a means to tailor a general model onto a particular machine history. Its applications to a one-dimensional framework are described in Chapter 5. The convergence properties of both LCA and PCA based on Newton's method are discussed in Chapter 6, while Chapter 7 provides a summary of the activities, along with a roadmap to unify LCA and PCA into a System Confluence Algorithm. Recommendations for future research are also given in the conclusions of Chapter 7.

CHAPTER II

THE LOAD CONFLUENCE ALGORITHM

2.1 Overview

The Load Confluence Algorithm (LCA) is an effective procedure for the mapping of the dynamic response using experimental measurements. The motivation comes from the need to monitor the response of components operating in rotating environments under complex loading as in the case of rotor blades and other rotating components in rotorcraft [59]. In this application, the main sources of vibrations are airloads, whose accurate prediction remains an outstanding challenge [84]. In contrast, structural dynamic codes have achieved an acceptable level of predictive accuracy, provided accurate air loads are available. The lack of predictive accuracy, from an usage monitoring perspective, leads to limited predictive capability in terms of fatigue, which ultimately results in overly-conservative designs. Therefore, reliable load and strain predictions are essential for fatigue tracking and life estimation of structural components such as rotor blades.

Major challenges are associated with the complex dynamic environment and associated loads, which make direct measurements and numerical predictions particularly difficult. Specifically, prediction of the unsteady aerodynamic loads acting on blades remains a difficult task, despite recent advances in computational fluid dynamics (CFD) [69]. Moreover, detailed measurement of airloads is extremely complex, costly, and impractical in most cases. A goal of this work is to determine a method where simplified airloads can be used and corrected to achieve high prediction accuracy in terms of fatigue cycles estimations with moderate computational costs. This general observation and the application to the rotorcraft environment lead to the assumption

that the applied loads vary periodically in time. Accordingly, the dynamic response is considered periodic and can be expanded through a Fourier series. The method can be applied to a variety of problems where the applied loads can be represented through harmonic series.

In this chapter, the algorithm is first conceptually described, along with its details. At the end of the chapter, an example in a numerical framework of an isotropic beam problem with both rigid and flexible support demonstrates its applicability.

2.2 Concept

Based on the schematic of Figure 4, the objective of the LCA is to numerically reconstruct the full-field dynamic response of the structure $w(x)$ from a (limited) number s of experimental measurements $\boldsymbol{w}(\boldsymbol{x})$, where $\boldsymbol{x}$ is a vector defining the location of the sensors $\boldsymbol{x} = [x_1, x_2, ..., x_s]^T$. The reconstruction is achieved through a modal expansion of the numerical model of the structure and an iterative process. At each iteration, the external loads are corrected to obtain an agreement between numerical predictions and experimental measurements at locations x_n. Iterations are needed in order to account for non-linearities, inaccuracies and unmodeled dynamics.

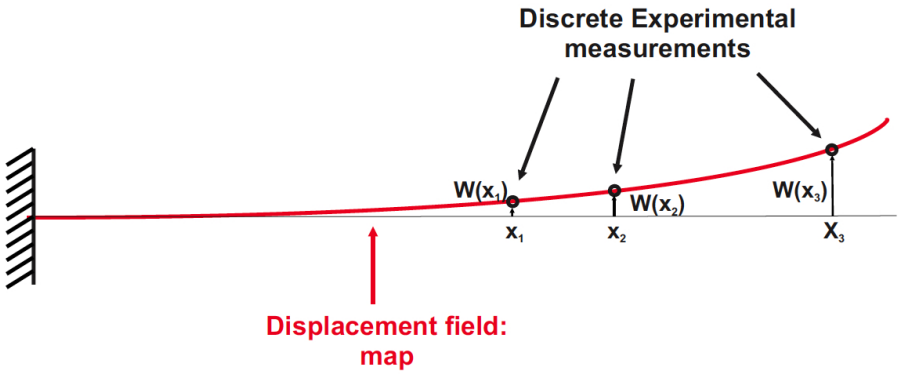

Figure 4: Schematic of the fitting process of the LCA through discrete measurements in the system.

The LCA consists in a numerical model of the structure, which is assumed to be

as accurate as possible, a set of experimental measurements at a limited number of locations, and an iterative procedure, which estimates the applied loads and maps the measured response over the structure. A schematic representation of the procedure is presented in Figure 5.

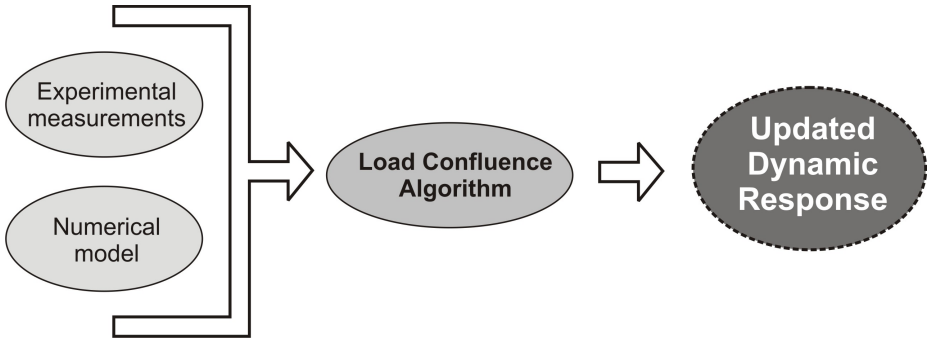

Figure 5: Concept of the LCA.

The dynamic model of the structure is generally described in terms of a mass matrix $\boldsymbol{M}$ and a stiffness matrix $\boldsymbol{K}$, while the set of experimental measurements is denoted as $\boldsymbol{e}_E(\boldsymbol{x})$ (with subscript E as Experimental). The linearized correction of the external loads is defined by approximating the behavior of the system with second order, undamped and linear equations of motion. Inaccuracies in damping are corrected by the external loads.

The following notation is used in the following: bold, lower case letters define vectors, while bold, upper case letters denote matrices. For the configuration depicted in Figure 4, for example, $\boldsymbol{x} = [x_1, \ldots, x_s]^T$, and $\boldsymbol{e}_E(\boldsymbol{x}) = [w(x_1), \ldots, w(x_s)]^T$. A general formulation allows for the measurement vector $\boldsymbol{e}_E(\boldsymbol{x})$ to include displacement, strain, velocity, or acceleration measurements.

The process shown schematically in Figure 6 can be summarized as the following sequence of steps:

- An initial guess for the load $\boldsymbol{F}_0$ is applied to the model.
- The dynamic response $\boldsymbol{e}_M(\boldsymbol{x})$ (with subscript M as Model) is estimated at the

sensor location $\boldsymbol{x}$ by solving the FE problem.

- Numerical and measured responses are compared and an error vector $\Delta \boldsymbol{e} = \boldsymbol{e}_M - \boldsymbol{e}_E$ is calculated.
- A load correction $\Delta \boldsymbol{F}$ is calculated based on $\Delta \boldsymbol{e}$ through the formulation of the problem in the modal domain. This is performed through the modal mapping procedure described in sections 2.3 and 2.4.
- The updated load $\boldsymbol{F} = \boldsymbol{F} + \Delta \boldsymbol{F}$ and the corresponding numerical response are computed, and a new error $\Delta \boldsymbol{e}$ is estimated.
- The process is iterated until $\Delta \boldsymbol{e}$ reaches the desired tolerance level.

At each iteration, the mapped response is expected to improve based on experimental measurements, as illustrated in Figure 7.

An iterative procedure is particularly important in case of systems including non-linearities, in the presence of unmodeled dynamics and noisy experimental data, or in situations where the number of modes considered in the modal expansion is lower than the number of experimental measurements. Discussion of the convergence properties of LCA is presented in Chapter 6.

2.3 Modal procedure for load estimation

The core of the LCA is based on a linearized and undamped model of the system. Damping (or differences in damping model) is considered as part of the external load to be updated by the algorithm. The applications of the algorithm are therefore not restricted to undamped systems. The modeling of structural damping is in fact generally not physically representative, and the addition of these terms as known terms would not to provide additional knowledge of the system. Nonlinearities in the system are dealt through multiple iterations.

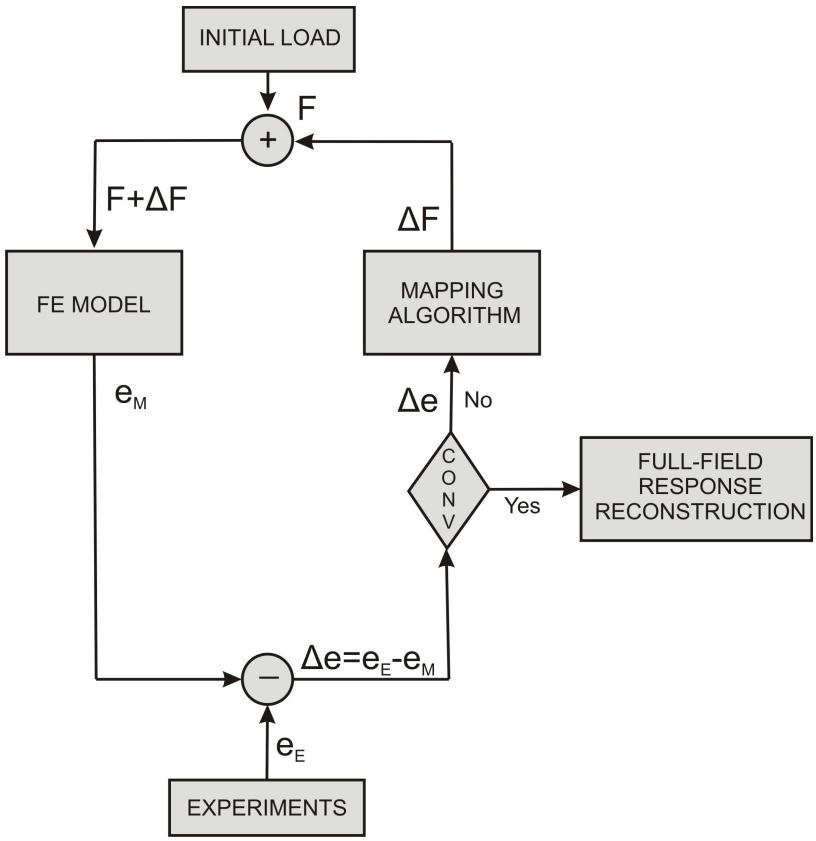

Figure 6: Schematic of the Load Confluence Algorithm.

Consider the second order equations of motion of a general undamped linear system:

$$\boldsymbol{M}\,\ddot{\boldsymbol{u}}(t) + \boldsymbol{K}\,\boldsymbol{u}(t) = \boldsymbol{F}(t) \tag{1}$$

where $\boldsymbol{M}$ and $\boldsymbol{K}$ are the mass and the stiffness matrix of the system, array $\boldsymbol{u}(t)$ stores the N degrees of freedom of the system, and $\boldsymbol{F}(t)$ is the vector of the generalized applied loads. The modal expansion of Eq. (1) requires that:

$$\boldsymbol{u}(t) = \boldsymbol{P}\,\boldsymbol{q}(t) \tag{2}$$

where $\boldsymbol{q}(t)$ are the modal coordinates and matrix $\boldsymbol{P}$ contains the N eigenvectors of the system. The generalized loads are expanded in a similar manner as

$$\boldsymbol{F}(t) = \boldsymbol{M}\,\boldsymbol{P}\boldsymbol{\lambda}(t) \tag{3}$$

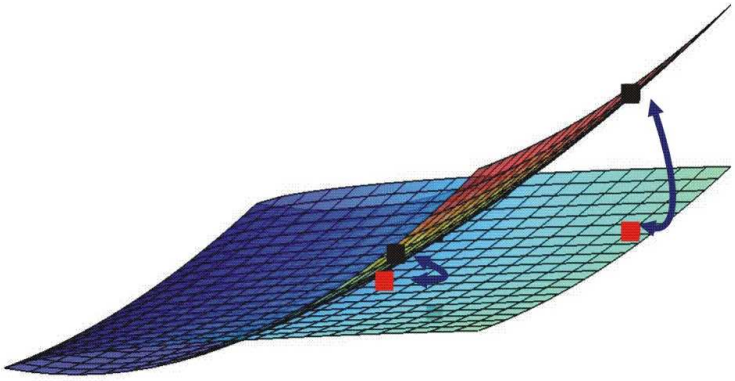

(a) Step 1

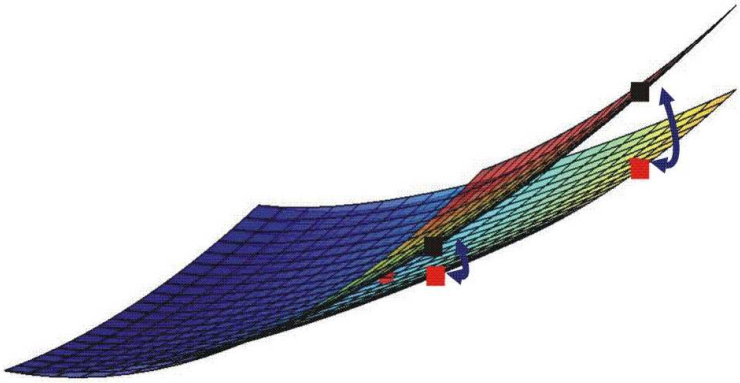

(b) Step 2

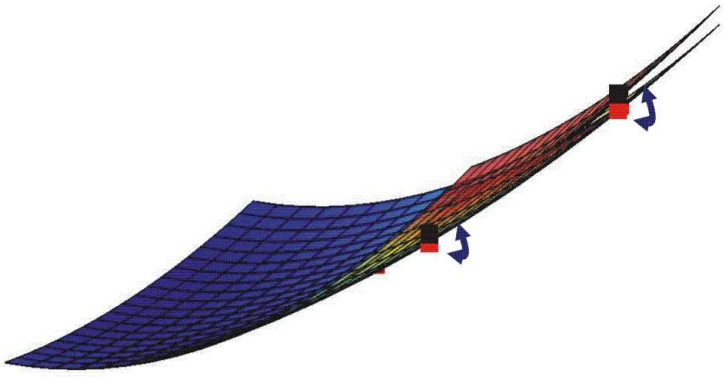

(c) Step 3

Figure 7: Effects of an iterative application of LCA.

for a unit-mass normalization of the eigenvectors ($\boldsymbol{\lambda}(t) = \boldsymbol{P}^T \boldsymbol{F}(t)$, assuming Eq. (3) $\boldsymbol{\lambda}(t) = \boldsymbol{P}^T \boldsymbol{M}\, \boldsymbol{P}\boldsymbol{\lambda}(t) = \boldsymbol{\lambda}(t)$).

A reduced modal base of m eigenvectors will be used to approximate the dynamic

response. A finite number of sensors s can in fact reconstruct up to s number of modes. The use of a complete modal expansion would therefore require an infinite number of measurement points.

The governing equations of motion of the system reduce to:

$$\ddot{q}_i(t) + \omega_i^2 q_i(t) = \lambda_i(t) \quad i = 1, \ldots, m \tag{4}$$

with ω_i denoting the natural frequencies of the system. The response of the system and the modal components of the loads are expanded using a Fourier series of frequency Ω (Ω is the fundamental excitation frequency):

$$\begin{aligned} \boldsymbol{q}(t) &\simeq \boldsymbol{q}_0 + \textstyle\sum_{j=1}^{M} \left[\boldsymbol{q}_{cj} \cos j\Omega t + \boldsymbol{q}_{sj} \sin j\Omega t\right] \\ \boldsymbol{\lambda}(t) &\simeq \boldsymbol{\lambda}_0 + \textstyle\sum_{j=1}^{M} \left[\boldsymbol{\lambda}_{cj} \cos j\Omega t + \boldsymbol{\lambda}_{sj} \sin j\Omega t\right] \end{aligned} \tag{5}$$

Measurements $\boldsymbol{e}_E(t) = [e_1, e_2, \ldots, e_s]^T$ in the structure are evaluated at s locations, and may consist of strains, displacements, velocities, accelerations or their combination. The response of each sensor can be also expanded in Fourier series:

$$\boldsymbol{e}_E(x_n, t) \simeq \boldsymbol{e}_{E_0}(x_n) + \sum_{j=1}^{M} \left[\boldsymbol{e}_{E_{cj}}(x_n) \cos j\Omega t + \boldsymbol{e}_{E_{sj}}(x_n) \sin j\Omega t\right] \quad n = 1, \ldots, s \tag{6}$$

Moreover, the measurements and the generalized coordinates can be related through the incomplete modal matrix $\boldsymbol{B}$ and its pseudo-inverse as:

$$\boldsymbol{e}_E(\boldsymbol{x}, t) = \boldsymbol{B}(\boldsymbol{x})\boldsymbol{q}(t), \qquad \boldsymbol{q}(t) = \boldsymbol{B}^{+}(\boldsymbol{x})\boldsymbol{e}_E(\boldsymbol{x}, t) \tag{7}$$

The definition of $\boldsymbol{B}$ depends on the measured quantities, that is, on the kind of sensors. For example, if e_{E_i} represents a displacement measurement at location (x_i), B_{ij} represents the contribution of the $j-th$ modal displacement at location i. If strain gages are considered, B_{ij} represents the contribution of the $j-th$ modal strain at location i. The number of measurements s and modes m retained define the dimensions of matrix $\boldsymbol{B}$, which are very important in the evaluation of its pseudo-inverse $\boldsymbol{B}^{+}$. Discussion of the choice of type of sensors can be found in section 2.5.

Introducing relations (5), (6) and (7) into the governing equations of motion of the problem, the following linear algebraic relationships among the Fourier components of the applied loads and local measurements hold:

$$\begin{aligned}
\boldsymbol{\lambda}_0 &= \mathrm{diag}\,(\omega_i^2)\,\boldsymbol{B}^+\boldsymbol{e}_{E_0} \\
\boldsymbol{\lambda}_{cj} &= \mathrm{diag}\,(\omega_i^2 - j^2\Omega^2)\,\boldsymbol{B}^+\boldsymbol{e}_{E_{cj}}, \qquad j = 1, 2, ..., M \\
\boldsymbol{\lambda}_{sj} &= \mathrm{diag}\,(\omega_i^2 - j^2\Omega^2)\,\boldsymbol{B}^+\boldsymbol{e}_{E_{sj}}, \qquad j = 1, 2, ..., M
\end{aligned} \tag{8}$$

These relations imply that if the time histories of the response are measured at a number of locations on the structure, their Fourier components are closely related to the Fourier coefficients of the modal loads, from which the equivalent applied load vector can be reconstructed as:

$$\boldsymbol{F}(t) = \boldsymbol{M}\,\boldsymbol{P}\boldsymbol{\lambda}(t) \tag{9}$$

for a unit-mass normalization of the eigenvectors. This observation gives the advantage that only the Fourier components of the measured time histories have to be stored during the acquisition, thus reducing the quantity of data. Moreover, a limited number of experimental measurements is necessary and sensor locations are not limited to the nodes of the finite element model. The measured data is in fact projected into the model with polynomial functions (FE shape functions) and their spatial incompleteness is recovered through the modal reconstruction of the system.

2.4 Procedure for response mapping

The modal procedure for load estimation described in section 2.3 is employed to define the load correction to be applied to the FE model at each iteration to improve the accuracy of the numerical response. The difference between experimental and numerical response at the sensor location can be expressed in terms of their Fourier

expansion as:

$$\begin{aligned}\Delta \boldsymbol{e}(\boldsymbol{x},t) &= \boldsymbol{e}_M(\boldsymbol{x},t) - \boldsymbol{e}_E(\boldsymbol{x},t) \\ &= \Delta \boldsymbol{e}_0(\boldsymbol{x}) + \sum_{j=1}^{M} [\Delta \boldsymbol{e}_{cj}(\boldsymbol{x}) \cos j\Omega t + \Delta \boldsymbol{e}_{sj}(\boldsymbol{x}) \sin j\Omega t] \end{aligned} \tag{10}$$

and:

$$\Delta \boldsymbol{q}(t) = \boldsymbol{B}^{+}(\boldsymbol{x}) \Delta \boldsymbol{e}(\boldsymbol{x},t) \tag{11}$$

Following the procedure described in section 2.3 for the computation of modal loads, the load correction is given by:

$$\Delta \boldsymbol{F}(t) = \boldsymbol{M}\,\boldsymbol{P} \Delta \boldsymbol{\lambda}(t) \tag{12}$$

These incremental loads are iteratively applied to the initial numerical system. Iterations are stopped by the user after the desired number of applications of the algorithm. As a consequence, the accuracy of the dynamic response at the control points is improved once the system reaches steady-state. The improvement of numerical predictions at measured locations results also in improvements in accuracy of the response of the entire system, due to the modal projection of the local information onto the entire domain. The application of this iterative procedure therefore produces accurate representations of the map of the response.

2.5 Numerical example: analysis of a beam in bending

The application of LCA to analyze dynamic systems can be demonstrated in a numerical framework, in which the reference data $\boldsymbol{e}_E$ are numerically generated. This solution allows for a detailed analysis of the obtained results that are not affected by measurement inaccuracies and noise. Experimental cases are analyzed in Chapter 3.

This analysis considers a beam in bending, modeled using finite elements. The beam is free at one end, and it is supported by a constraint of varying flexibility at the other end. The flexible support is modeled through a linear spring of stiffness k.

The presence of a flexible support introduces quasi-rigid body modes in the system, which need to be investigated with attention as part of LCA.

In practical applications, the response of the system is monitored by measuring different dynamic quantities, such as strains, displacements, velocities, accelerations and forces at different locations. Therefore, the capabilities of LCA need to be investigated in the presence of different types of measurements simultaneously acquired. Several examples are presented in this section to analyze the role of different types of sensors in the convergence of LCA. The first two examples analyze the performance of LCA in case of a cantilever beam. Initially, four strain sensors are considered as reference (case Beam 1), then four displacement measurements (case Beam 2). Then, the stiffness of the constraint is reduced, introducing a quasi-rigid-body mode in the system. The capabilities of LCA are again evaluated in case of four strain measurements (case Beam 3), and four displacements (case Beam 4). Next, mixed sensors are used as reference points. Case Beam 5 considers three strain and one displacement measurement, case Beam 6 three strains and one force measurement. Corrections based only on strain information are in fact not expected to be able to retrieve the information on rigid-body modes, for which different types of measurements (i.e. displacement, force) need to be considered. All conditions considered for the analysis are listed in Table 1.

Table 1: Description of parameters for analyzed cases for a spring-free beam configuration.

Case ID	k	sensor type
Beam 1.	∞	4 strain
Beam 2.	∞	4 displacement
Beam 3.	10^3 N/m	4 strain
Beam 4.	10^3 N/m	4 displacement
Beam 5.	10^3 N/m	3 strain, 1 displacement
Beam 6.	10^3 N/m	3 strain, 1 force

The beam of length 430.0 mm is discretized with 15 Timoshenko beam elements. It has a rectangular section of thickness $h = 8.4$ mm. The axial stiffness is $EA = 9.7{\times}10^6$ N, the bending stiffness $EI = 48$ Nm^2 and the shear stiffness is $kGA = 37.4{\times}10^6$ N. The mass per unit length of the beam is $m = 0.38$ kg/m, with a distributed mass moment of inertia of $I = 9.1025{\times}10^{-5}$ kg m. The natural frequencies of the beam are listed in Table 2 for a cantilever beam ($k = \infty$) and for a flexible support ($k = 10^3$ N/m).

The reference model and the initial numerical model (to be corrected by LCA) are supposed to be characterized by the same mass and stiffness distributions and boundary conditions, but differ in the definition of the external loads. Both systems are characterized by proportional damping.

An harmonic concentrated force of frequency $f = 10$ Hz is applied at the free end of the beam in the vertical direction. The reference external loads are a combination of a sine and cosine function, each characterized by a unit value Fourier coefficient ($F_{ref}(t) = \sin 20\pi t + \cos 20\pi t$). The system to be updated is characterized by an initial sinusoidal load of double amplitude ($F_{in}(t) = 2\sin 20\pi t$).

The reference values for LCA (denoted as $\boldsymbol{e}_E(\boldsymbol{x})$ in section 2.3) are the dynamic response at discrete locations of the beam for a load system for which the point of application and time function are supposed to be unknown.

Table 2: Natural frequencies of the beam for different values of tip spring.

f [Hz]	$k = \infty$	$k = 10^3$ N/m
f_1	36.7	12.2
f_2	226.0	60.2
f_3	614.4	307.5
f_4	1156.7	732.7
f_5	1823.7	1304.4

2.5.1 Cantilever beam

The first case (Beam 1) consists of a cantilever beam. Four strain gages are considered as reference points (Figure 8).

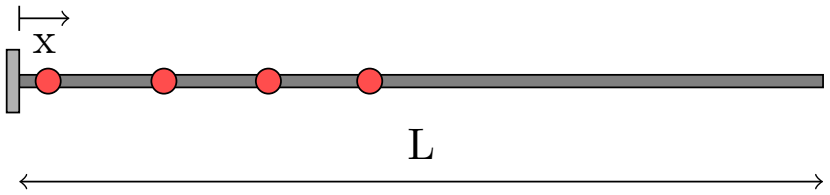

Figure 8: Beam 1. Cantilever beam. Strain sensors in red. Sensor 1 at the clamp.

Initially, a convergence analysis on the number of modes used in the modal expansion of the LCA is performed to define general criterions for the choice of number of modes and therefore number of sensors. The performance of LCA are described through convergence plots of the maximum difference in absolute value and phase between the reference and the reconstructed signals at the sensors, Figures 9 and 10. Given a Fourier representation of the response $\boldsymbol{e} = \boldsymbol{e}_0 + \sum_{j=1}^{M} [\boldsymbol{e}_{cj} \cos j\Omega t + \boldsymbol{e}_{sj} \sin j\Omega t]$, the absolute value and phase at each control point i are defined as $|e_i| = \left[\sum_{j=1}^{M} (e_{cj_i}^2 + e_{sj_i}^2)\right]^{1/2}$ and $\phi_i = \sum_{j=1}^{M} \tan^{-1} \frac{e_{sj_i}}{e_{cj_i}}$. In the figures, the difference in absolute value $|\Delta|$ is defined as the mean difference between the experimental and numerical peak-to-peak dynamic response at sensor location, $|\Delta| = \frac{1}{s} \sum_{i=1}^{s} |(|e_{Mi}| - |e_{Ei}|)|$. $\Delta\phi$ is defined as the mean phase difference between the experimental and numerical dynamic response at sensor location, $\Delta\phi = \frac{1}{s} \sum_{i=1}^{s} (\phi_{Mi} - \phi_{Ei})$. These analyses show that a few modes are sufficient to accurately identify the dynamic response of the system, and to achieve convergence of the iterative process. Results presented in the following as a baseline case consider the first three modes and are converged after three iterations.

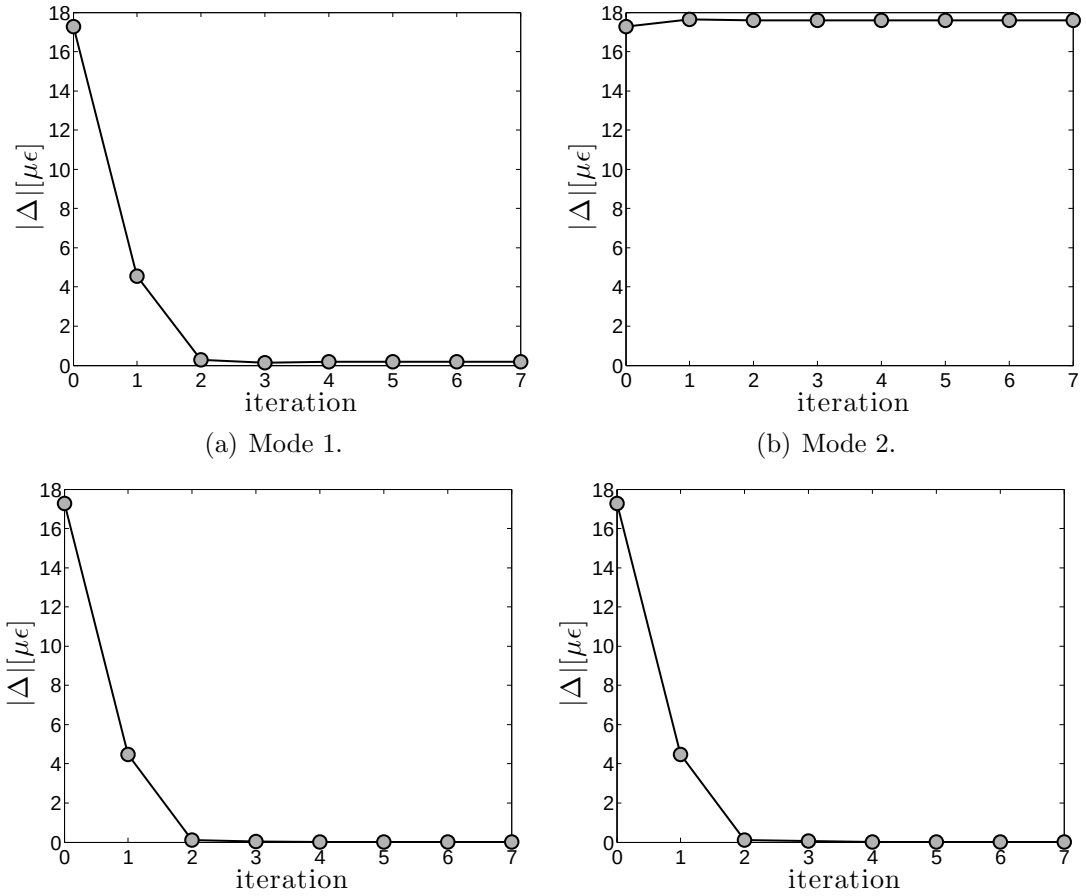

(a) Mode 1. (b) Mode 2.

(c) Modes 1-2. (d) Modes 1-2-3.

Figure 9: Convergence analysis of the mean absolute value changing the modal expansion included in LCA applied to a cantilever beam with four strain sensors.

The identified loads for the baseline case are represented in Figure 11 in terms of its sine and cosine coefficients. The loads applied to the reference system are not exactly identified, but instead an equivalent representation that accurately represents the dynamic response. Even if the initial and reference loads are concentrated loads applied to the tip, LCA identifies a set of nodal loads that represents the effect of the real applied loads.

The actual time histories at the sensor locations for Beam 1 are shown in Figure 12 at control points 1 and 4. An initial discrepancy of about 25% between the reference and initial strain is reduced to about 5% after one iteration and to less than 1% after the second application of LCA. Even if the problem is linear, a multiple number of

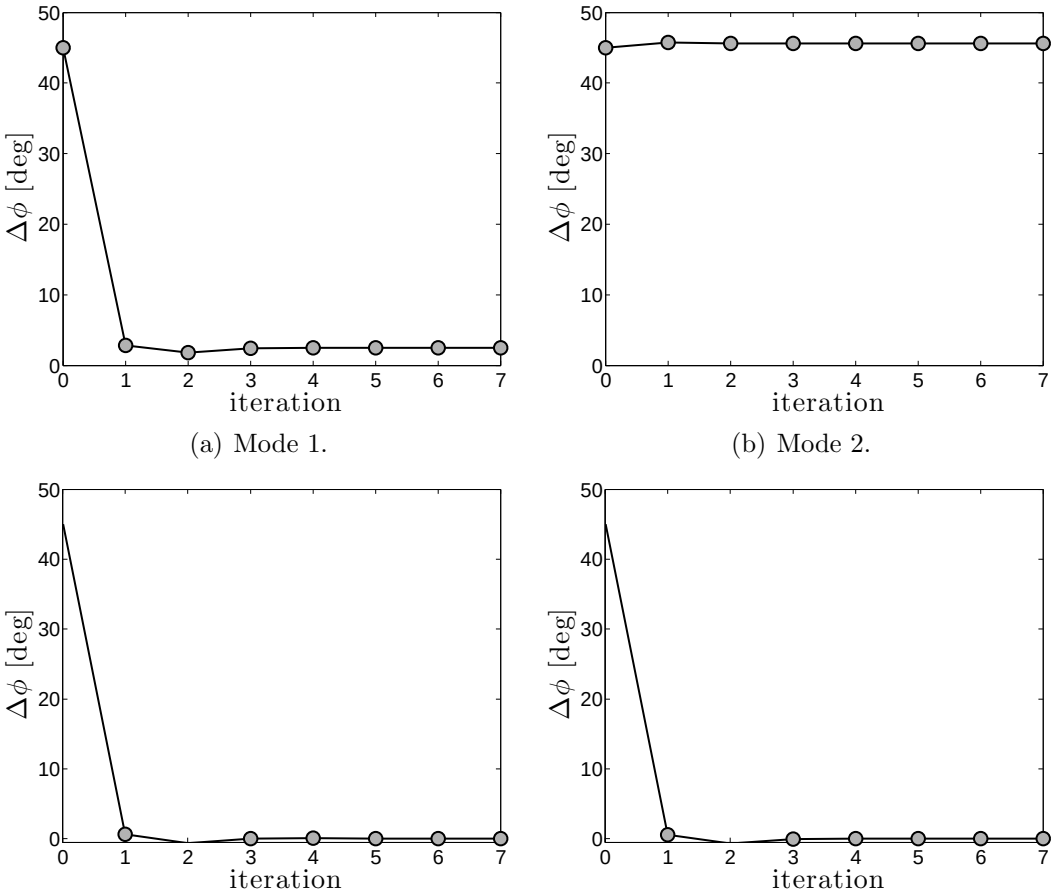

(a) Mode 1. (b) Mode 2.

(c) Modes 1-2. (d) Modes 1-2-3.

Figure 10: Convergence analysis of the mean phase changing the modal expansion included in LCA applied to a cantilever beam with four strain sensors.

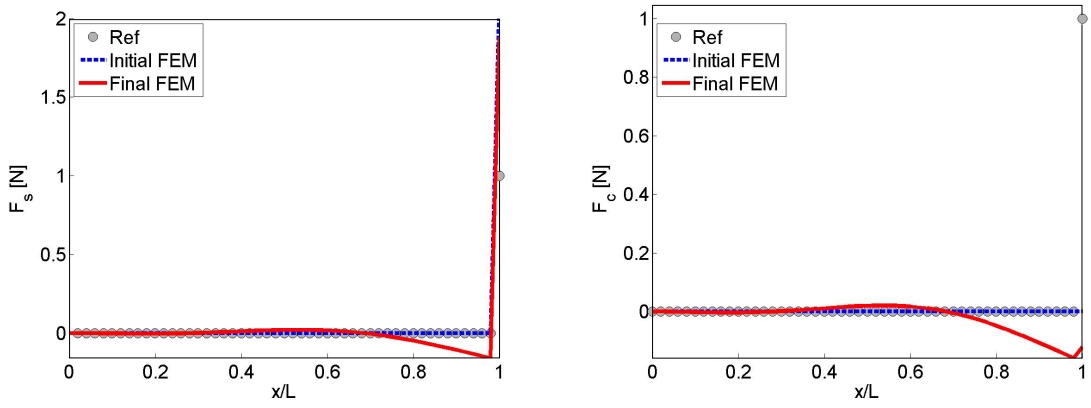

(a) Sine coefficient (b) Cosine coefficient

Figure 11: Beam 1. Sine and cosine coeffient of the applied load before and after the application of LCA. Reference (o). Initial FEM (--). Final LCA (-).

iterations is required because of the presence of damping. The effect of damping on convergence of LCA are discussed in Chapter 6.

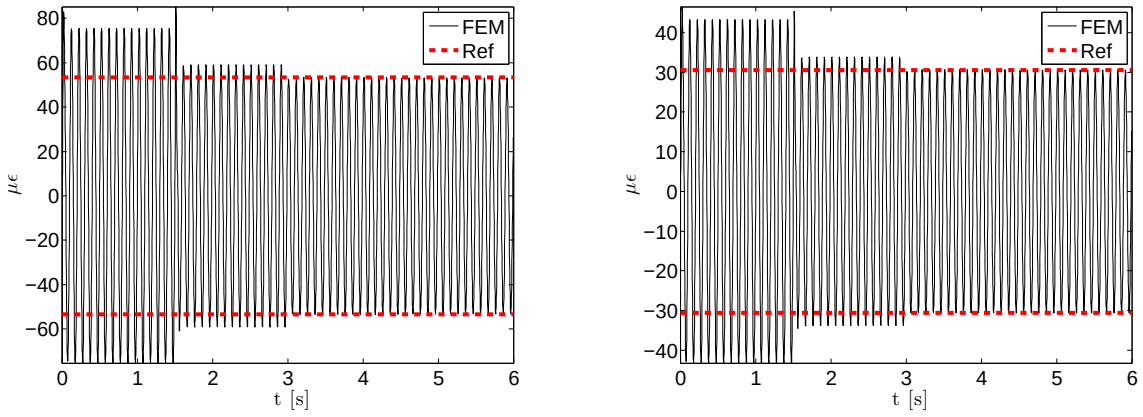

(a) Sensor 1 (b) Sensor 4

Figure 12: Beam 1. Convergence of time history of the signal at control points. Reference (--). Predicted (-)

Snapshots of the dynamic response at the sensors location are presented in Figure 13, both at the beginning of the simulation and after the application of LCA. Convergence is obtained not only on peak-to-peak values but also on the frequency content of the signal, as demonstrated by the convergence history of the Fourier coefficients (Figure 14). After three iterations, zeroth, sine and cosine coefficients converge to the reference values for all control points, and recover the initial differences between the reference and the numerical system.

The identified loads result in a very accurate representation of the instantaneous deformed shape of the beam (Figure 15), even if a slight inaccuracy is still present at the tip of the beam, due to the concentration of control points in the first half of the span. A more homogeneous sensor distribution results in improved overall response but is not considered representative of an actual experimental condition, because of the low strain level close to the free tip with respect to experimental noise.

A second case (Beam 2) considers four displacement sensors as control points, located along the span of the beam as shown in Figure 16. The convergence plots of

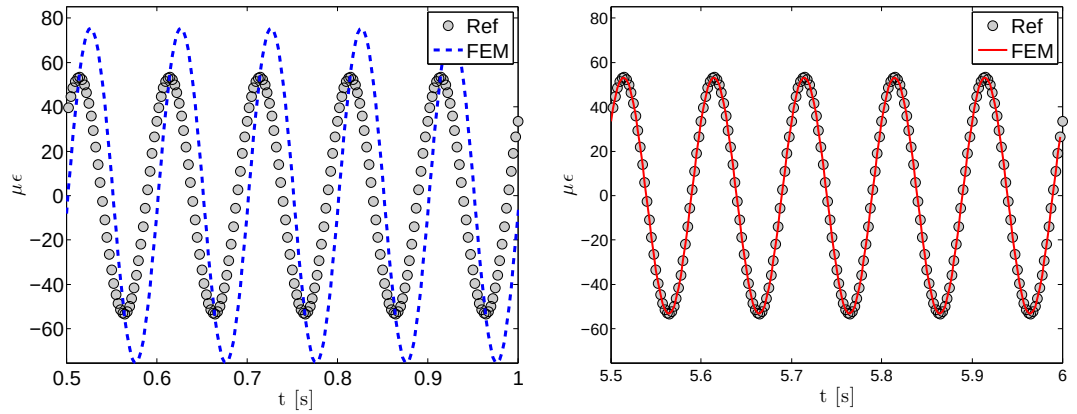

(a) Sensor 1. Before

(b) Sensor 1. After

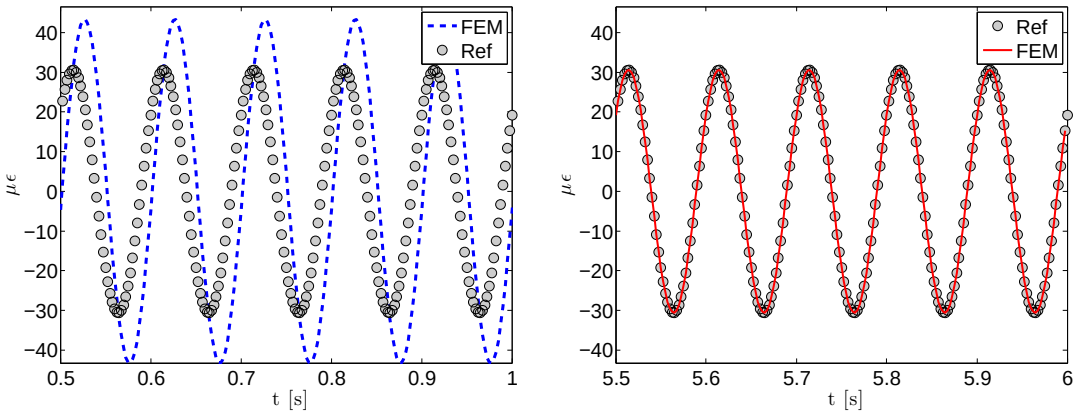

(c) Sensor 4. Before

(d) Sensor 4. After

Figure 13: Beam 1. Snapshot of time history of sensor 1 (top) and 4 (bottom) at the beginning of the analysis and after the application of LCA. Reference (o). Initial FEM (--). Final LCA (-).

the maximum difference in absolute value and phase between the reference and actual signals at the sensor are shown in Figure 17. The analysis is converged after three iterations also in this case. The time histories of the dynamic response at control points are depicted in Figure 18, snapshots of time histories in Figures 19 and 20 and the behavior of Fourier's coefficients in Figure 21. Good convergence is observed in this case similar to the cantilever beam case with strain gauges (Beam 1) previously analyzed. The instantaneous deformed shape of the beam (Figure 22) is also well simulated. Overall, no significant difference in behavior is observed whether strain or displacement sensors are considered for a cantilever beam example.

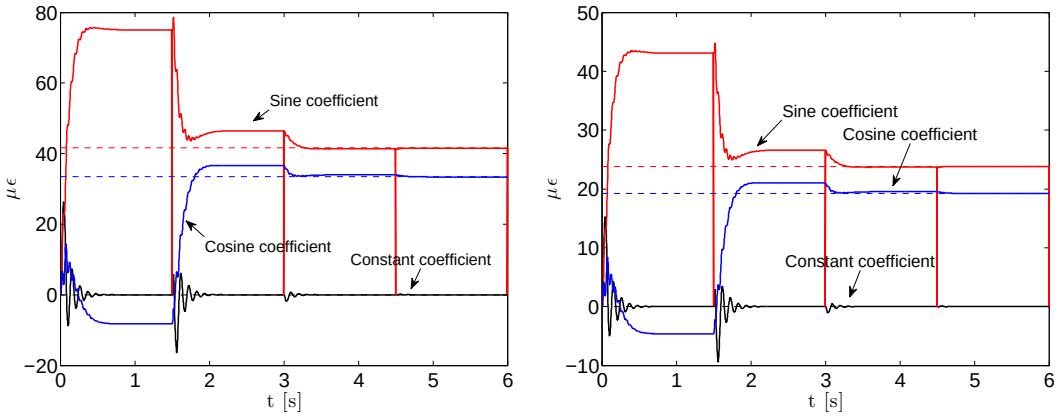

(a) Sensor 1 (b) Sensor 4

Figure 14: Beam 1. Convergence of Fourier coefficients of sensor 1 and 4 during the analysis. Predicted (-). Reference (--). Black line: constant coefficient. Red line: first sine harmonic. Blue line: first cosine harmonic.

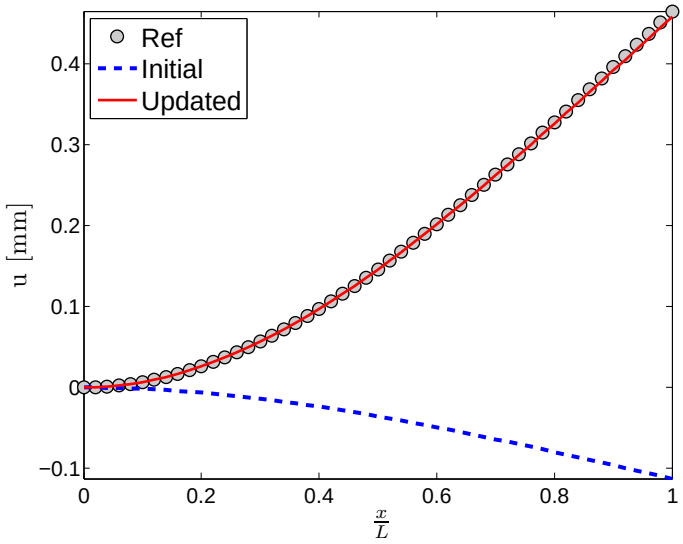

Figure 15: Beam 1. Instantaneous deformed shape of the beam. Reference (o). Initial FEM (--). Final FEM (-).

2.5.2 Flexible support

The presence of a flexible support introduces quasi-rigid-body modes into the system and affects the ability of the Load Confluence Algorithm to converge to the reference data. A linear spring of stiffness $k = 10^3$ N/m is added at the left end of the beam, and the clamp constraint is eliminated. The behavior of LCA in presence of strain sensors

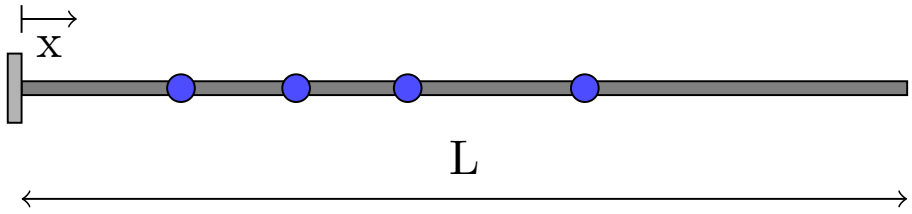

Figure 16: Beam 2. Cantilever beam. Displacement sensors in blue.

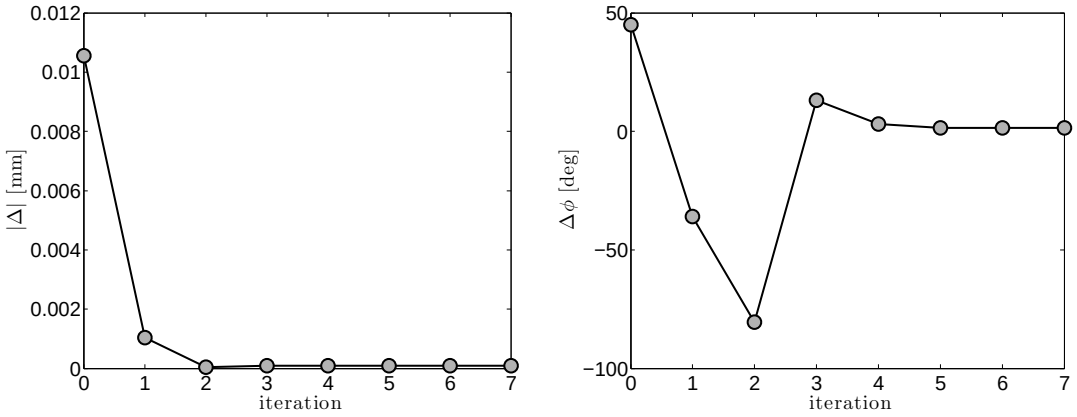

(a) Absolute value (b) Phase

Figure 17: Beam 2. Convergence analysis of maximum difference in absolute value and phase between the reference and actual signals at the sensors' location.

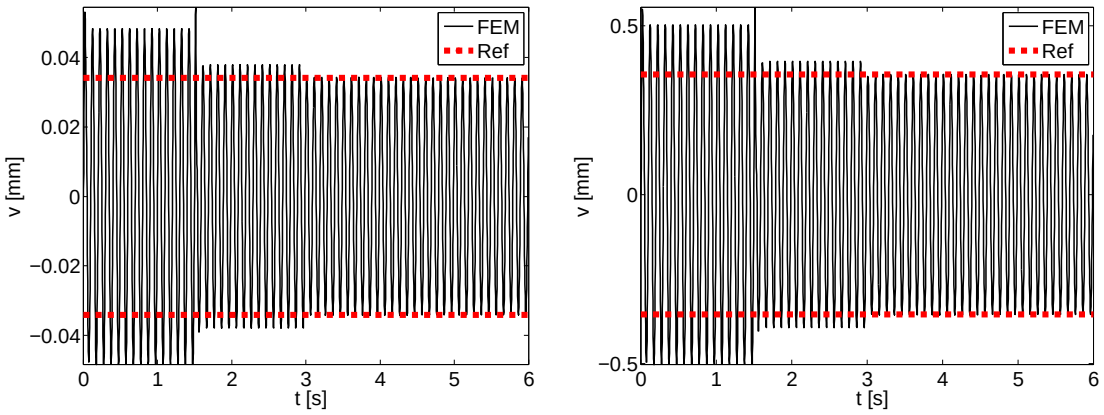

(a) Sensor 1 (b) Sensor 4

Figure 18: Beam 2. Convergence of time history of the signal at control points. Reference (--). Predicted (-).

(Beam 3), displacement sensors (Beam 4), and mixed sensors (strain/displacement - Beam 5, strain/force - Beam 6) is analyzed. In real operations, in fact, different types

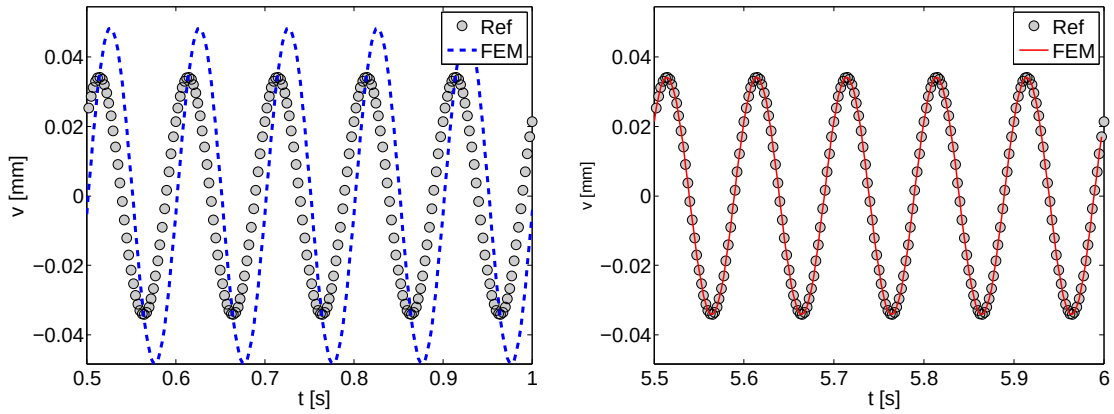

(a) Before (b) After

Figure 19: Beam 2. Snapshot of time history of sensor 1 at the beginning of the analysis and after the iterations of LCA. Reference (o). Initial FEM (--). Final FEM (-).

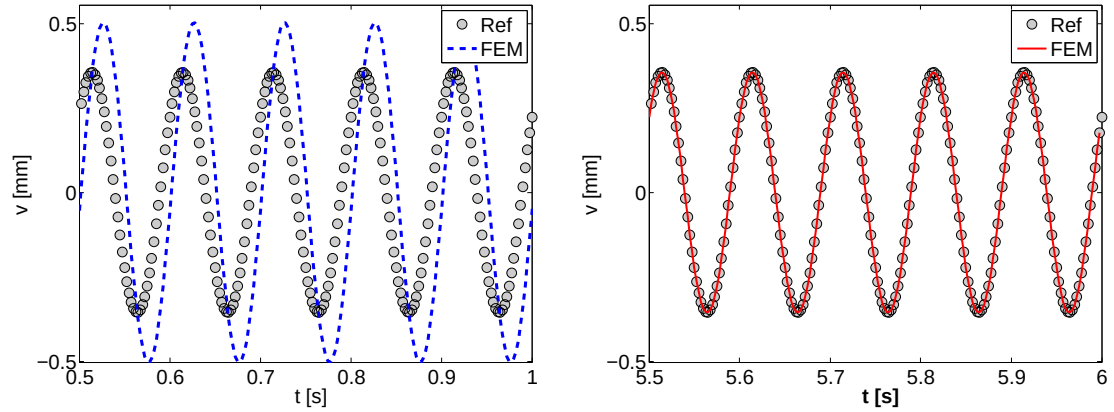

(a) Before (b) After

Figure 20: Beam 2. Snapshot of time history of sensor 4 at the beginning of the analysis and after the iterations of LCA. Reference (o). Initial FEM (--). Final FEM (-).

of measurements are generally available to monitor the behavior of a system. The position of the control points for case Beam 3 is shown in Figure 23.

Also in this case, the algorithm converges in three iterations considering three modes in LCA, as observed from the convergence plots of the maximum difference in absolute value and phase between the reference and actual signals at the strain sensors (Figure 24). However, inaccuracies in the identification of the instantaneous deformed shape are present (Figure 25) due to the quasi-rigid displacement of the

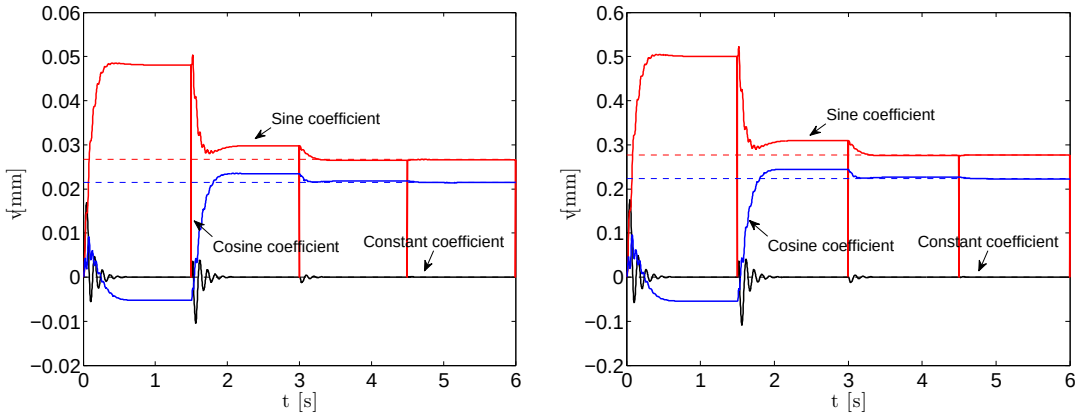

(a) Sensor 1 (b) Sensor 4

Figure 21: Beam 2. Convergence of Fourier coefficients of sensor 1 and 4 during the analysis. Final LCA (-). Reference (--). Black line: constant coefficient. Red line: first sine harmonic. Blue line: first cosine harmonic.

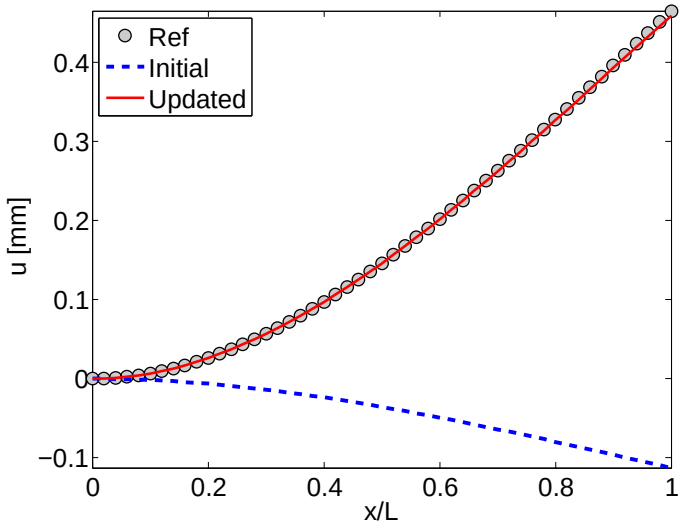

Figure 22: Beam 2. Deformed shape of the beam at a particular time instant. Reference (o). Initial FEM (--). Final FEM (-).

beam that does not affect the strain values at the control points.

If displacement sensors are used in spite of strain measurements (position of control points in Figure 26), the analysis converges after five iterations (Figure 27) and the inaccuracies on the identified deformed shape (Figure 28) are reduced with respect to the previous case. Displacement sensors are therefore able to recover both the quasi-rigid and the flexible content of the response.

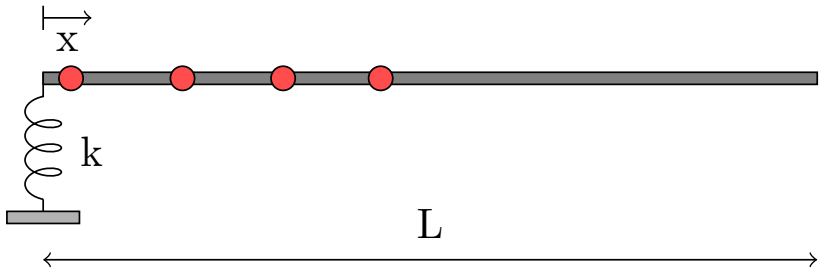

Figure 23: Beam 3. Linear spring-free beam. Strain sensors in red.

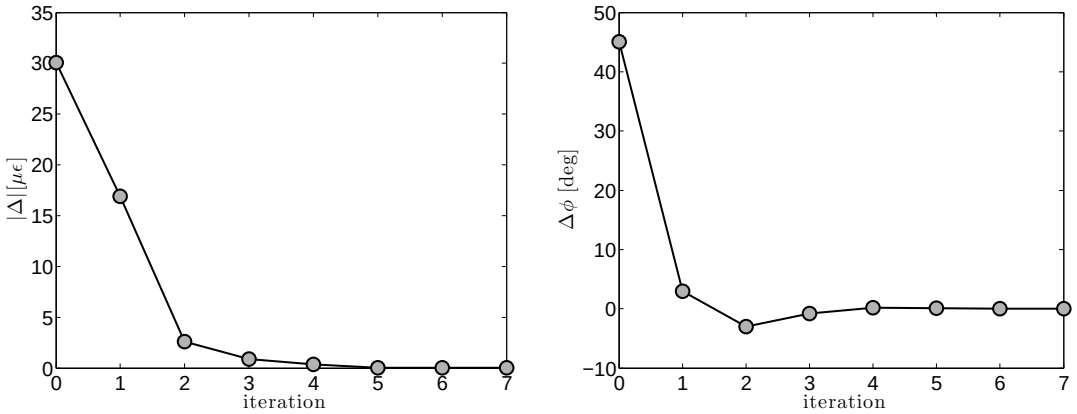

(a) Absolute value (b) Phase

Figure 24: Beam 3. Convergence analysis of maximum difference in absolute value and phase between the reference and actual signals at the sensors' location.

Another case is represented by the mixture of strain gages with a displacement sensor (case Beam 5, Figure 29(a)) or with a force sensor (Beam 6, Figure 29(b)). This last analysis represents a realistic case since it is generally possible to measure the load acting on an element of the system through a load cell sensor. The presence of a displacement/force sensor recovers the behavior due to quasi-rigid displacements and improves the behavior of LCA with respect to a pure strain case (Figures 30(a) - 30(b)).

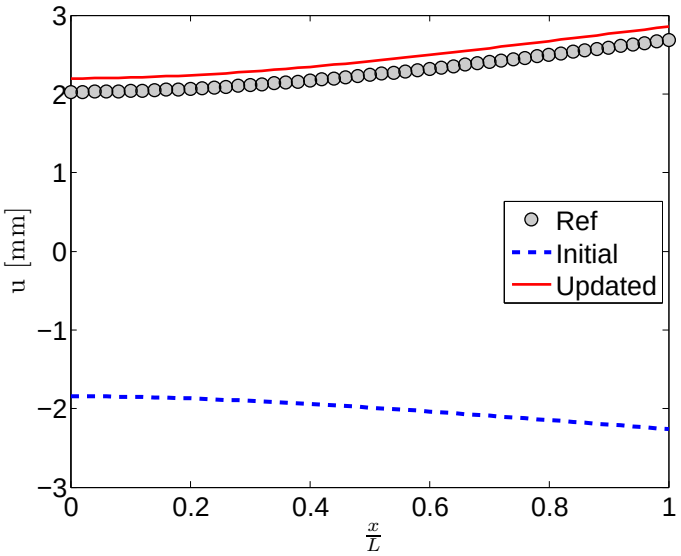

Figure 25: Beam 3. Instantaneous deformed shape of the beam. Reference (o). Initial FEM (--). Final FEM (-).

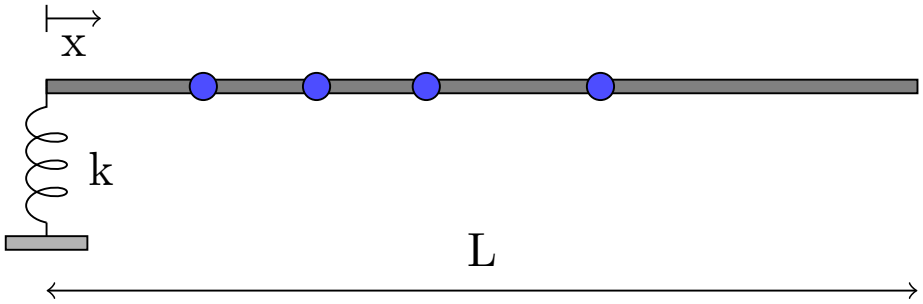

Figure 26: Beam 4. Linear spring-free beam. Displacement sensors in blue.

2.6 Conclusions

This chapter demonstrated that LCA can accurately represent the response of a system starting from a limited number of reference values at the control points in the absence of experimental noise and model inaccuracies. The next chapter analyzes the performance of LCA when reference values are experimentally generated. Three different cases are analyzed: a one-dimensional beam test, a two-dimensional plate experiment and in-flight tests of the UH-60A rotorcraft.

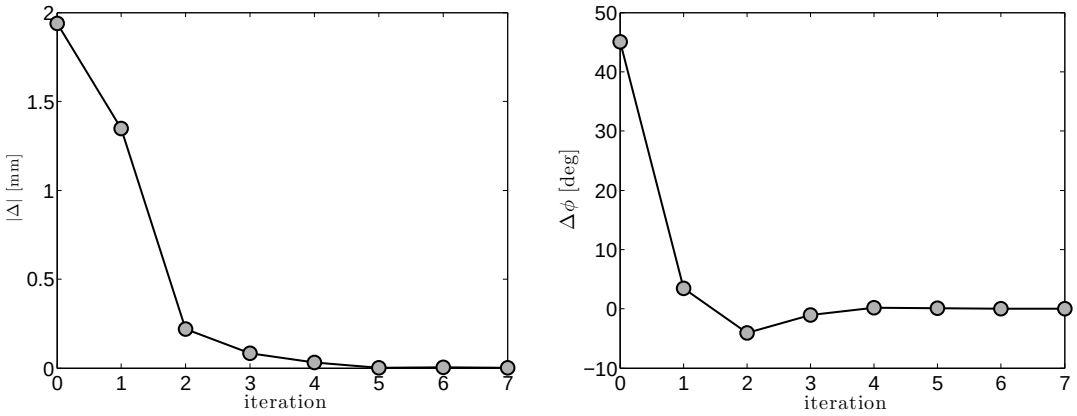

(a) Absolute value (b) Phase

Figure 27: Beam 4. Convergence analysis of maximum difference in absolute value and phase between the reference and actual signals at sensor location.

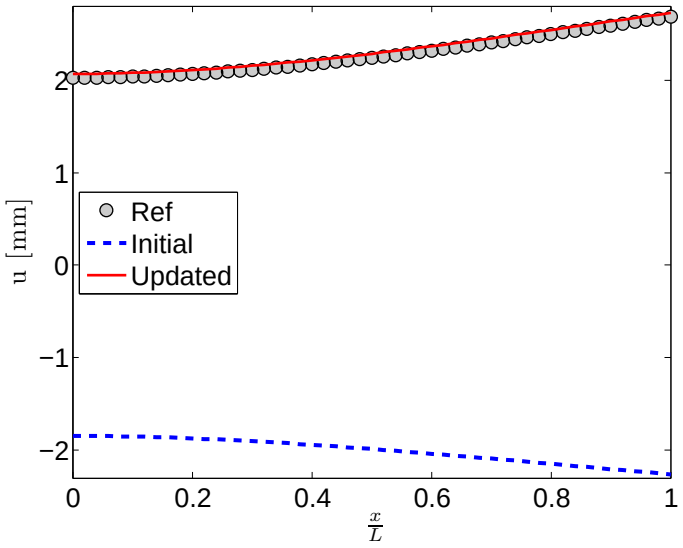

Figure 28: Beam 4. Instantaneous deformed shape of the beam. Reference (o). Initial FEM (--). Final FEM (-).

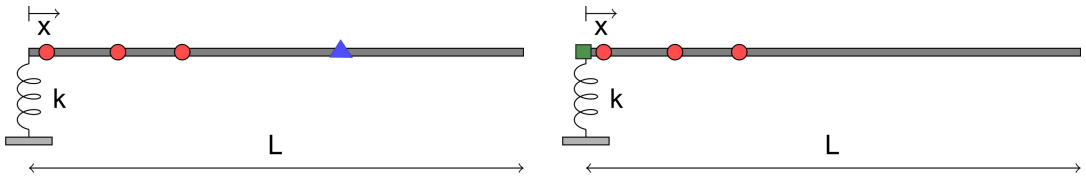

(a) Beam 5 (b) Beam 6

Figure 29: Vertical spring-free beam. Position of strain sensors in red (o). Position of displacement sensor in blue (△). Position of force sensor in green (□).

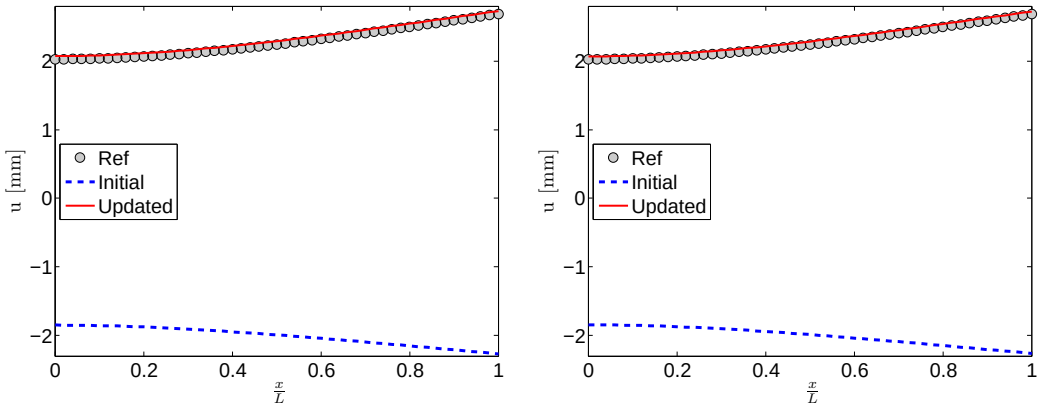

(a) Beam 5 (b) Beam 6

Figure 30: Instantaneous deformed shape of the beam. Reference (o). Initial FEM (- -). Final FEM (-).

CHAPTER III

APPLICATION OF THE LOAD CONFLUENCE ALGORITHM TO EXPERIMENTAL DATA

3.1 Overview

The efficiency of the Load Confluence Algorithm is initially evaluated through well-controlled lab experiments performed on an aluminum rotor blade and an aluminum plate. The objective of the experiments is to analyze the performance of LCA in the presence of measurement's errors and inaccuracies in the model as typical for practical applications. Then, the analysis of a more complex problem is presented in which flight test results of a UH-60A helicopter are used as reference.

3.2 Experiments on beams

3.2.1 Objectives

The first application of LCA to experimental results involves the analysis of a beam in bending. In this set of experimental analyses, an aluminum rotor blade is excited by a concentrated force and its response is measured through a set of strain gages [28, 26]. This one-dimensional test in a well-controlled environment allows to investigate the performance of LCA in case of minimal inaccuracies in the numerical model of the structure and minimal experimental noise. It provides indication of the characteristics of the approach, that will then be generalized by two-dimensional and in-flight tests. This analysis focuses on the behavior of LCA far from resonance. Its behavior close to resonance is analyzed in section 3.3.

3.2.2 Experimental set-up

The beam is straight and it is characterized by a thin-walled cross section (Figure 31). The properties are uniform along the span. The geometry of the beam is listed in Table 3.

Figure 31: Beam cross section.

Table 3: Physical and geometrical properties of the thin-walled beam.

Length	$L = 0.413$ m
Airfoil	NACA 0012
Chord	$c = 0.07$ m
Mass	$m = 178$ g

The beam is clamped at its bottom and it is excited by an electrodynamic shaker located at two-thirds of its span, Figure 32, with a sinusoidal concentrated load of frequency $f = 10$ Hz. This frequency is lower than the first natural frequency of the beam, and it is not affected by the resonant behavior of the structure.

The response is characterized through velocity and displacement measurements recorded by a scanning laser vibrometer (Polytec PSV-400). The laser scanning vibrometer measures the velocity of a grid of points on the surface of the beam. The velocity signals are then integrated to obtain displacement measurements. In addition, strain measurements are performed at five locations along the span with linear strain gages placed within two-thirds of the span close to the root. These locations are chosen because strains are expected to reach higher values. The location of the strain gages and a detail of a single strain gage mounted on the blade are shown in Figure 33.

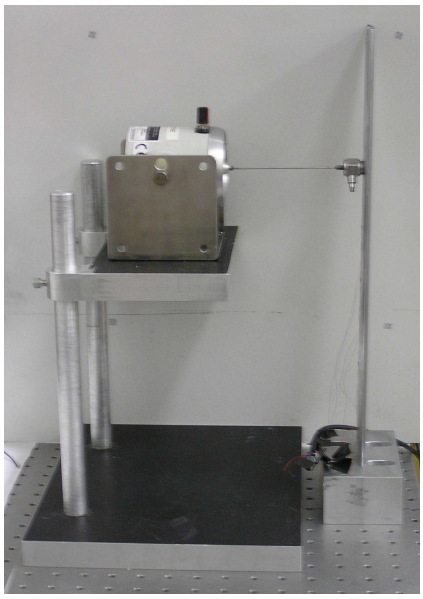

Figure 32: Experimental setup for shaker excitation of the blade.

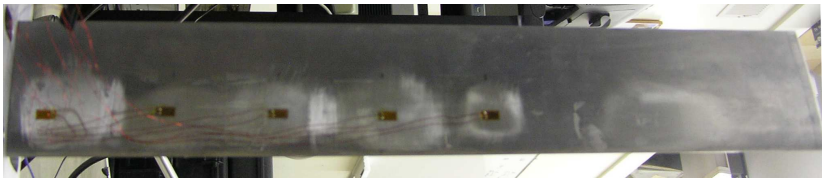

(a) Strain gages arrangement

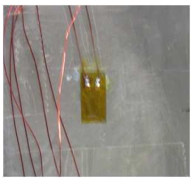

(b) Detail of a single gage

Figure 33: Location of the strain gages along the blade span and detail of a gage.

3.2.3 Beam model

The blade is modeled with finite elements and is discretized by 15 Timoshenko beam elements with third order polynomial shape functions (lock-free elements). This discretization is characterized by converged natural frequencies.

The mass and stiffness properties are optimized in order to match experimental and numerical bending natural frequencies with acceptable accuracy. The parameters for this simple optimization problem are the mass per unit length of the beam, the bending and shear stiffnesses. The objective function is defined as the difference

between estimated and experimental natural frequencies. Experimental natural frequencies are evaluated from the behavior of the operational frequency response function for a random excitation. The resulting choice of parameters accurately represents the dynamic behavior of the beam in terms of natural frequencies with inaccuracies of the order of 5% on the lower modes, Table 4.

Table 4: Comparison between numerical (f_n) and experimental (f_e) bending natural frequencies of the blade.

ID	f_e [Hz]	f_n [Hz]	Error [%]
f_1	36.21	36.63	1.2
f_2	227.5	229.3	0.8
f_3	632.5	641.1	1.3
f_4	1197.5	1253.3	4.5

The external load is modeled as a nodal concentrated load applied at two-third of the span, in correspondence of the position of the shaker in the experimental setup. The system is excited with a sinusoidal load of frequency 10 Hz. Initial differences exist between the magnitude and phase of the numerical and experimental load function, that result in inaccuracies in the computation of the dynamic response, both in its peak-to-peak values and in phase. LCA aims to correct these initial inaccuracies, as described in the following section.

3.2.4 Results of LCA

The LCA is applied to an initial model of the blade whose dynamic response is characterized by both phase and peak-to-peak differences with respect to the experimental measurements due to inaccuracies in the representation of the load. The identification process includes four strain sensors because the fifth sensor (closer to the tip, in proximity of the attachment point of the shaker) is characterized by a low level of measured strains, and it is therefore highly affected by measurement noise. In the following, the sensor close to the root will be referred as the "root" sensor, as opposed

to the "tip" sensor which is the closest to the tip.

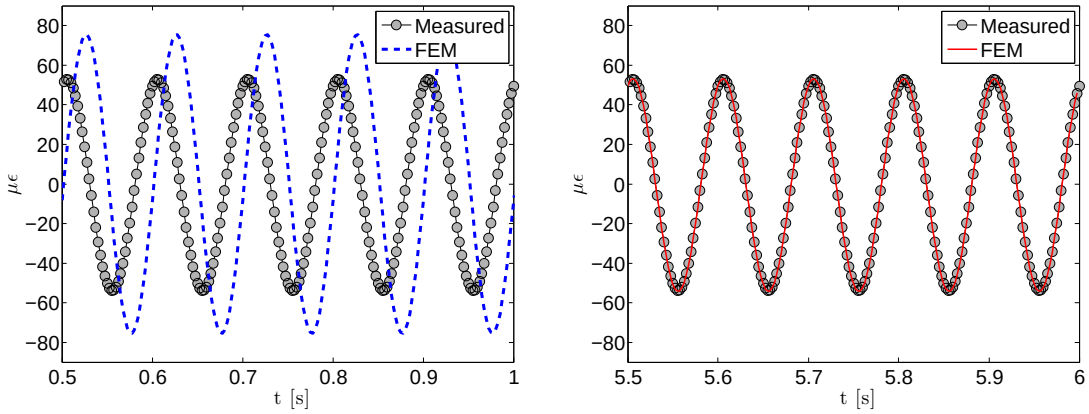

(a) Before (b) After

Figure 34: Measured and predicted strain at the root sensor at the beginning of the analysis and after the application of LCA. Measured (o). Initial FEM (--). Final FEM (-).

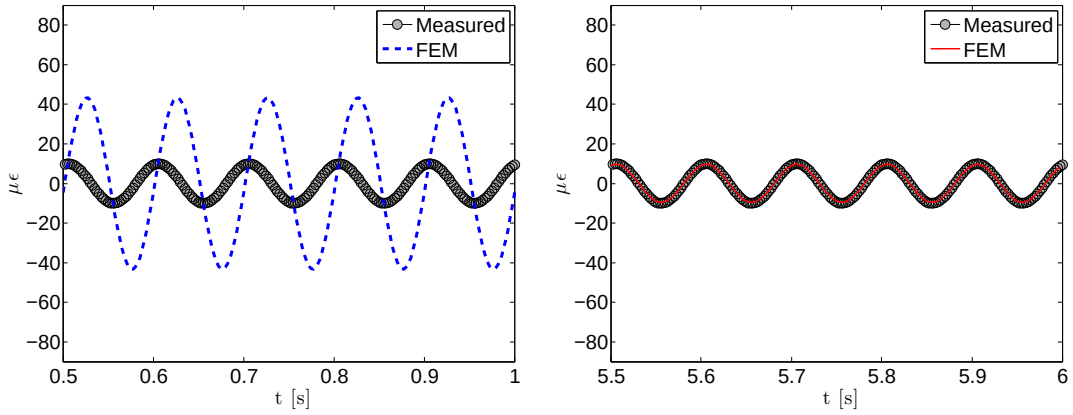

(a) Before (b) After

Figure 35: Measured and predicted strain at the tip sensor at the beginning of the analysis and after the application of LCA. Measured (o). Initial FEM (--). Final FEM (-).

Figures 34 and 35 show the comparison between the time histories of the measured and numerical strains estimated at the first step of the analysis and at the end of the simulation. The numerical response at the control points is accurately corrected by LCA. Initial differences of the order of $30\mu\epsilon$ on peak-to-peak values (Figure 36(a)) and

of 70 deg on the phase (Figure 36(b)) are improved to less than $5\mu\epsilon$ and 5 deg after the first iteration. Convergence of the algorithm is achieved after three iterations. As a result of these improvements, the difference in time history of the signals becomes almost constant (Figure 37).

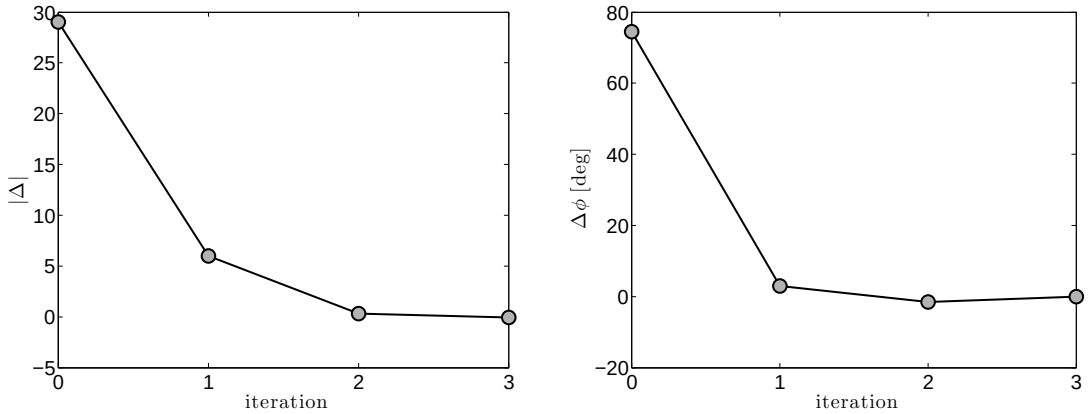

(a) Absolute value (b) Phase

Figure 36: Convergence analysis of maximum difference in absolute value and phase between the reference and numerical signals at the sensor location.

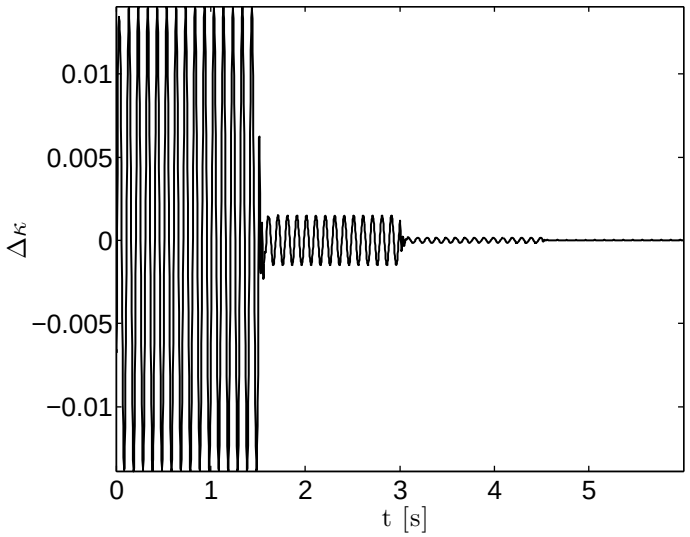

Figure 37: Maximum difference in time history after each application of the mapping algorithm.

This one-dimensional example shows that accurate representation of the response through correction of the external loads based on experimental measurements are

possible and accurate. The next section investigates the characteristic of LCA for a two-dimensional experimental case.

3.3 Experiments on plates

3.3.1 Objectives

The algorithm is now applied to experimental measurements in a two-dimensional problem. Due to its high flexibility, the LCA can in fact analyze many dynamic systems without requiring ad-hoc modifications. In this set of experimental analyses, an aluminum plate is excited by a concentrated force and its response is measured in terms of velocity. This example expands the application of LCA with respect to the previous one-dimensional analyses, showing the versatility of the algorithm [30]. It explores the performance of the algorithm in case of large discrepancies in the representation of the applied load (both in terms of value and of location) and close to resonant conditions.

3.3.2 Experimental set-up

Experiments are performed on an aluminum rectangular plate, 0.25×0.46 m of dimensions, and thickness 1.5 mm. The experimental set-up is shown in Figure 38.

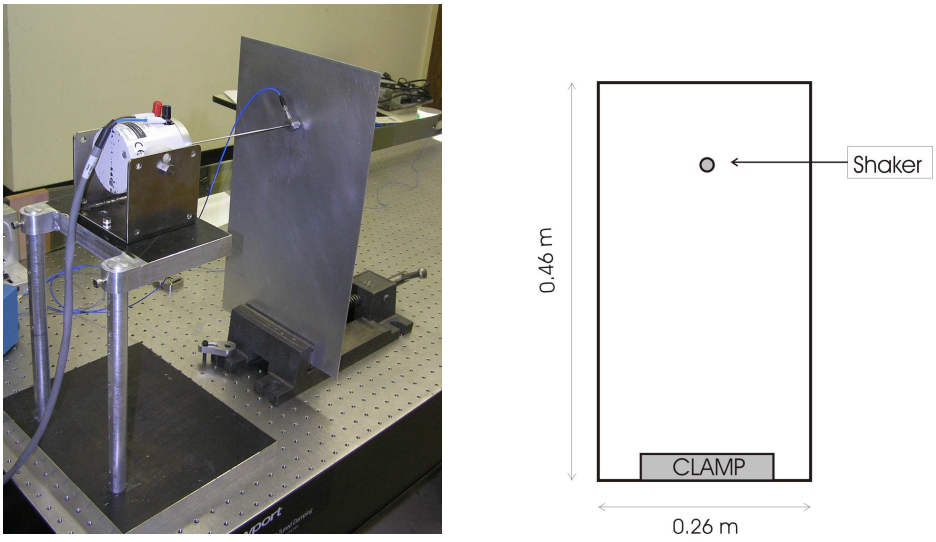

Figure 38: Experimental configuration for an aluminum rectangular plate.

The plate is partially cantilevered at its bottom edge and a concentrated force is applied through an electrodynamic shaker (model LDS V201/3) located at x_L = 0.125 m and y_L = 0.355 m from the lower left corner of the cantilever plate. The velocity distribution over the plate surface is measured by the scanning laser vibrometer (Polytec PSV-400), set to measure the response in 209 points of a grid covering the plate surface. The velocity field of the plate is integrated to obtain the corresponding displacement distribution. The measured set of points is divided in two subsets: a first small subset is used by LCA to identify the response, while a larger subset compares the full-field numerical predictions with the measured response of the plate. The two subsets are shown in Figure 39.

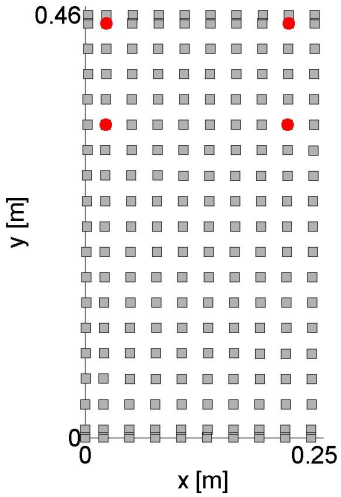

Figure 39: Measured grid points on the plate. Large subset: grey squares, small subset: red circles.

3.3.3 Plate numerical model

A finite element model of the aluminum plate is developed using the material and geometrical properties listed in Table 5. They result from an optimization procedure to match the numerical and experimental natural frequencies. The optimization parameters of this procedure consist of geometric dimensions (lengths of the plate in x- and y-directions), thickness, Young modulus and density of the material. The objective

function is defined as the difference in the lowest five natural frequencies between the experimental and numerical systems. The numerical natural frequencies are computed considering a mesh of 8x16, 8-node, Mindlin's isoparametric plate elements. The plate is partially clamped on one short edge and is excited by an harmonic concentrated load. The experimental natural frequencies are evaluated from the frequency response functions measured by the laser scanning vibrometer for a pseudo-random excitation. The objective function is minimized through an optimization approach for constraint problems. The results of this analysis define the physical properties of the system that better match the experimental measurements in terms of natural frequencies and are considered to define the input model to analyze the performance of LCA.

Table 5: Material and geometrical properties of the plate.

E	57136 MPa
ν	0.3
ρ	2600 kg/m^3
L_x	0.251 m
L_y	0.46 m
t	1.5 mm

The natural frequencies of the model show a very good agreement with the experimental measurements (Table 6), and the same holds for the modal shapes of the system. Therefore, a good correlation can be assumed between the numerical model and the experimental system in terms of mass and stiffness distributions. A discrepancy of 20% on the first natural frequency is observed due to excitation inaccuracies of the shaker at low natural frequencies. This is the reason why the optimized elastic modulus assumes a value that differ from the generally assumed value for aluminum.

The geometry and mesh are shown for different positions of the concentrated load in Figure 40, with the corresponding boundary conditions and applied load.

Table 6: Numerical f_n and experimental f_e natural frequencies for the plate.

Mode	f_n [Hz]	f_e [Hz]	Error [%]
f_1	6.10	5.00	22.0
f_2	22.3	22.5	0.89
f_3	37.8	37.5	0.80
f_4	73.0	77.5	5.80
f_5	104.1	100.0	4.10

3.3.4 Results

The harmonic response of the plate is analyzed for different excitation frequencies, $f = 10$ Hz and $f = 20$ Hz, chosen as representative of the behavior of the algorithm. Both the case of an initial accurate load distribution (concentrated load applied at the shaker location, Figure 40(a)) and of inaccurate distribution (concentrated load not applied at the shaker location, Figure 40(b)) are presented. The characteristics of each analysis are summarized in Table 7.

Table 7: Cases analyzed for the plate configuration.

Case ID	f [Hz]	No. sensors, No. modes	Load position
Plate 1	10	s = 4, m = 3	accurate
Plate 2	20	s = 3, m = 2	non-accurate

The dynamic responses at the beginning and end of each simulation are compared to demonstrate the ability of the algorithm. This comparison is presented for the following three points in the structure (Figure 41):

- Sensor 1 used by LCA as reference point.
- Point A (x = 0.05 m, y = 0.26 m, left edge of the plate) not used by LCA as reference point.
- Point B (x = 0.20 m, y = 0.14 m, center of the plate) not used by LCA as reference point.

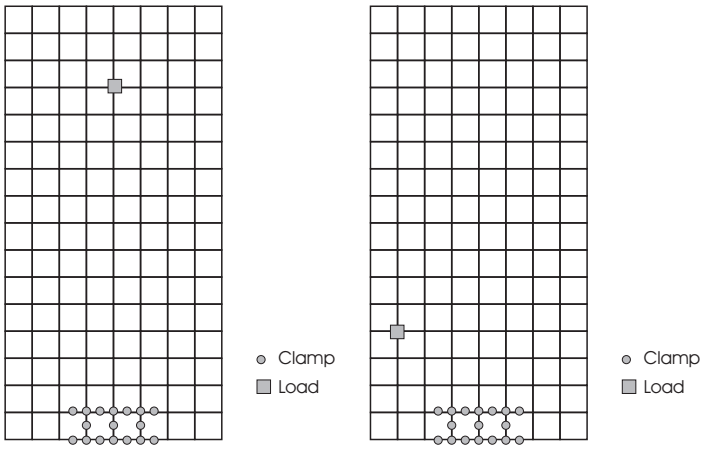

(a) Plate 1 (b) Plate 2

Figure 40: Geometry and mesh of the numerical model of the plate.

The first analysis considers an excitation frequency $f = 10$ Hz with an accurate placement of the concentrated load (Figure 40(a)), and includes in the identification process four sensors and three modes. This number of sensors and modes is seen to give an accurate prediction of the full-field response of the structure. The corresponding $\boldsymbol{B}$ matrix (refer to section 2.3) is in fact well-conditioned, as demonstrated by its singular values listed in Table 8 that are characterized by the same order of magnitude. The singular values of $\boldsymbol{B}$ in fact give an indication on how well the considered sensors are able to represent the modes included in LCA. The four sensors are placed in the top section of the plate, two on the left and two on the right side, Figure 41.

Table 8: Singular values of matrix $\boldsymbol{B}$ for cases Plate 1-2.

ID	σ_i	σ_i/σ_{max}
1	162.8	1.00
2	152.3	0.94
3	60.1	0.37

Initially, both magnitude and phase errors characterize the numerical response at the control points (Figure 42(a)) when compared to the experimental measurements. These differences are accurately recovered by LCA both at control points

(Figure 42(b)) and at other locations in the domain (Figures 43, 44). These results confirm the ability of LCA to identify the full-field response of the structure, as it is demonstrated by comparing the experimental and numerical deformed shapes of the plate before and after the application of the LCA (Figure 45). Moreover, the deformed shapes of two midspan cross sections in x and y directions are shown in Figure 46. The discontinuities in experimental response are due to measurement noise.

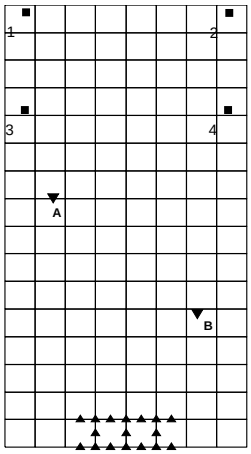

Figure 41: Location of control and comparison points used by LCA.

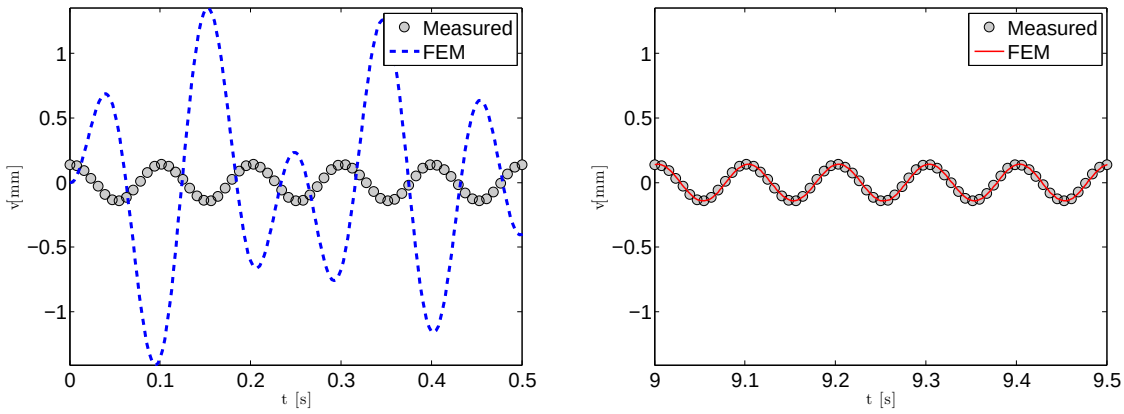

(a) Initial response

(b) Final response

Figure 42: Plate 1. Comparison of experimental and numerical response at sensor 1. Measured (o). Initial FEM (--). Final FEM (-).

The reconstructed response shows a good agreement with the experimental results. The peak-to-peak error is reduced of more than 90%, and the same behavior is noticed

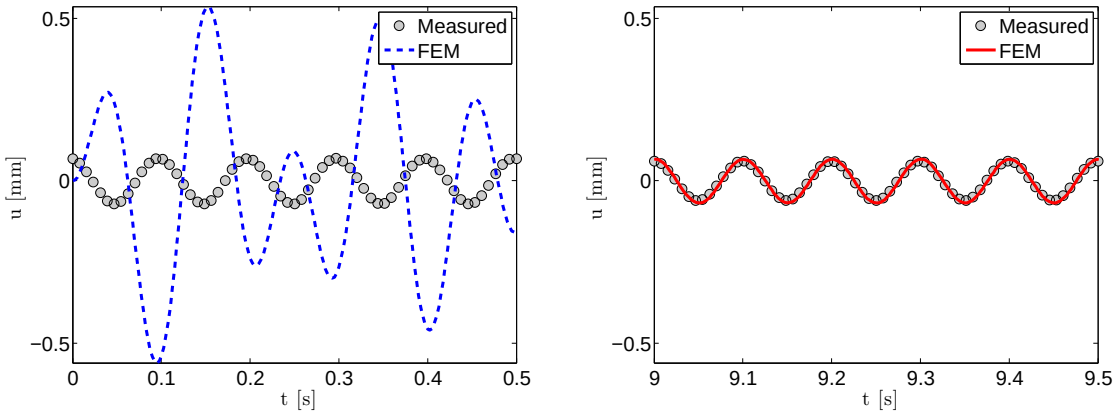

(a) Initial response (b) Final response

Figure 43: Plate 1. Comparison of experimental and numerical response at point A. Measured (o). Initial FEM (--). Final FEM (-).

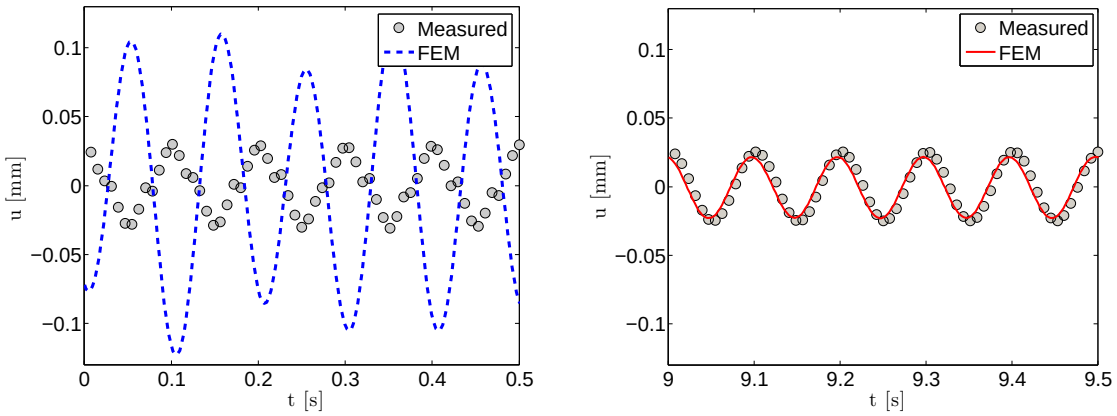

(a) Initial response (b) Final response

Figure 44: Plate 1. Comparison of experimental and numerical response at point B. Measured (o). Initial FEM (--). Final FEM (-).

for the phase difference between the signal, as shown in Figure 47.

In the second case, a large inaccuracy in load location is introduced into the model and the algorithm needs to perform in a more critical condition. The load is applied close to the left bottom corner of the plate ($x = 0.063$ m, $y = 0.115$ m, Figure 40(b)), while in the experimental set-up (Figure 38) is located in the central-top part of the plate. A reduced number of sensors and modes is also considered ($s = 3$, $m = 2$). The convergence of the simulation is reached in seven iterations, as shown in Figure 48 by the changes of the differences in absolute value and phase during the analysis.

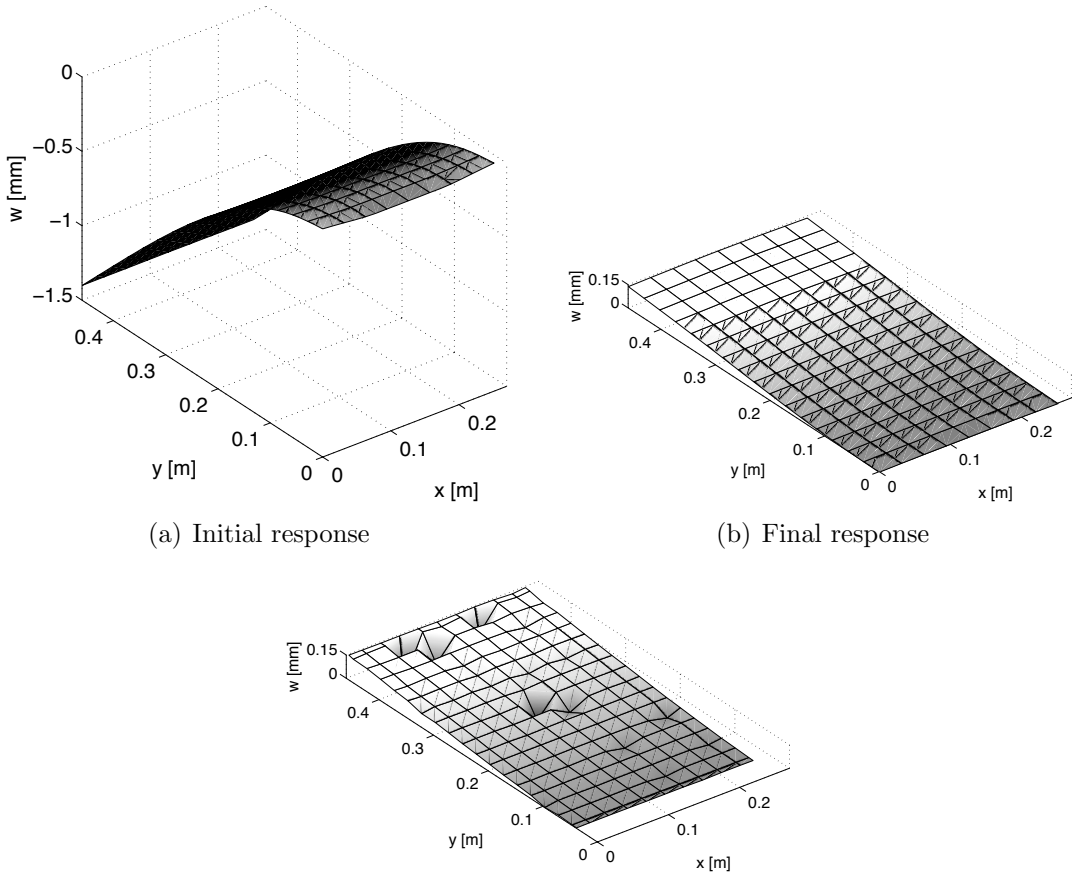

(a) Initial response

(b) Final response

(c) Experimental response

Figure 45: Plate 1. Comparison of numerical and experimental instantaneous deformed shapes before and after the application of LCA.

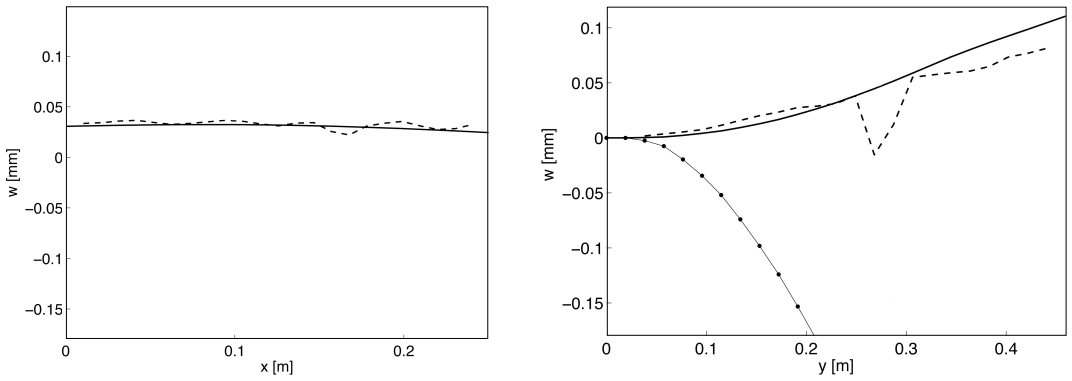

(a) Mid-Cross section in x-direction y = 0.23 m

(b) Mid-Cross section in y-direction x = 0.13 m

Figure 46: Plate 1. Comparison of cross sections deformed shapes in x and y directions. Measured (--). Initial FEM (o). Final FEM (-).

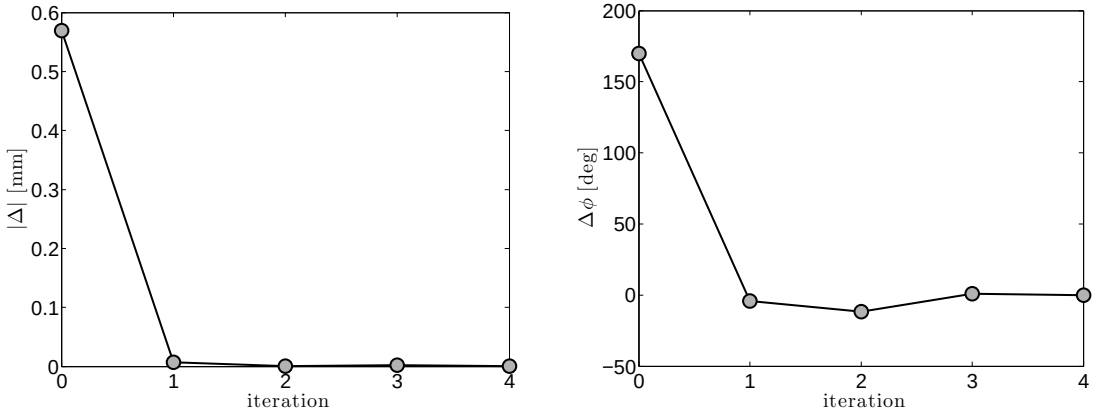

(a) Absolute value (b) Phase

Figure 47: Plate 1. Convergence of maximum absolute value and phase of the reference sensors during the analysis.

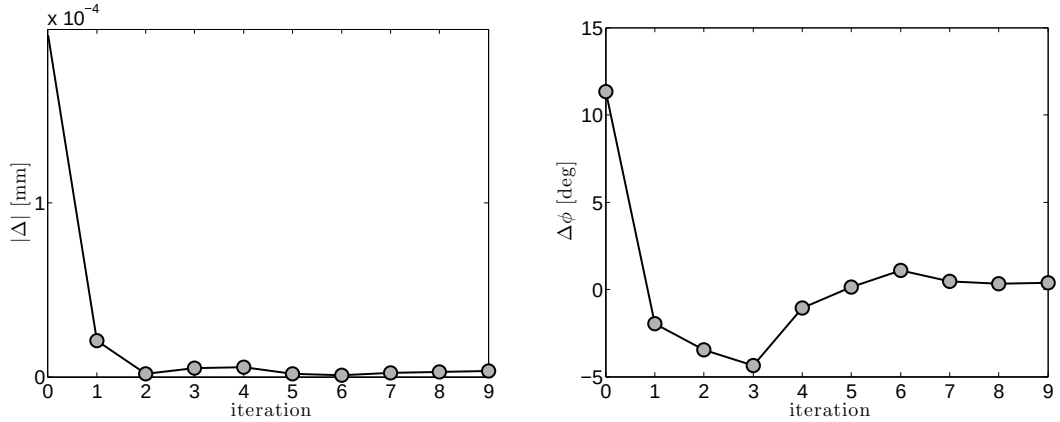

Figure 48: Plate 2. Convergence of maximum absolute value and phase of the reference sensors during the analysis.

The time histories of the displacement of the plate are compared before the application of the updating procedure and at the end of the simulation (Figures 49 and 50) and an improved representation of the response is achieved in this case as well. The experimental and numerical deformed shapes of the plate are compared before and after the application of LCA in Figure 51. The deformed shape of two midspan cross sections in x and y directions are shown in Figure 52. The experimental response is dominated by the first mode of the plate, even if the excitation frequency is closer to the second resonance (Figure 51(c)), because the shaker is located on a nodal line

for the second mode. This is not true for the initial numerical response, because of the inaccurate location of the concentrated load (Figure 51(a)). The LCA is able to recover also this critical case in which the response of the two systems are dominated by different modes, provided that all modes that participate in the response are considered in the identification process (Figure 51(b)).

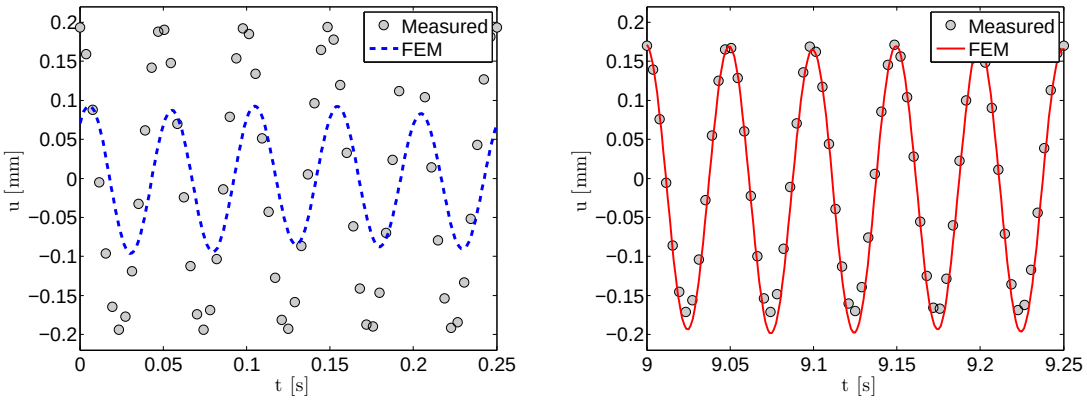

(a) Initial response (b) Final response

Figure 49: Plate 2. Comparison of experimental and numerical response at point A. Measured (o). Initial FEM (--). Final FEM (-).

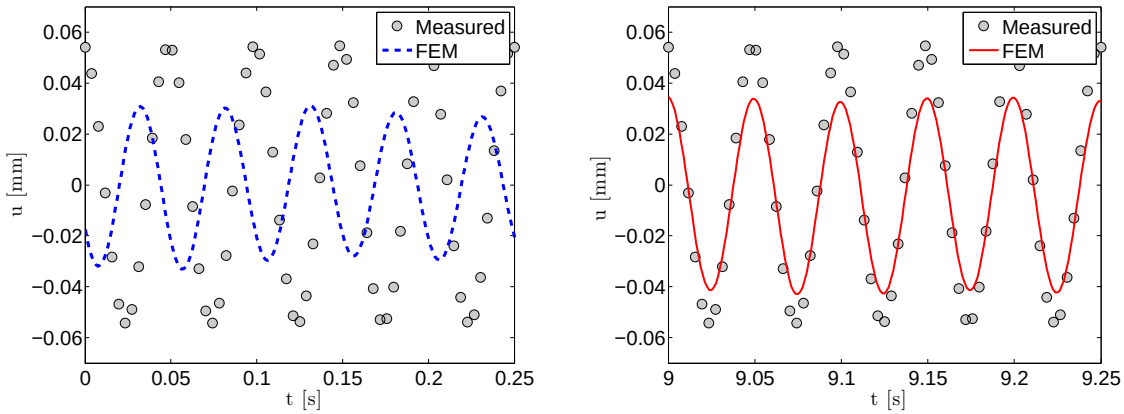

(a) Initial response (b) Final response

Figure 50: Plate 2. Comparison of experimental and numerical response at point B. Measured (o). Initial FEM (--). Final FEM (-).

These results demonstrate that the reconstruction of the complete mapping of the dynamic response is possible and accurate. In particular, Figures 46-52 show that accurate representations of the response in general points of the structure are achieved

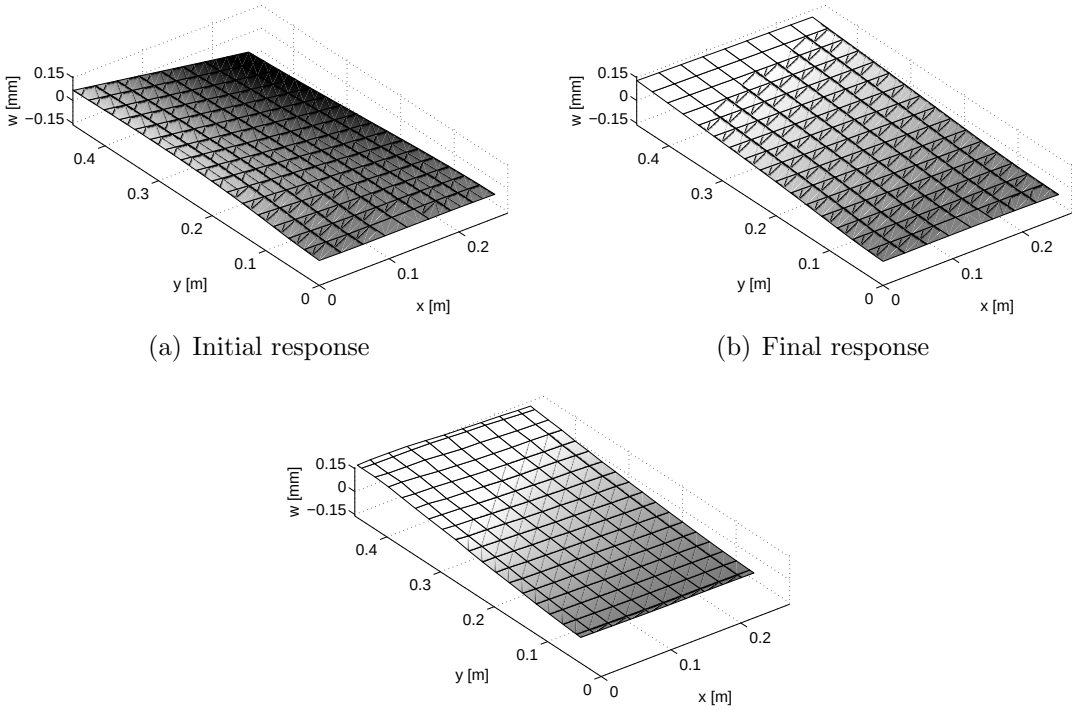

(a) Initial response

(b) Final response

(c) Experimental response

Figure 51: Plate 2. Comparison of numerical and experimental deformed shapes before and after the application of LCA.

with a small number of reference sensors and number of modes used in the modal expansion. In both cases, a few iterations (less than ten) are necessary to achieve a good accuracy of the numeral response in terms of peak-to-peak values and phase. The reconstruction of the response is therefore possible when both the load magnitude and the distribution are unknown.

3.4 UH-60A flight test data

A more complex scenario is investigated to understand the capabilities of the approach. In the previous sections, the LCA is applied to linear dynamical systems and the effects of non-linearities is not investigated. A non-linear case is now presented involving flight test data from a Sikorsky UH-60A rotorcraft as reference points to a rotor system modeled with multibody techniques [48, 10, 9].

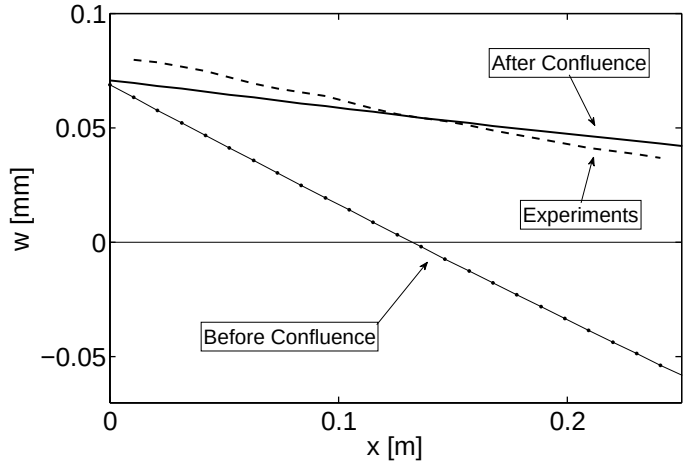

(a) Mid-Cross section in x-direction y = 0.23 m

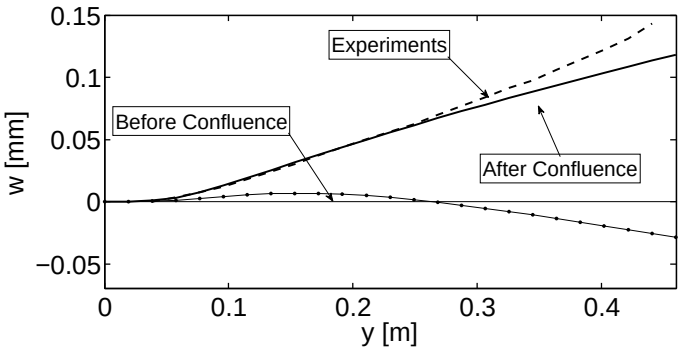

(b) Mid-Cross section in y-direction x = 0.13 m

Figure 52: Plate 2. Comparison of cross sections deformed shapes in x and y directions. Measured (--). Initial FEM (o). Final FEM (-).

3.4.1 Objectives

When using simplified aerodynamic models, state-of-the-art comprehensive codes predict the flapping bending moment distribution acting on the blade with fair accuracy, while the torsion and edgewise moments are predicted with lower accuracy, particularly at higher harmonics (3/rev and above) [1]. The accuracy of the prediction improves when using advanced CFD codes or measured aerodynamic loads [52, 69, 76]. For example, Datta et al. [34, 36] compare the predictions of the structural loads for the UH-60A helicopter when measured airloads are applied to the structural model and the results of coupled CFD/CSD analysis (RANS CFD/comprehensive analysis) with experimental measurements in three different flight conditions (high speed, low

speed, high thrust). The common findings of the different analyses are:

- the peak-to-peak values for bending and torsion moments are well predicted both by measured and CFD airloads. This is due to the fact that the low harmonics (1-3/rev) are well predicted in magnitude. The peak-to-peak values of the chord bending moment are instead generally underpredicted by both schemes,

- the accuracy of the predicted vibratory flap bending moments highly depends on the considered flight condition. The discrepancies are mostly due to the quality of airloads predictions. The 3/rev harmonic is in all conditions the dominant vibratory harmonic,

- the vibratory chord bending moment is predicted with large inaccuracies in all flight conditions, especially in the magnitude values of the 4-5/rev (errors of about 50%). These large errors are mainly due to structural dynamic deficiencies since the airloads model does not result in any improvement,

- the predicted vibratory torsional moments show large discrepancies in particular at 4-5/rev. The reason for these discrepancies is still not clear, probably related to unmodeled structural dynamics.

Unfortunately, measured airloads are generally not available. On the other hand, CFD formulations provide high fidelity, nonlinear aerodynamics that can overcome many of the shortcomings of simplified aerodynamic analyses, but are computationally too expensive to be considered in design and maintenance phases. However, when simplified airloads, such as lifting line theories, are coupled with the structural model, the predictions are less accurate [65, 49, 76]. Current trends [35] of rotorcraft research aim to improve the predictions of modern modeling approach by developing three-dimensional rotor structural dynamic analysis (coupled with three-dimensional

CFD approaches) that can model generic structural components to determine critical couplings and stresses that are neglected by current simplified one-dimensional representations of the dynamic of the blades. These methodologies require high computational costs and are therefore not considered a feasible approach in the present work, although their promising applications. This section demonstrates that the use of simplified airloads in combination with experimental measurements of the response can result in high prediction accuracy with moderate computational cost when LCA is applied. In the following analysis, the system is modeled as a flexible multibody system in which a simplified model of the airloads, based on lifting line theory, is coupled with the structural model. The pitch angle of the blades is imposed as input to the numerical model based on experimental measurements.

3.4.2 UH-60A dataset

Extensive in-flight experimental results of blade airloads and strain measurements are available through the UH-60A Airloads Project, as described in [73, 23, 54]. Highly-instrumented blades were designed, built, and installed on a standard UH-60A aircraft [52], as shown in Figure 53.

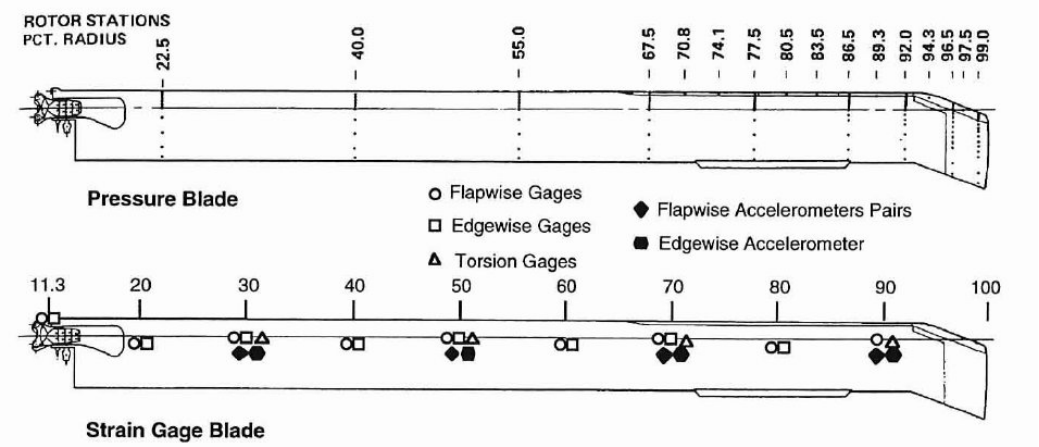

Figure 53: UH-60A instrumented blades with location of strain gages, accelerometers and pressure transducers (from [23]).

Of the four rotor blade, one blade was instrumented with a total of 221 pressure transducers installed in nine spanwise arrays, and 21 pressure transducers installed near the leading edge. A second blade was instrumented with strain gauges (9 sensors for flapping moment, 8 sensors for edgewise moment, 4 sensors for torsion). and 8 accelerometers to measure the blade structural loads and response. The aircraft was also instrumented to measure the vehicle state. The pressure data were sampled so that the effective bandwidth corresponded to about 120 harmonics. Structural data were recorded at a lower rate which corresponded to an effective bandwidth of about 24 harmonics. Sixty-eight test points (counters) obtained during the UH-60A Airloads Program are classified as maneuvers. This set includes classical maneuvers such as symmetric pull-ups and pushovers, rolling pullouts, roll reversals, and diving turns.

The LCA is applied to the analysis of three different flight conditions located at the boundary of the UH-60A flight envelope and generally used in the literature as benchmarks to assess numerical models. The first flight condition is characterized by high speed (C8534), the second by high thrust and dynamic stall (C9017), the third one by low speed (C8513). The application of the mapping algorithm has the advantage that it does not require an accurate representation of the aerodynamic loads, and simple aerodynamic models can be used thus reducing computational efforts [27].

3.4.3 Numerical model

The Sikorsky UH-60A is a four-bladed helicopter the physical properties of which are described in [22] and references therein. The structural model is comprised of four blades connected to the hub through blade root retention structures and lead-lag hydraulic dampers. Figure 54 shows the configuration of a typical blade, which is modeled using thirteen cubic beam elements. The system is modeled in DYMORE [9, 10, 8]. The root retention structure, from hub to blade, is separated into three

segments, having three, two, and two cubic beam elements, respectively, and labeled segment 1, 2 and 3 in Figure 54. The first segment is attached to the rigid hub. The first two segments are connected to each other by an elastomeric bearing modeled by three co-located revolute joints with the following sequence: lag, flap, pitch rotations. The physical characteristics of the bearing are simulated by springs and dampers in the joints. The next two segments are rigidly connected to each other and to the pitch horn. Finally, the last segment is rigidly connected to the blade and damper horn.

The pitch angle of the blade is set by the following control linkages: swashplate, pitch link, and pitch horn. The pitch link, modeled by three cubic beam elements, is attached to the rigid swashplate by means of a universal joint and to the rigid pitch horn by a spherical joint. The damper arm and damper horn are modeled as rigid bodies. The lead-lag damper is modeled as a hydraulic damper with pressure relief valves; its end points are connected to the damper arm and horn; the physical properties of the device and more detailed descriptions can be found in [46, 11].

3.4.4 High speed flight test data (counter C8534)

The application of LCA is analyzed for a level- high-speed flight condition (counter 8534: 158 kt, $\mu = 0.368$, $C_w/\sigma = 0.0783$). This condition is associated with high vibratory loads due to tip compressibility effects on the advancing side that result in high operating and maintenance costs and reduced crew and system performance [34, 53].

The accuracy of the prediction of the internal loads is investigated when the characteristic parameters of the LCA vary. The identified loads are influenced mainly by the number and position of the experimental sensors s, the number of harmonics M considered in the analysis, and the number of modes m used in the modal expansion. However, since previous experimental data are considered as reference, the location

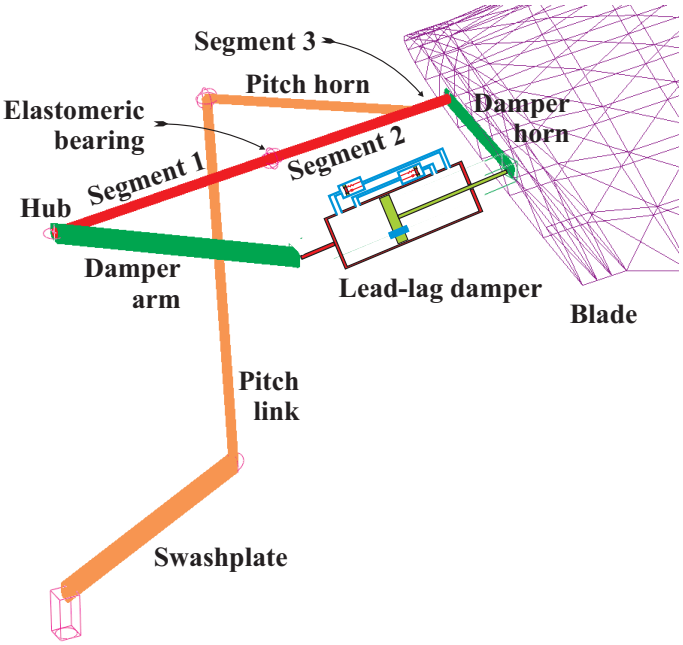

Figure 54: Configuration of Sikorsky's UH-60A rotor system: close-up view of the blade root retention structure, pitch link, pith horn, swashplate, and hydraulic damper (from [10]).

of the sensors cannot be modified. The convergence analyses focus on the influence of number of harmonics M and modes m. Four different cases are considered, in which up to six harmonics and ten modes are considered. In flight condition C8534, the measurements of 15 sensors are used as reference data: six flapping moments located at 20-30-40-60-70-90% of the span, six edgewise moments located at 20-30-40-60-70-90% of the span and three torsions, located at 30-70-90% of the span.

The convergence of the simulation is highly sensitive to the number of harmonics that are corrected by the LCA. The use of four harmonics and six modes, Figure 55, leads to good convergence of flap bending moments, while the chord bending moment and torsional moment are still not completely converged after 80 iterations of the algorithm.

The inclusion of higher harmonics makes the convergence of the algorithm particularly critical. The correction of the aerodynamic loads up to the sixth harmonic

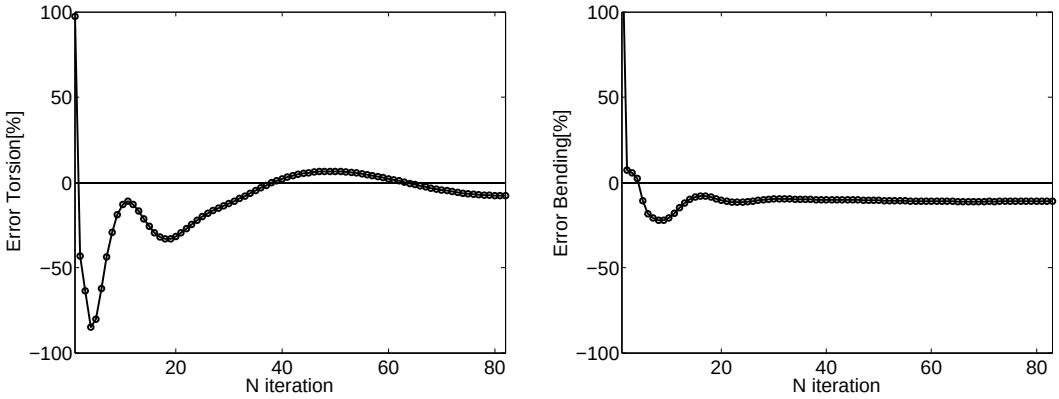

(a) Torsional moment

(b) Flap bending moment

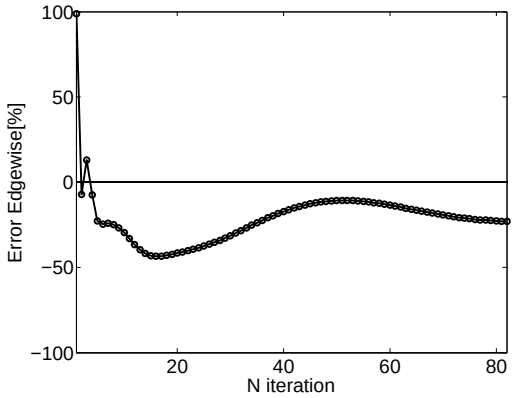

(c) Chord bending moment

Figure 55: Convergence of internal moments as the LCA is applied to the multibody system, $m = 6$, $M = 4$. High speed flight condition C8534.

prevents the convergence of the simulation, Figure 56, because these higher harmonic components cause high-frequency non-physical effects due to the fact that the frequency content of the strain measurements is concentrated in the first 4-5 harmonics. The choice of the number of harmonics included in the correction of the algorithm is therefore critical, and has to be specified in accordance to the frequency content of the experimental measurements.

The increase of the number of modes included in the modal expansion has instead a beneficial effect on the convergence of torsional, flap, and chord bending moments. In case of $m = 6$, Figure 55, the torsional and chord bending moments are still characterized by an oscillatory behavior after 80 iterations, and they reach an accuracy of

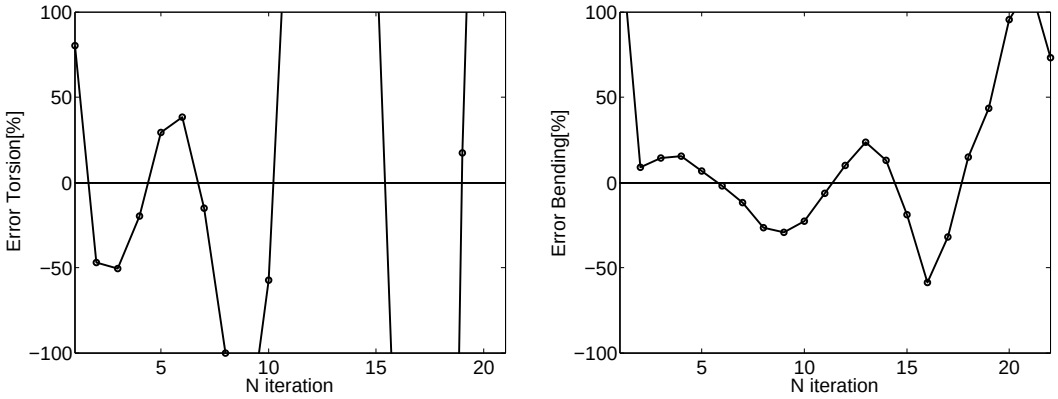

(a) Torsional moment

(b) Flap bending moment

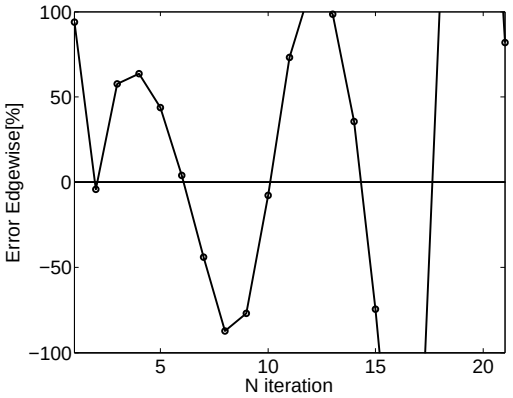

(c) Chord bending moment

Figure 56: Convergence of internal moments as the LCA is applied to the multibody system, $m = 6$, $M = 6$. High speed flight condition C8534.

approximately 10% and 25% respectively. The error is computed considering the difference between the numerical Fourier coefficients and the experimental measurements at the control points. The addition of two modes, $m = 8$, improves the convergence of the predictions, that reach a stable value after 70 iterations. Figure 57 shows that the torsional moment is predicted with an accuracy of about 15% with respect to the experimental measurements, and both the flap and chord bending moments are characterized by an error within 20%. The addition of higher modes, $m = 10$, not only results in a non-oscillating convergence after 50 iterations, but also improves the accuracy of the final predictions: Figure 58 shows that the accuracy of the torsional moment is improved to about 10%, the flap bending moments are predicted within

15% the flight test and the chord bending moments are characterized by an error of about 20%.

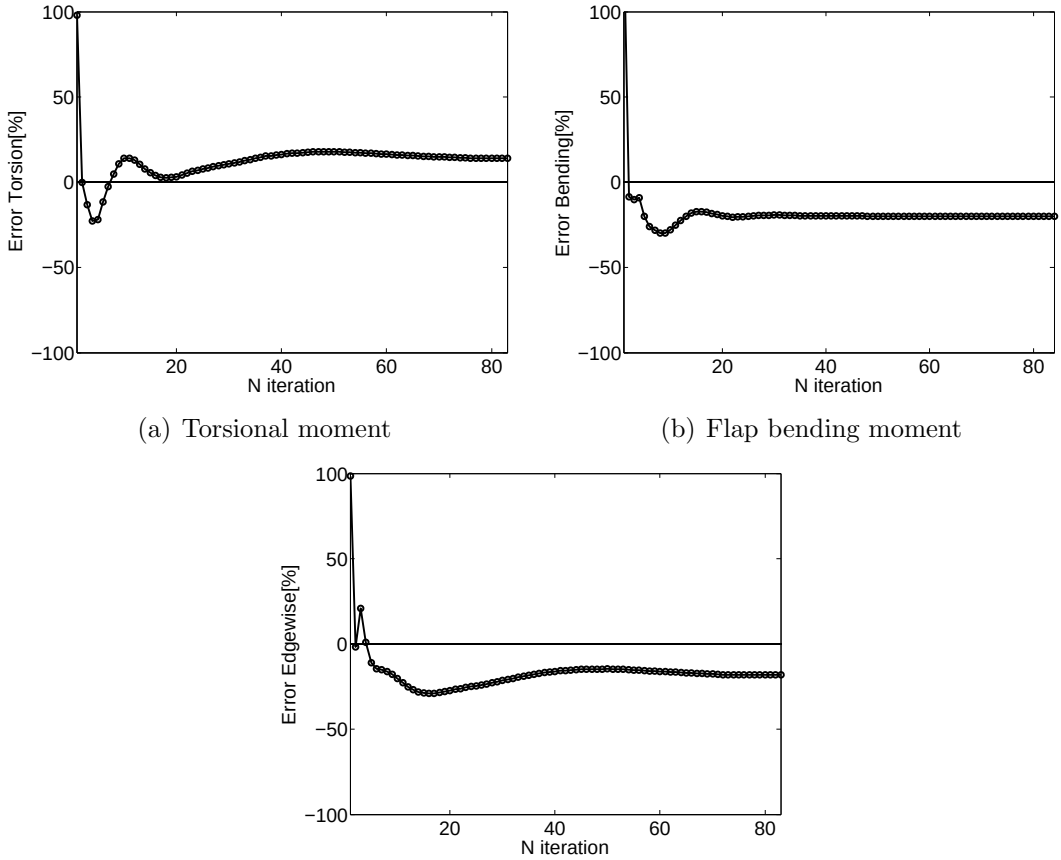

(a) Torsional moment

(b) Flap bending moment

(c) Chord bending moment

Figure 57: Convergence of internal moments as the LCA is applied to the multibody system, $m = 8$, $M = 4$. High speed flight condition C8534.

This behavior is better understood by comparing the time histories predicted by the LCA. In Figure 59, the variation of the torsional moment over a period at 70% span is presented for different choices of m and M. The choice of $m = 6$ and $M = 4$, Figure 59(a), improves the initial prediction of the torsional moment, but it is still not an adequate representation of the time history of the experimental measurements over a period. The increase of the number of harmonics, $M = 6$, Figure 59(b), adds non-physical high frequency content in the predictions, while the increase of the number of modes remarkably improves the numerical results, as shown in Figure 59(c) with

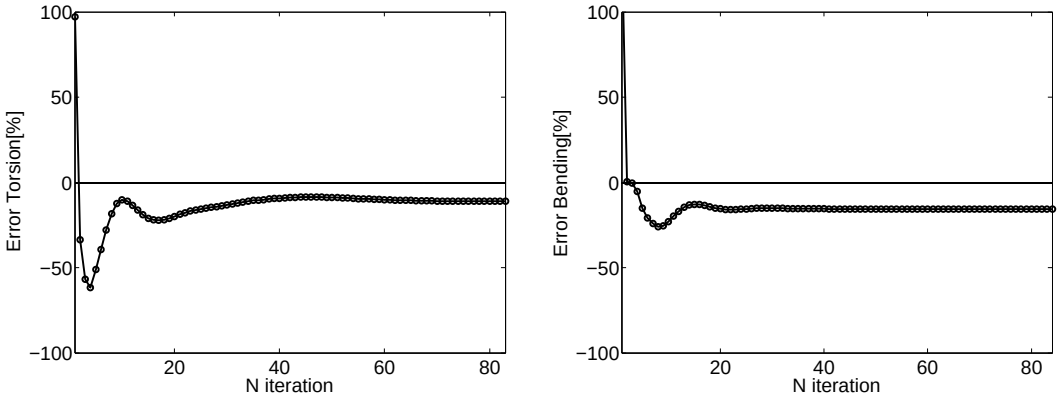

(a) Torsional moment

(b) Flap bending moment

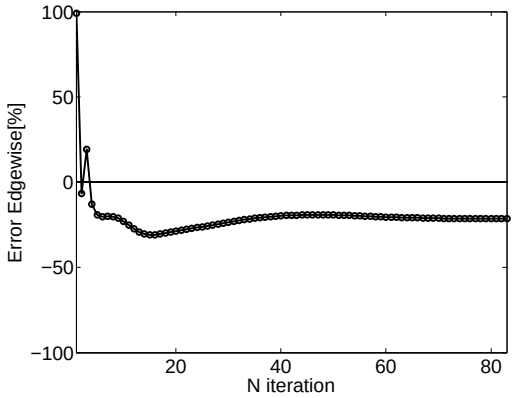

(c) Chord bending moment

Figure 58: Convergence of internal moments as the LCA is applied to the multibody system, $m = 10$, $M = 4$. High speed flight condition C8534.

8 modes, and in Figure 59(d) with 10 modes. Similar considerations hold for the flap (Figure 60) and chord (Figure 61) bending moments. The number of modes is not further increased because of the possible ill-conditioning in the computation of the pseudo-inverse of matrix $\boldsymbol{B}$. The number of modes must in fact be chosen to be lower than the number of reference sensors used in the analysis. The choice of $m = 10$ and $M = 4$ therefore appears as an optimal set of parameters in the LCA.

Extensive results are presented for flight counter C8534 to understand the predictive capabilities of the algorithm. The prediction of the pitch angle is shown in Figure 62. The model accurately represents the collective and cyclic control of the blade within 2-3%.

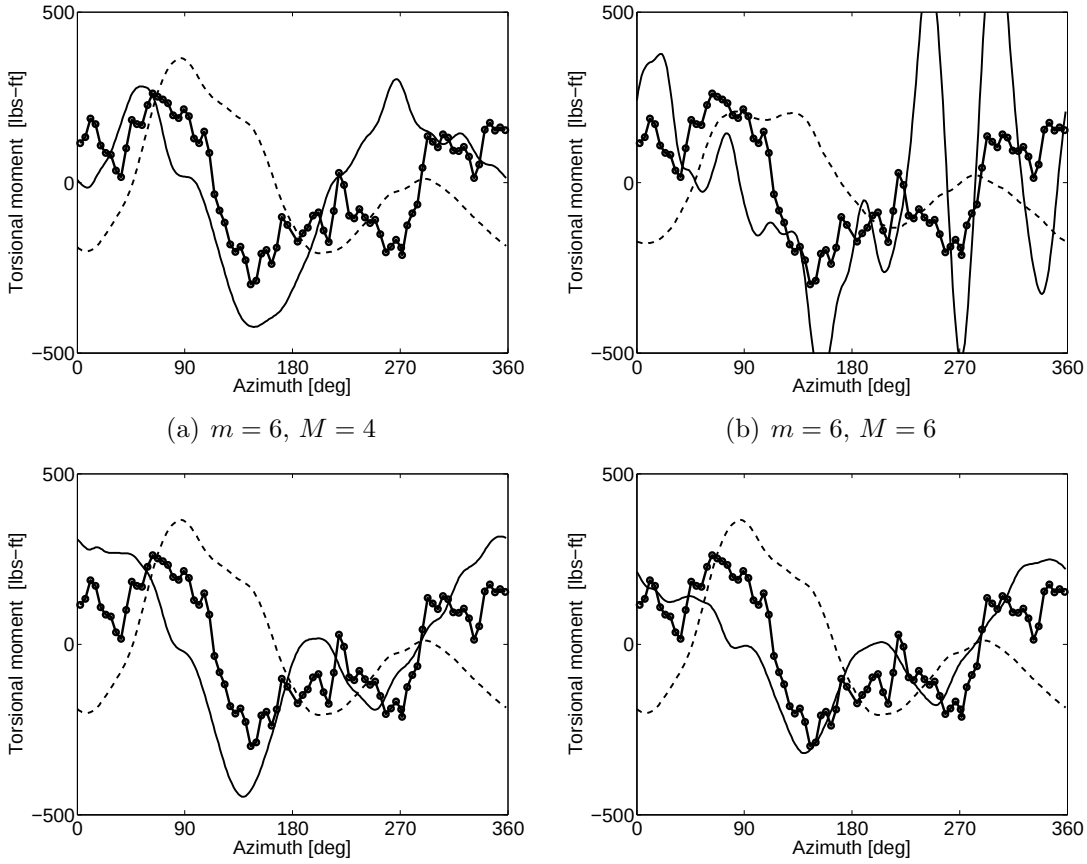

(a) $m = 6$, $M = 4$ (b) $m = 6$, $M = 6$

(c) $m = 8$, $M = 4$ (d) $m = 10$, $M = 4$

Figure 59: Analysis of torsional moments at 70% span for different choices of the number of modes m and harmonics M. High speed flight condition C8534. Steady loads removed. Measured (o). Initial numerical (--). Final numerical (-).

The prediction of the torsional moment (Figure 63) is important for the prediction of the 4/rev servo-loads. Their accuracy is greatly improved with respect to the initial results of the simulation across the span, although the predictions on the 3-4/rev present significant discrepancies. The magnitude and phase values for each harmonic across the span are shown in Figures 64 and 65, along with a comparison to results obtained from comprehensive CFD/CSD analyses [34]. The magnitude of the torsional loads is in general well predicted, in particular in the inboard part of the blade. Discrepancies in the higher harmonics, in particular in phase values, are due to structural modeling, as observed in [34], and are of the same order of magnitude of CFD/CSD analyses. This behavior is due to the lack of experimental data, since

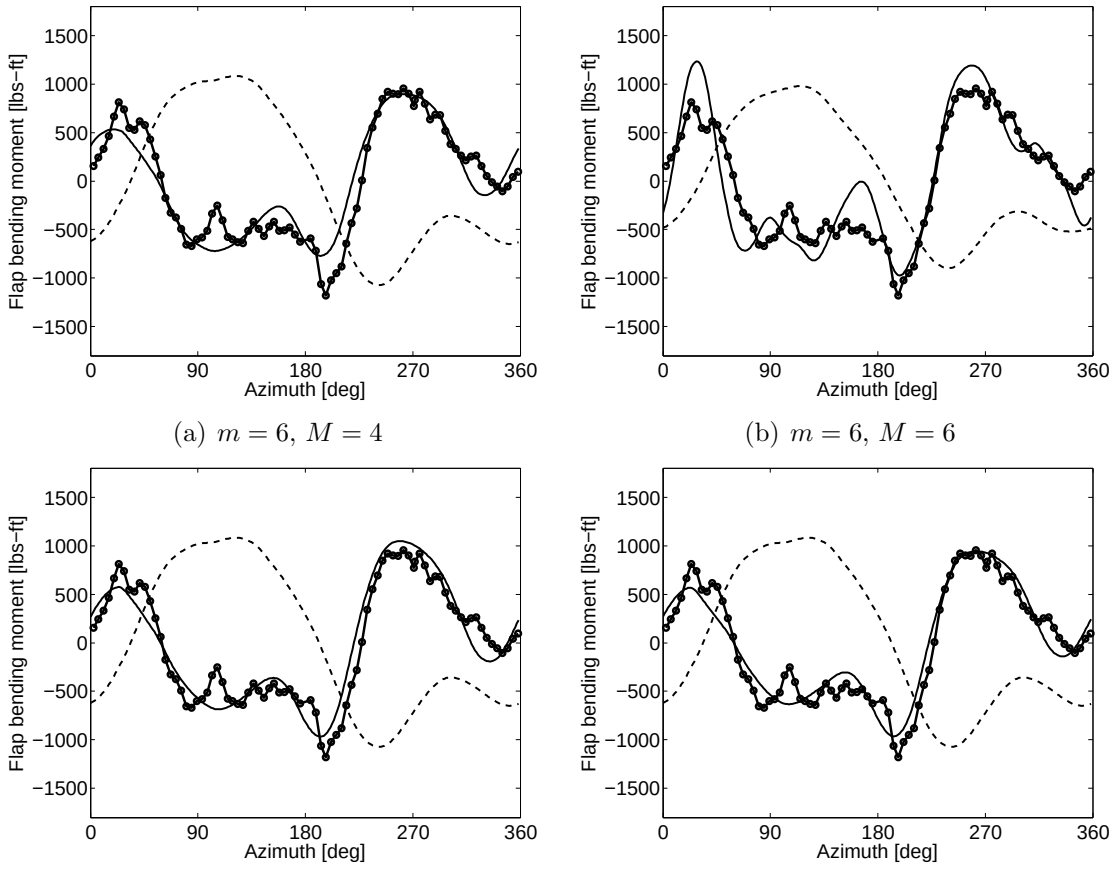

(a) $m = 6$, $M = 4$ (b) $m = 6$, $M = 6$

(c) $m = 8$, $M = 4$ (d) $m = 10$, $M = 4$

Figure 60: Analysis of flap bending moments at 70% span for different choices of the number of modes m and harmonics M. High speed flight condition C8534. Steady loads removed. Measured (o). Initial numerical (--). Final numerical (-).

the torsional moment is measured at only three stations along the blade. The sensor at 50% span is in fact characterized by noisy, zero-mean measurements.

The flap bending moment (Figure 66) is satisfactorily predicted both in peak-to-peak magnitude values and in frequency content (Figures 67 and 68). The dominant vibratory harmonics (3 and 5/rev) of the flap moments are the primary source of the 4/rev vibrations in the fuselage [1], and it is therefore important to be able to accurately predict them. The 3/rev is predicted within 3-5% of the flight test value except at the root. This achievement is very valuable considering the simplicity of the model of the aerodynamic loads, and it is comparable with results from CFD/CSD coupled analyses [33, 36, 34]. The 5/rev harmonic is not accurately predicted, similarly also

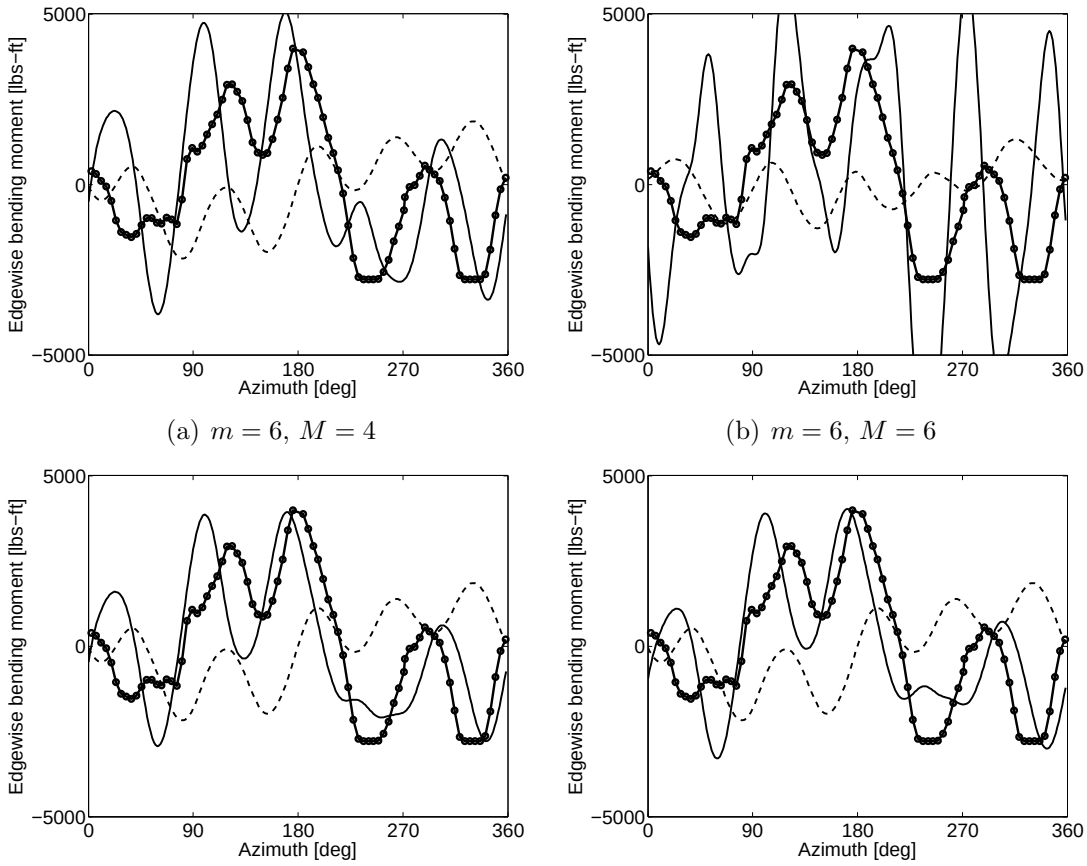

(a) $m = 6$, $M = 4$ (b) $m = 6$, $M = 6$

(c) $m = 8$, $M = 4$ (d) $m = 10$, $M = 4$

Figure 61: Analysis of chord bending moments at 50% span for different choices of the number of modes m and harmonics M. High speed flight condition C8534. Steady loads removed. Measured (o). Initial numerical (--). Final numerical (-).

in this case to CFD/CSD and to measured airloads analyses. This discrepancy is in fact due to limitations of the structural model, and cannot be corrected simply by updating the applied loads.

The chord bending moment (time histories at control points: Figure 69, harmonic content: Figures 70 and 71) are satisfactorily predicted across the blade up to the 4/rev harmonic. The sharp gradients in the lag bending moments near 180-200 deg of azimuth are directly related to the force in the damper. The numerical results capture this abrupt change in the waveform, even if lower accuracy is achieved with respect to the flapping moment distribution. Both magnitude and phase of the 2/rev and 4/rev harmonics are predicted within 8-12% the flight tests, while the discrepancy in

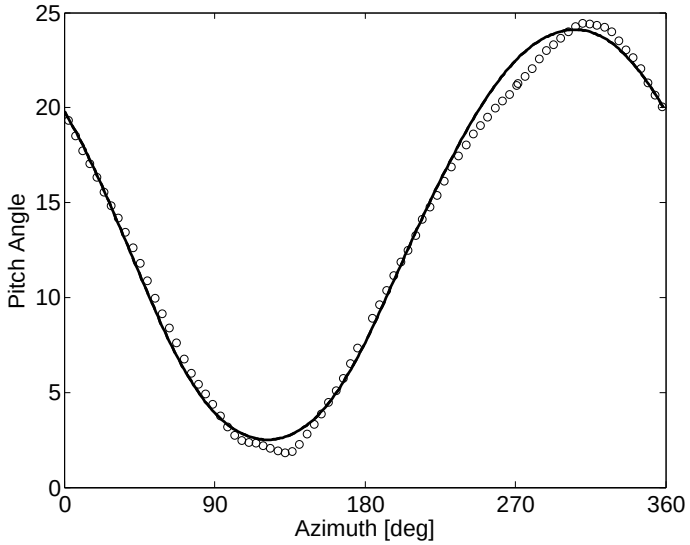

Figure 62: Time history of the pitch angle over one revolution. High speed flight condition C8534. Measured (o). Final numerical (-).

the 3/rev component is larger, but compatible with results in the literature [33, 36, 34]. The discrepancies in the magnitude predictions are probably due to unmodeled dynamic effects, such as the dynamic of the rotor drive train and coupling with the fuselage.

Consider now the abilities of LCA in recostructing the response of the system at points along the span not used as control points. In fact, the measurements of the flapwise bending moment at 50% span have not been considered as reference data in the LCA. The error on the maximum value of the time response over a period is about 8-9%, as shown in Figure 72. The procedure is therefore able to accurately compute the dynamic response across the span of the blade even at locations not included in the LCA as reference.

3.4.5 High thrust flight test data (counter C9017)

Flight counter C9017 is a high-thrust high-altitude level flight condition at moderate speed, and is dominated by dynamic stall events in the retreating side of the rotor. Difficulties in simulating this flight condition are mainly due to the fact that large

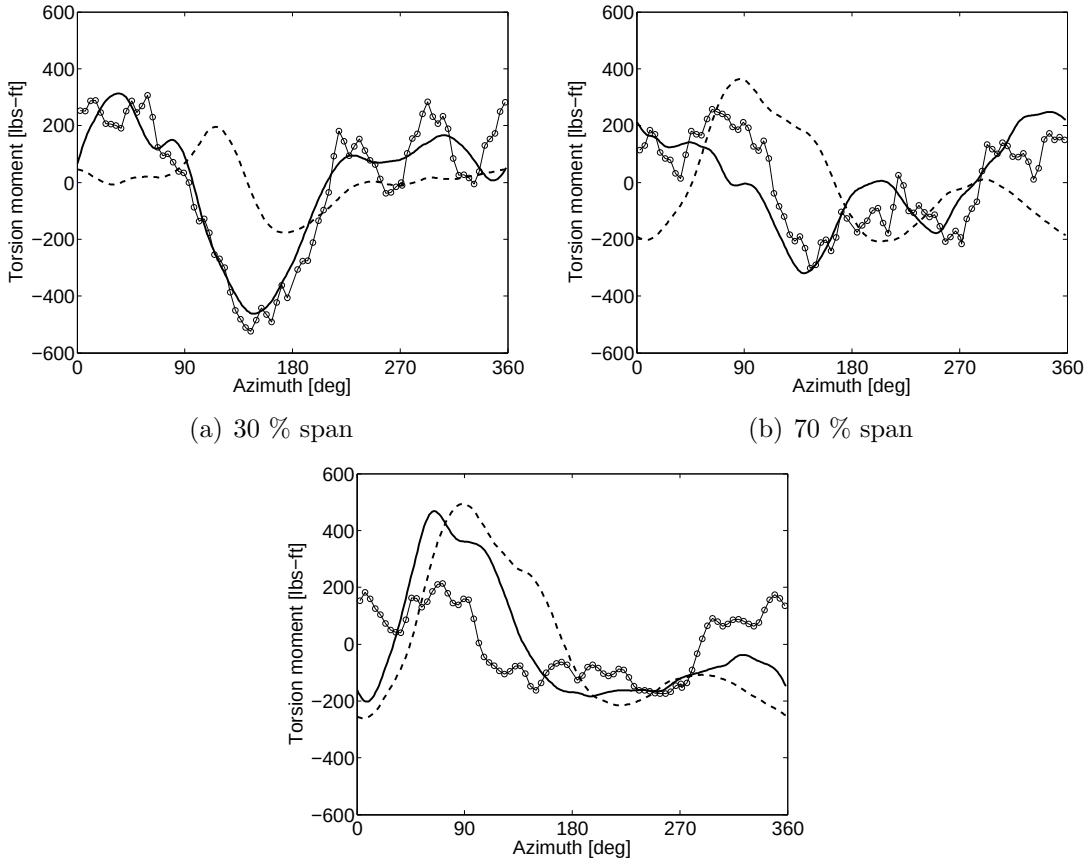

(a) 30 % span

(b) 70 % span

(c) 90 % span

Figure 63: Prediction of the torsional moment at different sensors along the span. High speed flight condition C8534. Steady loads removed. Measured (o), Initial numerical (--), Final numerical (-).

changes in control angles may not produce large changes in rotor loads since the blades may stall. The pitch angle of the blade for flight counter C9017 is represented in Figure 73, and it is predicted within 1-2% accuracy.

The convergence of the LCA for flight condition C9017 is critical because a lower number of undamaged sensors is available. The total number of sensors included in the algorithm as reference data is reduced to 11 (reduction of nearly 30% with respect to C8534), which makes the achievement of accurate numerical predictions more challenging. The sensors considered as control points are divided into five flapping moments located at 10-20-40-60-70% of the span, two edgewise moments located at 10-60% of the span and four torsions, located at 30-50-70-90% of the span.

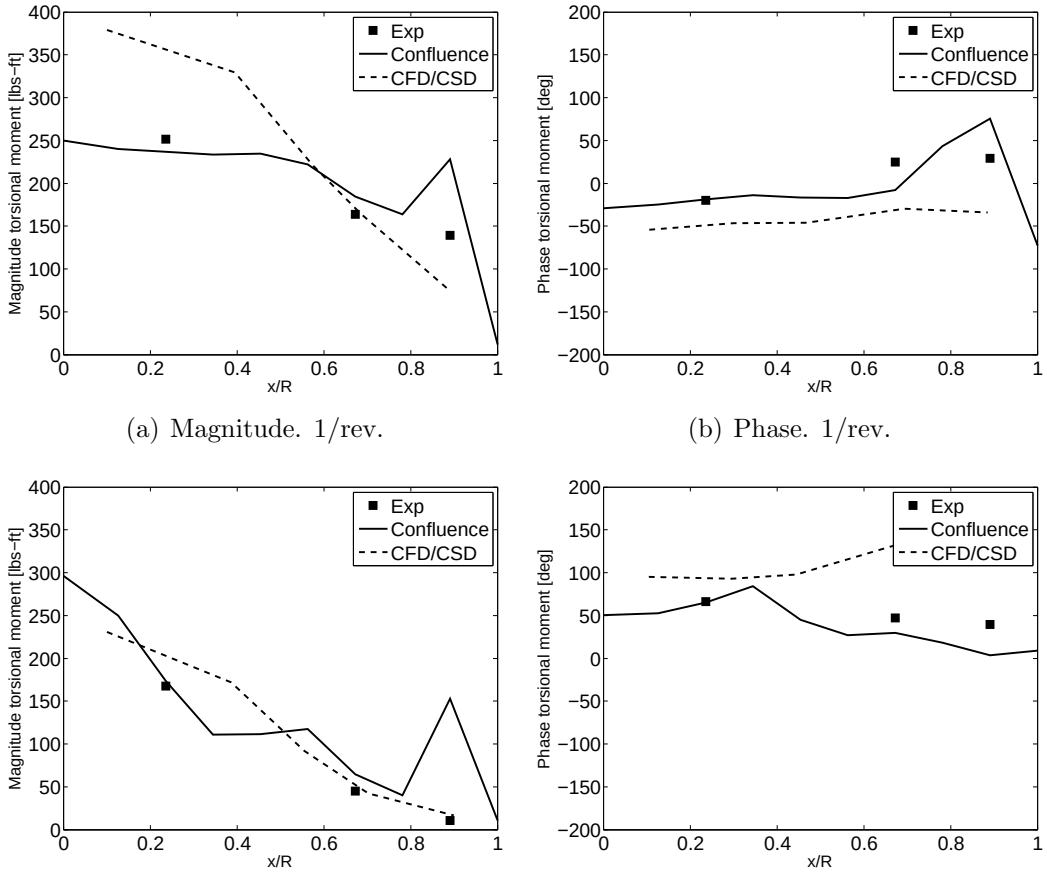

(a) Magnitude. 1/rev.

(b) Phase. 1/rev.

(c) Magnitude. 2/rev.

(d) Phase. 2/rev.

Figure 64: Torsional moment distribution along the span for harmonics 1 and 2. High speed flight condition C8534. Experimental (■). Predicted (-). CFD/CSD (--) from Datta et al. [34]

The reduction of number of sensors requires also the reduction of the modes included in the LCA. This analysis considers eight modes, $m = 8$, and four harmonics, $M = 4$. Figure 74 presents examples for a torsional, a flapwise and edgewise sensor. The overall accuracy of the predictions is also in this case greatly improved with respect to the initial predictions, but inaccuracies of more than 20% are still generally present.

The 4/ and 5/rev harmonics of the torsional moment are the source of torsion oscillations on the retreating blade, which are important for stall analyses, and are represented in Figure 76 in terms of absolute value and phase variation along the span. They are predicted within 20% accuracy, in accordance with CFD/CSD coupled

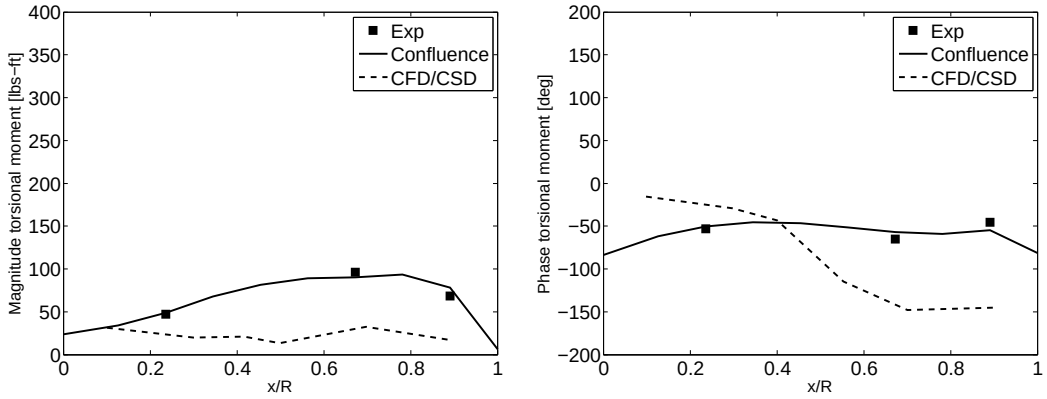

(a) Magnitude. 3/rev.

(b) Phase. 3/rev.

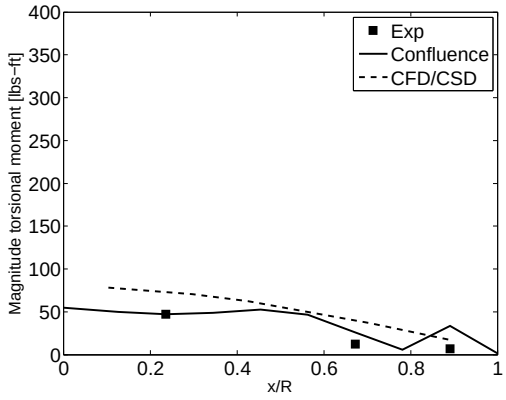

(c) Magnitude. 4/rev.

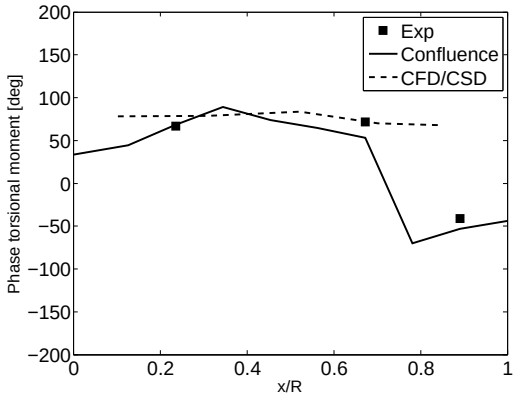

(d) Phase. 4/rev.

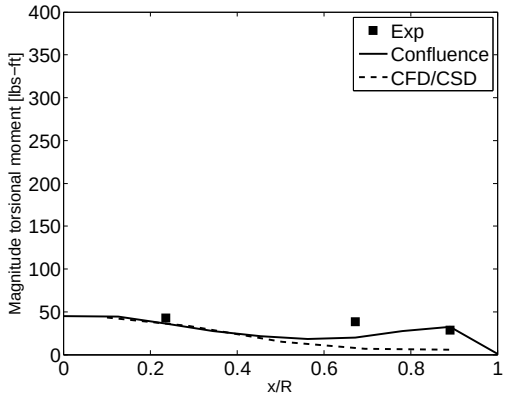

(e) Magnitude. 5/rev.

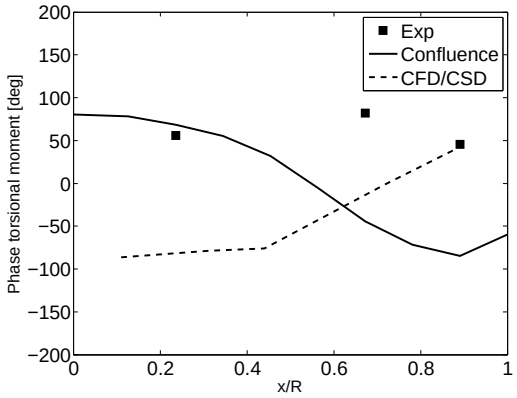

(f) Phase. 5/rev.

Figure 65: Torsional moment distribution along the span for harmonics 3 to 5. High speed flight condition C8534. Experimental (■). Predicted (-). CFD/CSD (--) from Datta et al. [34]

analyses [34]. It is expected that the availability of few more experimental stations (3-4) would result in improvements in the prediction that are comparable to the C8534

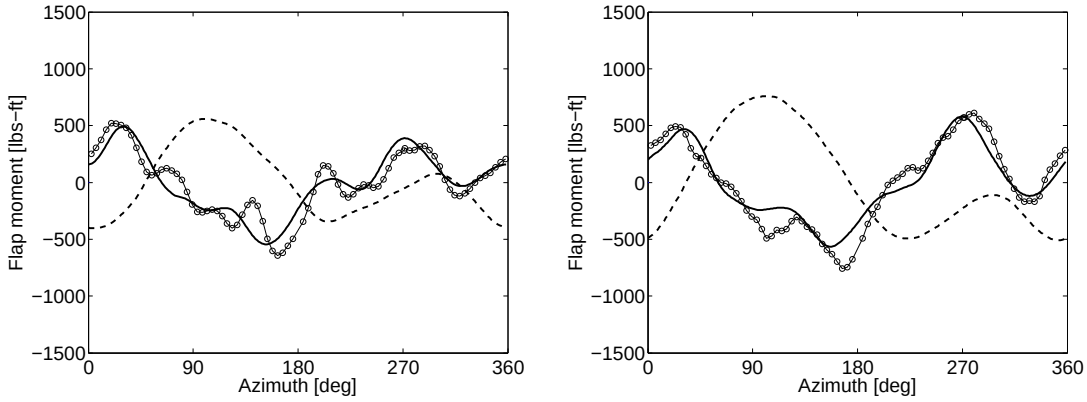

(a) 20 % span

(b) 30 % span

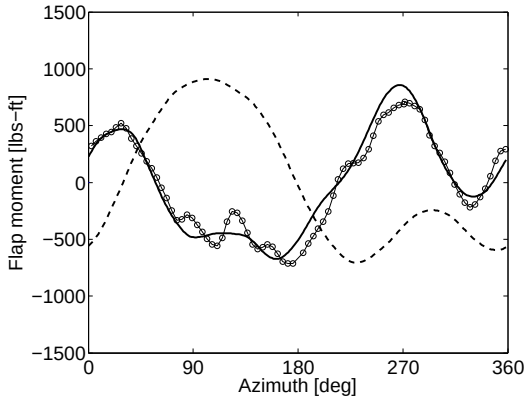

(c) 40 % span

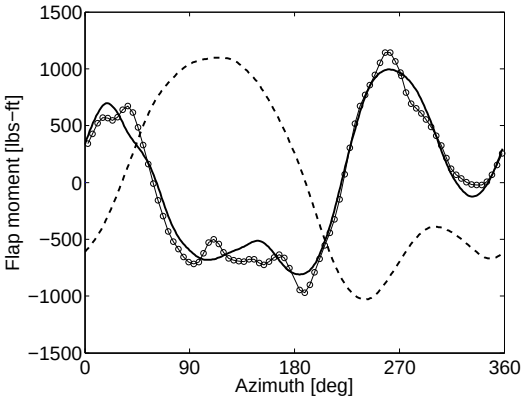

(d) 60 % span

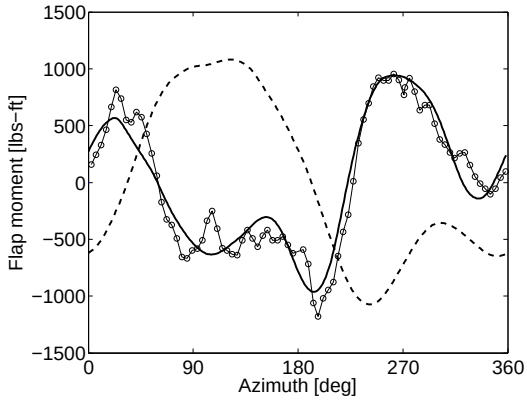

(e) 70 % span

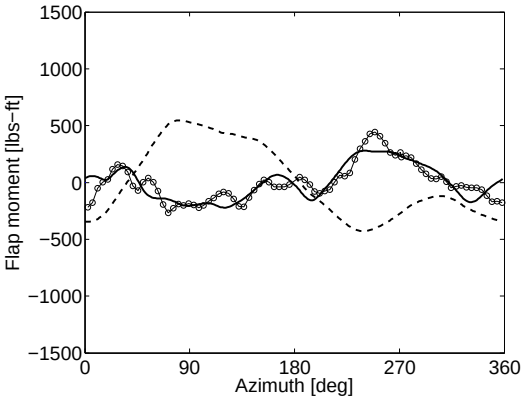

(f) 90 % span

Figure 66: Prediction of the flap bending moment at different sensors along the span. High speed flight condition C8534. Steady loads removed. Measured (o). Initial numerical (--). Final numerical (-).

flight condition.

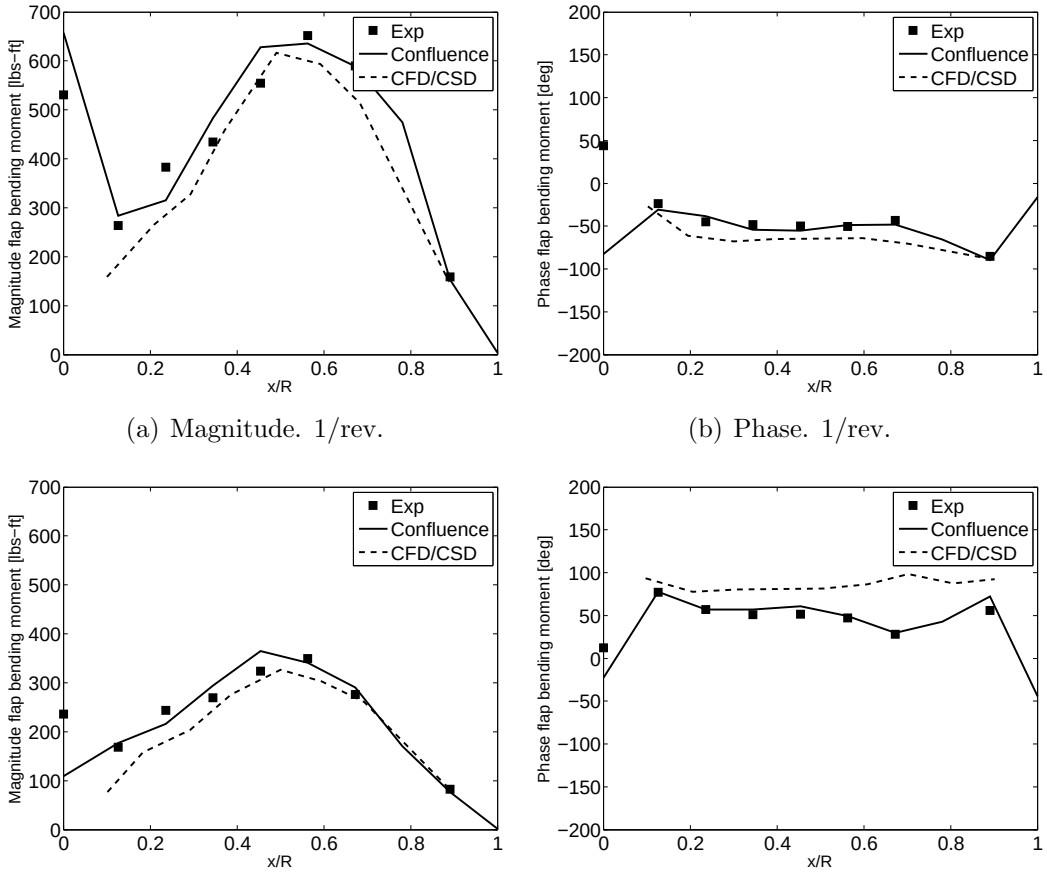

(a) Magnitude. 1/rev.

(b) Phase. 1/rev.

(c) Magnitude. 2/rev.

(d) Phase. 2/rev.

Figure 67: Flap bending moment distribution along the span for harmonics 1 and 2. High speed flight condition C8534. Experimental (■). Predicted (-). CFD/CSD (--) from Datta et al. [34]

3.4.6 Low speed flight test data (counter C8513)

The low speed case C8513 is dominated by blade-vortex interactions (BVI), which are generally difficult to capture. The pitch angle is also in this case accurately predicted as can be observed in Figure 77. As in flight condition C8534, the measurements of 15 sensors are used as reference data: six flapping moments located at 20-30-40-60-70-90% of the span, six edgewise moments located at 20-30-40-60-70-90% of the span and three torsions, located at 30-70-90% of the span. This analysis considers ten modes, $m = 10$, and four harmonics, $M = 4$. As in flight counter C8534, the torsional and flap and lag bending moments are well predicted, Figures 78, 79, 80

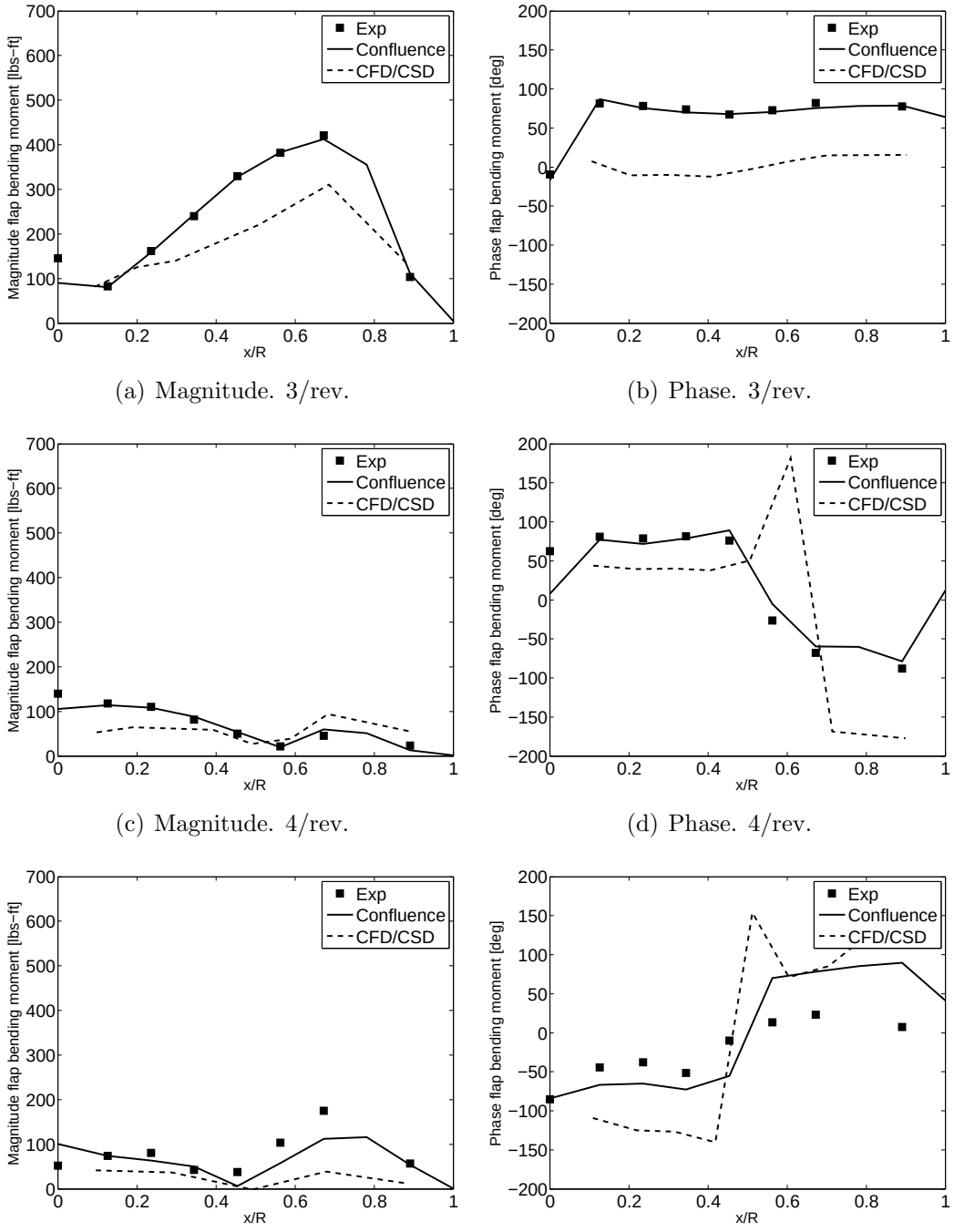

(a) Magnitude. 3/rev.

(b) Phase. 3/rev.

(c) Magnitude. 4/rev.

(d) Phase. 4/rev.

(e) Magnitude. 5/rev.

(f) Phase. 5/rev.

Figure 68: Flap bending moment distribution along the span for harmonics 3 to 5. High speed flight condition C8534. Experimental (■). Predicted (-). CFD/CSD (--) from Datta et al. [34]

and 83 respectively. More accurate results are achieved in the representation of the flap bending moment, with errors within 10% except at outboard stations (70% and

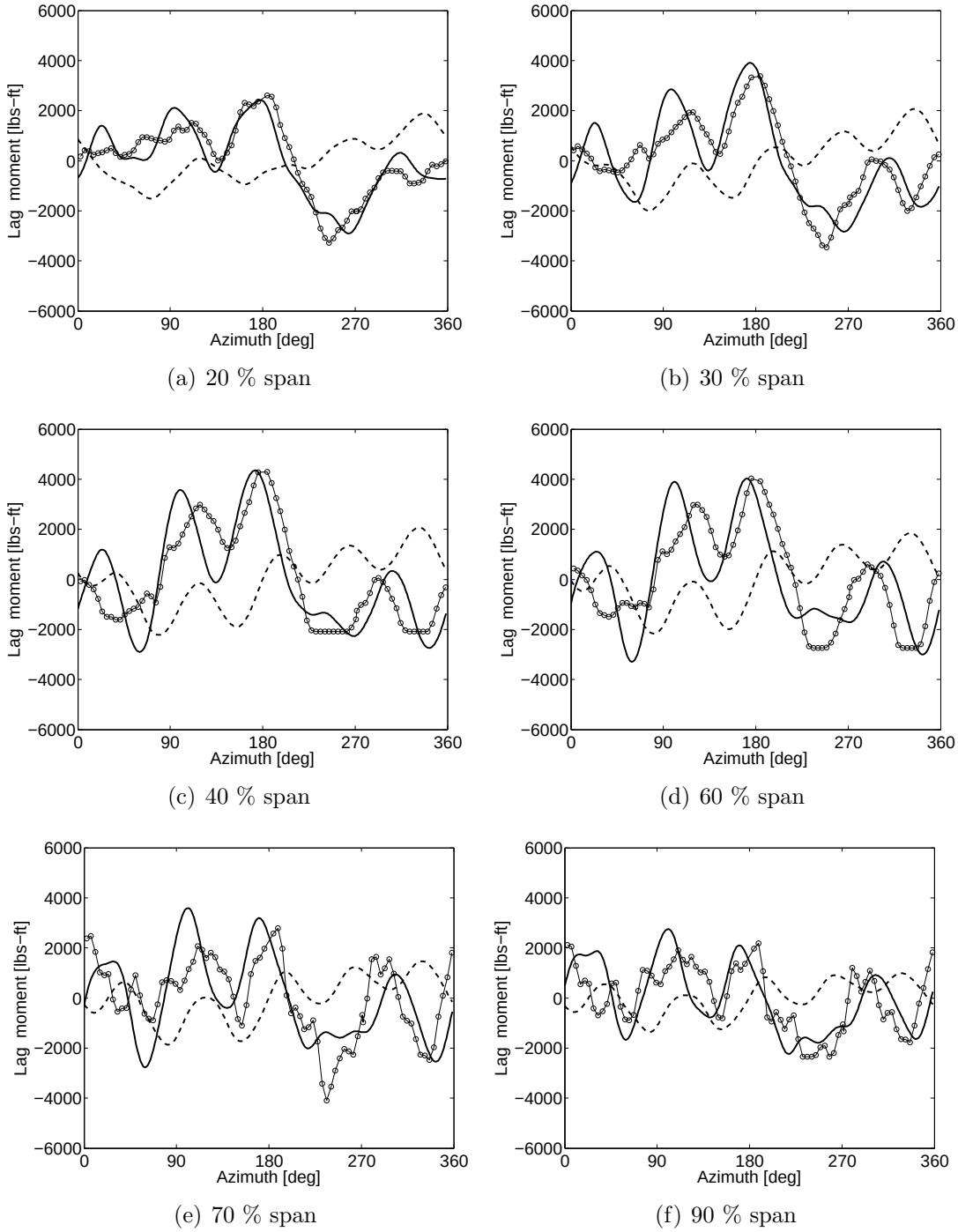

(a) 20 % span (b) 30 % span

(c) 40 % span (d) 60 % span

(e) 70 % span (f) 90 % span

Figure 69: Prediction of the lag bending moment at different sensors along the span. High speed flight condition C8534. Steady loads removed. Measured (o). Initial numerical (--). Final numerical (-).

90% of the span).

The torsion loads are shown in Figure 78. The trend of the waveform is accurately

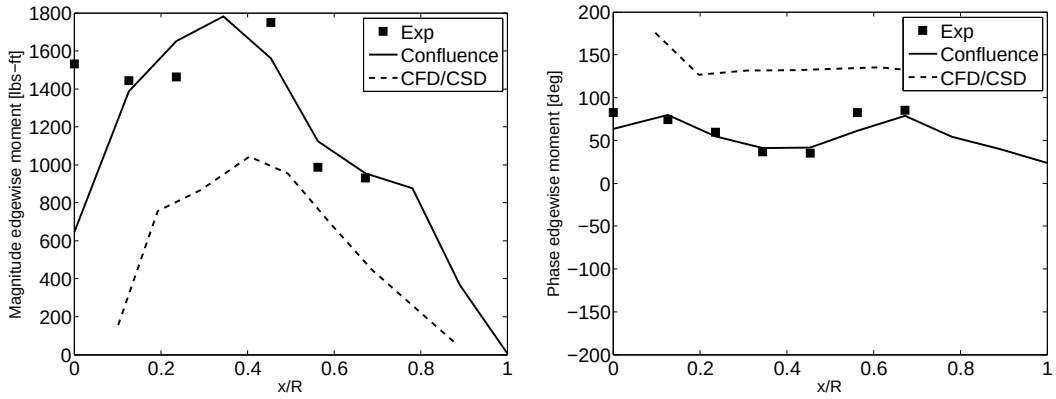

(a) Magnitude. 1/rev.

(b) Phase. 1/rev.

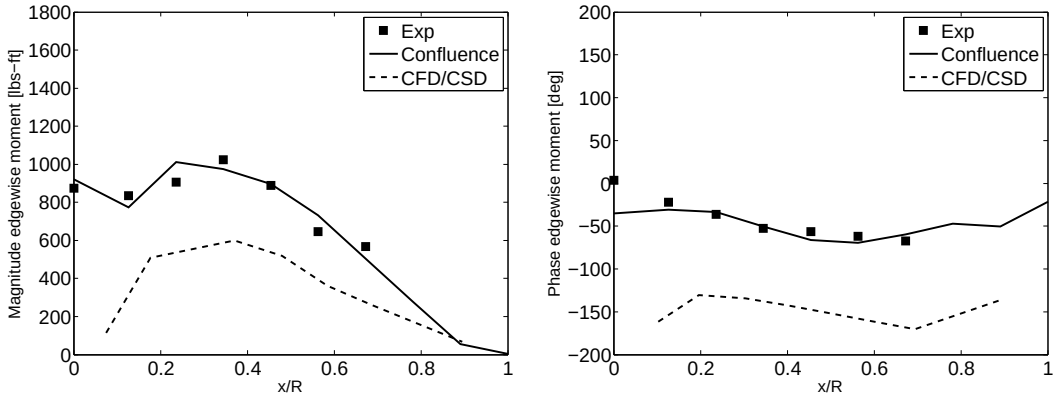

(c) Magnitude. 2/rev.

(d) Phase. 2/rev.

Figure 70: Chord bending moment distribution along the span for harmonics 1 and 2. High speed flight condition C8534. Experimental (■). Predicted (-). CFD/CSD (- -) from Datta et al. [34]

predicted at 30% and 70% span, while the numerical analysis does not capture the sharp gradients that characterize the 90% station because of unmodeled dynamics of the swashplates and of the control chains. Investigation on the improvement of the predictions for this flight condition is still an open problem for the rotorcraft community [34].

The time histories of the flap bending moments are accurately predicted across the span (Figures 79 and 80). The flap moment prediction at 50% is also in this case an indicator of the ability of the algorithm to reconstruct the response at non-reference locations, with an accuracy of about 10% over a period. The effect of the

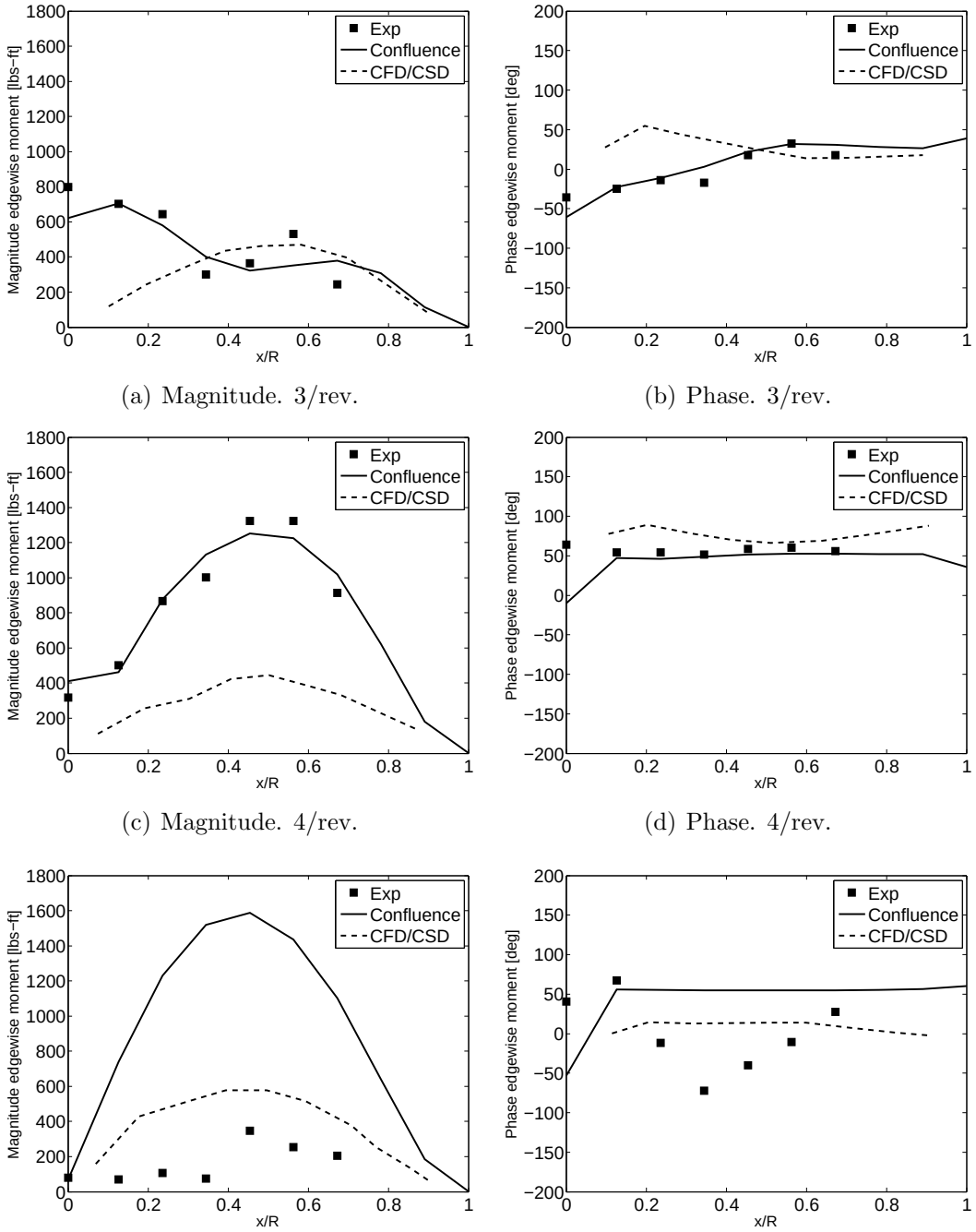

(a) Magnitude. 3/rev.

(b) Phase. 3/rev.

(c) Magnitude. 4/rev.

(d) Phase. 4/rev.

(e) Magnitude. 5/rev.

(f) Phase. 5/rev.

Figure 71: Chord bending moment distribution along the span for harmonics 3 to 5. High speed flight condition C8534. Experimental (■). Predicted (-). CFD/CSD (--) from Datta et al. [34]

damper force is important particularly for the inboard stations and the retreating side. Discrepancies within 5% characterize the 2/rev, 3/rev and 4/rev harmonics,

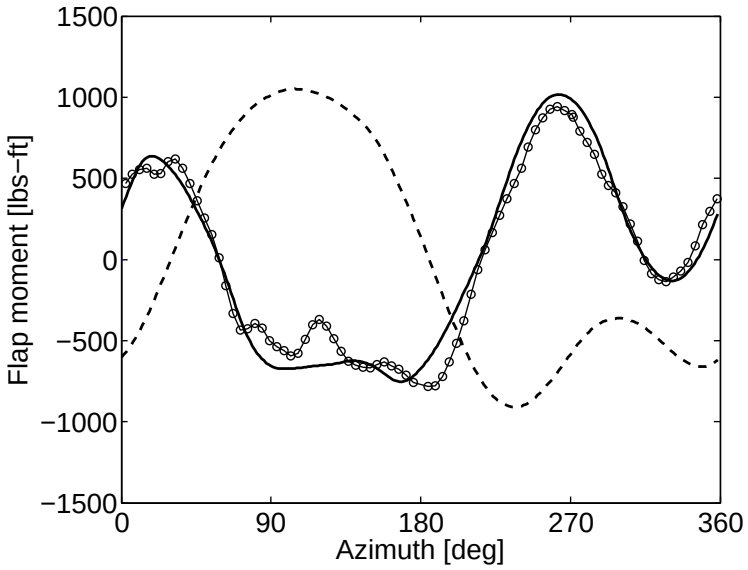

Figure 72: Flap bending moment at 50% span. High speed flight condition C8534. Steady loads removed. Measured (o). Initial numerical (--). Final numerical (-).

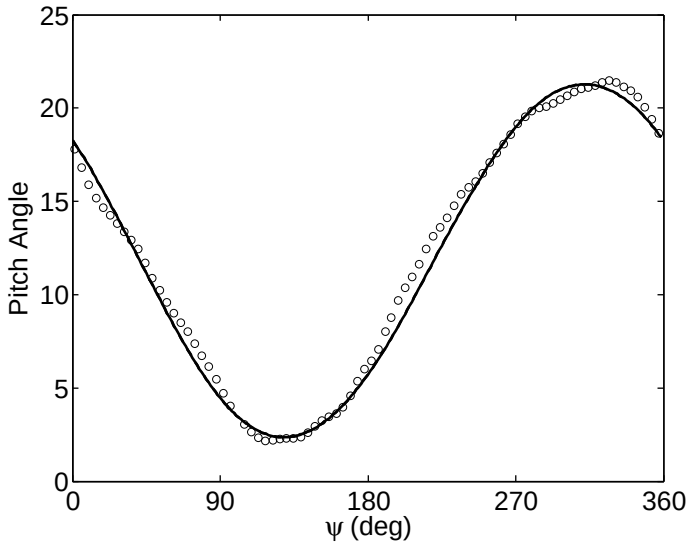

Figure 73: Pitch angle over a revolution. High-thrust flight condition 9017. Measured (o). Final numerical (-).

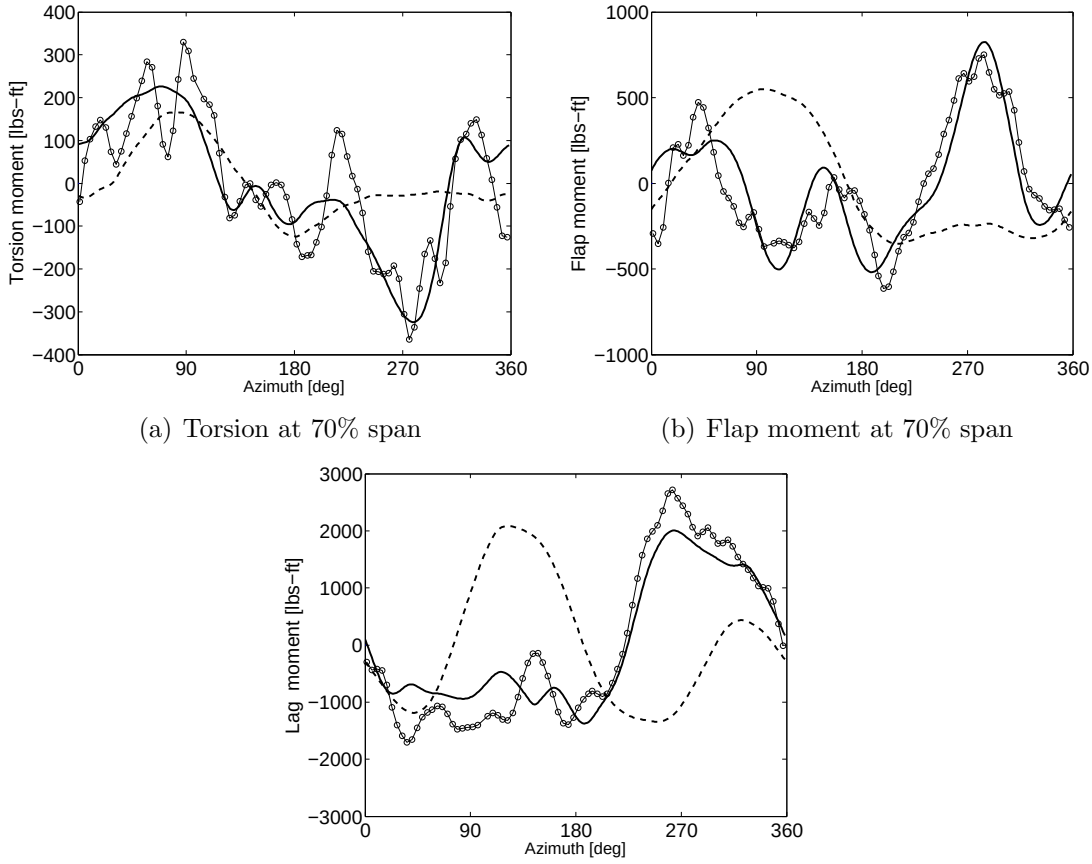

(a) Torsion at 70% span

(b) Flap moment at 70% span

(c) Edge moment at 10% span

Figure 74: Internal moments. High-thrust flight condition 9017. Steady loads removed. Measured (o). Initial numerical (--). Final numerical (-).

Figures 81 and 82. These figures show that, as in case C8534, the application of the LCA results in numerical predictions characterized by an accuracy compatible with CFD/CSD analysis [34], even if much more simple aerodynamic models are employed for this analysis.

The time histories of the lag moment over one revolution at different control points are illustrated in Figure 83, and show the significant improvement with respect to the initial representation of the system. The lag bending moment is predicted with an exceptional accuracy, both in magnitude and phase values, Figures 84 and 85. Harmonics 2/, 3/ and 4/rev are characterized by discrepancies within 5% with respect to flight tests. The error increases up to 20-25% for the 5/rev harmonic and is due

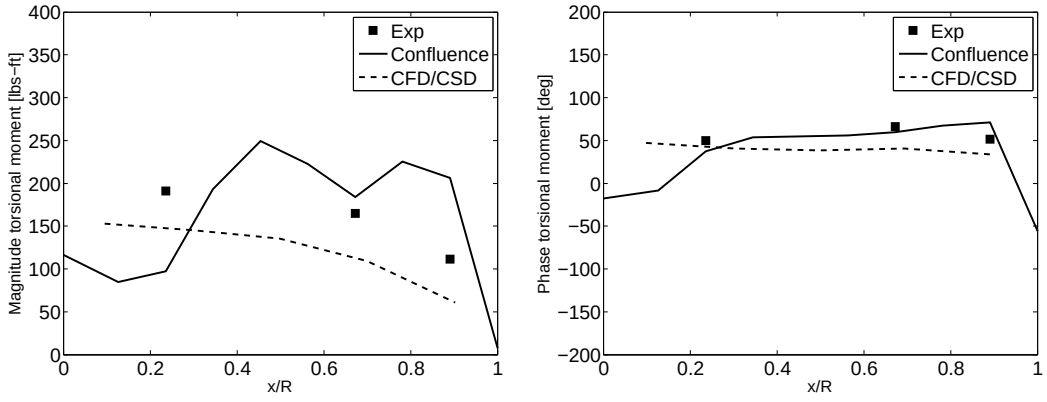

(a) Magnitude. 1/rev.

(b) Phase. 1/rev.

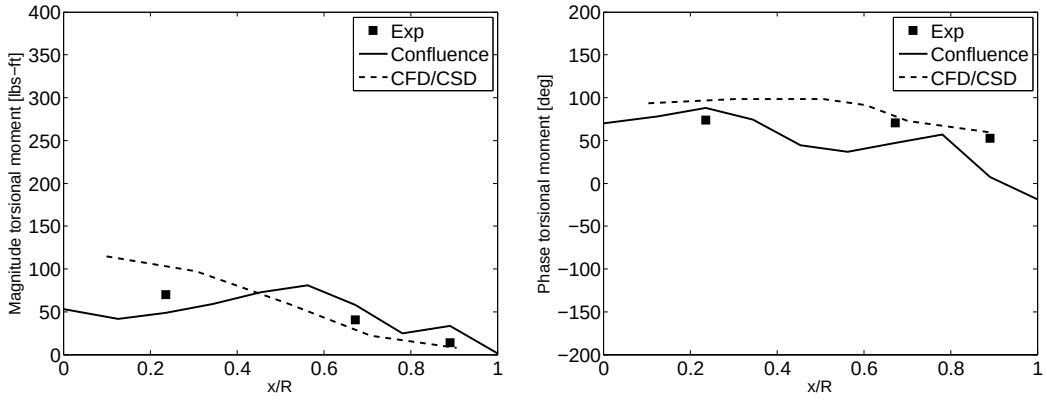

(c) Magnitude. 2/rev.

(d) Phase. 2/rev.

Figure 75: Torsional moment distribution along the span for harmonics 1 and 2. High thrust flight condition C9017. Experimental (■). Predicted (-). CFD/CSD (- -) from Datta et al. [34].

to unmodeled dynamics of the main rotor. These results are very satisfactory and represent an improvement to current studies that employ simplified aerodynamic theories [33]. The achieved errors can be considered of the same order of CFD/CSD analyses [34].

3.5 Comments on the computational cost required by LCA

The computational cost required by the algorihm to converge to an accurate solution is limited with respect to CFD/CSD analyses [69]. The analyses described in the previous section have been performed on a Intel Duo Quad machine, characterized by 8 Gb RAM, four core, 2.83 GHz of processor speed. The computational time

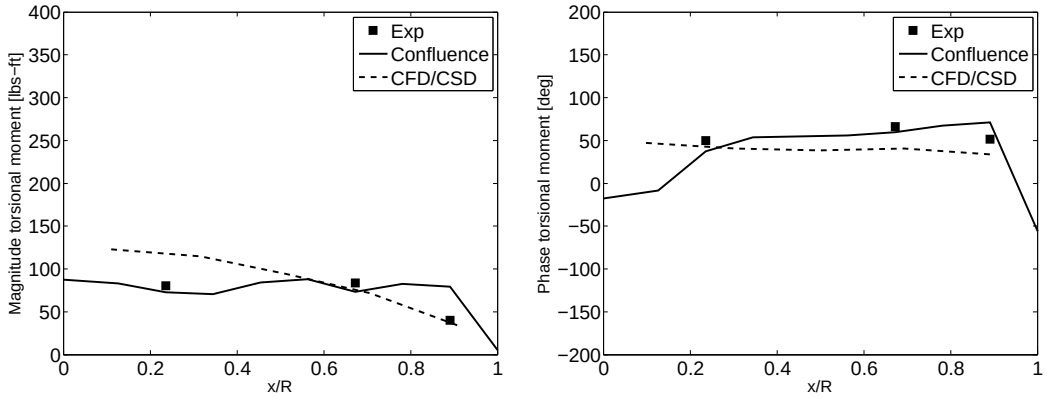

(a) Magnitude. 3/rev.

(b) Phase. 3/rev.

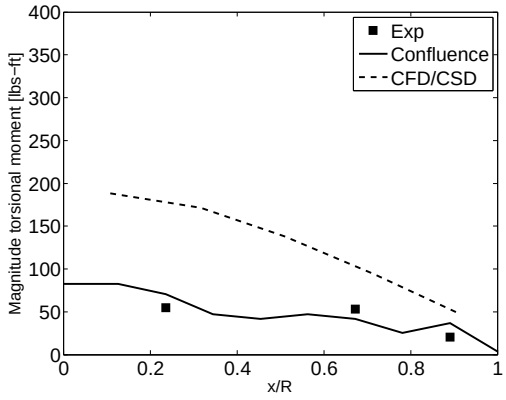

(c) Magnitude. 4/rev.

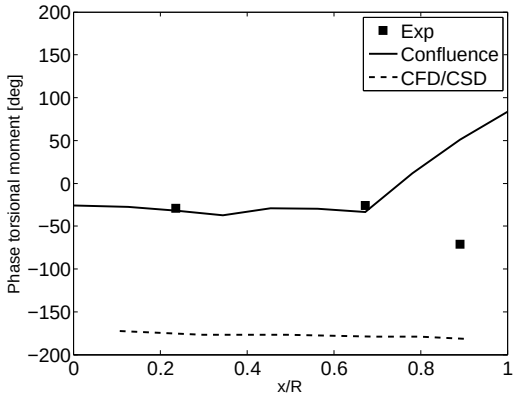

(d) Phase. 4/rev.

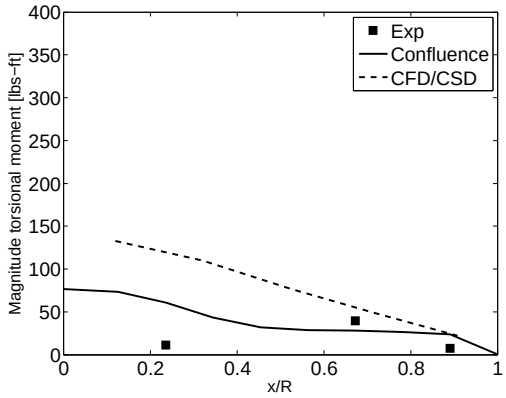

(e) Magnitude. 5/rev.

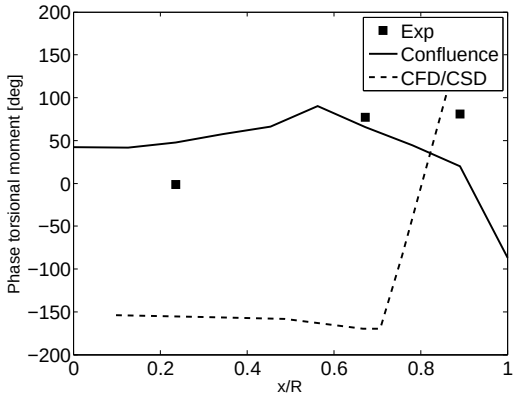

(f) Phase. 5/rev.

Figure 76: Torsional moment distribution along the span for harmonics 3 to 5. High thrust flight condition C9017. Experimental (■). Predicted (-). CFD/CSD (--) from Datta et al. [34].

required by the analyses have been listed in Table 9. In average, the analyses run in about 0.4 hours (1500 sec), which represents a remarkable saving in time with respect

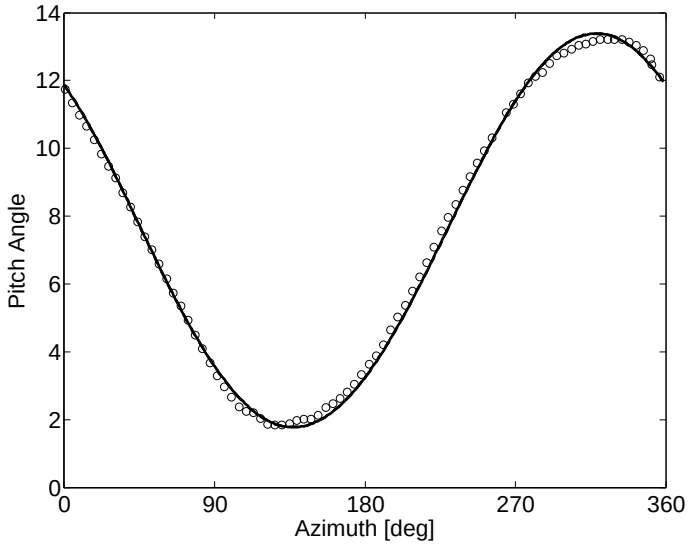

Figure 77: Time history of the pitch angle over one revolution. Low speed flight condition C8513. Measured (o). Final numerical (-).

Table 9: Computational Costs

Analysis	Parameters	CPU time [sec]
C-8534	m=6, M = 4, N = 15	1497.8
C-8534	m=8, M = 4, N = 15	1444.5
C-8534	m=10, M = 4, N = 15	1518.2
C-9017	m=8, M = 4, N = 11	1439.9
C-8513	m=10, M = 4, N = 15	1507.2

to more complex analyses tools. CFD/CSD simulations require in general thousand of times larger computational times on more powerful machines [69]. These CPU time are instead comparable to comprehensive analyses [76] that result in much lower accuracy in the representation of the response.

3.6 Conclusions

This chapter presented the applications of LCA to analyze experimental systems, such as a beam in bending (one-dimensional example), a plate in bending (two-dimensional case) and the behavior of a rotorcraft in multiple flight conditions [27]. All the analyses show that accurate representations of the response is possible, even when

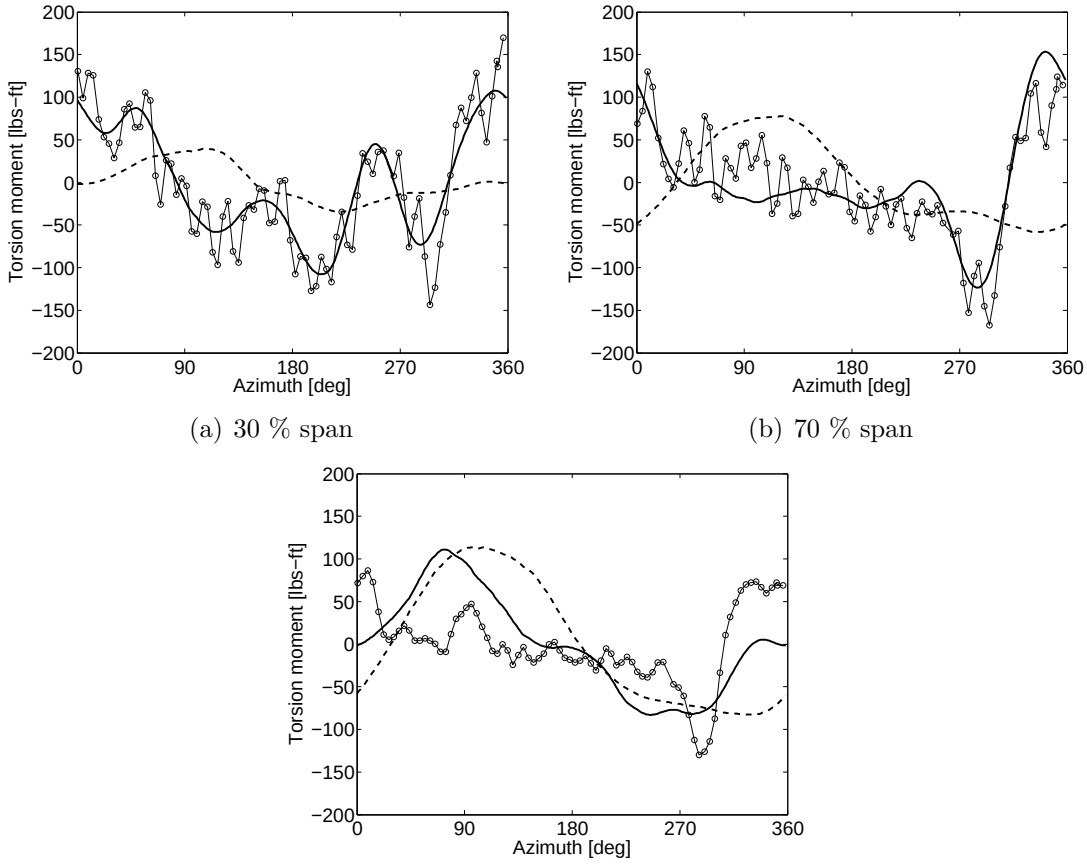

(a) 30 % span

(b) 70 % span

(c) 90 % span

Figure 78: Prediction of the torsional moment at different sensors along the span. Low speed flight condition C8513. Steady loads removed. Measured (o),. Initial numerical (--). Final numerical (-).

simplified numerical models are used, by combining the experimental measurements and the numerical analysis through the LCA.

The next chapter describes how an analogous algorithm can be formulated to correct for changes in physical properties (mass and stiffness) of the system, called the Property Confluence Algorithm. The characteristics of PCA are then evaluated through a numerical example of a beam in bending.

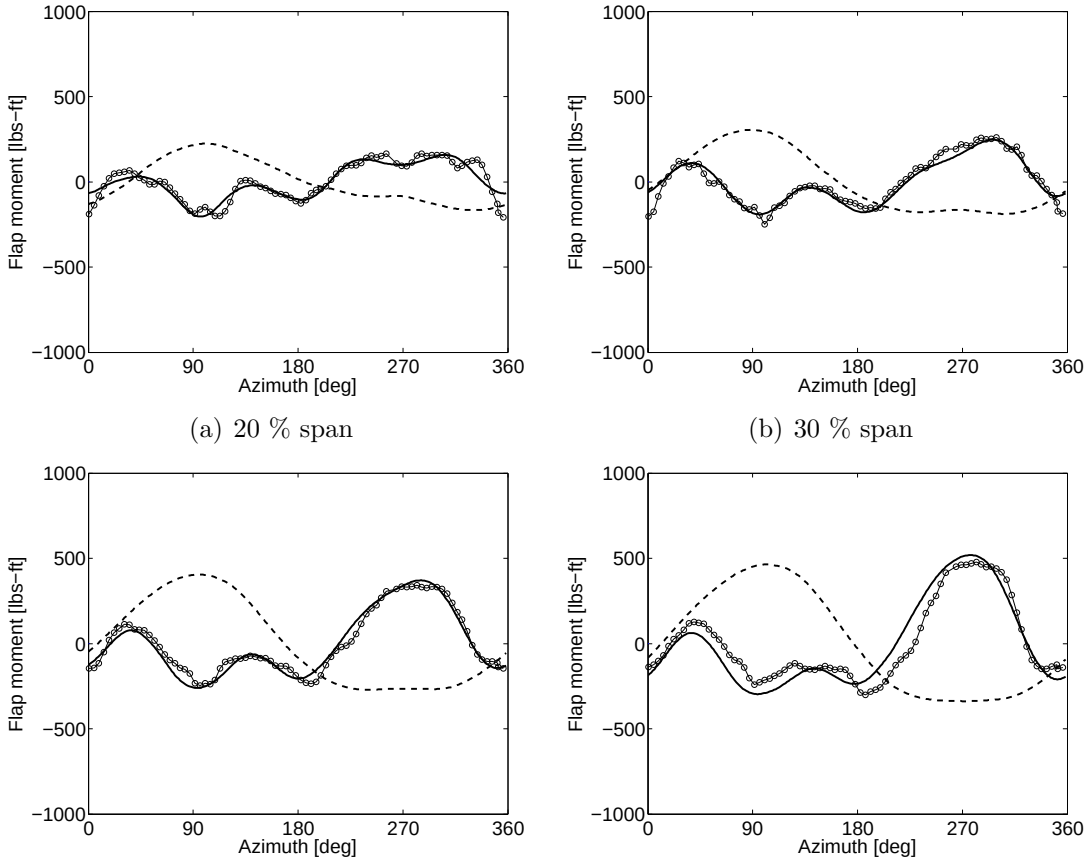

(a) 20 % span

(b) 30 % span

(c) 40 % span

(d) 50 % span

Figure 79: Prediction of the flap bending moment at different sensors along the span close to the root. Low speed flight condition C8513. Steady loads removed. Measured (o). Initial numerical (--). Final numerical (-).

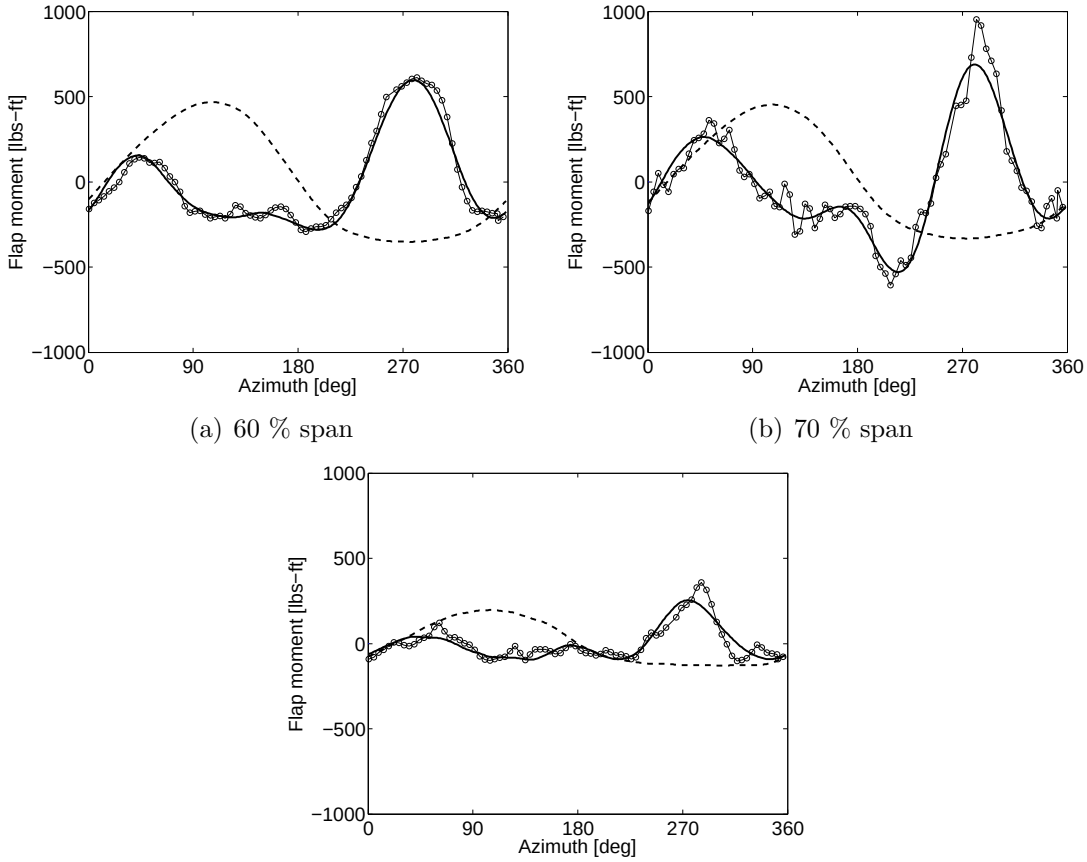

(a) 60 % span

(b) 70 % span

(c) 90 % span

Figure 80: Prediction of the flap bending moment at different sensors along the span close to the tip. Low speed flight condition C8513. Steady loads removed. Measured (o). Initial numerical (--). Final numerical (-).

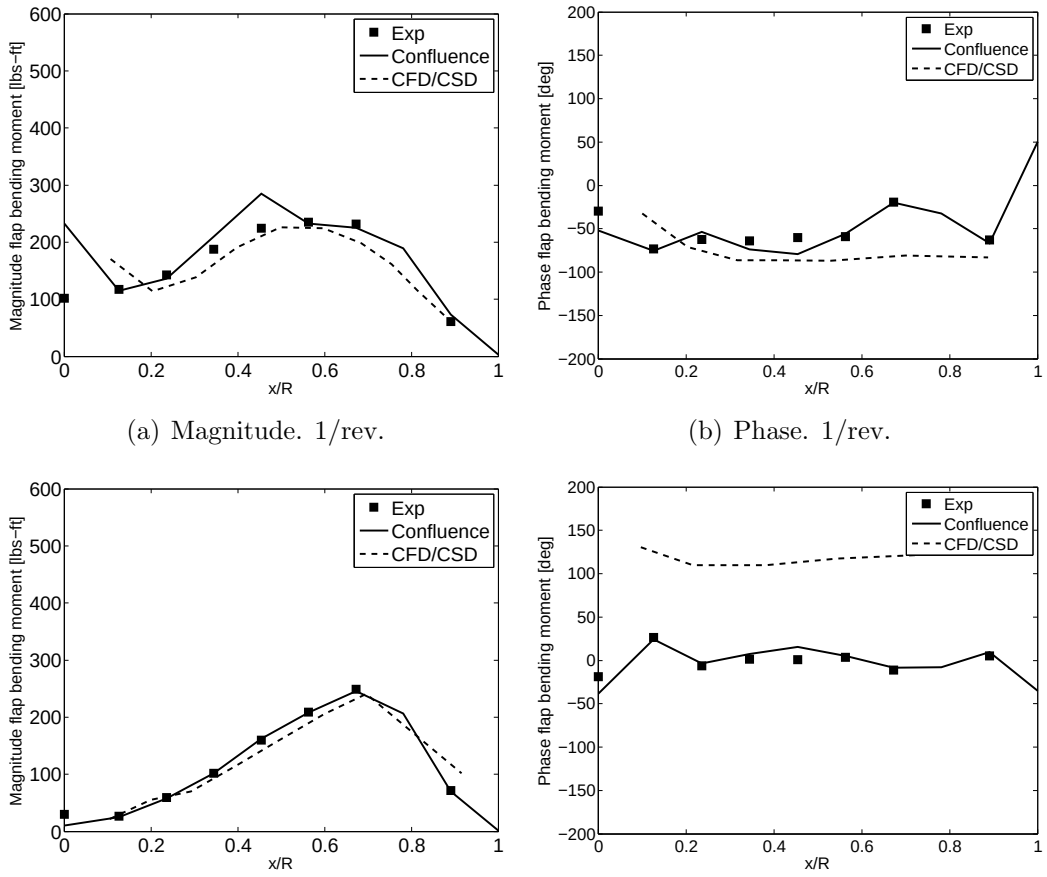

(a) Magnitude. 1/rev.

(b) Phase. 1/rev.

(c) Magnitude. 2/rev.

(d) Phase. 2/rev.

Figure 81: Flap bending moment distribution along the span for harmonics 1 and 2. Low speed flight condition C8513. Experimental (■). Predicted (-). CFD/CSD (--) from Datta et al. [34].

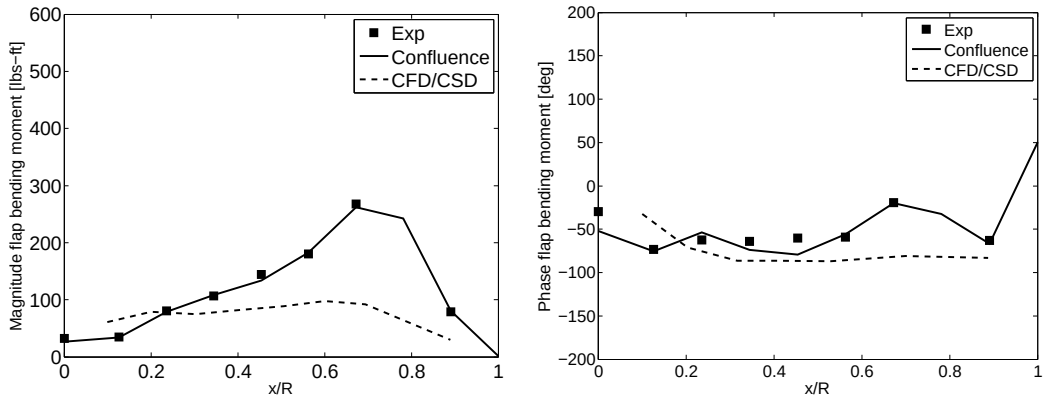

(a) Magnitude. 3/rev.

(b) Phase. 3/rev.

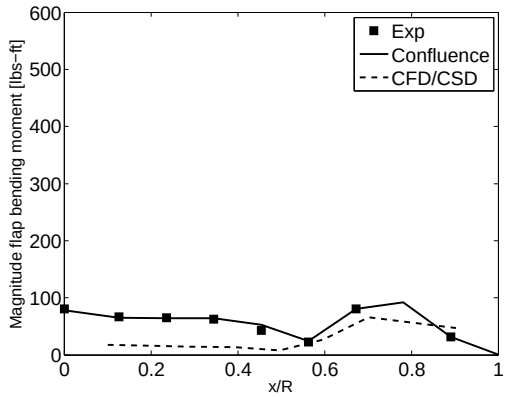

(c) Magnitude. 4/rev.

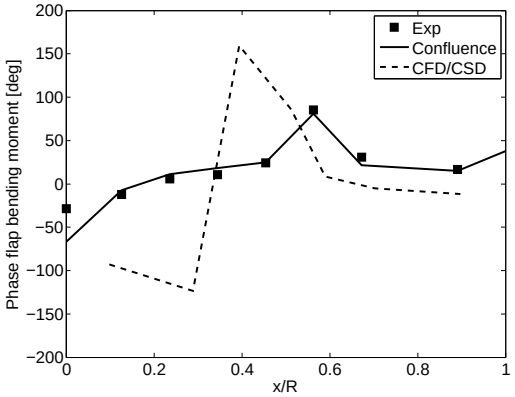

(d) Phase. 4/rev.

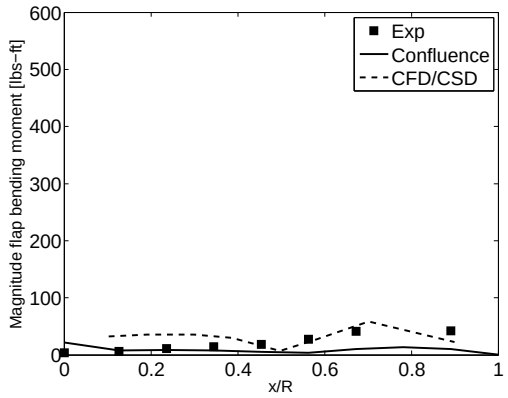

(e) Magnitude. 5/rev.

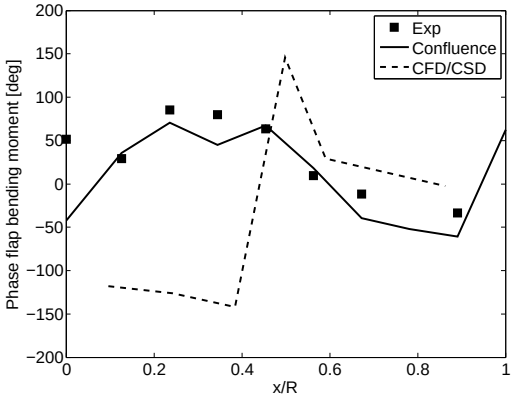

(f) Phase. 5/rev.

Figure 82: Flap bending moment distribution along the span for harmonics 3 to 5. Low speed flight condition C8513. Experimental (■). Predicted (-). CFD/CSD (--) from Datta et al. [34].

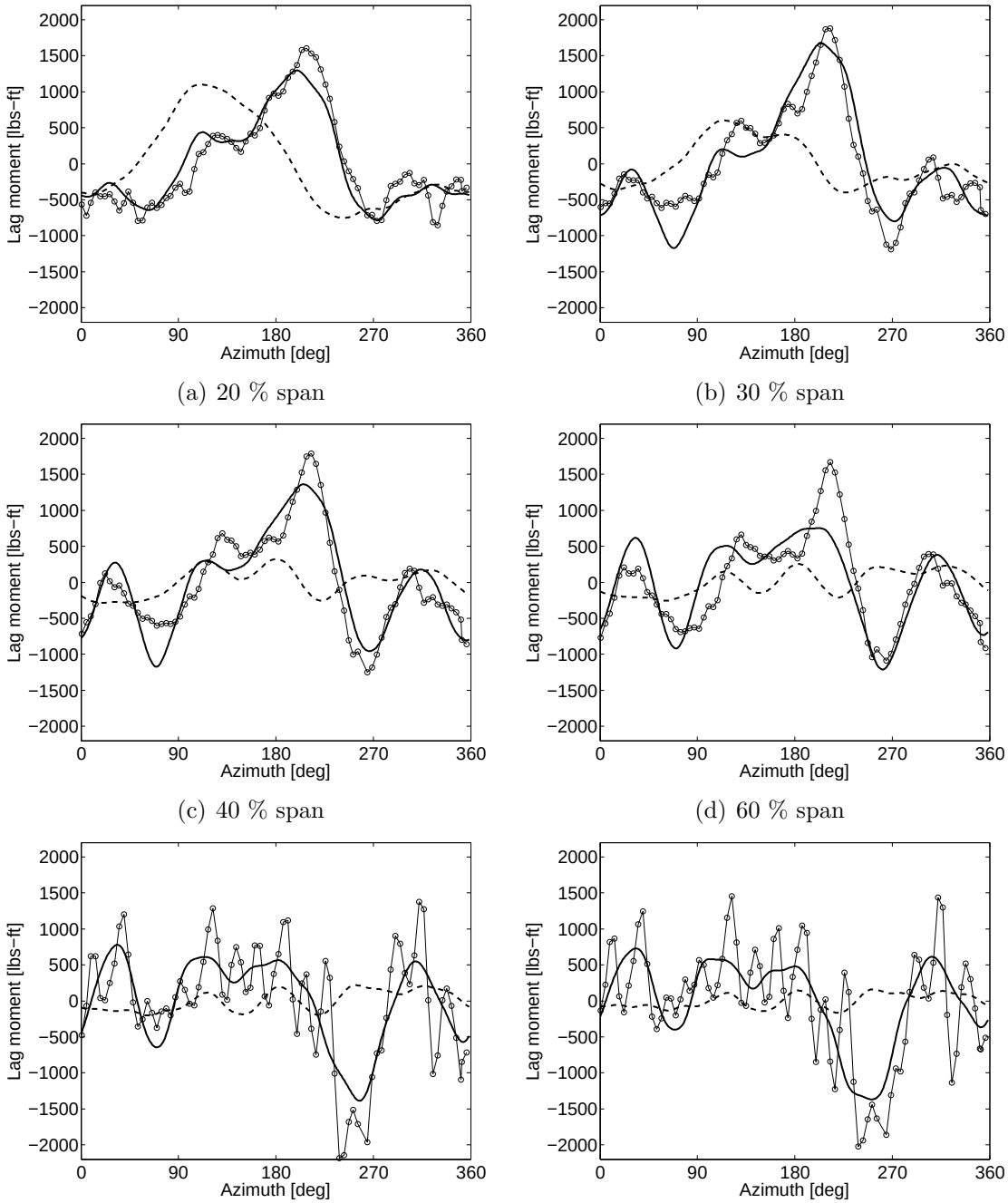

(a) 20 % span

(b) 30 % span

(c) 40 % span

(d) 60 % span

(e) 70 % span

(f) 90 % span

Figure 83: Prediction of the lag bending moment at different sensors along the span. Low speed flight condition C8513. Steady loads removed. Measured (o). Initial numerical (--). Final numerical (-).

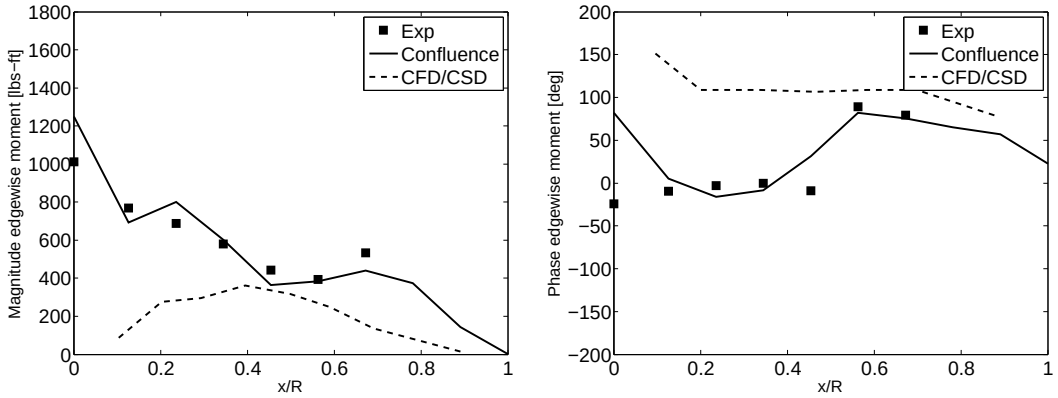

(a) Magnitude. 1/rev.

(b) Phase. 1/rev.

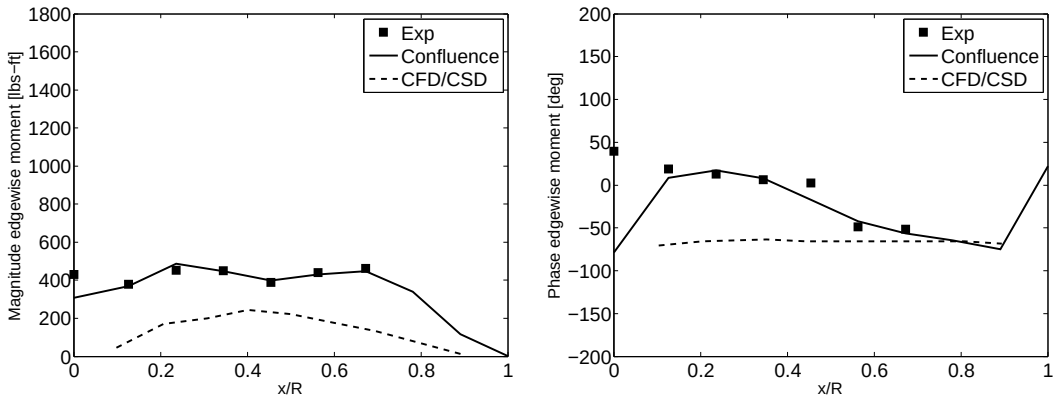

(c) Magnitude. 2/rev.

(d) Phase. 2/rev.

Figure 84: Chord bending moment distribution along the span for harmonics 1 and 2. Low speed flight condition C8513. Experimental (■). Predicted (-). CFD/CSD (- -) from Datta et al. [34].

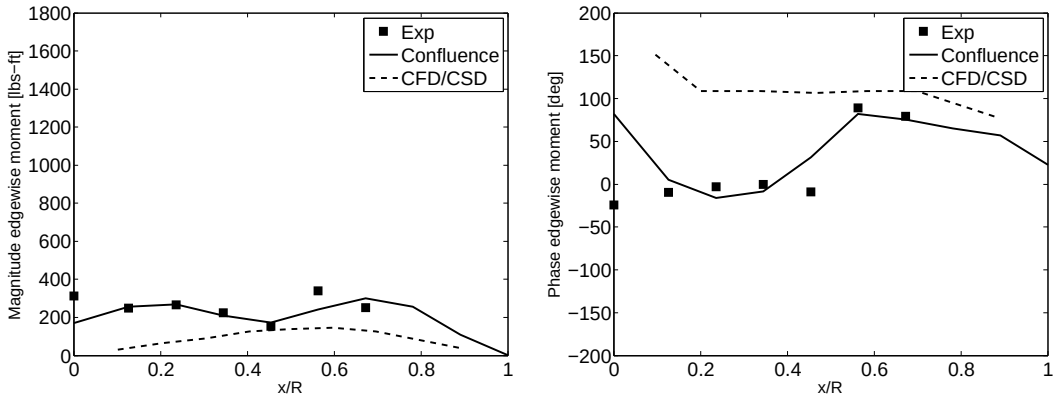

(a) Magnitude. 3/rev.

(b) Phase. 3/rev.

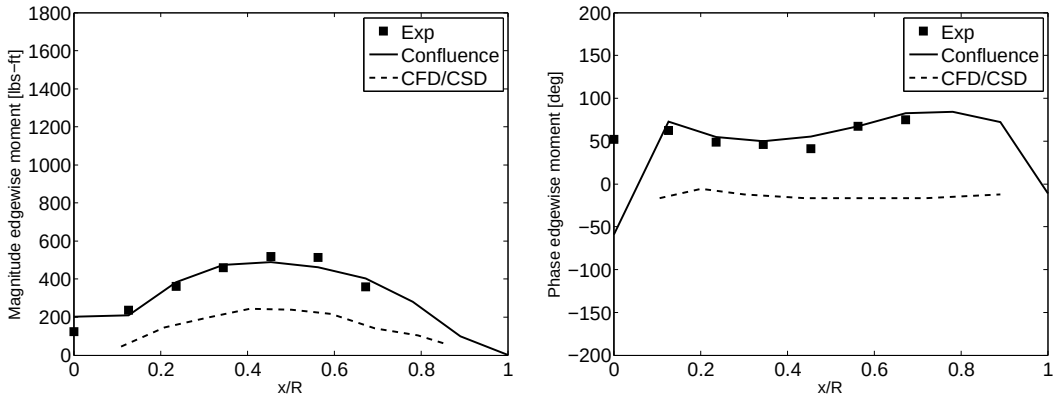

(c) Magnitude. 4/rev.

(d) Phase. 4/rev.

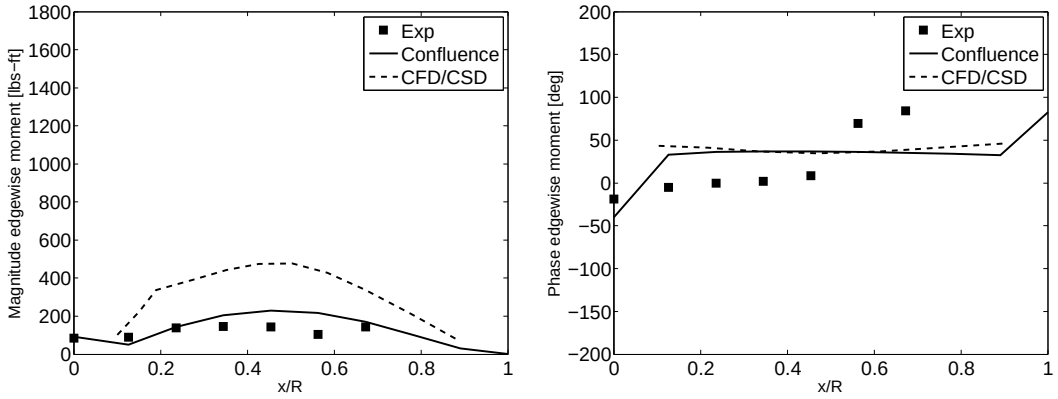

(e) Magnitude. 5/rev.

(f) Phase. 5/rev.

Figure 85: Chord bending moment distribution along the span for harmonics 3 to 5. Low speed flight condition C8513. Experimental (■). Predicted (-). CFD/CSD (--) from Datta et al. [34].

CHAPTER IV

THE PROPERTY CONFLUENCE ALGORITHM

4.1 Overview

The goal of the Property Confluence Algorithm (PCA) is the identification of changes in dynamic properties (natural frequencies and modes) of the system. The motivation comes from the necessity of monitoring changes in mass and stiffness distribution of components. Applications to a rotating environment as in the case of rotor blades and wind turbines is of particular interest [31].

This chapter initially presents a conceptual view of the Property Confluence Algorithm. Then, after its detailed description, numerical examples demonstrate its application to one-dimensional dynamic systems.

4.2 Concept

The PCA consists in an initial numerical model of the structure, a set of experimental measurements, and a procedure which estimates the difference in dynamic properties between the numerical model and the experimental measurements. A schematic representation of the procedure is presented in Figure 86. The application to a rotating environment leads to the assumption that the applied loads, and as a consequence the dynamic response, vary periodically with time and they can be expanded through a Fourier series. The applied loads are assumed to be accurately known.

The procedure is closely related to the Load Confluence Algorithm, and can be summarized as follows.

- A numerical model of the system is formulated from an initial guess of the physical properties of the system.

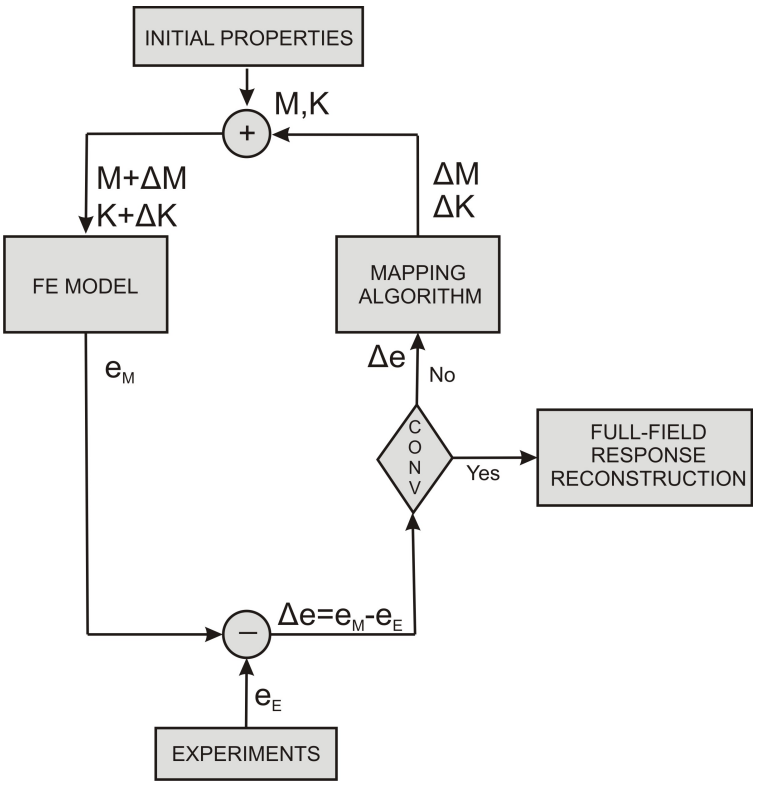

Figure 86: Schematic of the property identification algorithm.

- The solution of the FE model estimates the dynamic response $\boldsymbol{e}_M(\boldsymbol{x})$ at the sensor location $\boldsymbol{x}$.
- The numerical and measured responses are compared and a error vector $\Delta\boldsymbol{e} = \boldsymbol{e}_M - \boldsymbol{e}_E$ is calculated.
- Corrections for the mass and/or stiffness matrices are calculated based on $\Delta\boldsymbol{e}$ through the formulation of the problem in the modal domain. This is performed through a modal mapping procedure as described in section 4.3.
- The procedure is iteratively applied until convergence.

4.3 Modal procedure for property estimation

Consider a general undamped linear system:

$$\boldsymbol{M}\ddot{\boldsymbol{u}}(t) + \boldsymbol{K}\boldsymbol{u}(t) = \boldsymbol{F}(t) \tag{13}$$

where $\boldsymbol{M}$ and $\boldsymbol{K}$ are the mass and the stiffness matrices of the system, array $\boldsymbol{u}(t)$ stores the N degrees of freedom of the solution, and $\boldsymbol{F}(t)$ is the array of the generalized applied loads. This system is characterized by natural frequencies $\boldsymbol{\omega}$ and modes $\boldsymbol{P}$.

4.3.1 Change in stiffness

Suppose inaccuracies exist in the estimation of the stiffness matrix. The real model of the system is:

$$\boldsymbol{M}\ddot{\widehat{\boldsymbol{u}}} + (\boldsymbol{K} + \Delta\boldsymbol{K})\,\widehat{\boldsymbol{u}} = \boldsymbol{F}(t) \tag{14}$$

with $\Delta\boldsymbol{K}$ unknown. It is assumed that the applied loads are known and equal to the loads applied to the initial system. This model is characterized by natural frequencies $\widehat{\boldsymbol{\omega}}$ and modes $\widehat{\boldsymbol{P}}$. It is assumed that the eigenvectors of the real system $\widehat{\boldsymbol{P}}$ are a linear combination of the initial modes $\boldsymbol{P}$ through a matrix $\boldsymbol{\alpha}$ of coefficients:

$$\widehat{\boldsymbol{P}} = \boldsymbol{P}\boldsymbol{\alpha} \tag{15}$$

The change in stiffness matrix is assumed to take the form:

$$\Delta\boldsymbol{K} = \sum_{k=1}^{N_{par}} \gamma_k \frac{\partial \boldsymbol{K}}{\partial \gamma_k} \tag{16}$$

and it can be reasonably assumed that $\frac{\partial \boldsymbol{K}}{\partial \gamma_k}$ is known (either analytically or by finite difference). The difference between Eqns. (13) and (14) leads to:

$$\boldsymbol{M}\left(\ddot{\boldsymbol{u}} - \ddot{\widehat{\boldsymbol{u}}}\right) + \boldsymbol{K}\left(\boldsymbol{u} - \widehat{\boldsymbol{u}}\right) + \Delta\boldsymbol{K}\widehat{\boldsymbol{u}} = 0 \tag{17}$$

with

$$\boldsymbol{u} = \boldsymbol{P}\boldsymbol{q}, \qquad \widehat{\boldsymbol{u}} = \widehat{\boldsymbol{P}}\widehat{\boldsymbol{q}} = \boldsymbol{P}\boldsymbol{\alpha}\widehat{\boldsymbol{q}} \tag{18}$$

Defining the difference of the two systems in generalized coordinates as:

$$\overline{\Delta\boldsymbol{z}} = \boldsymbol{q} - \boldsymbol{\alpha}\widehat{\boldsymbol{q}} \tag{19}$$

the difference in nodal displacement is expressed as:

$$\boldsymbol{u} - \widehat{\boldsymbol{u}} = \boldsymbol{P}\boldsymbol{q} - \widehat{\boldsymbol{P}}\widehat{\boldsymbol{q}} = \boldsymbol{P}\left(\boldsymbol{q} - \boldsymbol{\alpha}\widehat{\boldsymbol{q}}\right) = \boldsymbol{P}\overline{\Delta\boldsymbol{z}} \tag{20}$$

Pre-multiply Eq. (17) by Eq. $\boldsymbol{P}^T$, and define $\boldsymbol{\mathcal{K}}_k = \boldsymbol{P}^T \dfrac{\partial \boldsymbol{K}}{\partial \gamma_k} \boldsymbol{P}$:

$$\boldsymbol{I}\overline{\Delta \ddot{\boldsymbol{z}}} + \operatorname{diag}\left(\omega_i^2\right) \overline{\Delta \boldsymbol{z}} + \sum_{k=1}^{N_{par}} \gamma_k \, \boldsymbol{\mathcal{K}}_k \, \boldsymbol{\alpha} \widehat{\boldsymbol{q}} = 0 \tag{21}$$

Matrix $\boldsymbol{\mathcal{K}}_k$ represents the change in stiffness due to each parameter projected in the modal domain. Then, the response and the generalized coordinates can be related through matrix $\boldsymbol{B}$ and its pseudo-inverse as:

$$\boldsymbol{e}_M(x,t) = \boldsymbol{B}(x)\boldsymbol{q}(t), \qquad \boldsymbol{e}_E(x,t) = \widehat{\boldsymbol{B}}(x)\widehat{\boldsymbol{q}}(t) \tag{22}$$

The definition of $\boldsymbol{B}$ depends on the measured quantities, that is, on the kind of sensors. Similarly to the procedure for load identification, a reduced number of modes m can be used in the analysis.

Assume that the relation between matrices $\boldsymbol{B}$ and $\widehat{\boldsymbol{B}}$ is the same as the relation between $\boldsymbol{P}$ and $\widehat{\boldsymbol{P}}$, such that $\widehat{\boldsymbol{B}} = \boldsymbol{B}\boldsymbol{\alpha}$. This assumption is valid in a linear or linearized framework. The difference between numerical response and measured signals is:

$$\boldsymbol{e}_M - \boldsymbol{e}_E = \boldsymbol{B}\left(\boldsymbol{q} - \boldsymbol{\alpha}\widehat{\boldsymbol{q}}\right) = \boldsymbol{B}\overline{\Delta \boldsymbol{z}}, \qquad \overline{\Delta \boldsymbol{z}} = \boldsymbol{B}^{+}\Delta \boldsymbol{e} \tag{23}$$

The externally applied loads are supposed to be harmonic, as well as the response of the system, and can expanded with a Fourier series of frequency Ω:

$$\Delta \boldsymbol{e} = \Delta \boldsymbol{e}_0 + \sum_{j=1}^{M} \left(\boldsymbol{e}_c \cos(j\Omega t) + \boldsymbol{e}_s \sin(j\Omega t)\right) \tag{24}$$

Introducing Eqns. (23) and (24) into Eq. (21), by harmonic balance the system of equations to be solved becomes:

$$\begin{aligned}
&\operatorname{diag}\left(\omega_i^2\right) \boldsymbol{B}^{+}\Delta \boldsymbol{e}_0 + \textstyle\sum_{k=1}^{N_{par}} \gamma_k \, \boldsymbol{\mathcal{K}}_k \boldsymbol{B}^{+} \boldsymbol{e}_{E0} = 0 \\
&\operatorname{diag}\left(-j^2\Omega^2 + \omega_i^2\right) \boldsymbol{B}^{+}\Delta \boldsymbol{e}_c + \textstyle\sum_{k=1}^{N_{par}} \gamma_k \, \boldsymbol{\mathcal{K}}_k \boldsymbol{B}^{+} \boldsymbol{e}_{Ec} = 0 \\
&\operatorname{diag}\left(-j^2\Omega^2 + \omega_i^2\right) \boldsymbol{B}^{+}\Delta \boldsymbol{e}_s + \textstyle\sum_{k=1}^{N_{par}} \gamma_k \, \boldsymbol{\mathcal{K}}_k \boldsymbol{B}^{+} \boldsymbol{e}_{Es} = 0
\end{aligned} \tag{25}$$

where the unknown of the system of equations are the changes in stiffness parameters γ_k. Equation (25) is a linear rectangular system of equations, that can be solved for

γ_k after rearranging it in matrix form, as in the following. A dimensional analysis reveals that $\boldsymbol{\mathcal{K}}_k \boldsymbol{B}^+ \widehat{\boldsymbol{e}}_c$ is a column-vector $\left(\boldsymbol{\mathcal{K}}_k \boldsymbol{B}^+ \widehat{\boldsymbol{e}}_c \in \mathbb{R}^{N\text{x}1}\right)$:

$$\begin{aligned} &\boldsymbol{\mathcal{K}}_k \in \mathbb{R}^{m\text{x}m} = \mathbb{R}^{m\text{x}N} \mathbb{R}^{N\text{x}N} \mathbb{R}^{N\text{x}m} \\ &\boldsymbol{B} \in \mathbb{R}^{s\text{x}m}, \quad \boldsymbol{B}^+ \in \mathbb{R}^{m\text{x}s} \\ &\boldsymbol{e}_E \in \mathbb{R}^{s\text{x}1} \end{aligned} \tag{26}$$

Equation (25) becomes:

$$\begin{bmatrix} \boldsymbol{\mathcal{K}}_1 \boldsymbol{B}^+ \boldsymbol{e}_{E0} & \boldsymbol{\mathcal{K}}_2 \boldsymbol{B}^+ \boldsymbol{e}_{E0} & \cdots & \boldsymbol{\mathcal{K}}_{N_{par}} \boldsymbol{B}^+ \boldsymbol{e}_{E0} \\ \boldsymbol{\mathcal{K}}_1 \boldsymbol{B}^+ \boldsymbol{e}_{Ec} & \boldsymbol{\mathcal{K}}_2 \boldsymbol{B}^+ \boldsymbol{e}_{Ec} & \cdots & \boldsymbol{\mathcal{K}}_{N_{par}} \boldsymbol{B}^+ \boldsymbol{e}_{Ec} \\ \boldsymbol{\mathcal{K}}_1 \boldsymbol{B}^+ \boldsymbol{e}_{Es} & \boldsymbol{\mathcal{K}}_2 \boldsymbol{B}^+ \boldsymbol{e}_{Es} & \cdots & \boldsymbol{\mathcal{K}}_{N_{par}} \boldsymbol{B}^+ \boldsymbol{e}_{Es} \end{bmatrix} \begin{Bmatrix} \gamma_1 \\ \gamma_2 \\ \vdots \\ \gamma_{N_{par}} \end{Bmatrix} =$$

$$= - \begin{Bmatrix} \text{diag}\left(\omega_i^2\right) \boldsymbol{B}^+ \Delta \boldsymbol{e}_0 \\ \text{diag}\left(-j^2\Omega^2 + \omega_i^2\right) \boldsymbol{B}^+ \Delta \boldsymbol{e}_c \\ \text{diag}\left(-j^2\Omega^2 + \omega_i^2\right) \boldsymbol{B}^+ \Delta \boldsymbol{e}_s \end{Bmatrix} \tag{27}$$

The system of equations in (27) is characterized by $(1 + 2M)\, m$ equations in N_{par} unknowns. By iteratively updating the stiffness matrix, the changes in properties in the system can be identified.

4.3.2 Change in mass

The change in dynamical properties due to a change in mass is analogous to the procedure described for the stiffness case. The differences between the two cases are underlined in the following. The modified system is in this case characterized by an unknown change in mass matrix such that:

$$\left(\boldsymbol{M} + \Delta \boldsymbol{M}\right) \ddot{\widehat{\boldsymbol{u}}} + \boldsymbol{K} \widehat{\boldsymbol{u}} = \boldsymbol{F}(t) \tag{28}$$

The objective is the estimation of the difference in mass $\Delta \boldsymbol{M}$ from the observation of the response of the real system at a limited number of points. The difference between

Eqns. (13) and (28) leads to:

$$\boldsymbol{M}\left(\ddot{\boldsymbol{u}}-\ddot{\widehat{\boldsymbol{u}}}\right)+\boldsymbol{K}\left(\boldsymbol{u}-\widehat{\boldsymbol{u}}\right)+\Delta\boldsymbol{M}\ddot{\widehat{\boldsymbol{u}}}=0 \tag{29}$$

The increment in mass matrix $\Delta\boldsymbol{M}$ is approximated as a linear combination of the contribution of all mass parameters μ_k. These parameters can be for example defined as the mass per unit length of the elements of the finite element model. The relation between each parameter μ_k and the mass increment is supposed to be known from the assembly of the numerical model:

$$\Delta\boldsymbol{M}=\sum_{k=1}^{N_{par}}\mu_k\frac{\partial\boldsymbol{M}}{\partial\mu_k} \tag{30}$$

that in modal coordinates is:

$$\boldsymbol{I}\overline{\Delta\ddot{\boldsymbol{z}}}+\operatorname{diag}\left(\omega_i^2\right)\overline{\Delta\boldsymbol{z}}+\sum_{k=1}^{N_{par}}\mu_k\,\boldsymbol{\mathcal{M}}_k\,\boldsymbol{\alpha}\ddot{\widehat{\boldsymbol{q}}}=0 \tag{31}$$

with $\boldsymbol{\mathcal{M}}_k=\boldsymbol{P}^T\dfrac{\partial\boldsymbol{M}}{\partial\mu_k}\boldsymbol{P}$. Equation (31) becomes:

$$\boldsymbol{B}^{+}\Delta\ddot{\boldsymbol{e}}+\operatorname{diag}\left(\omega_i^2\right)\boldsymbol{B}^{+}\Delta\boldsymbol{e}+\sum_{k=1}^{N_{par}}\mu_k\,\boldsymbol{\mathcal{M}}_k\,\boldsymbol{B}^{+}\ddot{\widehat{\boldsymbol{e}}}=0 \tag{32}$$

The application to rotating environments justifies the assumption that the system is subjected to periodic loads, so that its response is harmonic. A Fourier's series expansion of all quantities and harmonic balance of Eq. (32) results into:

$$\begin{aligned}
&\operatorname{diag}\left(\omega_i^2\right)\boldsymbol{B}^{+}\Delta\boldsymbol{e}_0=0\\
&\operatorname{diag}\left(-j^2\Omega^2+\omega_i^2\right)\boldsymbol{B}^{+}\Delta\boldsymbol{e}_c-j^2\Omega^2\textstyle\sum_{k=1}^{N_{par}}\mu_k\,\boldsymbol{\mathcal{M}}_k\boldsymbol{B}^{+}\boldsymbol{e}_{Ec}=0\\
&\operatorname{diag}\left(-j^2\Omega^2+\omega_i^2\right)\boldsymbol{B}^{+}\Delta\boldsymbol{e}_s-j^2\Omega^2\textstyle\sum_{k=1}^{N_{par}}\mu_k\,\boldsymbol{\mathcal{M}}_k\boldsymbol{B}^{+}\boldsymbol{e}_{Es}=0
\end{aligned} \tag{33}$$

where the unknown of the system of equations are the changes in mass parameters μ_k. The first equation on the zeroth harmonic is generally verified by itself, therefore only the other two equations are brought forward. Rearranging Eq. (33) in matrix

form, the resulting system of equations is:

$$j^2\Omega^2 \begin{bmatrix} \boldsymbol{\mathcal{M}}_1\boldsymbol{B}^+\boldsymbol{e}_{Ec} & \boldsymbol{\mathcal{M}}_2\boldsymbol{B}^+\boldsymbol{e}_{Ec} & \cdots & \boldsymbol{\mathcal{M}}_{N_{par}}\boldsymbol{B}^+\boldsymbol{e}_{Ec} \\ \boldsymbol{\mathcal{M}}_1\boldsymbol{B}^+\boldsymbol{e}_{Es} & \boldsymbol{\mathcal{M}}_2\boldsymbol{B}^+\boldsymbol{e}_{Es} & \cdots & \boldsymbol{\mathcal{M}}_{N_{par}}\boldsymbol{B}^+\boldsymbol{e}_{Es} \end{bmatrix} \begin{Bmatrix} \mu_1 \\ \mu_2 \\ \vdots \\ \mu_{N_{par}} \end{Bmatrix} =$$

$$= \begin{Bmatrix} \text{diag}\left(-j^2\Omega^2 + \omega_i^2\right)\boldsymbol{B}^+\Delta\boldsymbol{e}_c \\ \text{diag}\left(-j^2\Omega^2 + \omega_i^2\right)\boldsymbol{B}^+\Delta\boldsymbol{e}_s \end{Bmatrix} \tag{34}$$

The system in Eq. (34) is characterized by $2M$xm equations in N_{par} unknowns. By iteratively updating the mass matrix, the changes in properties in the system are identified.

Generally, it is possible to assume that $\boldsymbol{\mathcal{K}}_k$ and $\boldsymbol{\mathcal{M}}_k$ do not change during the analysis. This approximation is advantageous because it avoids the reassembly of the finite element model at every iteration. Moreover, the iteration matrix in Eqns. (27) and (34) does not change during the analysis, and the computation is more efficient.

The properties of the system depend on the initial definition of the model in terms of choice of modes, number of harmonics, sensor location, initial properties of the system, as well as reference response values (generally experimental measurements). An indication of the convergence of the algorithm can be drawn by observing the norm of the right-hand-side of Eqns. (27) and (34), as well as the norm of γ_k or μ_k. The effect of this choice is analyzed in the next section.

4.4 Numerical example: analysis of a beam in bending

This section describes an example of application of the Property Confluence Algorithm, in which numerical data are used as reference values. Consider a beam in bending subject to a concentrated harmonic force, modeled with finite elements. The beam is divided in 15 elements and it is characterized by two different properties

along the span, as depicted in Figure 87. The beam is excited by a single harmonic load with an excitation frequency of $f = 10$ Hz lower than the first natural frequency.

In this example, the PCA aims to update the bending stiffness EI of the two portions of the beam, referred as EI_1 and EI_2. The effect of number of modes and sensors considered by the updating algorithm is investigated, as well as the effects on the results of different choices of tolerance parameters. Initially, the parameter to establish convergence of the iterative procedure is defined as the norm of the changes in stiffness γ_k, and it is set to 10^{-4}.

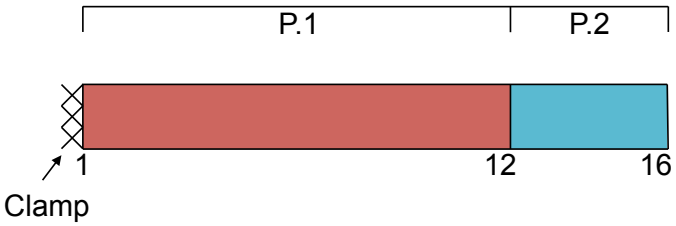

Figure 87: Schematic of the numerical model, division in two properties of the beam, with labels of boundary nodes.

The initial model is characterized by $EI_1 = 48$ N m^2, $EI_2 = 48$ N m^2, and the reference model by $EI_1 = 40$ N m^2, $EI_2 = 50$ N m^2. The two models therefore differ for a change of 20% on EI_1, and of 4% on EI_2. The number of modes and sensors play an important role in the convergence of the algorithm. Table 10 shows in fact that one mode is not sufficient to recover the difference in both parameters. Even if the analysis quickly converges in six iterations (Figure 88), the algorithm cannot properly identify the change in EI_2, even with an increase in number of sensors. To be able to properly represent both changes it is necessary to include the second mode. The number of iterations required to converge significantly increases, but the error on the identified properties decreases to less than 0.05%, Figure 91. The inclusion of additional modes (i.e. up to four modes) does not play a particular role other than increasing the number of iterations required to converge.

Even if a significant difference still exists on EI_2 at the end of the analysis, the

Table 10: Summary of identified stiffness properties. Initial properties: $EI_1 = 48$ N m^2, $EI_2 = 48$ N m^2. Reference properties $EI_1 = 40$ N m^2, $EI_2 = 50$ N m^2.

			Updated	
m	N	N_{it}	EI_1 [N m^2]	EI_2 [N m^2]
1	1	6	40.00 $5{\cdot}10^{-4}$%	47.98 -4.0%
1	3	6	40.00 $5{\cdot}10^{-4}$%	47.98 -4.0%
1	5	6	40.00 $5{\cdot}10^{-4}$%	47.98 -4.0%
2	5	39	40.00 0.0%	50.01 0.02%
4	5	45	39.99 $-1{\cdot}10^{-3}$%	50.01 0.02%

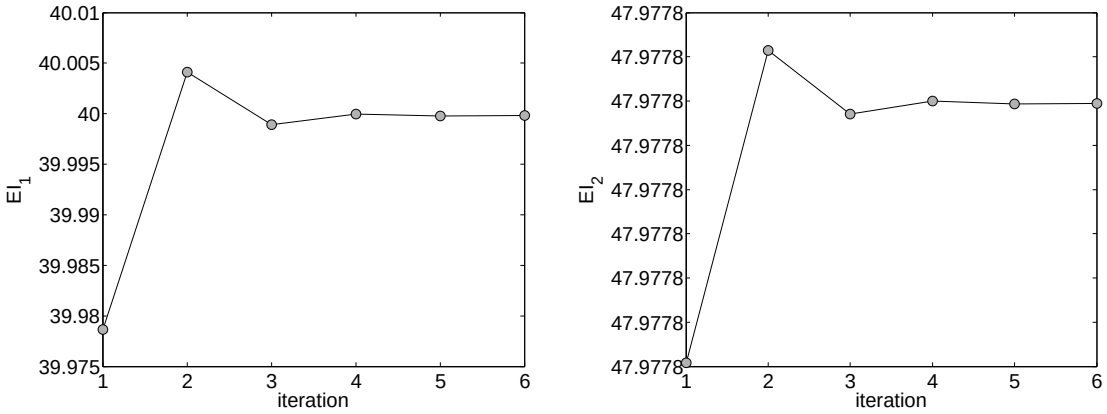

(a) γ_1 (b) γ_2

Figure 88: Identified stiffness parameters during iterations, $s = 1$, m =1.

deformed shape and the time history at the nodes are accurately represented, Figures 89 and 90. At this excitation frequency the response is in fact dominated by the first mode, that is accurately represented by the identified model, Table 11.

A summary of the effects of number of modes is presented in Figures 92 and 93. It is interesting to note that the relation between the number of sensors and modes also plays an important role. The choice of three sensors (Figure 92) does not ensure convergence to the reference properties even if multiple modes (up to three) are included in the analysis. It is observed that five sensors and two modes are necessary to achieve accurate results for both parameters.

Table 11: Comparison between initial, reference and identified natural frequencies.

	f [Hz]		
	Reference	Initial	Updated
f_1	33.56 -	37.75 8.7%	33.56 0.0%
f_2	207.51 -	225.95 -9.0%	207.30 -0.1%
f_3	573.74 -	614.40 -7.5%	571.56 -0.4%
f_4	1093.5 -	1157.0 -6.5%	1086.8 -0.6%
f_5	1721.4 -	1824.6 -6.7%	1710.9 -0.6%

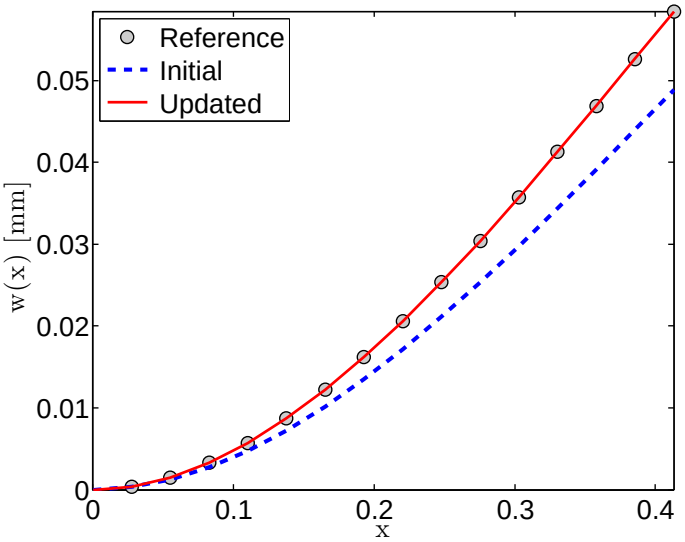

Figure 89: Instantaneous deformed shape, $s = 1$, m =1.

This simple example also allows investigating the effect of the choice of the tolerance parameter on the convergence of the algorithm. Two are the possible choices: first, the norm of the right hand side of Eq. (27), second the norm of the changes in properties γ_k. Figures 94 and 95 show both choices are appropriate to check whether of not PCA is converged. The figures show the convergence of the two bending stiffnesses for different tolerance values in the interval $[10^{-1}, 10^{-5}]$, for two different positions of the external concentrated load. The results of the identification are in

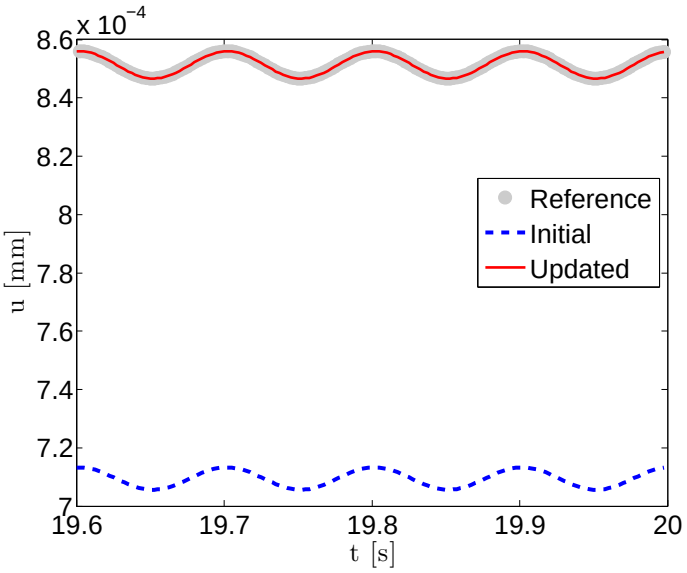

Figure 90: Time history of sensor 1, $s = 1$, m =1.

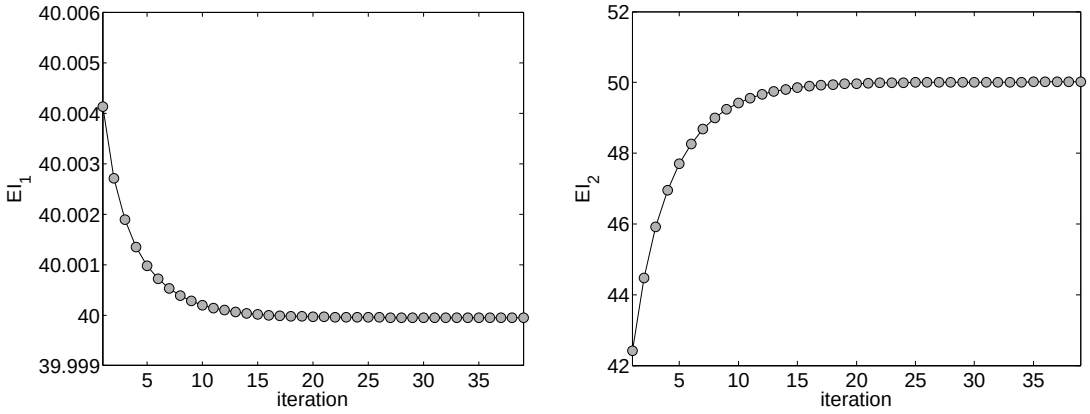

(a) γ_1 (b) γ_2

Figure 91: Identified stiffness parameters during iterations, $s = 5$, m =2.

fact dependent on the load applied to the system. It is interesting to notice that during the analysis the accuracy on EI_1 decreases from an error of 0.01% with respect to the reference properties to 0.05% in order to improve the accuracy of EI_2 from 2.3% to 0.03%. The analysis therefore finds the best combination of parameters given the response of the system.

The increase in number of iterations required for convergence is affected by the definition of tolerance parameter. The total number of iterations is related to the

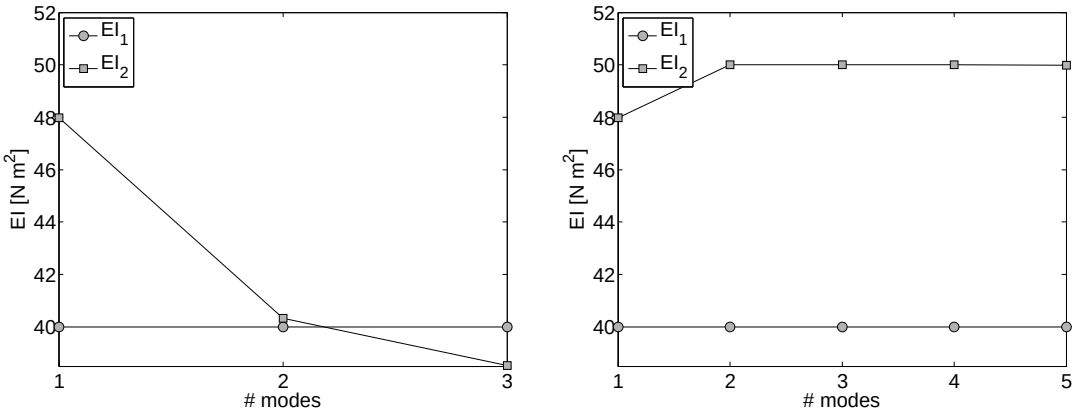

(a) 3 sensors (b) 5 sensors

Figure 92: Influence of number of modes on the updated EI_1 and EI_2. Reference properties: $EI_1 = 40$ N m^2, $EI_2 = 50$ N m^2. EI_1 (o), EI_2 (□).

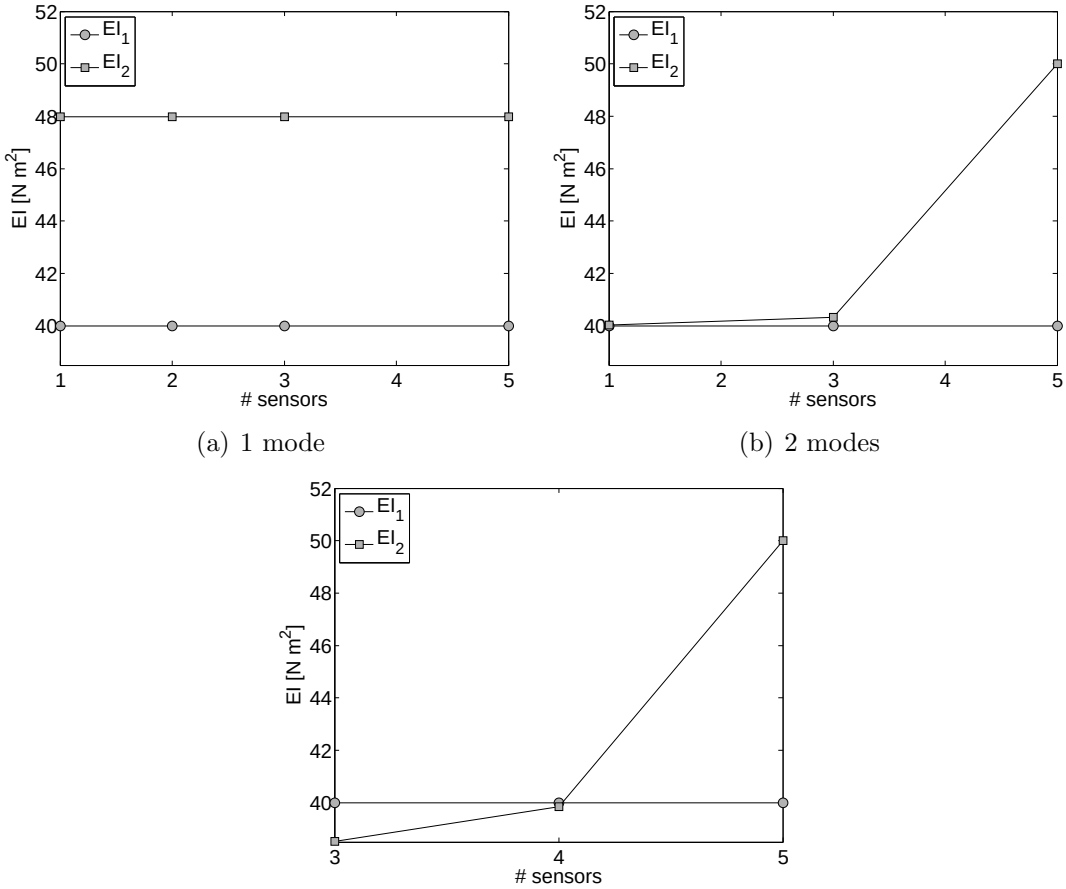

(a) 1 mode (b) 2 modes

(c) 3 modes

Figure 93: Influence of number of sensors on the updated EI_1 and EI_2. Reference properties: $EI_1 = 40$ N m^2, $EI_2 = 50$ N m^2. EI_1 (o), EI_2 (□).

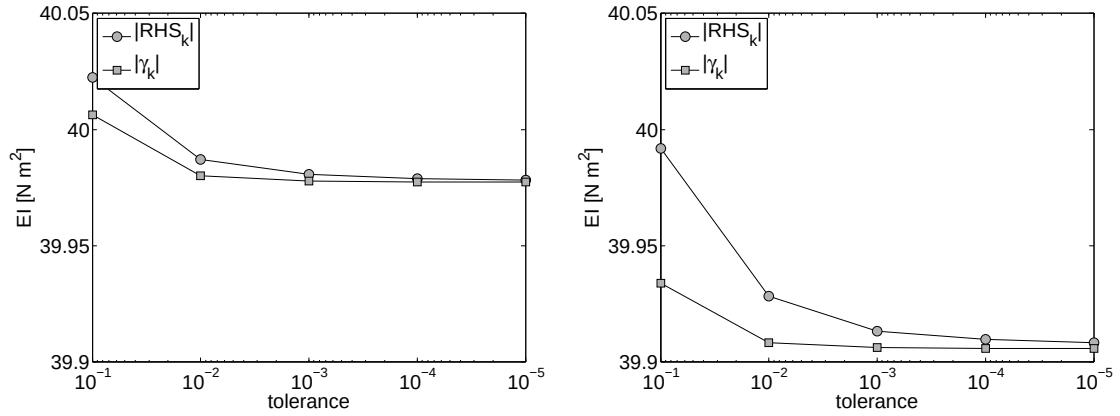

(a) load set 1 (b) load set 2

Figure 94: Influence of choice of convergence parameter on EI_1 for different load sets. Reference properties: $EI_1 = 40$ N m^2, $EI_2 = 50$ N m^2. $|RHS|$ (o), γ_k (□).

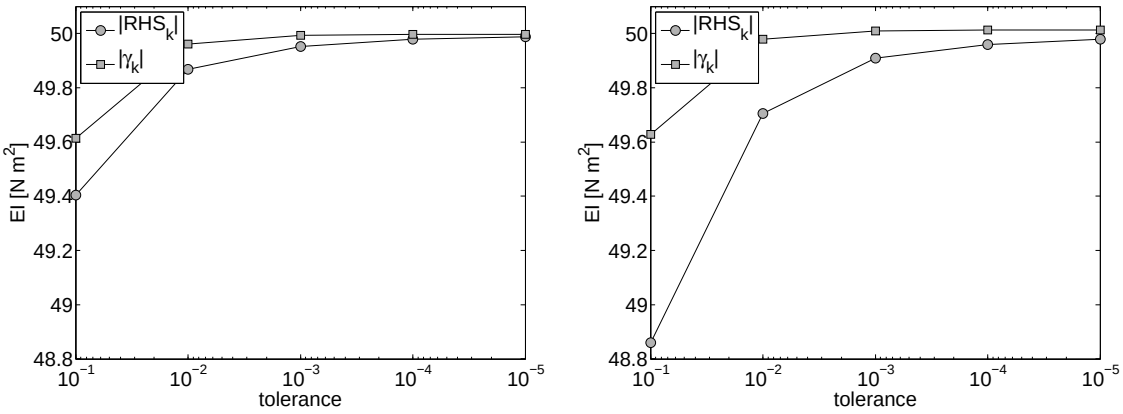

(a) load set 1 (b) load set 2

Figure 95: Influence of choice of convergence parameter on EI_2 for different load sets. Reference properties: $EI_1 = 40$ N m^2, $EI_2 = 50$ N m^2. $|RHS|$ (o), γ_k (□).

computational cost of the algorithm. Figure 96 shows that the number of iterations exponentially increases when the norm of the right hand side of Eq. (27) is considered, while a lower number of iterations are required when the absolute value of the changes in properties is considered. For this reason, $|\gamma_k|$ is chosen as tolerance parameter of the algorithm.

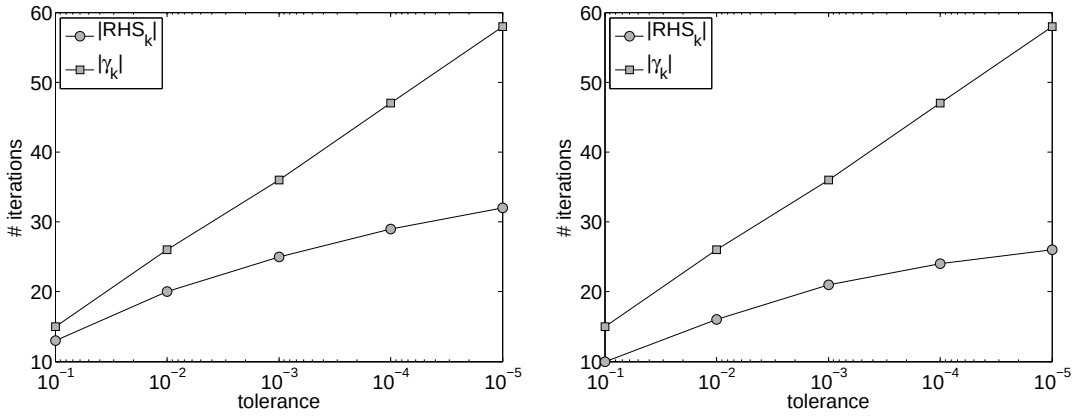

(a) load set 1 (b) load set 2

Figure 96: Influence of choice of convergence parameter on the number of iterations to converge for different load sets, $m = 5$, $s = 5$. Reference properties: $EI_1 = 40$ N m^2, $EI_2 = 50$ N m^2. $|RHS|$ (o), γ_k ($\square$).

4.5 Conclusions

This example shows that the PCA is adequate to reconstruct the response of the system in the presence of structural modifications such as changes in bending stiffnesses. The reference system is numerically defined in order to ensure the absence of inaccuracies in the modeling of external loads and of experimental noise. The performance of PCA to analyze experimental cases are assessed in the next chapter in the case of changes in mass properties of the system.

CHAPTER V

APPLICATION OF THE PROPERTY CONFLUENCE ALGORITHM TO EXPERIMENTAL DATA ON A BEAM

5.1 Overview

The Property Confluence Algorithm is now applied to experimental reference data. Starting from a uniform beam, three concentrated masses are progressively added to the experimental system. The PCA aims to identify the presence of these masses starting from a numerical model for the uniform beam configuration.

The analyses presented in the following are divided in two main groups. First, it is assumed that the locations of the added masses are known, and the parameters to be updated are nodal masses located in correspondence of the added masses (or blocks) in the experimental system. Then, these cases are generalized and the algorithm identifies a set of nodal masses on the entire beam span (the locations of the added masses is not known a priori).

5.2 Experimental set-up

The experimental set-up on which PCA is tested is similar to the experimental configuration presented in section 3.2. The beam is clamped at its bottom and it is excited by an electrodynamic shaker located at two-thirds of the span. The response is characterized through velocity and displacement measurements recorded by a scanning laser vibrometer, set to measure 93 points over the beam. The measured set of points is divided into two subsets. A small subset is used by the optimization algorithm to identify the response, while a larger subset is used to compare the full-field numerical predictions with the actual response of the beam.

The uniform beam case is considered as an initial guess for the PCA (Figure 97). Then, three concentrated masses are progressively added to the system that will be identified by the PCA starting from the uniform beam configuration. At first, a concentrated mass is added in proximity of the tip of the beam. This increases the total mass of the system by 22% (Figure 98(a)). Then, two masses are introduced in the system (Figure 98(b)) that increase by 34% the total initial mass. Lastly, a configuration with three masses is analyzed, providing a total increase in mass of about 40% (Figure 98(c)). The physical properties of the system are listed in Table 12.

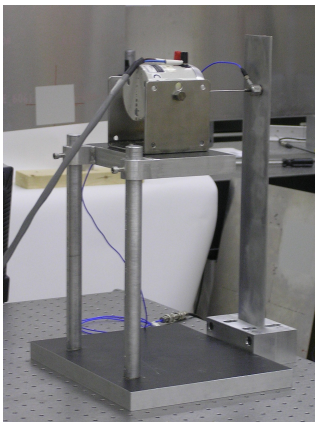

Figure 97: Experimental setup to define initial numerical guess.

Table 12: Mass properties of the experimental system.

Beam	mass m = 178 g length l = 41 cm
Mass 1	mass m_1 = 42 g location x_1 = 40 cm
Mass 2	mass m_2 = 22 g location x_2 = 25 cm
Mass 3	mass m_3 = 12 g location x_3 = 31 cm

A schematic of the experimental setup and numerical properties is depicted in Figure 99, with the location of the three masses and of the applied load.

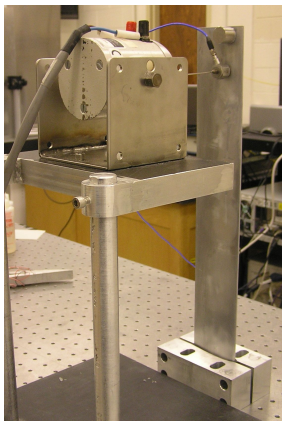

(a) one mass added (97% of span)

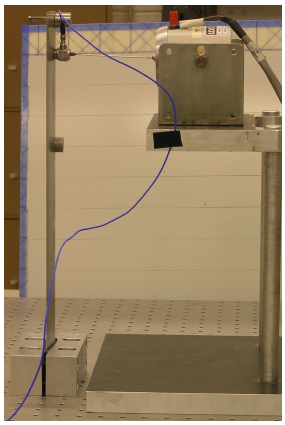

(b) two masses added (97% and 60% of span)

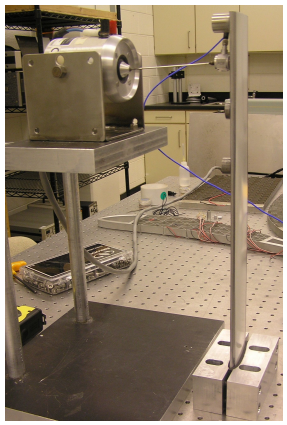

(c) three masses added (97%, 75% and 60% of span)

Figure 98: Experimental setup of the beam.

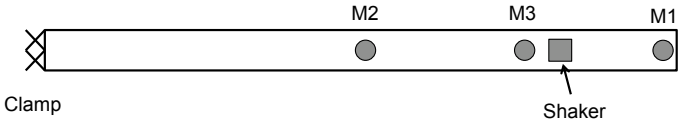

Figure 99: Schematic of the experimental setup.

The measured natural frequencies for the four different cases are listed in Table 13, as well as the percentage difference given by the additional masses with respect to the initial configuration. The addition of a mass (denoted as case: Mass 1) reduces the first bending frequency of about 20%. The addition of two masses (case: Mass 2) and three masses (case: Mass 3) lead to a frequency change of about 30%.

The frequency response functions (frf) for the different experimental cases are compared in Figure 100 to show the effect of the added mass on the dynamic behavior of the system. The frf are evaluated at the tip of the beam with respect to a pseudo-random concentrated load applied through the electrodynamic shaker at two-thirds of the span of the beam.

Table 13: Experimental bending natural frequencies of the blade for different mass distributions, with percentage difference with respect to the uniform beam configuration.

	f [Hz]			
	No Mass	Mass 1	Mass 2	Mass 3
f_1	33.7 -	26.3 22%	23.7 30%	23.7 30%
f_2	232.5 -	197.5 15%	183.7 21%	182.5 22%
f_3	642.5 -	568.7 11%	552.5 14%	540.0 16%
f_4	1195.0 -	1060.0 11%	1051.2 12%	1031.0 14%

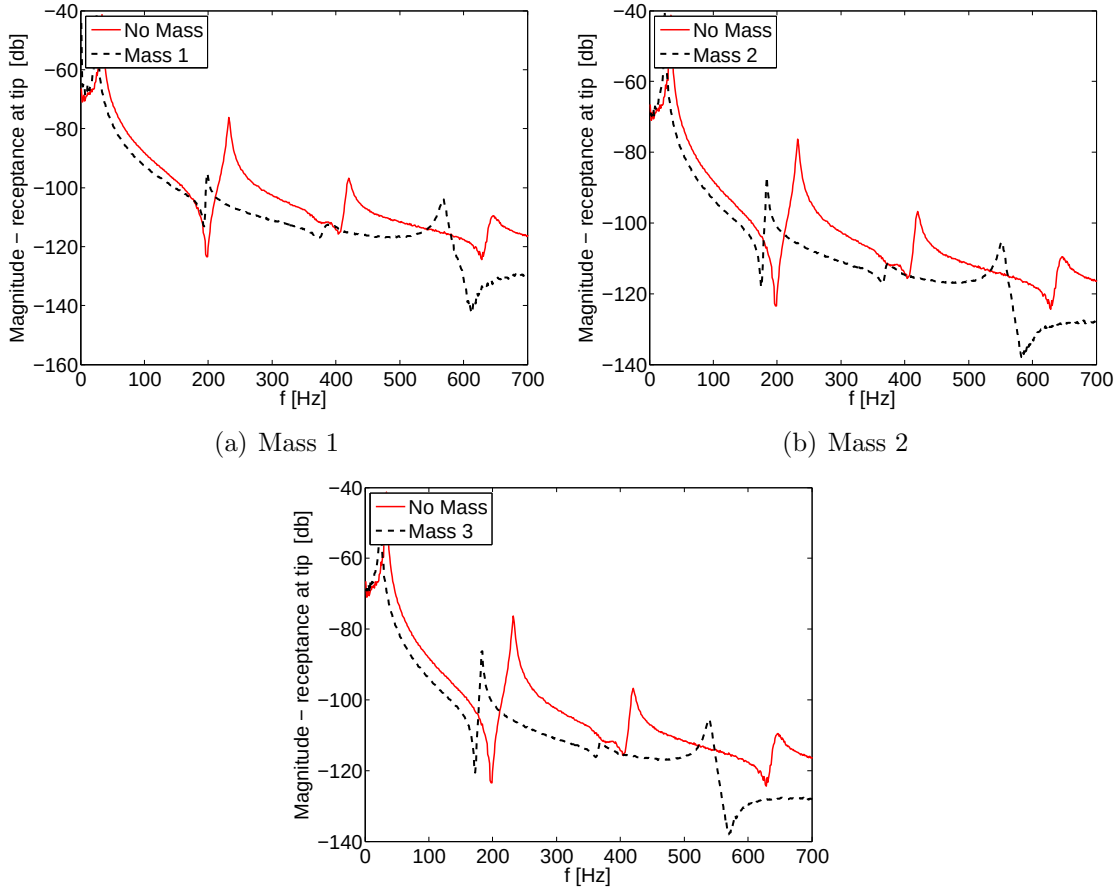

(a) Mass 1

(b) Mass 2

(c) Mass 3

Figure 100: Measured magnitude of frequency response function for different mass configurations. No mass (-). With mass (--).

5.3 Numerical model

The numerical model used to predict the behavior of the system consists in a one-dimensional beam finite element model. The beam is discretized with 20 Timoshenko elements, whose physical properties are defined to match the experimental natural frequencies of the uniform beam as close as possible, Table 14. The error on the lowest frequencies range from 5.5% on f_1 to less than 4% on higher frequencies. The comparison between the numerical and experimental frequency response functions, Figure 101, shows a good correlation. However, the model cannot capture the third peak in the experimental frequency response function (at $f = 420$ Hz) because it correponds to the first torsional mode. The torsional behavior is in fact neglected in the finite element model of the beam.

Table 14: Numerical natural frequencies before the application of the property identification algorithm, with percentage error with respect to all four experimental configurations.

		Error [%]			
	f [Hz]	No mass	Mass 1	Mass 2	Mass 3
f_1	35.6	-5.5	-35.6	-49.9	-49.9
f_2	223.3	3.9	-13.1	-21.5	-22.4
f_3	624.9	2.7	-9.9	-13.1	-15.7
f_4	1223.6	-2.4	-15.4	-16.4	-18.7

The percentage errors between the initial numerical frequencies and all the experimental cases are also listed in Table 14. The major differences are generally on the first mode, with a difference of more than 35%.

A set of concentrated masses is then added to the model as nodal masses. Starting from a zero value (uniform beam configuration), the PCA updates their values in order to match the experimental response. At first, the location of the added mass is assumed to be known and only the nodal masses corresponding to their physical location in the experiments are updated (node 21 for one mass, nodes [13, 21] for two

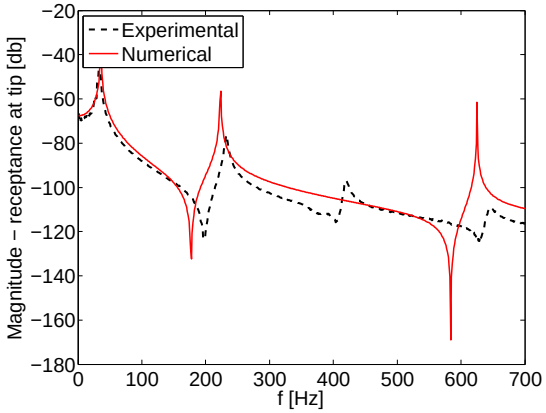

Figure 101: Comparison between experimental and numerical magnitude of frequency response function for a uniform beam configuration with no added mass. FEM (-). Experimental (--).

masses, nodes [13, 16, 21] for three masses - node 1: root, node 21: tip). Then, this assumption is removed and all the 21 nodal masses are considered as parameters to be updated.

The details of the characteristics of the PCA are analyzed considering a single excitation frequency at $f = 50$ Hz, at which the response of the system is dominated by the first mode. All the experimental data are analyzed at this frequency.

5.4 Identification of a single nodal mass

Initially, the performance of the PCA is discussed considering the addition of a single mass (Mass 1) to the uniform beam. Independently of the location and of the number of parameters to be updated, the algorithm converges in five iterations. The algorithm is considered converged when the change in total mass is lower than 5×10^{-5}. Convergence of the PCA is considered to be achieved when the change in the norm of the parameter vector is below the specified tolerance. A set of six control points is considered in the identification, whose distances from the root are listed in Table 15. Moreover, the PCA considers a single mode in the approximation of the response.

A typical behavior of the changes of the response during the analysis is shown in Figure 102. These plots depict the changes in magnitude and phase at control point 1.

Table 15: Position of the control points used by the PCA to approximate the response of the beam.

ID	Distance from root		ID	Distance from root
1	41 cm		4	22 cm
2	34 cm		5	16 cm
3	29 cm		6	11 cm

At first, both the magnitude and phase are characterized by large discrepancies with respect to the measured response. The initial difference in magnitude between the numerical and experimental signal measured at point 1 is 25%, and 13% on phase. These errors are defined as the percentage difference between magnitude and phase of the two signals. The update of the nodal masses progressively improves the prediction of the absolute value, while it cannot correct existing phase differences between the two systems. The additional mass in fact does not significantly influence the phase of the response.

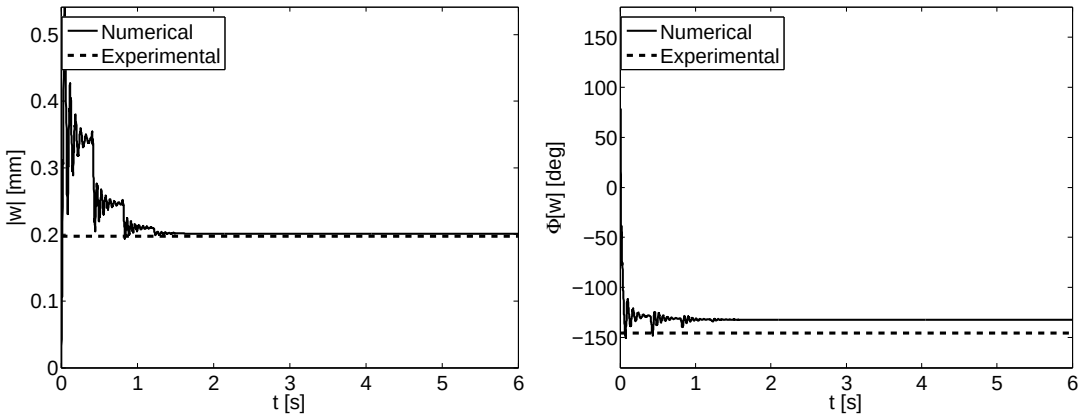

(a) $|w_1|$ (b) Φ_1

Figure 102: Magnitude and phase of the response of the system at control point 1. One mass added. Identification of a concentrated mass at node 21. Measured (--). FEM (-).

The first analyzed case updates the value of a nodal mass at node 21 (tip of the beam). As shown on Figure 103, after five iterations Δm reaches a converged value of $\Delta m = 15.3$ g. Even if this value is far below the block added in the experiments, this

increase in mass is sufficient to highly improve the accuracy of the numerical model. For example, the error on the first natural frequency is reduced from 36% to 16% (Table 16). This improvement is also testified by the change in frequency response function, Figure 104.

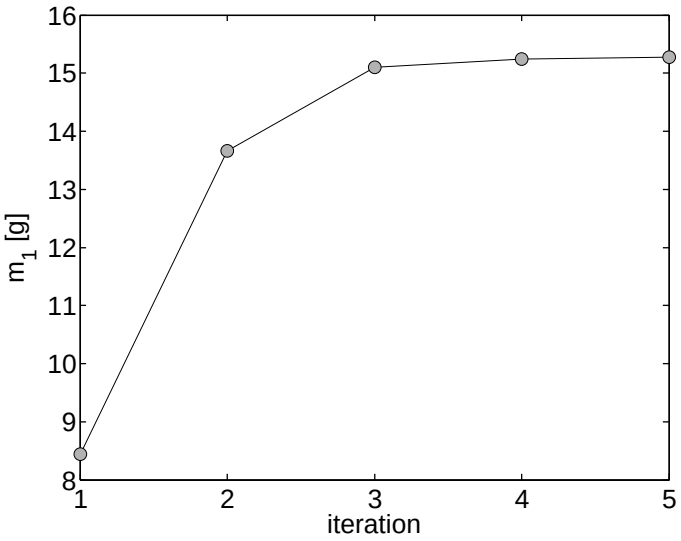

Figure 103: Identified mass during iterations. One mass added. Identification of a concentrated masses at node 21.

Table 16: Comparison between numerical and experimental bending natural frequencies of the blade for a single added mass, with percentage difference with respect to the experimental case, Mass 1.

			Final	
	Tests	Initial	Mass on node 21	Mass on all nodes
$f_1[Hz]$	26.2 -	35.6 -35.6%	30.5 -16.0%	30.5 -16.0%
$f_2[Hz]$	197.5 -	223.3 -13.1%	197.7 -0.1%	203.6 -3.1%
$f_3[Hz]$	568.7 -	624.9 -9.9%	565.3 0.6%	574.9 -1.1%
$f_4[Hz]$	1060.0 -	1223.6 -15.4%	1124.7 -6.1%	1128.3 -6.0%

The response of the system at control points is accurately identified by the PCA, Figure 105, as well as in other locations along the span. The error between the

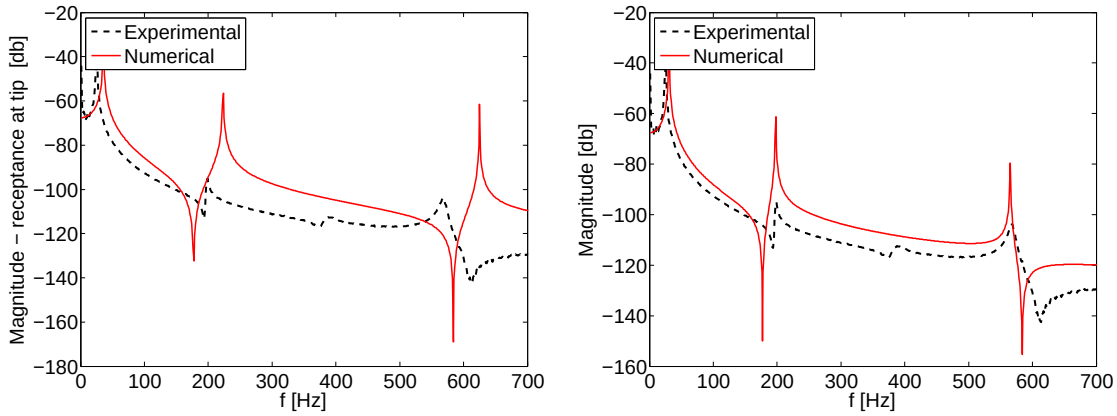

(a) Initial (b) Final

Figure 104: Comparison between measured and numerical magnitude of frequency response function before and after the application of PCA. One mass added. Identification of a concentrated masses at node 21. FEM (-). Experimental (--).

experimental and numerical maximum displacement is reduced from 12% to 4%.

The instantaneous deformed shape of the system is depicted in Figure 106, and demonstrates the ability of the algorithm to map the complete displacement field of the system.

The removal of the assumption of a known location of the added mass results in similar improvements to the accuracy of the numerical map of the response. Also in this case, the total added mass converges in five iterations to a value of $\Delta m = 24.3$ g (Figure 107).

The algorithm identifies a distribution of concentrated masses along the span (Figure 109), that corresponds to the form of the first mode shape, as depicted in Figure 108.

This is due to the fact that the PCA considers a one mode expansion of the dynamic response of the system. This mass distribution does not physically correspond to the added concentrated mass near the tip of the beam, but provides a remarkable improvement to the natural frequencies of the system and to the map of the dynamic response. The error on the first natural frequency, for example, is reduced from 35% at the beginning of the analysis to 16% after the convergence of PCA (Table 16).

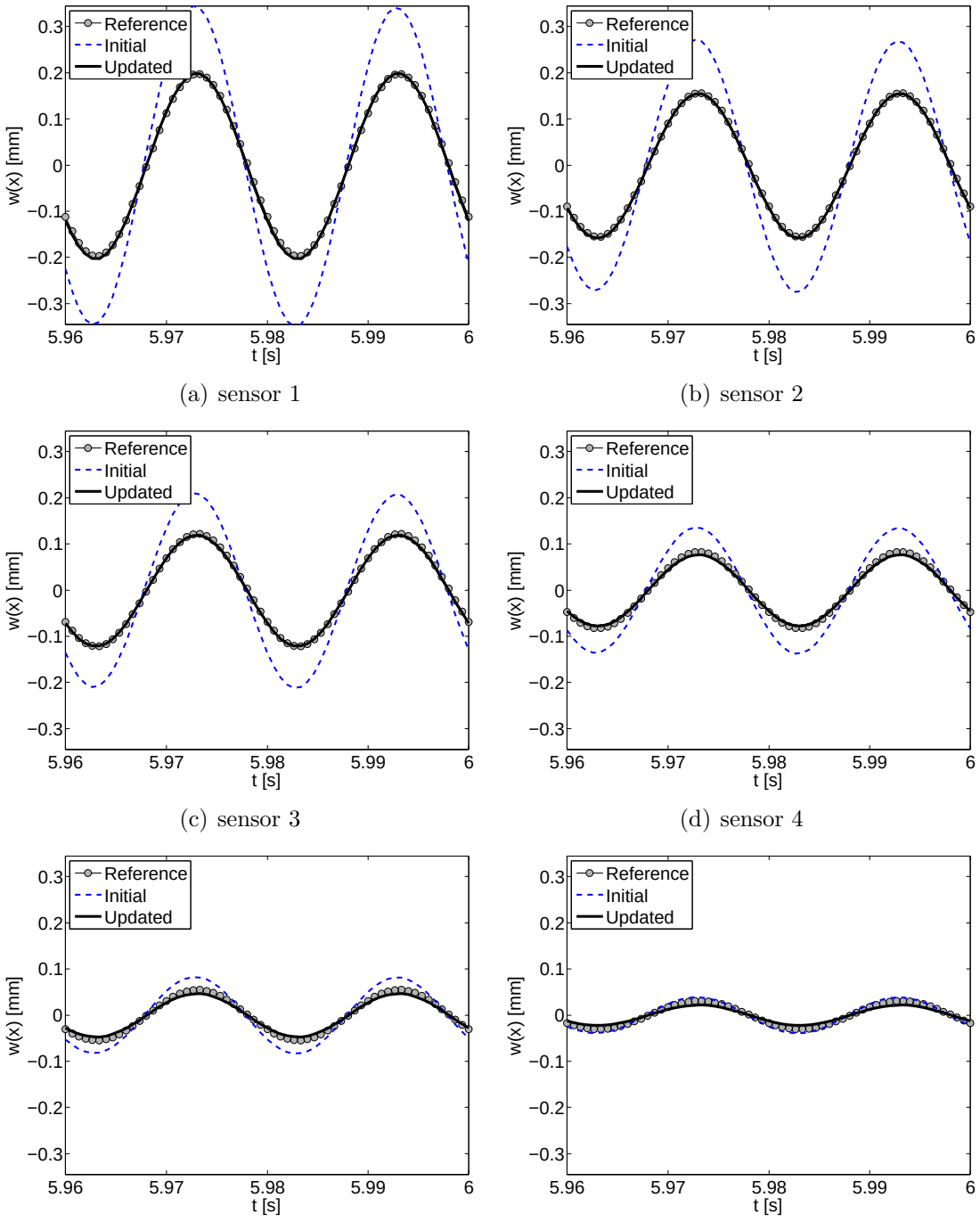

(a) sensor 1 (b) sensor 2

(c) sensor 3 (d) sensor 4

(e) sensor 5 (f) sensor 6

Figure 105: Response of the system at control points. One mass added. Identification of a concentrated mass at node 21. Measured (o). Initial FEM (--). Final FEM (-).

Moreover, the error on the maximum displacement of the system is reduced from 12% to 3% (Figure 110).

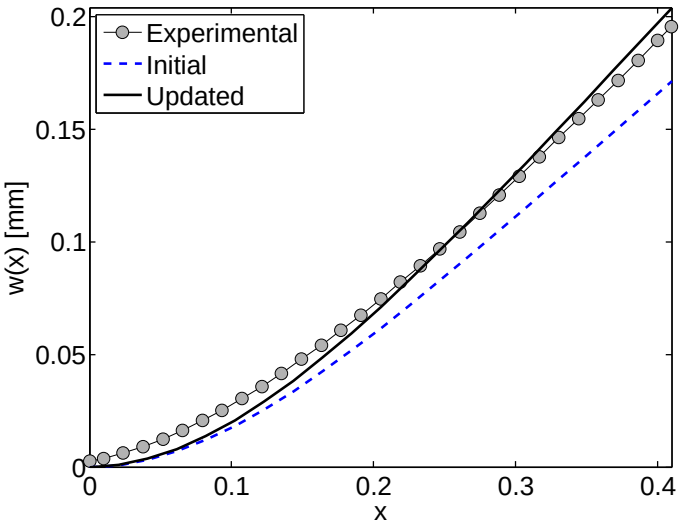

Figure 106: Comparison between measured and numerical instantaneous deformed shape before and after the application of PCA. One mass added. Identification of a concentrated mass at node 21. Measured (o). Initial FEM (--). Final FEM (-).

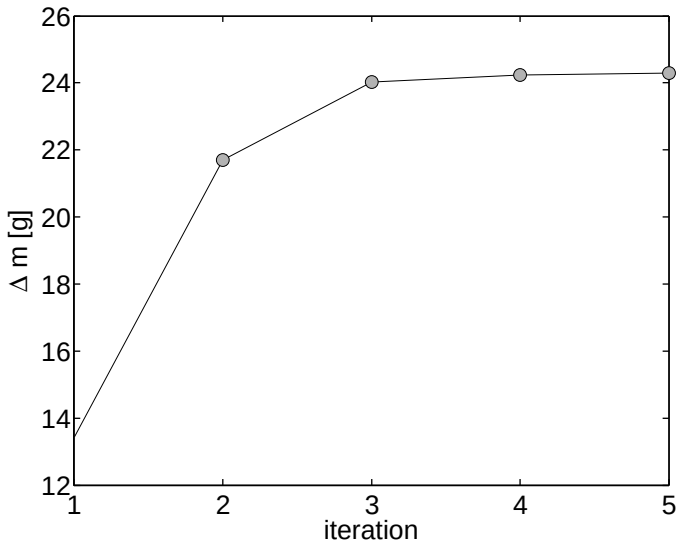

Figure 107: Identified mass during iterations. One mass added. Identification of 21 nodal masses.

Not only the algorithm provides improved representation of the dynamic response at control points, but also improves the map of the response along the span of the beam, Figure 110.

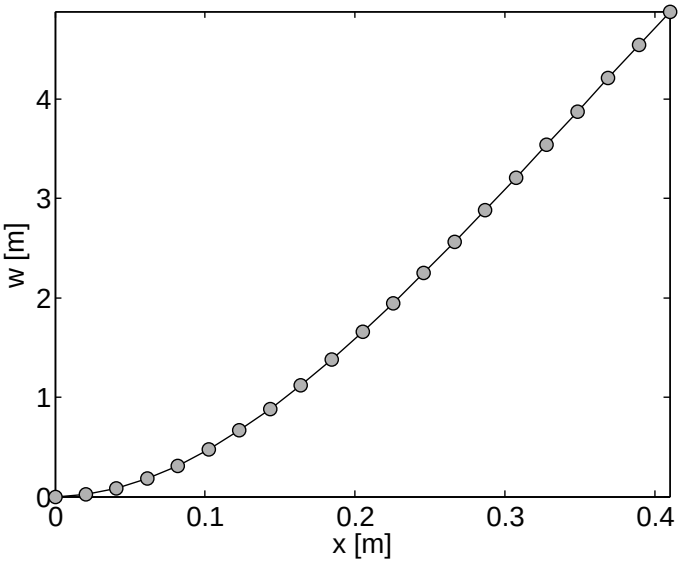

Figure 108: First beam mode. One mass added. Identification of 21 nodal masses.

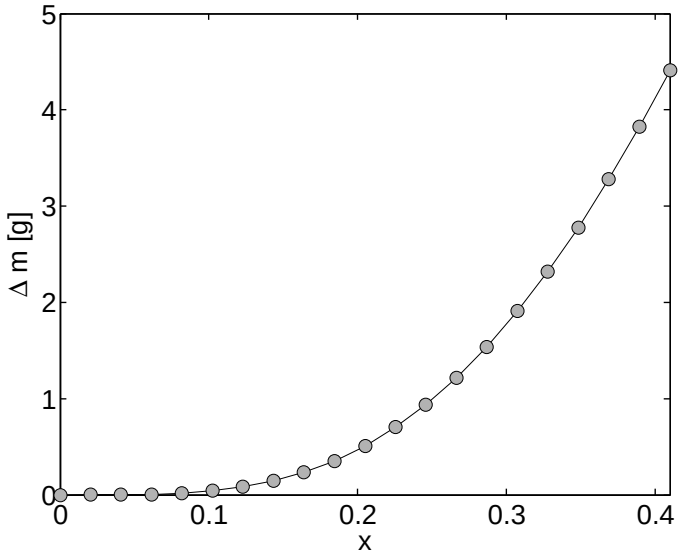

Figure 109: Distribution of identified masses along the span. One mass added. Identification of 21 nodal masses.

5.5 Identification of multiple masses

In this section the performance of the PCA is discussed considering the addition of multiple masses to the uniform beam. Two cases are described: first the PCA identifies the presence of two masses, then of three. The algorithm converges in five iterations also in these cases (convergence is achieved when incremental changes of

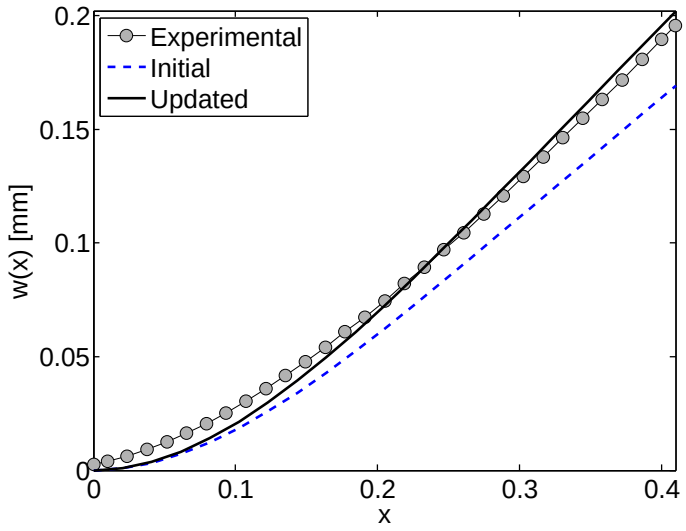

Figure 110: Comparison between measured and numerical instantaneous deformed shape before and after the application of PCA. One mass added. Identification of 21 nodal masses. Measured (o). Initial FEM (--). Final FEM (-).

the total mass are lower than 5×10^{-5}). A set of six control points is considered in the identification (Table 15). Moreover, the PCA considers a single mode in the approximation of the response.

It is now analyzed the two masses case, both assuming that the location of the blocks are known (concentrated masses at nodes [13,21]) and considering the location as unknown. In the first case, the algorithm identifies a total change in mass of $\Delta m = 20.3$ g, Figure 111, in the second of $\Delta m = 27.8$ g, Figure 111. Both cases result in an improvement of the error on the first natural frequency from about 50% to 26%, Table 17. The higher frequencies are more accurately approximated by the PCA, with errors with respect to experimental measurements reduced from about 20% to less than 5% for a known location for the masses and about 10% for unknown locations. Overall, the identication highly improves the accuracy of the numerical predictions, even if, as in the previous case, the accuracy for the case of a known location of the masses is higher than when their location is unknown. The error on the maximum displacement at control points is reduced from about 11% before the

application of the PCA to less than 5% for both cases, as shown by the instantaneous deformed shape, Figure 112.

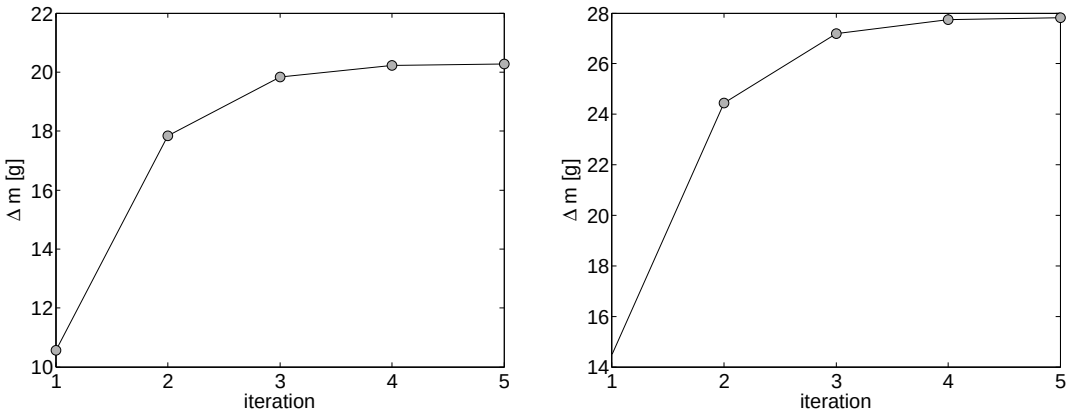

(a) mass on nodes (13, 21)

(b) mass on all nodes

Figure 111: Identified mass during iterations. Two masses added.

Table 17: Comparison between numerical and experimental bending natural frequencies of the blade for two added mass, with percentage difference with respect to the experimental case, Mass 2.

			Final	
	Tests	Initial	Mass on nodes [13, 21]	Mass on all nodes
$f_1[Hz]$	23.7 -	35.6 -49.9%	29.9 -25.9%	29.9 -25.9%
$f_2[Hz]$	183.7 -	223.3 -21.5%	192.9 -5.0%	201.3 -10.3%
$f_3[Hz]$	552.5 -	624.9 -13.1%	559.9 -1.3%	569.4 -3.1%
$f_4[Hz]$	1051.2 -	1223.6 -16.4%	1110.5 -5.6%	1117.7 -6.3%

Analogous results are obtained in the analyses of the three masses case, both assuming that the location of the blocks are known (concentrated masses at nodes [13, 16, 21]) and considering the location as unknown. In the first case, the algorithm identifies a total change in mass of $\Delta m = 26.4$ g, Figure 113, in the second of $\Delta m = 31.46$ g, Figure 113. As in the two masses case, the error on the first natural frequency is reduced from about 50% to 24%, Table 18, while the errors on higher

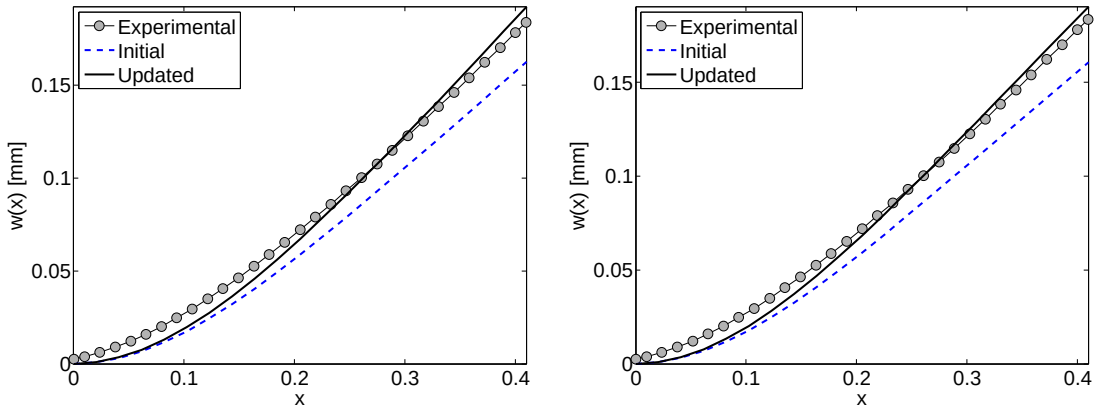

(a) mass on nodes (13, 21) (b) mass on all nodes

Figure 112: Comparison between measured and numerical instantaneous deformed shape before and after the application of PCA. Two masses added. Measured (o). Initial FEM (--). Final FEM (-).

frequencies are reduced from about 20% to less than 5% for a known location for the masses and less than 10% for unknown locations. The error on the maximum displacement at control points is reduced from about 11% before the application of the PCA to less than 5% for both cases, as shown by the instantaneous deformed shape, Figure 114.

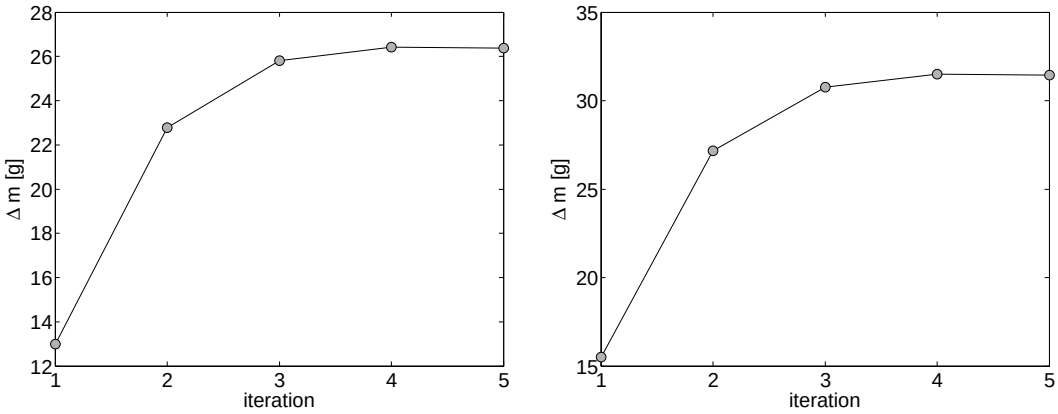

(a) mass on nodes (13, 16, 21) (b) mass on all nodes

Figure 113: Identified mass during iterations. Three masses added.

Table 18: Comparison between numerical and experimental bending natural frequencies of the blade for two added mass, with percentage difference with respect to the experimental case, Mass 3.

			Final	
	Tests	Initial	Mass on nodes [13, 16, 21]	Mass on all nodes
$f_1[Hz]$	23.7 -	35.6 -49.9%	29.4 -23.7%	29.4 -23.7%
$f_2[Hz]$	182.5 -	223.3 -22.4%	192.4 -5.4%	199.2 -9.1%
$f_3[Hz]$	540.0 -	624.9 -15.7%	544.3 -0.8%	563.9 -4.4%
$f_4[Hz]$	1031.0 -	1223.6 -18.7%	1091.3 -5.8%	1107.2 -7.3%

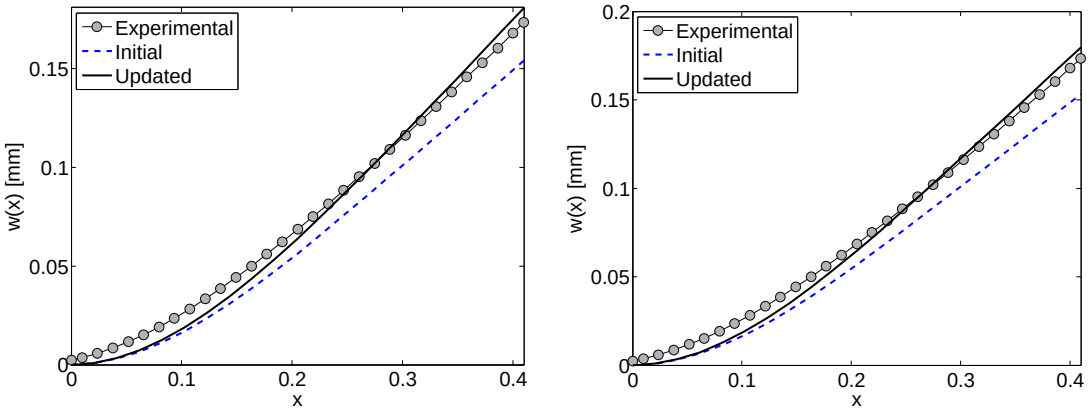

(a) mass on nodes (13, 16, 21)

(b) mass on all nodes

Figure 114: Comparison between measured and numerical instantaneous deformed shape before and after the application of PCA. Three masses added. Measured (o). Initial FEM (--). Final FEM (-).

5.6 Influence of number of sensors

The number of control points used by the PCA is an important parameter in the definition of the method. This section investigates how this parameter influences the accuracy of the updated response of the system in the analysis of the experimental set-up characterized by three added concentrated masses. This case is chosen as representative to demonstrate the abilities of the proposed approach. The number

of sensors is therefore reduced from five to one, in case of unknown locations of the added masses (update of 21 nodal masses). The sensors that are eliminated in the analysis are the ones closer to the root, as indicated by Table 15.

The change in mass identified by the algorithm varies from $\Delta m = 31.6$ g (five sensors) to $\Delta m = 32.6$ g (one sensor) with a variation of the identified total mass of less than 4% in the five cases. This small difference does not significantly affect the natural frequencies identified in the five cases (Table 19), that primarely vary less than 1%. All the analyses converge in less than six iterations. The change in number of sensors slightly affects the identified displacement, as shown in Figure 115, with errors on the maximum displacement ranging from 1% (one sensor) to 4% (five sensors).

Table 19: Comparison between numerical and experimental bending natural frequencies of the blade for three added masses, with percentage difference with respect to the experimental case, when the number of control points is reduced. Identification of 21 concentrated masses.

	5 sensors	4 sensors	3 sensors	2 sensors	1 sensor
$f_1[Hz]$	29.4 -23.7%	29.3 -23.4%	29.3 -23.4%	29.2 -22.9%	29.2 -22.9%
$f_2[Hz]$	199.1 -9.1%	198.9 -9.0%	198.7 -8.9%	198.5 -8.8%	198.4 -8.7%
$f_3[Hz]$	563.7 -4.4%	563.2 -4.3%	562.7 -4.2%	562.2 -4.1%	561.9 -4.0%
$f_4[Hz]$	1106.8 -7.3%	1106.0 -7.3%	1105.0 -7.2%	1104.1 -7.1%	1103.5 -7.0%

5.7 Conclusions

In summary, the PCA improves the accuracy of the numerical dynamic behavior (modal and physical response) with experimental results, both when the location of the change in system properties is known and when it is not. However, the PCA does not identify the real change in properties that occurs in the system, first of all because of the approximation of the response through a limited number of modes and sensors,

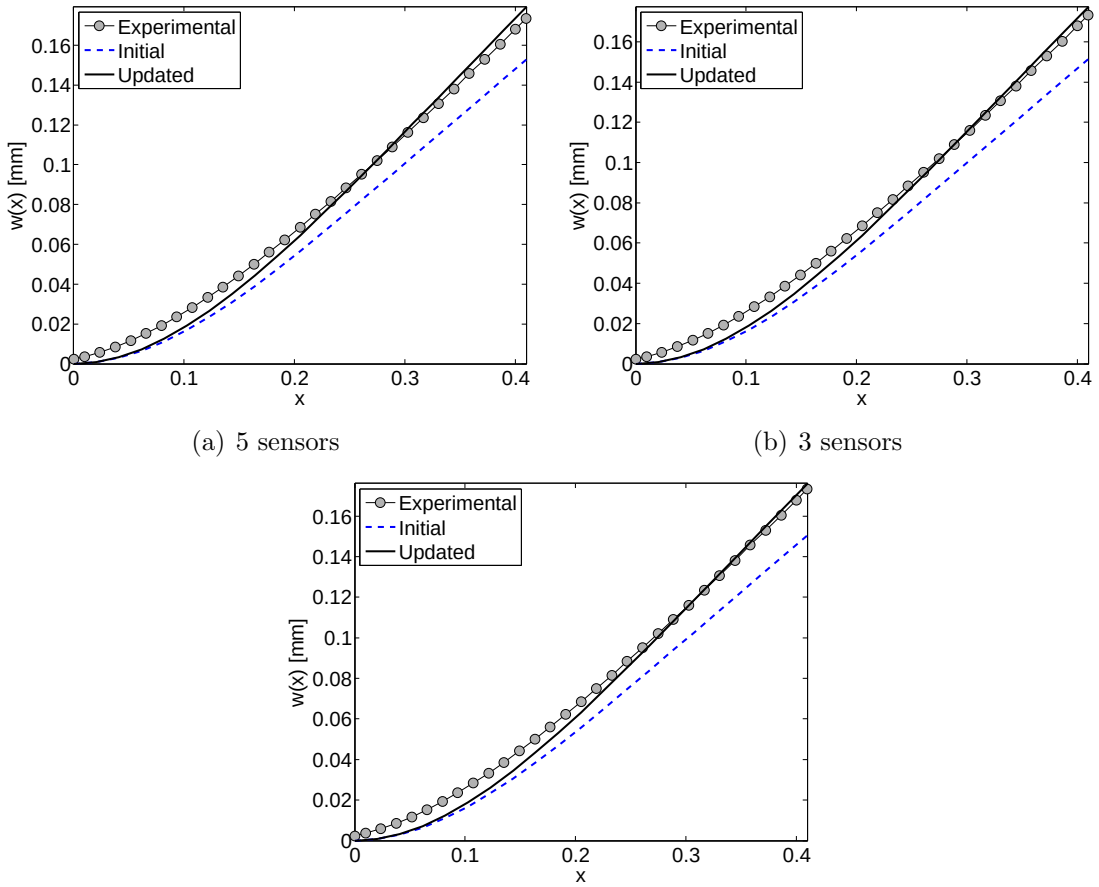

(a) 5 sensors

(b) 3 sensors

(c) 1 sensor

Figure 115: Comparison between measured and numerical instantaneous deformed shape before and after the application of PCA when the number of control points is increased. Three masses added. Identification of 21 concentrated masses. Measured (o). Initial FEM (--). Final FEM (-).

and second due to the presence of other inaccuracies in the model, for example in the modeling of external loads, and of noise in the experimental system [16, 15]. In the analyzed cases, the PCA showed the ability to recognize differential changes in the properties. For example, the Δm identified in the Mass 1 case is lower than the other two cases for a similar mass distribution. This capability is fundamental in giving indications of increasing differences in the properties of the system, as for example in cases of mass accumulation on blades due to debris or ice.

The discussion of the thesis shows that the tracking of experimental dynamic response through a numerical model of the system is possible and accurate. Two

different algorithms are described that improve the response either by iteratively correcting the external loads (LCA) or the dynamic properties in terms of mass and stiffness distributions (PCA). Examples in one- and two-dimensions are presented to support the discussion.

The next chapter analyzes the convergence properties of LCA and PCA by means of analytical examples. The discussion underlines the similarity of these approaches to classical Newton methods, and exploits the well-known convergence properties of this class of algorithms to describe the behavior of LCA and PCA.

CHAPTER VI

CONVERGENCE ANALYSIS OF LOAD AND PROPERTY CONFLUENCE ALGORITHMS

6.1 Overview

The Confluence Algorithm can be more generally formulated as an iterative Newton method for the solution of nonlinear algebraic problems. This is particularly useful in order to analyze the convergence properties of the approach. In fact, the CA aims to correct a general non-linear model by applying linearized corrections obtained through the approximation of the Jacobian matrix of the iterative method. This approximation may reduce the convergence rate of the algorithm, and the computational cost of the method.

This chapter initally presents a brief review of the general formulation of Newton method and its convergence properties. Then, the Load Confluence Algorithm is formulated as a Newton approach, and its convergence properties are investigated based on analytical examples. At the end of this chapter, the convergence of the Property Confluence Algorithm is analyzed, and some examples presented to support the discussion.

6.2 Newton method

A nonlinear system of equations can be expressed as:

$$\boldsymbol{F}(\boldsymbol{p}) = \boldsymbol{0} \tag{35}$$

where $\boldsymbol{F}(\boldsymbol{p})$ is a general non-linear vectorial functional of the parameters $\boldsymbol{p}$. The functional is linearized with a two-term linear expansion:

$$\boldsymbol{F}(\boldsymbol{p}) \approx \boldsymbol{F}(\boldsymbol{p}_k) + \boldsymbol{F}'(\boldsymbol{p}_k)\,(\boldsymbol{p}_{k+1} - \boldsymbol{p}_k) \approx \boldsymbol{0} \tag{36}$$

for which the roots need to be computed. At each $k-th$ iteration, the roots of the system are defined as $\boldsymbol{p}_k$. The term $\boldsymbol{F}'(\boldsymbol{p}_k)$ represents the Jacobian of the nonlinear system at the $k-th$ iteration. Newton method is formulated in terms of the transition equation from the iterate k to a new iterate $k+1$ as:

$$\boldsymbol{p}_{k+1} = \boldsymbol{p}_k - \boldsymbol{F}'(\boldsymbol{p}_k)^{-1}\boldsymbol{F}(\boldsymbol{p}_k) \tag{37}$$

For the method to converge to a solution, the following assumptions (defined as *standard assumptions*) must hold [51]. It is required that an exact solution $\boldsymbol{p}^*$ exists, and that the Jacobian is Lipschitz continuous[1] and non-singular. In addition, the initial iterate needs to be sufficiently close to the exact solution.

Under the standard assumptions, the Newton iteration converges quadratically to the exact solution $\boldsymbol{p}^*$ as:

$$||\tilde{\boldsymbol{e}}_{k+1}|| \leq K||\tilde{\boldsymbol{e}}_k||^2 \tag{38}$$

with $\tilde{\boldsymbol{e}}_k = \boldsymbol{p}_k - \boldsymbol{p}^*$ error at each iteration[2] and constant K.

In a classical Newton method, if the Jacobian $\boldsymbol{F}'(\boldsymbol{p})$ is well-conditioned, the size of the relative non-linear residual $\dfrac{||\boldsymbol{F}(\boldsymbol{p})||}{||\boldsymbol{F}(\boldsymbol{p}_0)||}$ is a good indicator of the size of the error at that iteration [51]

$$\frac{||\tilde{\boldsymbol{e}}||}{4\,||\tilde{\boldsymbol{e}}_0||\kappa(\boldsymbol{F}'(\boldsymbol{p}))} \leq \frac{||\boldsymbol{F}(\boldsymbol{p})||}{||\boldsymbol{F}(\boldsymbol{p}_0)||} \leq \frac{4\,||\tilde{\boldsymbol{e}}||\kappa(\boldsymbol{F}'(\boldsymbol{p}))}{||\tilde{\boldsymbol{e}}_0||} \tag{39}$$

where $\tilde{\boldsymbol{e}}_0$ is the initial error, $\boldsymbol{F}(\boldsymbol{p}_0)$ the initial value of the function to be minimized, and $\kappa(\boldsymbol{F}'(\boldsymbol{p}))$ the condition value of the Jacobian. Near the solution, the size of the step $||\boldsymbol{p}_{k+1} - \boldsymbol{p}_k||$ and the size of the error $||\tilde{\boldsymbol{e}}_{k+1}||$ are essentially the same, therefore the increment in the identified parameters is a good indicator of the convergence of the approach.

[1]Lipschitz continuity is a strong form of uniform continuity for functions. Definition: let $\Omega \subset R^N$ and let $G : \Omega \longrightarrow R^M$. G is Lipschitz continuous on Ω with Lipschitz constant γ if $||G(x) - G(y)|| \leq ||x - y||$ for all $x, y \in \Omega$.

[2]Let the standard assumptions hold. Then there are $K > 0$ and $\delta > 0$ such that if $x_c \in \mathcal{B}(\delta)$ the Newton iterate satisfies $||e_{k+1}|| \leq K||e_c||^2$. $\mathcal{B}(\delta)$ denotes the ball of radius δ about x^*: $\mathcal{B}(\delta) = \{x \,|\, ||e|| < \delta\}$ with $e = x - x^*$.

Suppose now that both the function $\boldsymbol{F}(\boldsymbol{p}_k)$ and its Jacobian $\boldsymbol{F}'(\boldsymbol{p}_k)$ are inaccurately computed, and $\boldsymbol{F}+\boldsymbol{\mathcal{E}}$ and $\boldsymbol{F}'+\boldsymbol{\Delta}$ are used instead of $\boldsymbol{F}$ and $\boldsymbol{F}'$ in the iteration. The terms $\boldsymbol{\mathcal{E}}$ and $\boldsymbol{\Delta}$ represent the error on the function and on the Jacobian and generally depend on the parameters to be identified. The transition equation is now expressed as:

$$\boldsymbol{p}_{k+1} = \boldsymbol{p}_k - \left[\boldsymbol{F}'(\boldsymbol{p}_k) + \boldsymbol{\Delta}(\boldsymbol{p}_k)\right]^{-1} \left(\boldsymbol{F}(\boldsymbol{p}_k) + \boldsymbol{\mathcal{E}}(\boldsymbol{p}_k)\right) \tag{40}$$

If the error on the Jacobian $\boldsymbol{\Delta}$ is sufficiently small, the error at each iterate is reduced to:

$$||\tilde{\boldsymbol{e}}_{k+1}|| \leq K\left[||\tilde{\boldsymbol{e}}_k||^2 + ||\boldsymbol{\Delta}(\boldsymbol{p}_k)||||\tilde{\boldsymbol{e}}_k|| + ||\boldsymbol{\mathcal{E}}(\boldsymbol{p}_k)||\right] \tag{41}$$

and the solution of the problem is an $\mathcal{O}(||\mathcal{E}||)$ approximation of the exact solution. In this case, the iteration reaches a stagnation point at which the non-linear residual cannot be further reduced by the iterations. The effect of an inexact evaluation of the Jacobian primarily consists in reduced convergence rates, but can be convenient because it may not require its computation at each iteration.

Several methods can be formulated considering different approximations of the Jacobian matrix, as for example the chord method and its variations. If the Jacobian is approximated as $\boldsymbol{A} \approx \boldsymbol{F}'(\boldsymbol{p})$, then:

$$||\boldsymbol{\Delta}(\boldsymbol{p}_k)|| = ||\boldsymbol{A} - \boldsymbol{F}'(\boldsymbol{p}_k)|| \leq ||\boldsymbol{A} - \boldsymbol{F}'(\boldsymbol{p}^*)|| + ||\boldsymbol{F}'(\boldsymbol{p}^*) - \boldsymbol{F}'(\boldsymbol{p}_k)|| \tag{42}$$

and it can be proven that the error of the iterative procedure becomes:

$$||\tilde{\boldsymbol{e}}_{k+1}|| \leq K_A\left(||\boldsymbol{e}_0|| + ||\boldsymbol{A} - \boldsymbol{E}'(\boldsymbol{p}^*)||\right)||\tilde{\boldsymbol{e}}_k|| \tag{43}$$

These general findings that characterize Newton method can be specified more precisely for the Confluence Algorithm as described in the next sections.

6.3 Definition of the CA as a Newton method

In order to express the Confluence Algorithm as a Newton iterative approach, the objective function of the analysis is defined as the difference between the numerical

and the measured response of the dynamic system at specific locations in terms of their Fourier coefficients:

$$\boldsymbol{F}(\boldsymbol{p}) = \boldsymbol{e}(\boldsymbol{p}) - \boldsymbol{e}_{ref} = \boldsymbol{0} \tag{44}$$

with $\boldsymbol{p}$ general parameters on which the numerical response depends. The response of the system can be expressed by tracking displacements, deformations, accelerations, velocities of the system without loss of generality. The objective of the analysis is to find the parameters $\boldsymbol{p}$ that best represent the experimental results in terms of forced dynamic response. Changes in numerical parameters $\boldsymbol{p}$ do not affect the reference response $\boldsymbol{e}_{ref}$. In case of the Load Confluence Algorithm, parameters $\boldsymbol{p}$ are related to the applied loads, while in case of the Property Confluence Algorithm they are related to the physical properties of the system.

In order to find the transition equation that characterizes the CA, an harmonic behavior of the system is assumed so that each quantity is approximated with a Fourier series. The response of the numerical system is:

$$\boldsymbol{e}(\boldsymbol{p}, t) = \boldsymbol{e}_0(\boldsymbol{p}) + \sum_{j=1}^{M} \left[\boldsymbol{e}_c(\boldsymbol{p}) \cos j\Omega t + \boldsymbol{e}_s(\boldsymbol{p}) \sin j\Omega t\right] \tag{45}$$

and the reference response is:

$$\boldsymbol{e}_{ref}(t) = \boldsymbol{e}_{0_{ref}} + \sum_{j=1}^{M} \left[\boldsymbol{e}_{c_{ref}} \cos j\Omega t + \boldsymbol{e}_{s_{ref}} \sin j\Omega t\right] \tag{46}$$

where the subscript 0 denotes the constant coefficient, c the cosine and s the sine terms. Each term of the objective function $\boldsymbol{F}(\boldsymbol{p})$ consists in the Fourier coefficients of the difference between the numerical and reference response, $\boldsymbol{F}(\boldsymbol{p}) = [\boldsymbol{e}_0(\boldsymbol{p}) - \boldsymbol{e}_{0_{ref}}, \boldsymbol{e}_c(\boldsymbol{p}) - \boldsymbol{e}_{c_{ref}}, \boldsymbol{e}_s(\boldsymbol{p}) - \boldsymbol{e}_{s_{ref}}]^T$.

The Jacobian can be approximated by using a simpler dynamic model of the system. In this case, second-order linearized and undamped equations of motion approximate the behavior of the system to approximate the Jacobian.

The following sections describe the details of the Newton formulation for the LCA and PCA, and present some analytical examples.

6.4 Load Confluence Algorithm as a Newton iterative method

The Load Confluence Algorithm assumes that the parameters to be updated $\boldsymbol{p}$ represent the applied loads.

Since the behaviour of the system is assumed to be periodic, the externally applied loads can be represented in terms of Fourier series:

$$\boldsymbol{f} = \boldsymbol{f}_0 + \sum_{j=1}^{M} [\boldsymbol{f}_{c\,j} \cos j\Omega t + \boldsymbol{f}_{s\,j} \sin j\Omega t] \tag{47}$$

and the parameters to be updated are defined in terms of its coefficients, $\boldsymbol{p} = [\boldsymbol{f}_0, \boldsymbol{f}_c, \boldsymbol{f}_s]^T$. At each iteration, the external loads $\boldsymbol{f}_k$ are updated based on its harmonic approximation. This assumption is adequate because only the steady-state behavior of the system is of interest.

In order to approximate the Jacobian matrix of the system, the dynamic system is approximated as a linear, undamped multi-degree-of-freedom system, whose equations of motion are expressed as:

$$\boldsymbol{M}\ddot{\boldsymbol{u}} + \boldsymbol{K}\boldsymbol{u} = \boldsymbol{f} \tag{48}$$

In order to express the response of the system, and define its derivative with respect to the parameters $\boldsymbol{p}$ of the problem, the behaviour of the system is projected to the modal domain, and the response $\boldsymbol{e}(x)$ is approximated with a finite modal expansion:

$$\boldsymbol{e}(\boldsymbol{p}) \approx \boldsymbol{B}\boldsymbol{q}(\boldsymbol{p}) \tag{49}$$

where $\boldsymbol{B}$ is the incomplete modal matrix that relates the dynamic response at the sensor location to the generalized modal coordinates, and $\boldsymbol{q}(\boldsymbol{p})$ the generalized modal coordinates. In the LCA, $\boldsymbol{p}$ corresponds to the load of the system, and the $\boldsymbol{B}$ is not affected by their changes. The Jacobian matrix is therefore expressed as:

$$\boldsymbol{F}'(\boldsymbol{p}) = \frac{\partial \boldsymbol{e}}{\partial \boldsymbol{p}} \approx \boldsymbol{B}\frac{\partial \boldsymbol{q}}{\partial \boldsymbol{p}} = \boldsymbol{B}\left[\frac{\partial \boldsymbol{q}}{\partial \boldsymbol{f}_0}, \frac{\partial \boldsymbol{q}}{\partial \boldsymbol{f}_c}, \frac{\partial \boldsymbol{q}}{\partial \boldsymbol{f}_s}\right]^T \tag{50}$$

The first order derivative of the generalized coordinates $\dfrac{\partial \boldsymbol{q}}{\partial \boldsymbol{p}}$ is defined from the linearized, undamped equations of motion solved through a modal expansion and the harmonic balance of the equation of motions, so that:

$$\begin{aligned} \boldsymbol{q}_0 &= \text{diag}\left(\frac{1}{\boldsymbol{\omega}^2}\right)\boldsymbol{P}^T\boldsymbol{f}_0 \\ \boldsymbol{q}_{c/s\,j} &= \text{diag}\left(\frac{1}{\boldsymbol{\omega}^2 - j^2\Omega^2}\right)\boldsymbol{P}^T\boldsymbol{f}_{c/s\,j} \end{aligned} \tag{51}$$

with:

$$\boldsymbol{q} = \boldsymbol{q}_0 + \sum_{j=1}^{N_h}\left[\boldsymbol{q}_{c\,j}\cos j\Omega t + \boldsymbol{q}_{s\,j}\sin j\Omega t\right] \tag{52}$$

The derivatives of the generalized coordinates are therefore defined as:

$$\begin{aligned} \frac{\partial \boldsymbol{q}_0}{\partial \boldsymbol{f}_0} &= \text{diag}\left(\frac{1}{\boldsymbol{\omega}^2}\right)\boldsymbol{P}^T \\ \frac{\partial \boldsymbol{q}_{c/s\,j}}{\partial \boldsymbol{f}_{c/s\,j}} &= \text{diag}\left(\frac{1}{\boldsymbol{\omega}^2 - j^2\Omega^2}\right)\boldsymbol{P}^T \end{aligned} \tag{53}$$

from which the derivatives of the physical response, that coincide with the terms of the Jacobian matrix, can be reconstructed through matrix $\boldsymbol{B}$ as:

$$\begin{aligned} \boldsymbol{F}'_0 &= \frac{\partial \boldsymbol{e}_0}{\partial \boldsymbol{f}_0} = \boldsymbol{B}\text{diag}\left(\frac{1}{\boldsymbol{\omega}^2}\right)\boldsymbol{P}^T \\ \boldsymbol{F}'_{c/s\,j} &= \frac{\partial \boldsymbol{e}_{c/s\,j}}{\partial \boldsymbol{f}_{c/s\,j}} = \boldsymbol{B}\text{diag}\left(\frac{1}{\boldsymbol{\omega}^2 - j^2\Omega^2}\right)\boldsymbol{P}^T \end{aligned} \tag{54}$$

and, by introducing the unit-mass normalization[3], its inverse is:

$$\begin{aligned} \left[\boldsymbol{F}'_0\right]^{-1} &= \boldsymbol{M}\boldsymbol{P}\text{diag}\left(\boldsymbol{\omega}^2\right)\boldsymbol{B}^+ \\ \left[\boldsymbol{F}'_{c/s\,j}\right]^{-1} &= \boldsymbol{M}\boldsymbol{P}\text{diag}\left(\frac{1}{\boldsymbol{\omega}^2 - j^2\Omega^2}\right)\boldsymbol{B}^+ \end{aligned} \tag{55}$$

where $\boldsymbol{B}^+$ is the pseudo-inverse of the incomplete modal matrix.

The transition equation for the LCA is therefore expressed as:

$$\begin{aligned} \boldsymbol{f}_{k+1_0} &= \boldsymbol{f}_{k_0} - \boldsymbol{M}\boldsymbol{P}\text{diag}\left(\boldsymbol{\omega}^2\right)\boldsymbol{B}^+\left(\boldsymbol{e}_{k_0} - \boldsymbol{e}_{ref_0}\right) \\ \boldsymbol{f}_{k+1_{c/s\,j}} &= \boldsymbol{f}_{k_{c/s\,j}} - \boldsymbol{M}\boldsymbol{P}\text{diag}\left(\frac{1}{\boldsymbol{\omega}^2 - j^2\Omega^2}\right)\boldsymbol{B}^+\left(\boldsymbol{e}_{k_{c/s\,j}} - \boldsymbol{e}_{ref_{c/s,j}}\right) \end{aligned} \tag{56}$$

[3]From the definition of matrix inverse of a general matrix $\boldsymbol{A}$: $\boldsymbol{A}\boldsymbol{A}^{-1} = I$, thereforefor this case $\boldsymbol{P}^T\boldsymbol{P}^{-T} = \boldsymbol{P}^T\boldsymbol{M}\boldsymbol{P}^{-1} = I$

As defined in section 6.2, the convergence of the algorithm depends on the approximation of the Jacobian matrix and of the numerical response. The parameters that influence this approximation are the proximity of the chosen approximate model (linear and undamped) to the real model in which the response $\boldsymbol{e}(\boldsymbol{p})$ is evaluated, the number of modes included in the modal approximation and the accuracy of the representation of the model to the reference system.

Consider that the numerical response is evaluated through an incomplete modal representation, so that an error in the evaluation of the function is introduced. Due to the error in the function, the method converges to a stagnation point in which the reference response is not properly represented. By increasing the number of modes, the size of the error in the approximation of the function decreases, and the method converges to the exact solution. The incompleteness of the modal approximation also introduces an error in the evaluation of the Jacobian that in this case does not affect the convergence of the algorithm. The truncation error in fact does not depend on the load parameters, and is canceled in the computation of the derivatives.

In the previous section, Eq. (39) shows that the convergence of the method depends on the well-conditioned nature of the Jacobian matrix. For the LCA Jacobian to be well-conditioned, the matrix:

$$\boldsymbol{B}\text{diag}\left(\frac{1}{\boldsymbol{\omega}^2 - j^2\Omega^2}\right)\boldsymbol{P}^T \tag{57}$$

needs to be well-conditioned. The condition number of $\boldsymbol{B}$ plays a fundamental role in the total condition number of the matrix, and is related to the choice of number of sensors, of modes and to the location of the sensors. To have a well-conditioned $\boldsymbol{B}$, the control points must be sufficient to reconstruct the chosen modes. Therefore, when the number of modes to be reconstructed increases, the number of control points needs to increase as well. They also need to be properly spaced so that all included modes can be observed. Another important term is given by the difference between the natural frequencies and the driving frequency, and implies that an excitation at a resonant

frequency may affect the convergence of the method. The term $\boldsymbol{P}^T$ does not affect the condition number of Eq. (57), because in case of real $\boldsymbol{P}$, the condition number of its transpose is always unity, according to the following relations: $\boldsymbol{P}^T\boldsymbol{M}\boldsymbol{P} = \boldsymbol{I}$, $\kappa(\boldsymbol{P}^T) = ||\boldsymbol{P}^T||||\boldsymbol{P}^{-T}|| = ||\boldsymbol{P}^T||||\boldsymbol{M}\boldsymbol{P}|| = 1$.

6.5 Analysis of LCA with analytical examples

The convergence properties of the LCA are illustrated by way of an analytical example describing a uniform beam in bending hinged at both ends. At the beginning of the discussion, the Jacobian is expressed through a linear, undamped approximation of the equations of motion. Then, the convergence properties of the algorithm for different approximations of the response and for different definitions of the reference system are analyzed.

Similarly to the discussion in the previous sections, the Jacobian matrix of the system is approximated with linear, undamped equations of motion, that take the form:

$$EIw^{IV}(x,t) + m\,\ddot{w}(x,t) = f(x,t) \tag{58}$$

where $w(x,t)$ is the transverse displacement of the beam, $f(x,t)$ the applied load, EI its bending stiffness and m the mass per unit length. A simply supported beam is characterized by null tip displacement and bending moment, that corresponds to the boundary conditions:

$$w(0,t) = 0 \qquad w(L,t) = 0 \qquad EIw^{II}(0,t) = 0 \qquad EIw^{II}(L,t) = 0 \tag{59}$$

with L denoting the length of the beam. It is assumed that its motion starts from a rest position, so that the initial conditions on the displacement and velocity are:

$$w(x,0) = 0 \qquad \dot{w}(x,0) = 0 \tag{60}$$

This equation of motion is solved conveniently by modal analysis. Assume a modal

decomposition for the displacement of the beam:

$$w(x,t) = \sum_{r=1}^{\infty} P_r(x)\, q_r(t) \tag{61}$$

The modal equation of motion results in:

$$\ddot{q}_r(t) + \omega_r^2 q_r(t) = \lambda_r(t) \qquad r = 1, 2, ..., \infty \tag{62}$$

with generalized modal loads $\lambda_r(t) = \int_0^L P_r(x) f(x,t) dx$. When the analysis is limited to periodic loads, $\lambda_r(t) = \lambda_{r_0} + \sum_{j=1}^{M} [\lambda_{r_c} \cos j\Omega t + \lambda_{r_s} \sin j\Omega t]$, with Ω fundamental excitation frequency, the solution of Eq. (62) can be computed by harmonic balance. A further approximation on the spatial nature of the applied periodic loads is now introduced to allow for an analytical solution. The load $f(x,t)$ are assumed to be approximated by a Fourier series also along the span of the beam using the eigenvectors of the system as spatial function, so that:

$$f(x,t) = \sum_{g=1}^{N_f} P_g(x)\lambda_g(t) = \sum_{g=1}^{N_f} P_g(x) \left\{ \lambda_{g_0} + \sum_{j=1}^{M} \left[\lambda_{g_{c_j}} \cos j\Omega t + \lambda_{g_{s_j}} \sin j\Omega t \right] \right\} \tag{63}$$

In this example, the LCA identifies the parameters λ_g, where N_f is the number of modes required to describe the considered load distribution.

The natural frequencies and modes shapes of a simply supported beam have the form

$$P_r(x) = \sqrt{\frac{2}{mL}} \sin\left(\frac{r\pi x}{L}\right), \qquad \omega_r = (r\pi)^2 \sqrt{\frac{EI}{mL^4}} \tag{64}$$

In order to express the Jacobian matrix, the objective function to be minimized has to be expressed in terms of the load parameters for this specific case, and it is defined as the difference between the approximated and the reference response at the control points in terms of their Fourier coefficients. It is now assumed for sake of clarity that the reference response is known in term of displacements at the control point. It will be assumed in the following that $e(x_i) = w(x_i)$. Each element of the

approximated function $\boldsymbol{F}$ of Newton method from which $\boldsymbol{F}'$ is evaluated is therefore:

$$\begin{aligned} F_{i_0} &= w_0(x_i) - w_{ref_0}(x_i) = \sum_{r=1}^{\infty} P_r(x_i) q_{r_0} - w_{ref_{i_0}} \\ F_{i_{c/s_j}} &= w_{c/s_j}(x_i) - w_{ref_{c/s_j}}(x_i) = \sum_{r=1}^{\infty} P_r(x_i) q_{r_{c/s_j}} - w_{ref_{i_{c/s_j}}} \end{aligned} \tag{65}$$

The approximated Newton function for the definition of the Jacobian is expressed by:

$$\begin{aligned} F_{i_0}(\lambda_{g_0}) &= \sum_{r=1}^{\infty} \frac{P_r(x_i)}{\omega_r^2} \int_0^L P_r(x) \sum_{r=1}^{N_f} P_g(x) \lambda_{g_0} dx - w_{ref_{i_0}} \\ &= \sum_{r=1}^{\infty} \frac{P_r(x_i)}{m\omega_r^2} \lambda_{r_0} - w_{ref_{i_0}} \\ F_{i_{c/s_j}}(\lambda_{g_{c/s}}) &= \sum_{r=1}^{\infty} \frac{P_r(x_i)}{\omega_r^2 - j^2\,\Omega^2} \int_0^L P_r(x) \sum_{r=1}^{N_f} P_g(x) \lambda_{g_{c/s_j}} dx - w_{ref_{i_{c/s_j}}} \\ &= \sum_{r=1}^{\infty} \frac{P_r(x_i)}{m(\omega_r^2 - j^2\,\Omega^2)} \lambda_{r_{c/s_j}} - w_{ref_{i_{c/s_j}}} \end{aligned} \tag{66}$$

The Jacobian at every control point follows from these relations as:

$$\begin{aligned} F'_{i_0} &= \frac{\partial e_0(x_i)}{\partial \lambda_l} = \frac{P_l(x_i)}{m\omega_l^2} \\ F'_{i_{c/s_j}} &= \frac{\partial e_{c/s_j}(x_i)}{\partial \lambda_l} = \frac{P_l(x_i)}{m(\omega_l^2 - j^2\,\Omega^2)} \end{aligned} \tag{67}$$

This approximation of the Jacobian of the system will be used in the next sections to assess the properties of LCA for linear, non-linear, and damped reference systems. For sake of clarity, two constant coefficients are introduced, $\gamma_g = \dfrac{1}{m\omega_g^2}$ and $\bar{\alpha}_g = \dfrac{1}{m(\omega_g^2 - j^2\Omega^2)}$ so that:

$$\begin{aligned} F'_{i_0} &= P_l(x_i)\gamma_l \\ F'_{i_{c/s_j}} &= P_l(x_i)\bar{\alpha}_l \end{aligned} \tag{68}$$

The general Newton iteration for each term is therefore expressed as

$$\begin{aligned} f_{g_{0_{k+1}}} &= f_{g_{0_k}} - \left[P_g(x_i)\gamma_g\right]^{-1} \left(w_{0_k} - w_{ref_0}\right) \\ f_{g_{sj_{k+1}}} &= f_{g_{s_{j_k}}} - \left[P_g(x_i)\bar{\alpha}_g\right]^{-1} \left(w_{sj_k} - w_{ref_s}\right) \\ f_{g_{cj_{k+1}}} &= f_{g_{c_{j_k}}} - \left[P_g(x_i)\bar{\alpha}_g\right]^{-1} \left(w_{cj_k} - w_{ref_c}\right) \end{aligned} \tag{69}$$

The introduction of forms of damping in the definition of the Jacobian woul not introduce complexity or increase the computational cost of the Load Confluence Algorithm. However, it is generally not possible to reasonably estimate the damping of a real system from experimental measurements, and/or to accurately represent it with a numerical model. It is therefore preferable to identify any contribution to the damping forces as general external loads. This approximation results in the fact that the updated loads are not accurately achieved by a single-step correction and multiple iterations are necessary to obtain a converged $f(x,t)$.

6.5.1 Analysis of a linear system

Consider in this case that both the numerical and reference systems are linear, and their motion can be approximated as:

$$EIw^{IV}(x,t) + m\,\ddot{w}(x,t) + c\,\dot{w}(x,t) = f(x,t) \tag{70}$$

with boundary oonditions:

$$w(0,t) = 0 \qquad w(L,t) = 0 \qquad EIw^{II}(0,t) = 0 \qquad EIw^{II}(L,t) = 0 \tag{71}$$

and initial conditions:

$$w(x,0) = 0 \qquad \dot{w}(x,0) = 0 \tag{72}$$

where L is the length of beam, EI its bending stiffness, m the mass per unit length and c the damping. The cases of an undamped system, as well as proportionally and non-proportionally damped systems are here investigated.

The response of a general linear system can be approximated according to Ritz method by considering an approximation of the response through approximate shape functions that correspond to the modes of the linear, undamped system, defined as $P_r(x)$, and unknown time functions $q_r(t)$:

$$w(x,t) = \sum_{r=1}^{N_e} P_r(x) q_r(t) \tag{73}$$

In case of a periodic behavious of the structure, functions $q_r(t)$ in terms of their Fourier coefficients can be obtained through harmonic balance of the equations of motion of the system. Given a generic periodic load

$$f(x,t) = \sum_{g=1}^{N_f} P_g(x) \left[\lambda_{g_0} + \sum_{j=1}^{M} \left[\lambda_{g_{c\,j}} \cos j\Omega t + \lambda_{g_{s\,j}} \sin j\Omega t \right] \right] \tag{74}$$

the time-dependent functions are expressed as:

$$q_r(t) = q_{r_0} + \sum_{j=1}^{M} \left[q_{r_{c\,j}} \cos j\Omega t + q_{r_{s\,j}} \sin j\Omega t \right] \tag{75}$$

In a proportionally damped system, each sine and cosine coefficient of each harmonic term of $q_r(t)$ depend both on the sine and cosine coefficients of the corresponding $j-th$ harmonics of the external loads through the relations:

$$\begin{aligned} q_{r_0} &= \gamma_r \lambda_{r_0} \\ q_{r_{s_j}} &= \beta_{r_j} \lambda_{r_{c_j}} + \alpha_{r_j} \lambda_{r_{s_j}} \\ q_{r_{c_j}} &= \alpha_{r_j} \lambda_{g_{c_j}} - \beta_{r_j} \lambda_{g_{s_j}} \end{aligned} \tag{76}$$

with:

$$\begin{aligned} \gamma_r &= \frac{1}{\omega_r^2} \\ \alpha_{r_j} &= \frac{\omega_g^2 - j^2\Omega^2}{(\omega_g^2 - j^2\Omega^2)^2 + \left(\frac{j\Omega c}{m}\right)^2} \\ \beta_{g_j} &= \frac{\frac{j\Omega c}{m}}{(\omega_g^2 - j^2\Omega^2)^2 + \left(\frac{j\Omega c}{m}\right)^2} \end{aligned} \tag{77}$$

Eq. (76) is valid for a proportionally damped, linear, second order system. The response of the system $w(x,t)$ at location i is therefore expressed as:

$$\begin{aligned} w(x_i,t) \;\; = \sum_{r=1}^{N_e} P_r(x_i) \Big\{ \gamma_r \lambda_{r_0} + \Big[\beta_{r_j} \lambda_{r_{c_j}} + \alpha_{r_j} \lambda_{r_{s_j}} \Big] \sin j\Omega t + \\ + \Big[\alpha_{r_j} \lambda_{g_{c_j}} - \beta_{r_j} \lambda_{g_{s_j}} \Big] \cos j\Omega t \Big\} \end{aligned} \tag{78}$$

The terms λ_{r_0}, $\lambda_{r_{s\,j}}$, $\lambda_{r_{c\,j}}$ are the unknown parameters that need to be found by LCA. Relations (78) can now be specified for different values of the damping coefficient, so that its effects can be evaluated.

Case 1: perfect undamped linear model and linear loads This first case considers a linear and undamped initial numerical system (to define $\boldsymbol{e}_k$) as well as a linear and undamped reference system (to define $\boldsymbol{e}_{ref}$). The physical properties of the reference system are exactly represented by the numerical model.

The reference response is described by the equation of motion and boundary and initial conditions:

$$\begin{aligned} &EIw^{IV}_{ref}(x,t) + m\,\ddot{w}_{ref}(x,t) = f_{ref}(x,t) \\ &w_{ref}(0,t) = 0 \quad w_{ref}(L,t) = 0 \quad EIw^{II}_{ref}(0,t) = 0 \quad EIw^{II}_{ref}(L,t) = 0 \\ &w_{ref}(x,0) = 0 \quad \dot{w}_{ref}(x,0) = 0 \end{aligned} \tag{79}$$

and the initial numerical response by:

$$\begin{aligned} &EIw^{IV}(x,t) + m\,\ddot{w}(x,t) = f(x,t) \\ &w(0,t) = 0 \quad w(L,t) = 0 \quad EIw^{II}(0,t) = 0 \quad EIw^{II}(L,t) = 0 \\ &w(x,0) = 0 \quad \dot{w}(x,0) = 0 \end{aligned} \tag{80}$$

The reference response is therefore:

$$w_{ref}(x_i,t) = \sum_{r=1}^{N_e} P_r(x_i) \left\{ \gamma_r \lambda_{ref_{r_0}} + \bar{\alpha}_{r_j} \lambda_{ref_{r_{s_j}}} \sin j\Omega t + \bar{\alpha}_{r_j} \lambda_{ref_{r_{c_j}}} \cos j\Omega t \right\} \tag{81}$$

and the numerical response at the $k-th$ iteration:

$$w_k(x_i,t) = \sum_{r=1}^{N_e} P_r(x_i) \left\{ \gamma_r \lambda_{r_{0_k}} + \bar{\alpha}_{r_j} \lambda_{r_{s_{j_k}}} \sin j\Omega t + \bar{\alpha}_{r_j} \lambda_{r_{c_{j_k}}} \cos j\Omega t \right\} \tag{82}$$

The transition equations result:

$$\begin{aligned} \lambda_{g0_{k+1}} &= \lambda_{g0_k} - \left[P_g(x_i)\gamma_g\right]^{-1} P_g(x_i)\gamma_g \left(\lambda_{g0_k} - \lambda_{g0_{ref}}\right) \\ \lambda_{g_{c/s_{k+1}}} &= \lambda_{g_{c/s_k}} - \left[P_g(x_i)\bar{\alpha}_g\right]^{-1} P_g(x_i)\bar{\alpha}_g \left(\lambda_{g_{c/s_k}} - \lambda_{g_{c/s_{ref}}}\right) \end{aligned} \tag{83}$$

that are simplified to:

$$\begin{aligned} \lambda_{g0_{k+1}} &= \lambda_{g0_{ref}} \\ \lambda_{g_{c/s_{k+1}}} &= \lambda_{g_{c/s_{ref}}} \end{aligned} \tag{84}$$

The reference loads are therefore exactly found in one iteration.

The simplicity of this example allows analysing the contribution of the number of modes and sensors introduced in the Newton iteration. It is in fact possible to update only a few of the modal coefficients of the loads and still obtain an accurate representation of the response of the system. Consider for example a uniform load distribution $f(x) = 1$ N/m, that can be approximated by Fourier serie as:

$$f(x) = \sum_{g=1}^{N_f} \sin\left(\frac{g\pi x}{L}\right) f_g \tag{85}$$

with $N_f = \infty$ and $f_g = \frac{2}{\pi g}\left[1 - \cos(g\pi)\right]$.

If the response of the system is approximated with a number of modes m lower than the number of terms in the load expansion N_f, the truncation error in the evaluation of the function is:

$$\mathcal{E}(\lambda)_i = \sum_{r=m+1}^{N_f} \frac{P_r(x_i)}{m(\omega_r^2 - j^2\,\Omega^2)}\lambda_r \tag{86}$$

while the Jacobian is exactly defined. The modal content of the constant load $f(x,t)$ is shown in Figure 116. It is clear that the higher is the mode, the lower is its contribution to the external loads. Figure 117 illustrates the cumulative sum of the modal contribution of the loads with respect to its maximum value. This plot illustrates that to achieve an accurate description of the loads, with truncation errors of less than 10%, about 40 modes are necessary, and consequently of control points, which is in general not possible because it would result in a very complex experimental set-up. On the contrary, a good representation of the response of the system can be achieved with a much lower number of modes. The modal content of the response is in fact dominated by mode 3, as shown in Figure 118. The cumulative sum of the modal contribution to the response, Figure 119, confirms this observation. Therefore, the response of the system can be accurately predicted with only few modes.

Consider the case in which the response of the system is represented by a number of modes that is higher than the number of modes used by LCA, i.e. $m < N_f$. An

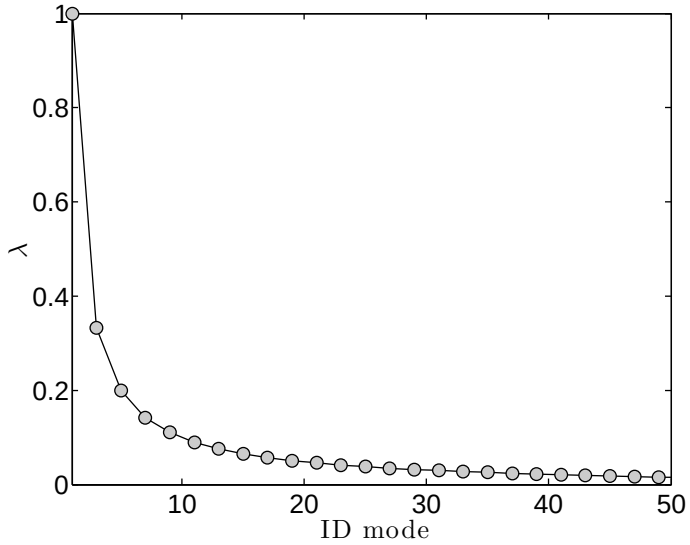

Figure 116: Variation of the modal content of the external loads λ_r for a uniform distributed load.

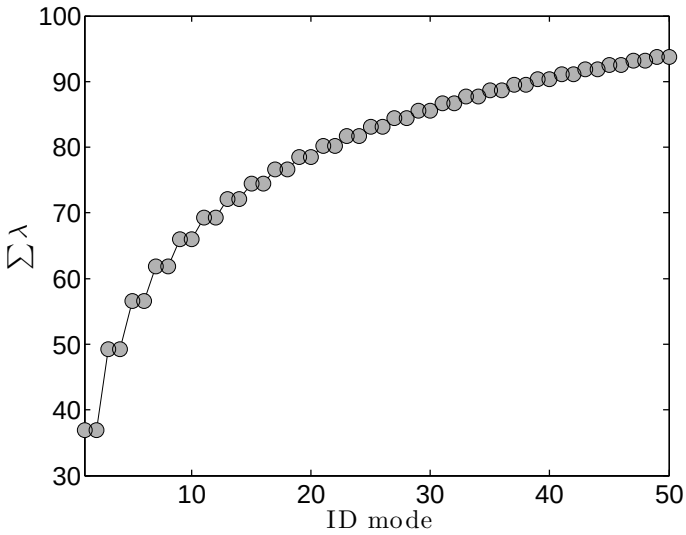

Figure 117: Cumulative sum of modal loads λ for a uniform distributed load as the number of modes increases.

error in the evaluation of the function $\mathcal{E}$ is introduced, and LCA will not reach a zero value, but the method converges to a stagnation point.

In order to identify the response, a sufficient number of control points needs to be selected so that the components $w(x_i, t)$ are an effective representation of the

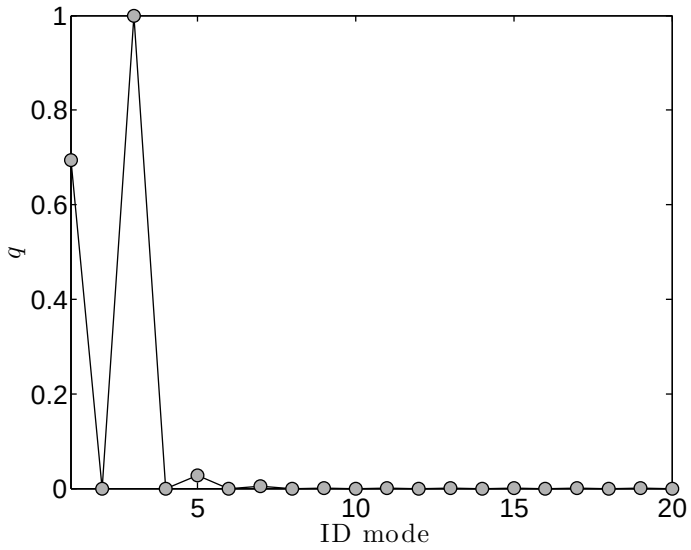

Figure 118: Variation of a representative Fourier coefficient of the modal response for a uniform distributed load.

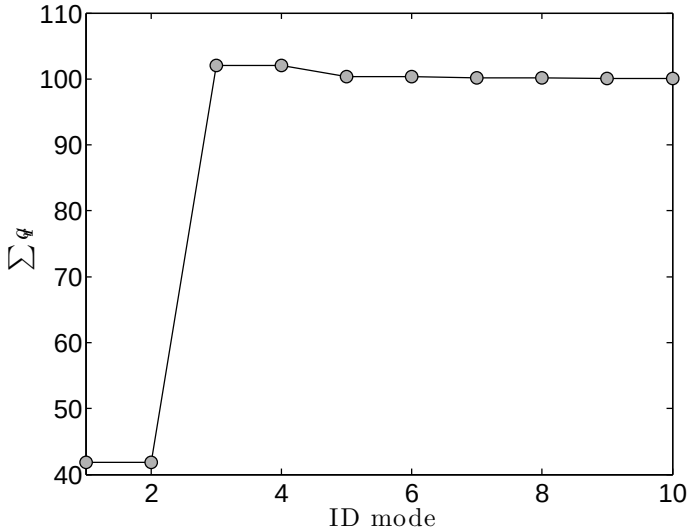

Figure 119: Cumulative sum of modal response q for a uniform distributed load as the number of modes increases

response of the beam. Moreover, in order to have a non-singular Jacobian, the number of response points must be larger than the number of load parameters, so that the Jacobian can be inverted. This constraint implies that matrix $\boldsymbol{B}$, with elements $B_{gi} = P_g(x_i)$, is well-conditioned. The influence of the difference in frequencies on the

Jacobian matrix is noticed only at exactly a resonant frequency. If the excitation frequency is just a few percentage off a resonance frequency, no harm to the convergence is noticed.

Case 2: influence of unmodeled damping This second case considers a linear and undamped initial numerical system (to define e_k) and a linear and proportionally damped reference system (to define e_{ref}). The damping in the reference system is not represented in the model, and its effects are recovered as additional contributions to the external loads. The mass and stiffness of the reference system are exactly represented by the numerical model. The reference response is described by equations of motion and boundary and initial conditions:

$$\begin{aligned} &EIw^{IV}_{ref}(x,t) + c\,\dot{w}_{ref}(x,t) + m\,\ddot{w}_{ref}(x,t) = f_{ref}(x,t) \\ &w_{ref}(0,t) = 0 \quad w_{ref}(L,t) = 0 \quad EIw^{II}_{ref}(0,t) = 0 \quad EIw^{II}_{ref}(L,t) = 0 \\ &w_{ref}(x,0) = 0 \quad \dot{w}_{ref}(x,0) = 0 \end{aligned} \tag{87}$$

and the numerical response is represented by:

$$\begin{aligned} &EIw^{IV}(x,t) + m\,\ddot{w}(x,t) = f(x,t) \\ &w(0,t) = 0 \quad w(L,t) = 0 \quad EIw^{II}(0,t) = 0 \quad EIw^{II}(L,t) = 0 \\ &w(x,0) = 0 \quad \dot{w}(x,0) = 0 \end{aligned} \tag{88}$$

The reference response is therefore:

$$\begin{aligned} w_{ref}(x_i,t) \;= &\sum_{r=1}^{N_e} P_r(x_i) \left[\gamma_r \lambda_{ref_{r_0}} + \left(\beta_{r_j}\lambda_{ref_{r_{c_j}}} + \alpha_{r_j}\lambda_{ref_{r_{s_j}}}\right)\sin j\Omega t + \right. \\ &\left. + \left(\alpha_{r_j}\lambda_{ref_{r_{c_j}}} - \beta_{r_j}\lambda_{ref_{r_{s_j}}}\right)\cos j\Omega t\right] \end{aligned} \tag{89}$$

and the numerical response at the $k-th$ iteration:

$$w_k(x_i,t) = \sum_{r=1}^{N_e} P_r(x_i)\left(\gamma_r\lambda_{r_{0_k}} + \bar{\alpha}_{r_j}\lambda_{r_{s_{j_k}}}\sin j\Omega t + \bar{\alpha}_{r_j}\lambda_{r_{c_{j_k}}}\cos j\Omega t\right) \tag{90}$$

In this case both the sine and cosine components of the loads contribute to the each sine and cosine coefficient of the response because of the presence of damping.

However, the contribution of each mode is uncoupled. The transition equations for the sine and cosine coefficients (the constant coefficient is not affected by the presence of damping) are:

$$\begin{aligned}
\lambda_{g0_{k+1}} &= \lambda_{g0_k} - [P_g(x_i)\gamma_g]^{-1} P_g(x_i)\gamma_g \left(\lambda_{g0_k} - \lambda_{g0_{ref}}\right) \\
\lambda_{g_{s_{k+1}}} &= \lambda_{g_{s_k}} - \lambda_{g_{s_k}} + [P_g(x_i)\bar{\alpha}_g]^{-1} P_g(x_i) \left(\alpha_{s_j}\lambda_{g_{s_{ref}}} + \beta_{g_j}\lambda_{g_{c_{ref}}}\right) \\
\lambda_{g_{c_{k+1}}} &= \lambda_{g_{c_k}} - \lambda_{g_{c_k}} + [P_g(x_i)\bar{\alpha}_g]^{-1} P_g(x_i) \left(\alpha_{g_j}\lambda_{g_{c_{ref}}} - \beta_{g_j}\lambda_{g_{s_{ref}}}\right)
\end{aligned} \tag{91}$$

that are simplified to:

$$\begin{aligned}
\lambda_{g0_{k+1}} &= \lambda_{g0_{ref}} \\
\lambda_{g_{s_{k+1}}} &= \frac{\alpha_{g_j}}{\bar{\alpha}_g}\lambda_{g_{s_{ref}}} + \frac{\beta_{g_j}}{\bar{\alpha}_g}\lambda_{g_{c_{ref}}} \\
\lambda_{g_{c_{k+1}}} &= \frac{\alpha_{g_j}}{\bar{\alpha}_g}\lambda_{g_{s_{ref}}} - \frac{\beta_{g_j}}{\bar{\alpha}_g}\lambda_{g_{c_{ref}}}
\end{aligned} \tag{92}$$

Note that the updating equation of the zero coefficient does not change with respect to the previous case, because not dependent on damping. Also in this case, iterations of the approach are not necessary and LCA identifies a new set of loads so that the numerical response accurately represents the reference response. However, Eq. (92) shows that the identified loads do not exactly represent the real applied loads of the reference system, but contain contributions of the damping terms. LCA identifies an equivalent representation of the external loads that takes into account the differences in damping loads.

If the reference system is characterized by non-proportional damping, such as a concentrated damper along the span of the beam, each modal coefficient of the load is coupled with the other modal coefficients. However, since no damping is considered in the numerical model, no iterations would be necessary to find an equivalent form of the reference load.

Case 3: influence of modeled damping Consider now a numerical model in which damping is included in the system. In this case, iterations become necessary to converge to a solution. The reference response is described by the equation of motion

and boundary and initial conditions:

$$
\begin{aligned}
&EIw^{IV}_{ref}(x,t) + c\,\dot{w}_{ref}(x,t) + m\,\ddot{w}_{ref}(x,t) = f_{ref}(x,t) \\
&w_{ref}(0,t) = 0 \quad w_{ref}(L,t) = 0 \quad EIw^{II}_{ref}(0,t) = 0 \quad EIw^{II}_{ref}(L,t) = 0 \\
&w_{ref}(x,0) = 0 \quad \dot{w}_{ref}(x,0) = 0
\end{aligned}
\tag{93}
$$

and similarly the numerical response is represented by:

$$
\begin{aligned}
&EIw^{IV}(x,t) + c\,\dot{w}(x,t) + m\,\ddot{w}(x,t) = f(x,t) \\
&w(0,t) = 0 \quad w(L,t) = 0 \quad EIw^{II}(0,t) = 0 \quad EIw^{II}(L,t) = 0 \\
&w(x,0) = 0 \quad \dot{w}(x,0) = 0
\end{aligned}
\tag{94}
$$

The reference response is therefore:

$$
\begin{aligned}
w_{ref}(x_i,t) \;= &\sum_{r=1}^{N_e} P_r(x_i) \left[\gamma_r \lambda_{ref_{r_0}} + \left(\beta_{r_j}\lambda_{ref_{r_{c_j}}} + \alpha_{r_j}\lambda_{ref_{r_{s_j}}}\right)\sin j\Omega t + \right. \\
&\left. + \left(\alpha_{r_j}\lambda_{ref_{r_{c_j}}} - \beta_{r_j}\lambda_{ref_{r_{s_j}}}\right)\cos j\Omega t\right]
\end{aligned}
\tag{95}
$$

and the numerical response at the $k-th$ iteration:

$$
\begin{aligned}
w_k(x_i,t) \;= &\sum_{r=1}^{N_e} P_r(x_i) \left[\gamma_r \lambda_{k_{r_0}} + \left(\beta_{r_j}\lambda_{k_{r_{c_j}}} + \alpha_{r_j}\lambda_{k_{r_{s_j}}}\right)\sin j\Omega t + \right. \\
&\left. + \left(\alpha_{r_j}\lambda_{k_{r_{c_j}}} - \beta_{r_j}\lambda_{k_{r_{s_j}}}\right)\cos j\Omega t\right]
\end{aligned}
\tag{96}
$$

The Newton iteration in this case becomes:

$$
\begin{aligned}
\lambda_{g_{0_{k+1}}} &= \lambda_{g_{0_{ref}}} \\
\lambda_{g_{s_{k+1}}} &= \lambda_{g_{s_k}} - \left[\frac{\alpha_{g_j}}{\bar{\alpha}_g}\left(\lambda_{g_{s_k}} - \lambda_{g_{s_{ref}}}\right) + \frac{\beta_{g_j}}{\bar{\alpha}_g}\left(\lambda_{g_{c_k}} - \lambda_{g_{c_{ref}}}\right)\right] \\
\lambda_{g_{c_{k+1}}} &= \lambda_{g_{c_k}} - \left[\frac{\alpha_{g_j}}{\bar{\alpha}_g}\left(\lambda_{g_{s_k}} - \lambda_{g_{s_{ref}}}\right) - \frac{\beta_{g_j}}{\bar{\alpha}_g}\left(\lambda_{g_{c_k}} - \lambda_{g_{c_{ref}}}\right)\right]
\end{aligned}
\tag{97}
$$

that converges in few iterations to the reference loads.

Case 4: influence of unmodeled dynamics (linear elastic foundation) Consider now the presence of a difference in the dynamic properties between the numerical model and the reference system. As an example, the reference system consists in a simply supported beam on a linear elastic foundation characterized by a distributed

spring k_b, that is neglected in the numerical response. Also in this case, an iteration is sufficient to reconstruct an equivalent representation of the external loads of the reference system.

The reference response is described by the equation of motion and boundary and initial conditions:

$$\begin{aligned} &EIw^{IV}_{ref}(x,t) + k_b w_{ref}(x,t) + m\,\ddot{w}_{ref}(x,t) = f_{ref}(x,t) \\ &w_{ref}(0,t) = 0 \quad w_{ref}(L,t) = 0 \quad EIw^{II}_{ref}(0,t) = 0 \quad EIw^{II}_{ref}(L,t) = 0 \\ &w_{ref}(x,0) = 0 \quad \dot{w}_{ref}(x,0) = 0 \end{aligned} \tag{98}$$

where k_b is the stiffness of the elastic support, while the numerical response is represented by:

$$\begin{aligned} &EIw^{IV}(x,t) + m\,\ddot{w}(x,t) = f(x,t) \\ &w(0,t) = 0 \quad w(L,t) = 0 \quad EIw^{II}(0,t) = 0 \quad EIw^{II}(L,t) = 0 \\ &w(x,0) = 0 \quad \dot{w}(x,0) = 0 \end{aligned} \tag{99}$$

The reference response is characterized by the contribution of the elastic foundation:

$$w_{ref}(x_i,t) = \sum_{r=1}^{N_e} \frac{P_r(x_i)}{\omega_r^2}\lambda_{ref_{r_0}} + \frac{P_r(x_i)}{\omega_r^2 + \frac{k_b}{m} - j^2\Omega^2}\left[\lambda_{ref_{r_{s_j}}}\sin j\Omega t + \lambda_{ref_{r_{c_j}}}\cos j\Omega t\right] \tag{100}$$

and the numerical response at the $k-th$ iteration:

$$w_k(x_i,t) = \sum_{r=1}^{N_e} P_r(x_i)\left(\gamma_r\lambda_{r_{0_k}} + \bar{\alpha}_{r_j}\lambda_{r_{s_{j_k}}}\sin j\Omega t + \bar{\alpha}_{r_j}\lambda_{r_{c_{j_k}}}\cos j\Omega t\right) \tag{101}$$

The transition equations become:

$$\begin{aligned} \lambda_{g_{0_{k+1}}} &= \lambda_{g_{0_k}} - \left[\frac{P_g(x_i)}{\omega_g^2}\right]^{-1}\frac{P_g(x_i)}{\omega_g^2}\left(\lambda_{g_{0_k}} - \frac{\omega_g^2}{\omega_g^2 + \frac{k_b}{m}}\lambda_{g_{0_{ref}}}\right) \\ \lambda_{g_{s_{k+1}}} &= \lambda_{g_{s_k}} - \left[\frac{P_g(x_i)}{\omega_g^2 - j^2\Omega^2}\right]^{-1}\frac{P_g(x_i)}{\omega_g^2 - j^2\Omega^2}\left(\lambda_{g_{s_k}} - \frac{\omega_g^2 - j^2\Omega^2}{\omega_g^2 + \frac{k_b}{m} - j^2\Omega^2}\lambda_{g_{s_{ref}}}\right) \\ \lambda_{g_{c_{k+1}}} &= \lambda_{g_{c_k}} - \left[\frac{P_g(x_i)}{\omega_g^2 - j^2\Omega^2}\right]^{-1}\frac{P_g(x_i)}{\omega_g^2 - j^2\Omega^2}\left(\lambda_{g_{c_k}} - \frac{\omega_g^2 - j^2\Omega^2}{\omega_g^2 + \frac{k_b}{m} - j^2\Omega^2}\lambda_{g_{c_{ref}}}\right) \end{aligned} \tag{102}$$

that result into:

$$\begin{aligned}\lambda_{g_{0_{k+1}}} &= \frac{\omega_g^2}{\omega_g^2 + \frac{k_b}{m}}\lambda_{g_{0_{ref}}} \\ \lambda_{g_{s_{k+1}}} &= \frac{\omega_g^2 - j^2\Omega^2}{\omega_g^2 + \frac{k_b}{m} - j^2\Omega^2}\lambda_{g_{s_{ref}}} \\ \lambda_{g_{c_{k+1}}} &= \frac{\omega_g^2 - j^2\Omega^2}{\omega_g^2 + \frac{k_b}{m} - j^2\Omega^2}\lambda_{g_{c_{ref}}}\end{aligned} \tag{103}$$

The reconstructed load coincides with the equivalent loads acting on the reference system:

$$f_{eq}(x,t) = \sum_{g=1}^{N_f} P_g(x)\lambda_g(t) - k_b w(x,t) \tag{104}$$

and:

$$\lambda_{g_{eq}}(t) = \lambda_g(t) - k_b \frac{1}{\omega_g^2 + \frac{k_b}{m} - \Omega^2}\lambda_g(t) = \frac{\omega_g^2 - \Omega^2}{\omega_g^2 + \frac{k_b}{m} - \Omega^2}\lambda_g(t) \tag{105}$$

Case 5: influence of imperfect loads and unmodeled dynamics (difference in mass) Consider now a reference system that differs from the numerical model both in the external loads and in the mass properties. The reference response is described by the equation of motion and boundary and initial conditions:

$$\begin{aligned}&EIw_{ref}^{IV}(x,t) + \hat{m}\,\ddot{w}_{ref}(x,t) = f_{ref}(x,t) \\ &w_{ref}(0,t) = 0 \quad w_{ref}(L,t) = 0 \quad EIw_{ref}^{II}(0,t) = 0 \quad EIw_{ref}^{II}(L,t) = 0 \\ &w_{ref}(x,0) = 0 \quad \dot{w}_{ref}(x,0) = 0\end{aligned} \tag{106}$$

and the numerical response is represented by:

$$\begin{aligned}&EIw^{IV}(x,t) + m\,\ddot{w}(x,t) = f(x,t) \\ &w(0,t) = 0 \quad w(L,t) = 0 \quad EIw^{II}(0,t) = 0 \quad EIw^{II}(L,t) = 0 \\ &w(x,0) = 0 \quad \dot{w}(x,0) = 0\end{aligned} \tag{107}$$

The reference response is therefore:

$$w_{ref}(x_i,t) = \sum_{r=1}^{N_e} \frac{\hat{P}_r(x_i)}{\hat{\omega}_r^2}\lambda_{ref_{r_0}} + \frac{\hat{P}_r(x_i)}{\hat{\omega}_r^2 - j^2\Omega^2}\left[\lambda_{ref_{r_{s_j}}}\sin j\Omega t + \lambda_{ref_{r_{c_j}}}\cos j\Omega t\right] \tag{108}$$

with $\hat{m}$ distributed mass of the reference system, and $\hat{P}_r(x) = \sqrt{\frac{m}{\hat{m}}}P_r(x)$ and $\hat{\omega}_r = \sqrt{\frac{m}{\hat{m}}}\omega_r$ modes and natural frequencies respectively. The numerical response at the

$k-th$ iteration is:

$$w_k(x_i,t) = \sum_{r=1}^{N_e} P_r(x_i) \left\{ \gamma_r \lambda_{r0_k} + \bar{\alpha}_{r_j} \lambda_{r s_{j_k}} \sin j\Omega t + \bar{\alpha}_{r_j} \lambda_{r c_{j_k}} \cos j\Omega t \right\} \tag{109}$$

The transition equations become:

$$\begin{aligned} \lambda_{g0_{k+1}} &= \frac{m}{\hat{m}} \frac{\omega_r^2}{\hat{\omega}_r^2} \lambda_{g0_{ref}} \\ \lambda_{gs_{k+1}} &= \frac{m}{\hat{m}} \frac{\omega_r^2 - \Omega^2}{\hat{\omega}_r^2 - \Omega^2} \lambda_{gs_{ref}} \\ \lambda_{gc_{k+1}} &= \frac{m}{\hat{m}} \frac{\omega_r^2 - \Omega^2}{\hat{\omega}_r^2 - \Omega^2} \lambda_{gc_{ref}} \end{aligned} \tag{110}$$

The identified loads correspond to equivalent loads that take into account both of difference in load model and of physical properties of the system (in mass). LCA converges in one iteration.

It is of interest to be able to separately identify the contributions of the external loads and of the changes in properties, so that the occurrence of structural modifications could also be analyzed. In this case, an additional reference system is necessary that is characterized only by differences in the external loads. The LCA identifies the changes in load from this system, and then extract the changes in properties:

$$\begin{aligned} f_a &= f_{ref} \\ f_b &= \frac{m}{\hat{m}} \frac{\omega_r^2 - \Omega^2}{\hat{\omega}_r^2 - \Omega^2} f_{ref} \end{aligned} \tag{111}$$

Case 6: influence of noise in the reference response When noise affects the reference response, the algorithm reconstructs the best averaged response that represents the real response. As an example, a random noise is added to the reference response, and the results of the identification process are analyzed. In this case, iterations affect the results only in the measure in which damping is present. If no damping is considered, a single-step identification is sufficient. An example of reconstructed response with and without noise is shown in Figure 120.

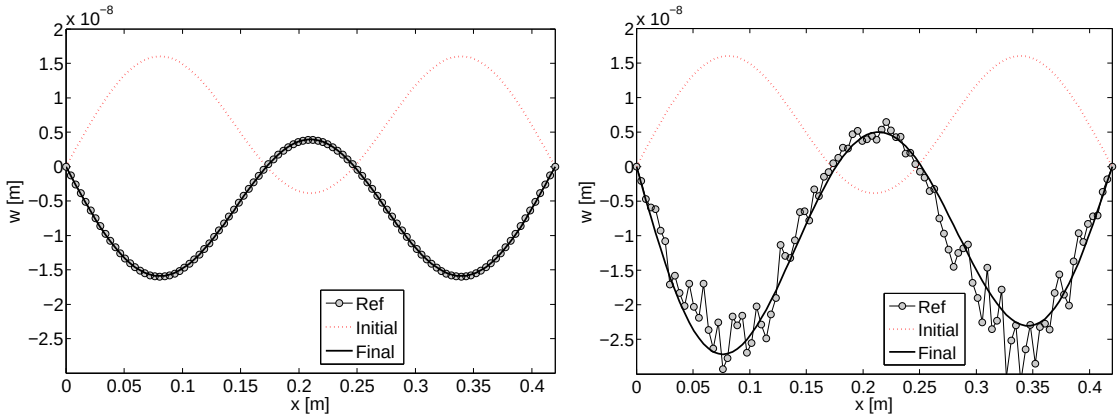

(a) Absence of noise

(b) Noise affects the response

Figure 120: Comparison of updated response with and without noise in the measurements

6.5.2 Analysis of a non-linear system

Consider now the presence of non-linearities both in the numerical model and in the reference system, as for example a cubic distributed spring. The reference response is described by equations of motion:

$$EIw_{ref}^{IV}(x,t) + m\,\ddot{w}_{ref}(x,t) + k_b\,w_{ref}(x,t) + \epsilon\gamma\,w_{ref}^3(x,t) = f(x,t) \tag{112}$$

and boundary and initial conditions

$$\begin{aligned} &w_{ref}(0,t) = 0 \quad w_{ref}(L,t) = 0 \quad EIw_{ref}^{II}(0,t) = 0 \quad EIw_{ref}^{II}(L,t) = 0 \\ &w_{ref}(x,0) = 0 \quad \dot{w}_{ref}(x,0) = 0 \end{aligned} \tag{113}$$

This equation can be solved considering a single mode Galerkin discretization [55]. This discretization procedure has three main drawbacks. First, nonlinear terms that are orthogonal to the eigenmodes are neglected, second, the couplings between modal components are not considered, third, the shape of the motion is fixed a priori. These errors can be neglected in the present discussion, so that simplified close form expressions for the nonlinear terms can be evaluated. The response is approximated as:

$$w(x,t) = \phi_r(x)q_r(t) \tag{114}$$

where $q_r(t)$ are the generalized modal coordinates, and $\phi_r(x)$ the seleted mode r of the linear system:

$$\phi_r(x) = \sqrt{\frac{2}{mL}} \sin \frac{r\pi x}{L} \tag{115}$$

that results in the modal equation:

$$\ddot{q}_r + \omega_r^2 q_r + \epsilon \frac{3}{2m^2L^2} \gamma q_r^3 = \lambda_r(t) \tag{116}$$

with $\lambda_r = \int_0^L f(x)\phi_r(x)dx$ and $\omega_r^2 = \left(r^4\pi^4 \frac{EI}{mL^4} + \frac{k_b}{m}\right)$. Since the main interest of this work deals with the steady state response of a forced system, an harmonic balance approach is considered. Assume that cosinusoidal loads are applied to the system

$$\begin{aligned} \lambda_r(t) &= \Lambda_r \cos \Omega t \\ q_r(t) &= Q_r \cos \Omega t \end{aligned} \tag{117}$$

After rearranging, Eq. (116) becomes:

$$\left(-\Omega^2 + \omega_r^2\right) Q_r \cos \Omega t + \epsilon \frac{3}{2m^2L^2} \gamma Q_r^3 \cos^3 \Omega t = \Lambda_r \cos \Omega t \tag{118}$$

Introducing the relation between the cube of a cosine and linear terms, Eq. (118) becomes:

$$\left(-\Omega^2 + \omega_r^2\right) Q_r \cos \Omega t + \epsilon \frac{3}{2m^2L^2} \gamma \frac{Q_r^3}{4} \left(3 \cos \Omega t + \cos 3\Omega t\right) = \Lambda_r \cos \Omega t \tag{119}$$

By harmonic balance of the driving terms (only the response close to the forcing frequency is of interest), the following relation is obtained:

$$\left(-\Omega^2 + \omega_r^2\right) Q_r + \epsilon \frac{9}{8m^2L^2} \gamma Q_r^3 = \Lambda_r \tag{120}$$

This algebraic equation can be solved via a second order perturbation approach such that:

$$Q_r = Q_{r0} + \epsilon Q_{r1} + \epsilon^2 Q_{r2} + \mathcal{O}(\epsilon^3) \tag{121}$$

and results in the following equations to be solved (up to the second order perturbation):

$$\begin{aligned}
\mathcal{O}(\epsilon^0) &: \left(-\Omega^2+\omega_r^2\right) Q_{r0} = \Lambda_r \\
\mathcal{O}(\epsilon^1) &: \left(-\Omega^2+\omega_r^2\right) Q_{r1} = -\frac{9}{8m^2L^2}\gamma Q_{r0}^3 \\
\mathcal{O}(\epsilon^2) &: \left(-\Omega^2+\omega_r^2\right) Q_{r2} = -3\frac{9}{8m^2L^2}\gamma Q_{r0}^2 Q_{r1}
\end{aligned} \tag{122}$$

Therefore the response is:

$$w(x,t) = \frac{P_r(x)}{-\Omega^2+\omega_r^2}\left[\Lambda_r - \epsilon\frac{\frac{9}{8m^2L^2}\gamma}{(-\Omega^2+\omega_r^2)^3}\Lambda_r^3 + \epsilon^2 3\frac{\frac{81}{64m^4L^4}\gamma^2}{(-\Omega^2+\omega_r^2)^6}\Lambda_r^5\right]\cos\Omega t \tag{123}$$

Considering a sine load distribution in the span of the beam $f(x,t) = f_c \sin\frac{\pi x}{L}\cos(\Omega t)$, the modal contribution is: $\Lambda_r = f_c\sqrt{\frac{L}{2m}}$. The Newton iteration is therefore expressed as:

$$\begin{aligned}
f_{k+1} &= f_k - \left[P_1(x_i)\tfrac{1}{\omega_1^2-\Omega^2}\sqrt{\tfrac{L}{m2}}\right]^{-1} P_1(x_i)\tfrac{1}{\omega_1^2-\Omega^2}\sqrt{\tfrac{L}{m2}}\left[(f_k - \epsilon\alpha f_k^3 + \right. \\
&\left. +\epsilon^2\beta f_k^5) - \left(f_{ref} - \epsilon\alpha f_{ref}^3 + \epsilon^2\beta f_{ref}^5\right)\right] \\
f_{k+1} &= f_{ref} + \epsilon\alpha\left(f_k^3 - f_{ref}^3\right) - \epsilon^2\beta\left(f_k^5 - f_{ref}^5\right)
\end{aligned} \tag{124}$$

with $\alpha = \frac{9}{16m^3L(-\Omega^2+\omega_r^2)^3}\gamma$ and $\beta = \frac{243}{256m^6L^2(-\Omega^2+\omega_r^2)^6}\gamma^2$.

An example of the convergence of a non-linear case is shown in Figure 121, in which the loads are evaluated with different orders of non-linearity.For first and second order approximations the load converges quickly to the reference loads even in case of large initial discrepancies between the numerical and reference systems.

6.6 Property Confluence Algorithm as a Newton iterative method

Similar to the LCA, the PCA can be expressed as a Newton approach. In this case, the parameters $\boldsymbol{p}$ are related to the physical properties of the system, as for example the mass per unit length of an element. As in the case of the LCA, in order to express the Newton iteration it is first necessary to approximate the Jacobian of the system at the $k-th$ iteration. It is then assumed that the system is characterized by a periodic behavior, so that each quantity can be approximated with a Fourier series.

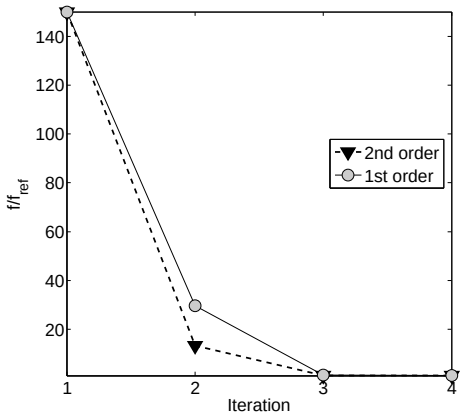

Figure 121: Convergence of the Newton iterations for a non-linear system in case of first and second order approximations of the response.

Each Fourier coefficient of the dynamic response can be expressed through its modal components by means of the incomplete modal matrix, $\boldsymbol{e}(\boldsymbol{p}) = \boldsymbol{B}(\boldsymbol{p})\boldsymbol{q}(\boldsymbol{p})$. Differently than the previous approach, the modal matrix $\boldsymbol{B}$ depends on the parameters $\boldsymbol{p}$, and its derivatives need to be evaluated in order to compute the Jacobian of the system. The Jacobian matrix is evaluated from the second-order, linear and undamped equations of motion. Initially, it is assumed that the system undergoes changes in mass properties only and that the stiffness matrix and the external loads are accurately represented. The equations of motion for the evaluation of the Jacobian are therefore:

$$\boldsymbol{M}_k \ddot{\boldsymbol{u}}_k + \boldsymbol{K}_0 \boldsymbol{u}_k = \boldsymbol{F}_0 \tag{125}$$

Derive Eq. (125) with respect to a parameter p_l:

$$\left.\frac{\partial \boldsymbol{M}}{\partial p_l}\right|_k \ddot{\boldsymbol{u}}_k + \boldsymbol{M}_k \left.\frac{\partial \ddot{\boldsymbol{u}}}{\partial p_l}\right|_k + \boldsymbol{K}_0 \left.\frac{\partial \boldsymbol{u}}{\partial p_l}\right|_k = \boldsymbol{0} \tag{126}$$

Due to the change in mass, at each $k-th$ iteration the eigenvectors of the system change. The new eigenvectors are assumed to be a linear combination of the eigenvectors of the initial system $\boldsymbol{P}_k = \boldsymbol{P}_0 \boldsymbol{\alpha}_k$. These combination coefficients also link matrix $\boldsymbol{B}$ at different iterations to the initial matrix $\boldsymbol{B}_k = \boldsymbol{B}_0 \boldsymbol{\alpha}_k$. The derivative of the dynamic response with respect to a parameter p_l is therefore:

$$\boldsymbol{F}'(\boldsymbol{p}) = \left.\frac{\partial \boldsymbol{e}}{\partial p_l}\right|_k = \boldsymbol{B}_0 \left.\frac{\partial (\boldsymbol{\alpha q})}{\partial p_l}\right|_k \tag{127}$$

The derivative of the displacement similarly depends on the derivative of the generalized modal coordinates:

$$\left.\frac{\partial \boldsymbol{u}}{\partial p_l}\right|_k = \boldsymbol{P}_0 \left.\frac{\partial(\boldsymbol{\alpha q})}{\partial p_l}\right|_k \tag{128}$$

Introducing this relation into Eq. (126):

$$\left.\frac{\partial \boldsymbol{M}}{\partial p_l}\right|_k \ddot{\boldsymbol{u}}_k + \boldsymbol{M}_k \boldsymbol{P}_0 \left.\frac{\partial(\boldsymbol{\alpha}\ddot{\boldsymbol{q}})}{\partial p_l}\right|_k + \boldsymbol{K}_0 \boldsymbol{P}_0 \left.\frac{\partial(\boldsymbol{\alpha q})}{\partial p_l}\right|_k = \boldsymbol{0} \tag{129}$$

Assume now that the change in mass matrix linearly depends on the mass parameter p_l and that their relation $\dfrac{\partial \boldsymbol{M}}{\partial p_l}$ is known and kept constant during the iterations, so that:

$$\boldsymbol{M}_k = \boldsymbol{M}_{k-1} + \sum_{l=1}^{N_p} \left.\frac{\partial \boldsymbol{M}}{\partial p_l}\right|_0 \left(p_{l_k} - p_{l_{k-1}}\right) \tag{130}$$

with N_p number of parameters to be identified.

Similarly to the LCA, the dynamic response of the system is characterized by a periodic response of frequency Ω, so that each element of the Newton function corresponds to a Fourier coefficient of the response of the system. The derivative of each sine and cosine coefficient with respect to each parameter p_l therefore coincides. In order to isolate the derivative of the generalized coordinates, Eq. (129) is pre-multiplied by the initial eigenvectors of the system, and assuming an harmonic behavior of the system:

$$-j^2\Omega^2 \boldsymbol{P}_0^T \frac{\partial \boldsymbol{M}_0}{\partial p_l} \boldsymbol{u}_k + \left(-j^2\Omega^2 \boldsymbol{P}_0^T \boldsymbol{M}_k \boldsymbol{P}_0 + \boldsymbol{P}_0^T \boldsymbol{K}_0 \boldsymbol{P}_0\right) \left.\frac{\partial \boldsymbol{\alpha q}}{\partial p_l}\right|_k = \boldsymbol{0} \tag{131}$$

from which:

$$\left.\frac{\partial \boldsymbol{\alpha q}}{\partial p_l}\right|_k = \left[-j^2\Omega^2 \boldsymbol{P}_0^T \boldsymbol{M}_k \boldsymbol{P}_0 + \boldsymbol{P}_0^T \boldsymbol{K}_0 \boldsymbol{P}_0\right]^{-1} \left[j^2\Omega^2 \boldsymbol{P}_0^T \frac{\partial \boldsymbol{M}_0}{\partial p_l} \boldsymbol{u}_k\right] \tag{132}$$

The displacement of the system is linked to the generalized response of the system through the incomplete modal matrix, $\boldsymbol{u}_k = \boldsymbol{P}_0 \boldsymbol{B}_0^+ \boldsymbol{e}_k$. The Jacobian results:

$$\left.\frac{\partial \boldsymbol{e}}{\partial p_l}\right|_k = \boldsymbol{B}_0 \left[-j^2\Omega^2 \boldsymbol{P}_0^T \boldsymbol{M}_k \boldsymbol{P}_0 + \boldsymbol{P}_0^T \boldsymbol{K}_0 \boldsymbol{P}_0\right]^{-1} \left[j^2\Omega^2 \boldsymbol{P}_0^T \frac{\partial \boldsymbol{M}_0}{\partial p_l} \boldsymbol{P}_0 \boldsymbol{B}_0^+ \boldsymbol{e}_k\right] \tag{133}$$

and the transition equation:

$$\begin{aligned}\boldsymbol{p}_{k+1} &= \boldsymbol{p}_k - \left\{\boldsymbol{B}_0\left[-j^2\Omega^2\boldsymbol{P}_0\boldsymbol{M}_k\boldsymbol{P}_0 + \boldsymbol{P}_0\boldsymbol{K}_0\boldsymbol{P}_0\right]^{-1}\left[j^2\Omega^2\boldsymbol{P}_0^T\frac{\partial \boldsymbol{M}_0}{\partial \boldsymbol{p}}\boldsymbol{P}_0\boldsymbol{B}_0^+\boldsymbol{e}_k\right]\right\}^+(\boldsymbol{e}_k - \boldsymbol{e}_{ref}) \\ \boldsymbol{p}_{k+1} &= \boldsymbol{p}_k - \left[j^2\Omega^2\boldsymbol{P}_0^T\frac{\partial \boldsymbol{M}_0}{\partial \boldsymbol{p}}\boldsymbol{P}_0\boldsymbol{B}_0^+\boldsymbol{e}_k\right]\left[-j^2\Omega^2\boldsymbol{P}_0\boldsymbol{M}_k\boldsymbol{P}_0 + \right. \\ &\quad \left. + \boldsymbol{P}_0\boldsymbol{K}_0\boldsymbol{P}_0\right]\boldsymbol{B}_0^+(\boldsymbol{e}_k - \boldsymbol{e}_{ref})\end{aligned} \tag{134}$$

In order to avoid singularities in the solution of this system, different approximations for parameters $\boldsymbol{p}$ are obtained from the sine and cosine components. These values are then averaged to find the best approximation of $\boldsymbol{p}$.

Following a similar procedure, in case of a change in stiffness properties, the transition equations are:

$$\boldsymbol{p}_{k+1} = \boldsymbol{p}_k + \left[\boldsymbol{P}_0^T\frac{\partial \boldsymbol{K}_0}{\partial \boldsymbol{p}}\boldsymbol{P}_0\boldsymbol{B}_0^+\boldsymbol{e}_{0_k}\right]\boldsymbol{P}_0\boldsymbol{K}_0\boldsymbol{P}_0\boldsymbol{B}_0^+\left(\boldsymbol{e}_{0_k} - \boldsymbol{e}_{0_{ref}}\right) \tag{135}$$

for the constant coefficient, and:

$$\boldsymbol{p}_{k+1} = \boldsymbol{p}_k + \left[\boldsymbol{P}_0^T\frac{\partial \boldsymbol{K}_0}{\partial \boldsymbol{p}}\boldsymbol{P}_0\boldsymbol{B}_0^+\boldsymbol{e}_{c/s_k}\right]\left[-j^2\Omega^2\boldsymbol{P}_0\boldsymbol{M}_k\boldsymbol{P}_0 + \boldsymbol{P}_0\boldsymbol{K}_0\boldsymbol{P}_0\right]\boldsymbol{B}_0^+\left(\boldsymbol{e}_{c/s_k} - \boldsymbol{e}_{c/s_{ref}}\right) \tag{136}$$

for the sine and cosine coefficients.

6.7 Analysis of PCA with analytical examples

The convergence properties of PCA are investigated with the use of an analytical example. A simply supported beam is considered with a change in mass per unit length m.

The Jacobian of the iteration is found through the second order, linear, and undamped equations of motion with homogeneous boundary and initial conditions. Following the procedure described in the previous section, in case of a single harmonic load, it is expressed as:

$$\frac{\partial e(x_i)}{\partial m} = P_0(x_i)\frac{\Omega}{m_k\left(\omega_k^2 - \Omega^2\right)}\left(\alpha_k q_k\right) \tag{137}$$

with ω_k natural frequencies of the system at iteration k.

Case 1: exact representation of the external loads Consider a case in which the numerical external loads exactly represent the reference system and in which both systems are characterized by linear and undamped equations of motion. The reference response is described by the equation of motion and boundary and initial conditions:

$$\begin{aligned} &EIw_{ref}^{IV}(x,t) + \hat{m}\,\ddot{w}_{ref}(x,t) = f(x,t) \\ &w_{ref}(0,t) = 0 \quad w_{ref}(L,t) = 0 \quad EIw_{ref}^{II}(0,t) = 0 \quad EIw_{ref}^{II}(L,t) = 0 \\ &w_{ref}(x,0) = 0 \quad \dot{w}_{ref}(x,0) = 0 \end{aligned} \tag{138}$$

and the numerical response is represented by:

$$\begin{aligned} &EIw^{IV}(x,t) + m\,\ddot{w}(x,t) = f(x,t) \\ &w(0,t) = 0 \quad w(L,t) = 0 \quad EIw^{II}(0,t) = 0 \quad EIw^{II}(L,t) = 0 \\ &w(x,0) = 0 \quad \dot{w}(x,0) = 0 \end{aligned} \tag{139}$$

The reference response is therefore:

$$w_{ref}(x_i,t) = \sum_{r=1}^{N_e} \frac{\hat{P}_r(x_i)}{\hat{\omega}_r^2}\lambda_{ref_{r_0}} + \frac{\hat{P}_r(x_i)}{\hat{\omega}_r^2 - j^2\Omega^2}\left[\lambda_{r_{s_j}}\sin j\Omega t + \lambda_{r_{c_j}}\cos j\Omega t\right] \tag{140}$$

with $\hat{P}_r(x) = \sqrt{\frac{m}{\hat{m}}}P_r(x)$, $\hat{\omega}_r = \sqrt{\frac{m}{\hat{m}}}\omega_r$ and $\hat{m}$ modes, natural frequencies and mass of the reference system respectively. The numerical response at the $k-th$ iteration is:

$$w_k(x_i,t) = \sum_{r=1}^{N_e} P_r(x_i)\left\{\gamma_r\lambda_{r_{0_k}} + \bar{\alpha}_{r_j}\lambda_{r_{s_{j_k}}}\sin j\Omega t + \bar{\alpha}_{r_j}\lambda_{r_{c_{j_k}}}\cos j\Omega t\right\} \tag{141}$$

The Newton iteration is expressed as:

$$m_{k+1} = m_k - \frac{m_k\left(\omega_k^2 - \Omega^2\right)}{\Omega^2}\left[1 - \frac{m_k\left(\omega_k^2 - \Omega^2\right)}{\hat{m}\left(\hat{\omega}^2 - \Omega^2\right)}\right] \tag{142}$$

with $\hat{m}$ and $\hat{\omega}$ distributed mass and natural frequencies of the reference system. No errors in the evaluation of the Jacobian and objective function exist, so the iteration converges to the reference solution.

Multiple iterations are necessary to converge to a solution even for this simple case, Figure 122, due to the non-linear relation between the physical properties of the system and its response.

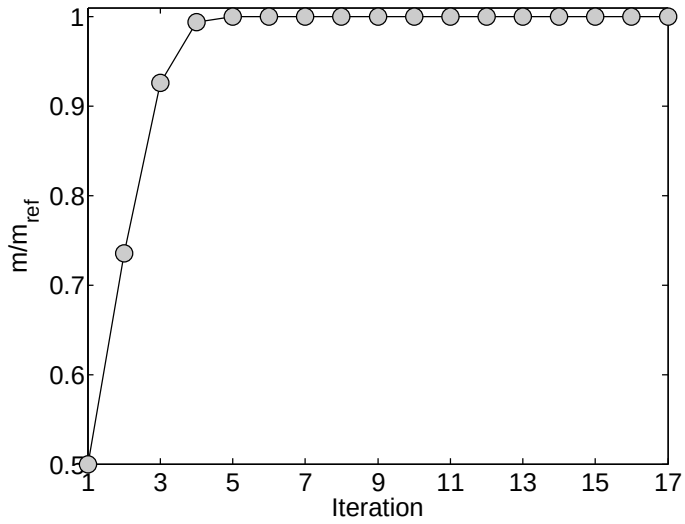

Figure 122: Convergence of the Newton iterations for a linear system in case of a difference in distributed mass, f = 10 Hz.

Moreover, for this simple system, one mode is sufficient to extrapolate all the information regarding the change in mass. In fact, the relationship between the eigenvectors and natural frequencies at different iteration does not change for higher modes, $P_{i_k} = \sqrt{\frac{m_{ref}}{m_k}} P_{i_{ref}}$, $\omega_{i_k} = \sqrt{\frac{m_{ref}}{m_k}} \omega_{i_{ref}}$.

Case 2: inexact representation of the external loads When applying the property identification algorithm to a real system, it can also happen that the external loads are not exactly modeled, and that errors in its representation exist. In this case, the identified properties represent both the inaccuracies in mass and stiffness distributions and the errors on the external load. This introduces an error in the definition of the Jacobian and of the objective function that can prevent the convergence of the Property Confluence Algorithm. The problem is in fact that the iterations try to represent any error in the system as an inertial load (or elastic in case of differences in stiffness), but not every external load can be represented in such a form. This is very different from the Load Confluence Algorithm, since every change in properties can be represented as an equivalent external load.

The type of errors existing between the numerical and reference system are therefore critical for the ability of the iterations to converge. Figure 123 illustrates this concept for different errors on the loads with respect to the case of exact representation of the loads. It shows that the progressive increase of the difference in loads breaks the convergence of the iterations, and the identified mass becomes even negative. The iteration at this point is interrupted because a negative mass breaks the physics of the dynamic system. This observation suggests that it is necessary to ensure that the external loads are adequately represented by the numerical system.

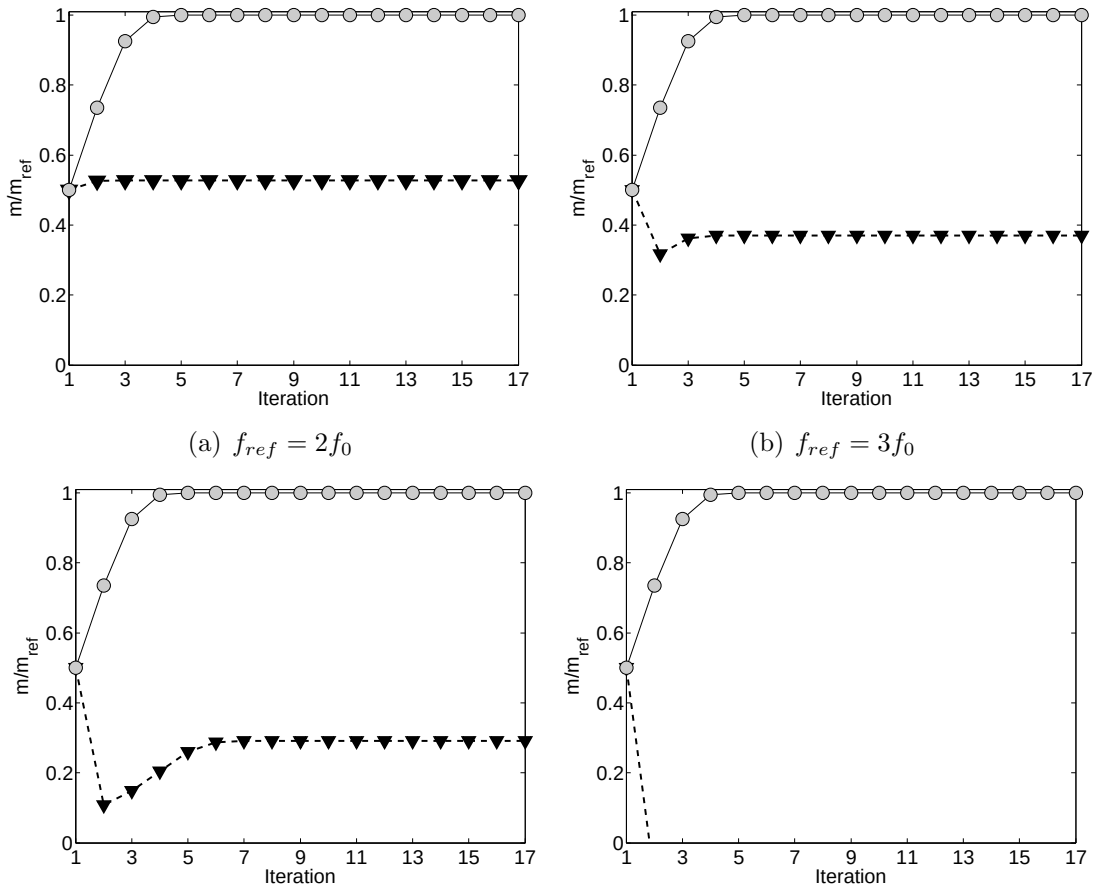

(a) $f_{ref} = 2f_0$ (b) $f_{ref} = 3f_0$

(c) $f_{ref} = 4f_0$ (d) $f_{ref} = 5f_0$

Figure 123: Convergence of the Newton iterations for a linear system in case of a difference in distributed mass and loads, f = 10 Hz. Exact loads (o), inexact loads (▼).

6.8 Conclusions

This chapter shows that the LCA and PCA can be formulated as a Newton approach, and their convergence properties can be analyzed through classical approaches. The objective function to be minimized is defined as the difference between numerical and reference response in terms of Fourier coefficients. The parameters to be evaluated correspond to the external loads in LCA and to the increment in physical properties in PCA. The algorithms converge to the reference response provided that the objective function is represented with sufficient accuracy. This is achieved if all participating modes that characterize the dynamic response are included in the identification process.

CHAPTER VII

CONCLUDING REMARKS

7.1 Summary

The research presented in this work investigates the possibility of improving the accuracy of numerical models through a combined analytical and experimental algorithm, called Confluence Algorithm. Experimental measurements of the dynamic response (stresses, strains and displacements) are embedded into a non-linear numerical model based on which linearized corrections of loads and properties of the system are updated. The need for this research comes from the application to rotating environments for which the accurate prediction of aerodynamic loads, as well as their measurement, still remains a difficult task, and justifies the general assumption of periodic systems. The integration of experimental measurements has the potential of improving fatigue estimation for a less conservative design by correcting modeling inaccuracies.

The Confluence Algorithm is an iterative procedure that consists of two different modules that update the dynamic response based on a correction of the external loads or of the dynamic properties of the system. These corrections are determined through the modal approximations of the undamped equations of motion of the system, and are formulated assuming a periodic behavior, as typical for rotating components. The first module, called Load Confluence Algorithm, updates the externally applied loads to account for modeling inaccuracies and unmodeled dynamics. Reconstruction of the external loads is shown to improve the accuracy of the dynamic response after a few iterations, both in case of simple systems such as beams and plates and in case of complex rotating systems. The second module, called Property Confluence Algorithm,

corrects the dynamic response of the system by iteratively applying linearized corrections to the mass and stiffness properties. An exact knowledge of the external loads is assumed. Applications of the Property Confluence Algorithm to one-dimensional structures indicate its promising possibilities for monitoring structural degradations and modifications.

The Confluence Algorithm represents a valuable tool for the achievement of tailored models for complex dynamic components. Accurate reconstruction of the response of the structure from few experimental measurements is guaranteed in case of inaccuracies in the modeling of external loads and/or dynamic properties, without requiring strict assumptions on the nature of the inaccuracy. Moreover, a very accurate model of the system is not necessary. Due to its flexibility and generality, it can be applied to map the response of very different and complex systems, such as helicopters and wind turbines. It therefore represents a general approach that can be easily extended to different cases, or structures.

7.2 Research Contributions

The research presented in this work offers the following unique contributions:

- formulation and implementation of a combined analytical and experimental procedure for loads and model updating,
- application of the algorithm to well-controlled experimental environments (one- and two-dimensional),
- application of the algorithm to complex rotating systems, such as rotorcraft,
- analysis of the convergence properties of the iterative algorithm.

7.3 Roadmap to the System Confluence Algorithm

The Load Confluence Algorithm and the Property Confluence Algorithm separately correct the external loads and the mass and stiffness properties of the system. The removal of the assumption of a separate occurrence of load and property inaccuracies, and the desire to isolate these two kinds of errors, require the formulation of a new algorithm, called System Confluence Algorithm, that relies on the measurement of the response of multiple systems operating in similar conditions and applies multiple times the LCA and PCA. In this way, the two algorithms are combined to create a tailored, high-fidelity model of the dynamic system.

A possible formulation of the System Confluence Algorithm compares the dynamic response of three different systems: an initial numerical model ("initial guess"), a first reference system that differs from the initial model for the definition of external loads, and a second reference that is subject to the same loads as the first reference but differs from it for its physical properties (mass/stiffness) because of structural modifications. The initial numerical system and this second reference system will therefore differ both because of inaccuracies in the physical properties and in the loads.

The difference in loads is extracted by comparing the response of the first reference system and the guess model, by applying the Load Confluence Algorithm. Then, the LCA is applied between the guess model and the second reference, and an equivalent difference in loads is identified that accounts both for inaccuracies in loads and properties. The comparison of these two sets of identified loads extrapolates the difference in physical properties.

The algorithm can be summarized as:

1. apply the Load Confluence Algorithm between the initial guess system and reference system 1 in order to identify a first set of loads $\boldsymbol{f}_1$,

2. apply the Load Confluence Algorithm between the initial guess system and reference system 2 in order to identify a second set of loads $\boldsymbol{f}_2$,

3. extract the difference in mass and stiffness properties between reference 1 and 2 from the difference between the two load sets ($\boldsymbol{f}_2 - \boldsymbol{f}_1$).

Following this procedure, the System Confluence Algorithm systematically corrects the external loads and the physical properties of the initial model based on the measured response. Practical applications in a rotating system could be implemented as follows:

- initial properties of the system are accurately defined in the design and validation phase, and are assumed to be known thereafter. An initial model of the system is constructed based on this information,

- a particular set of operating conditions is chosen as reference, and will be used to compare the response of the system at different moments in its life,

- the dynamic response is measured and recorded in each reference condition, and the model of the external loads is updated to match the experimental results by applying the Load Confluence Algorithm,

- when the actual condition of the system needs to be checked, the response of the structure in the specified set of reference flight conditions is recorded, and external loads identified,

- the new set of loads is compared to the previously identified set of loads, and the change in mass and stiffness that generated their eventual discrepancy is computed according to the following linearized relations:

$$\begin{aligned} (\boldsymbol{M} - \boldsymbol{\Delta M})\,\ddot{\boldsymbol{u}} + (\boldsymbol{K} - \boldsymbol{\Delta K})\,\boldsymbol{u} &= \boldsymbol{F} \\ \boldsymbol{M}\ddot{\boldsymbol{u}} + \boldsymbol{K}\boldsymbol{u} &= \underbrace{\boldsymbol{F} + \boldsymbol{\Delta M}\ddot{\boldsymbol{u}} + \boldsymbol{\Delta K}\boldsymbol{u}}_{\boldsymbol{F}_{eq}} \end{aligned} \tag{143}$$

A block diagram of the System Confluence Algorithm is shown in Figure 124 to illustrate this concept.

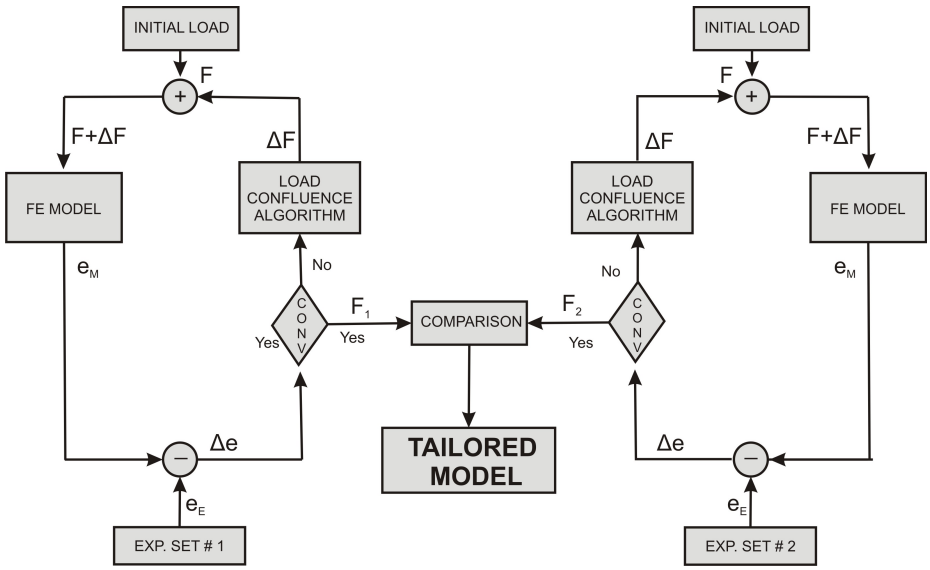

Figure 124: Block diagram of the System Confluence Algorithm

7.4 Recommendation for future work

7.4.1 Validation of PCA and SCA

In this thesis, the applications of the Property Confluence Algorithm have been limited to linear numerical and experimental examples. However, the monitoring of changes in mass and stiffness properties during operations is a challenging problem for any type of systems, in particular for rotorcrafts and wind turbines. The PCA needs therefore to be validate in case of non-linearities in the response.

More research needs to be done to define the formulation and validation of the System Confluence Algorithm so that external loads and physical properties can be simultaneously monitored during operations. In this case, CA can be included in usage monitoring systems on helicopters and wind turbines as a step toward Condition Based Maintenance.

7.4.2 Estimation of servo loads on helicopters

Ample opportunities for further research are provided by the inaccuracy in the estimation of servo loads on helicopters, such has the force in the hydraulic damper and in the pitch-link, in order to monitor the fatigue behaviour of these components. The LCA could be used as a means to improve their numerical prediction with respect to experimental measurements, similarly to Force Determination techniques described in section 1.4.2. By improving the accuracy of the response along the blades and therefore at their root, it is expected that the servo-loads will be improved as well.

7.4.3 Addition of a bottom-up approach to include response of non-rotating components

In this thesis, the CA is proposed for applications to rotorcrafts. In the previous paragraph, the prediction of hub loads is obtained from measurements of the response of the blades. This approach can be referred to as "top-down". Another interesting aspect to be studied deals with the development of a similar approach that, from the measurements in the fixed frame, such as on the fuselage, predicts the hub loads with a "bottom-up" approach. By unifying the two methods, both the information in the rotating and in the fixed frame could be exploited to achieve very accurate information on the hub-loads.

7.4.4 Analysis of non-periodic unsteady loading conditions

As described in [73, 23, 54] for the UH-60A, the flight envelope of a rotorcraft is limited by level-flight conditions as well as manouvres. Manouvres often represent limiting conditions for the helicopter and its components, and need therefore to be monitored and well predicted in order to study their effects on critical components. The analysis of LCA, and of PCA, are currently limited to study level-flight conditions. However, their expansion to study more general flight conditions would be valuable. This extension requires the formulation of the methods for non-periodic systems.

7.4.5 Monitoring of the weight of helicopters during operations

The weight of an helicopter changes during operations due to fuel consumption, payload release or increase. This value determines the inertial loads acting on the system, and needs to be well-evaluated. The LCA and PCA could be expanded to monitor the weight of the rotorcraft during operations and to provide its accurate estimate.

7.4.6 Application to trimming

Further opportunities for research are also provided by the study of the capabilities of LCA to "train" a numerical model based on a limited number of flight conditions, and to then use this model to analyze different flight conditions, and for trimming. For example, the information presented in this thesis on flight condition C9017 could be used to improve the predictions of similar manoeuvres, such as C9020, without the need of reapplying the LCA, in order to achieve"blind" predictions.

7.5 Conclusions

The Confluence Algorithm represents a promising tool for the monitoring of dynamic components at non-accessible locations. Examples in linear and non-linear conditions demonstrates that CA could be implemented in conjunction with simple numerical models of the experimental system and obtain accurate results with reduced computational effort.

The applicability of the algorithm to the analysis of periodic systems limits the range of problems that can be analyzed. However, in case of rotating systems such as wind-turbines and rotorcraft, it represents a simple and valuable tool for the improvement of numerical predictions.

REFERENCES

[1] Abhishek, A., Datta, A., and Chopra, I., "Prediction of UH-60A structural loads using multibody analysis and swashplate dynamics," *Journal of the Aircraft*, vol. 46, no. 2, pp. 474–490, 2009.

[2] Agneni, A., Balis Crema, l., and Coppotelli, G., "Operational modal analysis," *Mechanical systems and signal processing*, vol. 24, no. 5, pp. 1240–1249, 2010.

[3] Agneni, A., Coppotelli, G., and Grappasonni, C., "A method for the harmonic removal in operational modal analysis in rotating blades," *Mechanical Systems and Signal Processing*, vol. 27, pp. 604–618, 2012.

[4] Alonso, F., Del Castillo, J., and Pintado, P., "Motion data processing and wobbling mass modelling in the inverse dynamics of skeletal models," *Mechanism and Machine Theory*, vol. 42, no. 9, pp. 1153–1169, 2007.

[5] Ambrosio, J. and Kecskemethy, A., *Multibody Dynamics of biomechanical models for human motion via optimization, in Multibody Dynamics (Computational Methods and Applications)*. Dordrecht: Springer, 1 ed., 2007.

[6] Andersen, M., Benit, D., Damsgaard, M., Ramsey, D., and Rasmussen, J., "Do kinematic models reduce the effects of soft tnumber artefacts in skin marker-based motion analysis? An in vivo study of knee kinematics," *Journal of Biomechanics*, vol. 43, no. 2, pp. 268–273, 2010.

[7] Bartlett, F. and Flannelly, W., "Model verification of force determination for measuring vibratory loads," *Journal of the American Helicopter Society*, vol. 24, no. 2, pp. 10–18, 1979.

[8] Bauchau, O., "DYMORE: a finite element based tool for the analysis of nonlinear flexible multibody systems." http://www.ae.gatech.edu/people/obauchau/dymore.pdf.

[9] Bauchau, O., Bottasso, C., and Nikishkov, Y., "Modeling rotorcraft dynamics with finite element multibody procedures," *Mathematical and Computer Modeling*, vol. 33, no. 10–11, pp. 1113 – 1137, 2001.

[10] Bauchau, O. and Kang, N., "A multibody formulation for helicopter structural dynamic analysis," *Journal of The American Helicopter Society*, vol. 38, no. 2, pp. 3–14, 1993.

[11] Bauchau, O. and Liu, H., "On the modeling of hydraulic components in rotorcraft systems," *Journal of the American Helicopter Society*, vol. 51, no. 2, pp. 175–184, 2006.

[12] Berman, A. and Fuh, J., "Structural system identification using multiple tests," in AIAA *Dynamics Specialists Conference*, (Long Beach, CA), April 1990.

[13] Berman, A., "System identification of a complex structure," in ASME*, and* SAE*, Structures, Structural Dynamics, and Materials Conference, 16th*, (Denver, CO), May 1975.

[14] Berman, A., "Improved orthogonality check for measured modes," *AIAA Journal*, vol. 18, no. 9, pp. 1151–1152, 1980.

[15] Berman, A., "System identification of structural dynamic models. theoretical and practical bounds," AIAA*–1984–929*, 1984.

[16] Berman, A., "Multiple acceptable solutions in structural model improvement," *AIAA Journal*, vol. 33, no. 5, pp. 924–927, 1995.

[17] Berman, A. and Nagy, E., "Improvement of analytical dynamic models using modal test data," in *Structures, Structural Dynamics, and Materials Conference, 23rd*, (New Orleans, LA), May 1982.

[18] Berman, A. and Nagy, E., "Improvement of a large analytical model using test data," *AIAA Journal*, vol. 21, no. 8, pp. 1168–1173, 1983.

[19] Berman, A., Wei, F., and Rao, K. V., "Improvement of analytical dynamic models using modal test data," in *Structures, Structural Dynamics, and Materials Conference, 21st*, (Seattle, Washington), May 1980.

[20] Bogert, P., Haugse, E., and Gehrki, R., "Structural shape identification from experimental strains using a modal transformation technique," in *44th* AIAA/ASME/ASCE/AHS *Structures, Structural Dynamics, and Materials Conference*, (Norfolk, VA), April 7–10 2003.

[21] Bousman, W., "Estimation of blade airloads from rotor blade bending moments," NASA TM*–100020*, 1987.

[22] Bousman, W., "An investigation of helicopter rotor blade flap vibratory loads," in *American Helicopter Society International 48th Annual Forum Proceedings*, (Washington D.C., USA), June 3–5 1992.

[23] Bousman, W. and Kufeld, R., "UH-60A airloads catalog," NASA TM*–212827*, 2005.

[24] Calapodas, N. and Hoff, K., "Force determination sensitivities study for full-scale helicopter ground vibration testing," *USAAVSCOM TM-89-D-4*, 1989.

[25] Cappozzo, A., Catani, F., Leardini, A., Benedetti, M., and Della Crce, U., "Position and orientation in space of bones during movement: experimental artefacts," *Clinical Biomechanics*, vol. 11, no. 2, pp. 90–100, 1996.

[26] Chierichetti, M., McColl, C., Palmer, D., Ruzzene, M., and Bauchau, O., "Combined analytical and experimental approaches to rotor components stress predictions," in *The 1st Joint International Conference on Multibody System Dynamics*, (Lappeenranta, Finland), May 25–27 2010.

[27] Chierichetti, M., Ruzzene, M., Bauchau, O., McColl, C., and Palmer, D., "Prediction of UH-60 blade loads: an insight on confluence algorithm to correct internally generated airloads," in *American Helicopter Society International 67th Annual Forum Proceedings*, (Virginia Beach, VA), May 3–5 2011.

[28] Chierichetti, M., McColl, C., Palmer, D., Ruzzene, M., and Bauchau, O., "Combined analytical and experimental approaches to rotor components stress predictions," *Proceedings of the Institution of Mechanical Engineers - Part K, Journal of Multibody Dynamics*, vol. 225, pp. 322–330, 2011.

[29] Chierichetti, M. and Ruzzene, M., "Model updating in structural dynamics through a confluence algorithm," *Journal of Theoretical and Applied Mechanics*, vol. 49, no. 3, 2011.

[30] Chierichetti, M. and Ruzzene, M., "Dynamic displacement field reconstruction through a limited set of point measurements: application to plates," *Journal of Sound and Vibrations*, vol. 10.1016/j.jsv.2012.05.031, 2012.

[31] Chierichetti, M. and Ruzzene, M., "Model updating in structural dynamics through a confluence algorithm," in *Proceedings of the 53rd* AIAA/ASME/ASCE/AHS/ASC *Structures, Structural Dynamics*, (Honolulu, USA), 23–26 April 2012.

[32] Ciang, C. C., Lee, J.-R., and Bang, H.-J., "Structural health monitoring for a wind turbine system: a review of damage detection methods," *Measurement Science and Technology*, vol. 19, no. 12, p. 122001, 2008.

[33] Datta, A. and Chopra, I., "Validation of structural and aerodynamic modeling using UH-60A airloads program data," *Journal of the American Helicopter Society*, vol. 51, no. 1, pp. 43–58, 2006.

[34] Datta, A. and Chopra, I., "Prediction of the UH-60A main rotor structural loads using computational fluid dynamics/comprehensive analysis coupling," *Journal of the American Helicopter Society*, vol. 53, no. 4, pp. 351–365, 2008.

[35] Datta, A. and Johnson, W., "Three-dimensional finite element formulation and scalable domain decomposition for high-fidelity rotor dynamic analysis,"

Journal of the American Helicopter Society, vol. 56, no. 2, pp. 22003–22003–14(–1), 2011.

[36] Datta, A., Nixon, M., and Chopra, I., "Review of rotor loads with the emergence of rotorcraft CFD," *Journal of the American Helicopter Society*, vol. 52, no. 4, 2007.

[37] Devriendt, C., De Sitter, G., Vanlanduit, S., and Guillaume, P., "Operational modal analysis in the presence of harmonic excitations by the use of transmissibility measurements," *Mechanical Systems and Signal Processing*, vol. 23, no. 3, pp. 621–635, 2009.

[38] Fabunmi, J. A., "Modal constraints on structural dynamic force determination," *Journal of the American Helicopter Society*, vol. 30, no. 4, pp. 48–54, 1985.

[39] Farrar, C. R. and Worden, K., "An introduction to structural health monitoring," *Philosophical Transactions: mathematical, physical and engineering sciences*, vol. 365, no. 1851, pp. 303–315, 2007.

[40] Friswell, M. and Mottershead, J., *Finite element model updating in structural dynamics*. Kluwer Academic Publishers, 1993.

[41] Glaessgen, E., Smith, S., and Stargel, D., "The digital twin paradigm for future nasa and u.s. air force vehicles," in *53rd* AIAA/ASME/ASCE/AHS/ASC *Structures, Structural Dynamics and Materials Conference*, (Honolulu, Hawaii), April 23–26 2012.

[42] Guice, J., "Renewable energy grows up," *www.renewableenergyworld.com*, 2007.

[43] Hahn, B., Durstewitz, M., and Rohrig, K., "Reliability of wind turbines. experiences of 15 years with 1500 W," *Wind Energy*, pp. 329–332, 2007.

[44] Herlufsen, H., Andersen, P., Gade, S., and Møller, N., "Identification techniques for operational modal analysis–an overview and practical experiences," in *Proceedings 1st IOMAC Conference*, 2005.

[45] Hild, F. and Roux, S., "Digital image correlation: from displacement measurement to identification of elastic properties–a review," *Strain*, vol. 42, no. 2, pp. 69–80, 2006.

[46] Howlett, J. J., "UH-60A Black Hawk engineering simulation program: Vol. i - mathematical model," NASA CR-*166309*, 1981.

[47] Jiang, X. and Hu, H., "Reconstruction of distributed dynamic loads on a thin plate via mode-selection and consistent spatial expression," *Journal of Sound and Vibration*, vol. 323, no. 3–5, pp. 626–644, 2008.

[48] Johnson, W., "Rotorcraft dynamics models for a comprehensive analysis," in *American Helicopter Society Internation 54th Annual Forum Proceedings*, (Washington, D.C.), May 20–22, 1998.

[49] Johnson, W., "Milestones in rotorcraft aeromechanics," NASA TP–*2011–215971*, 2011.

[50] Jones, R., Flannelly, W., Nagy, E., and Fabunmi, J., "Experimental verification of force determination and ground flying on a full-scale helicopter," *USAAVRADCOM TR-81-D-11*, 1981.

[51] Kelley, C., *Iterative methods for linear and nonlinear equations*. Philadelphia: SIAM, 1 ed., 1995.

[52] Kufeld, R. M., Balough, D. L., Cross, J. L., Studebaker, K. F., Jennison, C. D., and Bousman, W. G., "Flight testing of the UH-60A aircraft," in *American Helicopter Society International 50th Annual Forum Proceedings*, (Washington, D.C.), May 11–13, 1994.

[53] Kufeld, R. and Bousman, W., "High load conditions measured on a UH-60A in manoeuvring flight," *Journal of the American Helicopter Society*, vol. 43, no. 3, pp. 202–211, 1998.

[54] Kufeld, R. and Bousman, W., "Technical note. UH-60A airloads program azimuth reference correction," *Journal of the American Helicopter Society*, vol. 50, no. 2, pp. 211–213, 2005.

[55] Lacarbonara, W., "A theoretical and experimental investigation of nonlinear vibrations of buckled beams," *Master thesis for Virginia Polytechnic Institute and State University*, 1997.

[56] Leclerc, H., Périé, J., Roux, S., and Hild, F., "Integrated digital image correlation for the identification of mechanical properties," in *Proceedings of the 4^{th} conference on Computer Vision/Computer Graphics CollaborationTechniques*, pp. 161–171, Springer, 2009.

[57] Liu, Y. and Shepard, W., "An improved method for the reconstruction of a distributed force acting on a vibrating structure," *Journal of Sound and Vibration*, vol. 291, no. 1–2, pp. 369–387, 2006.

[58] Lombardo, D., "Helicopter structures - a review of loads, fatigue design techniques and usage monitoring," *AR-007-137*, 1993.

[59] McColl, C., Palmer, D., Chierichetti, M., Bauchau, O., and Ruzzene, M., "Comprehensive UH-60 loads model validation," in *American Helicopter Society Internation 66th Annual Forum Proceedings*, (Phoenix, AZ), May 11–13 2010.

[60] Mottershead, J. and Friswell, M., "Model updating in structural dynamics: A survey," *Journal of Sound and Vibration*, vol. 167, no. 2, pp. 347–375, 1993.

[61] Oosterhuis, E. J., Eidhof, W. B., van der Hoogt, P. J., and de Boer, A., "Force prediction via the inverse FRF using experimental and numerical data from a demonstrator with tunable nonlinearities," in *The 13th International Congress on Sound and Vibration*, (Wien, Austria), July 2–6 2006.

[62] Peeters, B., Cornelis, B., Janssens, K., and Van der Auweraer, H., "Removing disturbing harmonics in operational modal analysis," in *Proceedings of International Operational Modal Analysis Conference, Copenhagen, Denmark*, 2007.

[63] Pezerat, C. and Guyader, J., "Force analysis technique: reconstruction of force distribution on plates," *ACUSTICA - acta acustica*, vol. 86, no. 2, pp. 322–332, 2000.

[64] Piascik, B., Vickers, J., Lowry, D., Scotti, S., Stewart, J., and Calomino, A., "Draft: Materials, structures, mechanical systems, and manufacturing roadmap," *Technology Area 12,* NASA*, November 2010.*

[65] Potsdam, M., Yeo, H., and Johnson, W., "Rotor airloads prediction using multidisciplinary coupling," in *DOD 2005 Users Group Conference*, (Nashville, TN), June, 27–30 2005.

[66] Réthoré, J., "A fully integrated noise robust strategy for the identification of constitutive laws from digital images," *International Journal for Numerical Methods in Engineering*, vol. 84, no. 6, pp. 631–660, 2010.

[67] Shafto, M., Conroy, M., Doyle, R., Glaessgen, E., Kemp, C., LeMoigne, J., and Wang, L., "Draft: Modeling, simulation, information techonology and processing roadmap," *Technology Area 11,* NASA*, November 2010.*

[68] Simms, D. and Butterfield, C., "A comparison of spanwise aerodynamic loads estimated from measured bending moments versus direct pressure measurements on horizontal axis wind turbine blades," in *Windpower'91 Conference and exposition*, (Palm Springs, CA), September 24–27 1991.

[69] Smith, M. J., Lim, J. W., van der Wall, B., Baeder, J. D., Biedron, R., Boyd, D. Douglas, J., Jayaraman, B., and Jung, S. N., "An assessment of CFD/CSD prediction state-of-the-art using the HART II international workshop data," in *Proceedings of the 68th American Helicopter Society Forum*, (Ft. Worth, TX), May 1–3 2012.

[70] Tessler, A., "Structural analysis methods for structural health management of future aerospace vehicles," NASA TM*–2007–214871*, 2007.

[71] Tessler, A. and Spangler, J., "A variational principle for reconstruction of elastic deformations in shear deformable plates and shells," NASA TM–*2003–212445*, 2003.

[72] Tessler, A. and Spangler, J., "Inverse FEM for full-field reconstruction of elastic deformations in shear deformable plates and shells," in *2nd European Workshop on Structural Health Monitoring*, (Munich, Germany), July 7–9 2004.

[73] NASA, "UH-60A airloads project." http://halfdome.arc.nasa.gov/research/uh-60.html.

[74] Tuegel, E., "The airframe digital twin: Some challenges to realization," in *53rd* AIAA/ASME/ASCE/AHS/ASC *Structures, Structural Dynamics and Materials Conference*, (Honolulu, Hawaii), April 23–26 2012.

[75] Tuegel, E. J., Ingraffea, A. R., Eason, T. G., , and Spottswood, S., "Reengineering aircraft structural life prediction using a digital twin," *International Journal of Aerospace Engineering, Article ID 154798*, 2011.

[76] van der Wall, B. G., Lim, J., Smith, M., Jung, S. N., Bailly, J., Amiraux, M., and Boyd, D. D., J., "An assessment of comprehensive code prediction state-of-the-art using the HART II international workshop data," in *Proceedings of the 68th American Helicopter Society Forum*, (Ft. Worth, TX), May 1–3 2012.

[77] Vaughan, R., Chang, J., and Rogers, M., "Obtaining usage credits from monitoring of helicopter dynamic components without impacting safe life reliability," in *American Helicopter Society Internation 63rd Annual Forum Proceedings*, (Virginia Beach, BA), May 1–3, 2007.

[78] Volkin, R. S., "Estimation of rotor blade torsional deformations from measured blade torsional moments," *Master thesis for the Naval Postgraduate School*, 2002.

[79] Walford, C., "Wind turbine reliability: understanding and minimizing wind turbine operation and maintenance costs," *SANDIA Report, SAND2006-1100*, 2006.

[80] Wang, B., "Prediction of impact and harmonic forces acting on arbitrary structures: theoretical formulation," *Mechanical Systems and Signal Processing*, vol. 16, no. 6, pp. 935–953, 2002.

[81] Wang, W., Mottershead, J., Ihle, A., Siebert, T., and Schubach, H. R., "Finite element model updating from full-field vibration measurement using digital image correlation," *Journal of Sound and Vibration*, vol. 330, no. 8, pp. 1599–1620, 2011.

[82] Wang, W., Mottershead, J., and Mares, C., "Vibration mode shape recognition using image processing," *Journal of Sound and Vibration*, vol. 326, no. 3–5, pp. 909–938, 2009.

[83] Wang, W., Mottershead, J., Sebastian, C., and Patterson, E., "Shape features and finite element model updating from full-field strain data," *International Journal of Solids and Structures*, vol. 48, no. 11–12, pp. 1644–1657, 2011.

[84] Yeo, H. and Johnson, W., "Comparison of rotor structural loads calculated using comprehensive analysis," in *31st European Rotorcraft Forum*, (Firenze, Italy), September 13–15, 2005.

[85] Zhang, L., "An overview of operational modal analysis: major development and numbers," *Time*, no. 1, pp. 179–190, 2004.